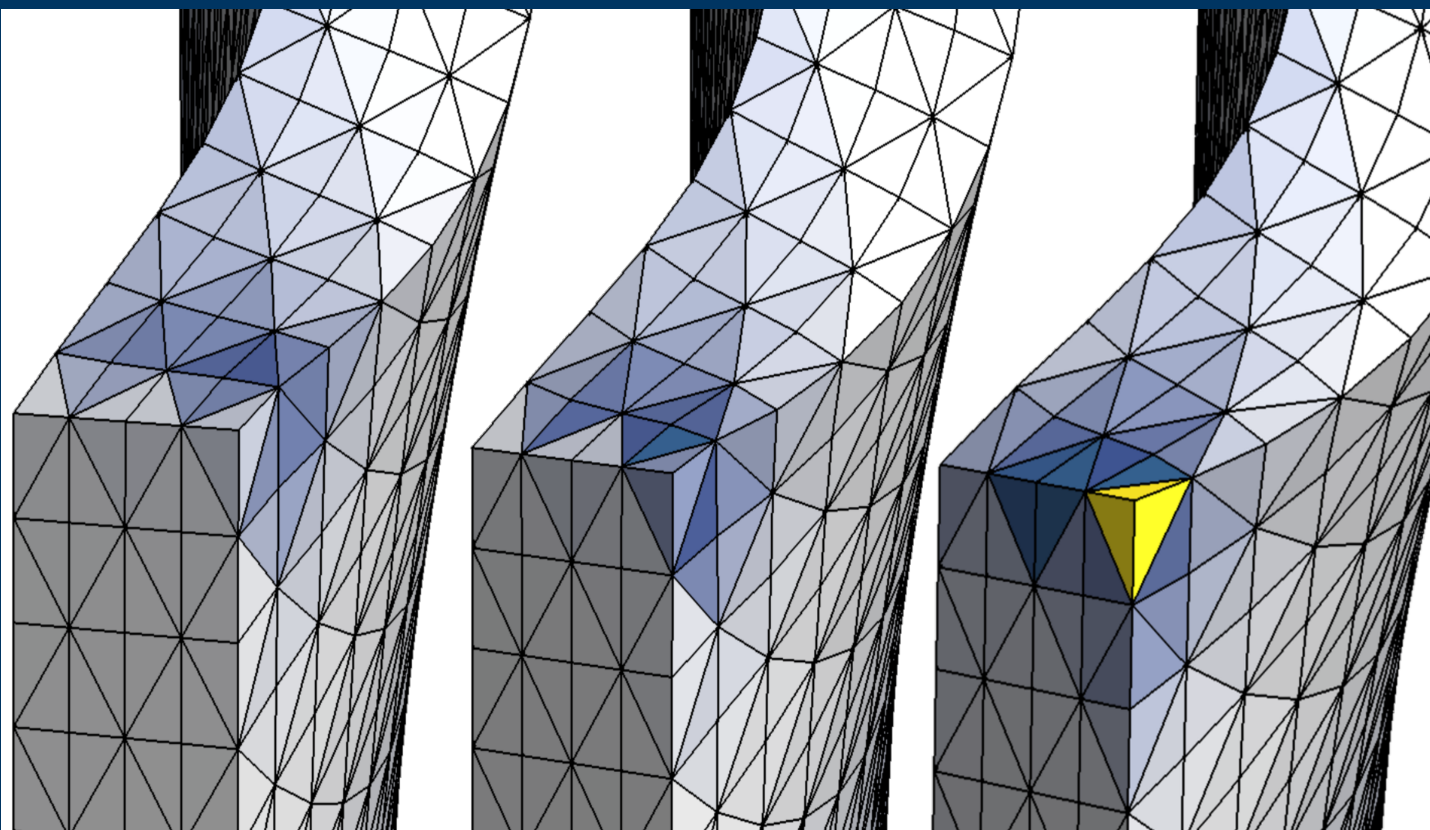


Finite Element Formulations for Gradient-Enhanced Models in Solid Mechanics

Johannes Riesselmann



Finite Element Formulations for Gradient-Enhanced Models in Solid Mechanics

Zur Erlangung des Grades
Doktor-Ingenieur
an der Fakultät Maschinenbau
der Ruhr-Universität Bochum
genehmigte Dissertation

von
Johannes Riesselmann
aus Münster

Bochum 2024

Mitteilungen aus dem Institut für Mechanik
Nr. 194

Publisher:

Institute of Mechanics
Ruhr University Bochum
D-44780 Bochum

Prof. Dr.-Ing. habil. Daniel Balzani
Chair for Continuum Mechanics

Herausgeber:

Institut für Mechanik
Ruhr-Universität Bochum
D-44780 Bochum

Prof. Dr.-Ing. habil. Daniel Balzani
Lehrstuhl für Kontinuumsmechanik

ISBN: 978-3-935892-72-8

Copyright © 2024 by Johannes Riesselmann

All rights reserved.

No parts of this work may be reproduced or used in any matter without written permission of the copyright holder.

Dieses Werk ist urheberrechtlich geschützt.

Alle Rechte, einschließlich der Vervielfältigung, Veröffentlichung, Bearbeitung und Übersetzung, bleiben vorbehalten.

Dissertation eingereicht am (Thesis submission):
Mündliche Prüfung am (Thesis Defense):
Erstgutachter (First referee):
Zweitgutachter (Second referee):
Prüfungsvorsitz (Committee chair):

29.04.2024

04.07.2024

Prof. Dr.-Ing. habil. Daniel Balzani

Prof. Dr.-Ing. habil. Jörg Schröder

Prof. Dr.-Ing. Martin Mönningmann

Preface

The work presented within this thesis was done during my time as PhD student and research assistant at the Chair of Continuum Mechanics at the Ruhr University Bochum. I would like to thank all the people who supported me during this time inside and outside the university. In particular, but not exclusively:

First of all, my academic teacher Professor Daniel Balzani for his excellent professional and personal advice, his interest for my research, numerous fruitful discussions and creating a space for exploration of scientific ideas. His great ability to build important scientific connections with numerous collaboration partners laid the essential foundation for the present work. My special thanks go also to Professor Jörg Schröder for his interest in my research and with his extensive knowledge sparking numerous productive discussions after my presentations at the great number of conferences, workshops and annual meetings, many of which within the DFG Priority Program 1748, which he is also the spokesperson of. At this point, I need to point out my gratitude for the DFG for the financial funding of our project BA2823/15-1 within the aforementioned SPP 1748.

Of course, my very particular thanks go also to Professor Mira Schedensack and Jonas Kettler for contributing with their mathematical expertise to the analytical results of our joint publications as well as helping me get for this work very relevant deeper insights into the mathematical foundations of mixed finite element formulations. Further, I want to thank Professor Luca Placidi and Nasrin Rezaei for helping to propel ideas forward during our numerous constructive discussions. Next, I would like to thank Professor Philipp Junker for helpful councils and productive discussions. Lastly, I want to thank all my colleagues and friends who helped make (not only) the last years an exciting and very enjoyable chapter of my life.

At the end I would like to dedicate a distinguished hearty thanks to my family, especially my mother, my father, my brother and my deceased grandmother for giving me support at the very fundamental level. Finally, my extraordinary thanks go to my partner Johanna for her encouragement and patience, especially during the final stages of producing this work.

Bochum, April 2024

Johannes Riesselmann

Abstract

Gradient enhanced continuum formulations provide the ability to model size effects, avoid non-physical stress singularities and enable corresponding numerical solution schemes to remain mesh independent. Further, specifically in the context of damage modeling they procure the modeled partial differential equations to remain elliptic even in the regime of severe damage and loss of material stiffness allowing for corresponding suitable numerical schemes to remain robust. However, due to the occurrence of higher gradients matching finite element formulations are generally challenged with higher continuity requirements of the approximated fields increasing complexity and costliness. The present thesis contributes various mixed finite element formulations for gradient elasticity and gradient damage, which have the advantage that through the introduction of mixed and Lagrange multiplier variables, simpler interpolation schemes become feasible. Moreover, by choosing suitable corresponding approximation functions, the increase in global degrees of freedom compared to classical formulations is kept at a minimum. For gradient elasticity, several mixed formulations akin to the Hu-Washizu variational principle are proposed with approximation functions that allow for the condensation of degrees of freedom corresponding to the mixed and Lagrange multiplier variable. Followed by that is the introduction of a formulation, which through incorporation of a rotation-free displacement gradient variable, enables for a reduced size of the problem by decoupling the displacements from the main equation while fulfilling the relevant mathematical stability conditions. For gradient damage a formulation is proposed in which by utilizing the values of the Lagrange multiplier to distinguish between damage loading and unloading conditions no additional sub-iterations and storage of history parameters is required. Corresponding approximation functions enable for the static condensation of the degrees of freedom of the Lagrange multiplier as well as parts of the damage modeling variable, further minimizing computing cost. The presented formulations are accompanied by various numerical tests on several benchmark problems, verifying the consistency, numerical robustness and mesh convergence behavior as well as computing times not far from classical local finite elements.

Zusammenfassung

Gradientenerweiterte kontinuumsmechanische Formulierungen bieten die Möglichkeit Größeneffekte zu modellieren, unphysikalische Spannungssingularitäten zu vermeiden und führen somit zu Netzunabhängigkeit von zugehörigen numerischen Simulationen. Speziell im Zusammenhang mit der Schädigungsmodellierung sorgt die Gradientenerweiterung außerdem dafür, dass die zugrunde liegenden partiellen Differentialgleichungen auch bei starker Schädigung und einhergehender Abnahme der Materialsteifigkeit ihre Elliptizität beibehalten und entsprechende Lösungsverfahren ihre numerische Robustheit bewahren. Aufgrund des Auftretens höherer Gradienten sind zugehörige Finite-Elemente-Formulierungen jedoch mit höheren Anforderungen an die Kontinuität der approximierten Felder konfrontiert, was zu grundsätzlich zu einer Zunahme an Komplexität und Rechenaufwand führt. In der vorliegenden Arbeit werden verschiedene Finite-Elemente-Formulierungen für gradientenerweiterte Elastizität und Schädigung vorgestellt, welche durch die Einführung von gemischten und Lagrange-Multiplikator-Variablen die Verwendung einfacher Interpolationsfunktionen ermöglichen. Darüber hinaus wird durch die Wahl geeigneter Approximationsfunktionen die Zunahme der globalen Freiheitsgrade gegenüber klassischer Formulierungen minimiert. Für die Gradientenelastizität werden mehrere gemischte Formulierungen in Anlehnung an das Hu-Washizu-Variationsprinzip mit Approximationsfunktionen vorgeschlagen, die ein Auskondensieren der zu den gemischten- und Lagrange-Multiplikator-Variablen gehörigen Freiheitsgrade ermöglichen. Darauf folgend wird eine Formulierung eingeführt, welche durch die Einbeziehung einer rotationsfreien Gradientenvariable einen entkoppelten Gleichungssatz ermöglicht, der die mathematischen Stabilitätsbedingungen erfüllt. Für die Modellierung gradientenerweiterter Schädigung wird eine Formulierung präsentiert, bei welcher der Lagrange-Multiplikator zur Auswertung der Schädigungsevolutionsbedingung verwendet wird. Dadurch werden weder zusätzliche Sub-Iterationen noch die Speicherung von Geschichtsvariablen benötigt. Darüber hinaus ermöglichen entsprechend gewählte Approximationsfunktionen das Auskondensieren von Freiheitsgraden und minimieren so den Rechenaufwand. Die vorgestellten Formulierungen werden von zahlreichen numerischen Tests begleitet, in denen die Konsistenz, die numerische Robustheit und die Netzkonvergenz sowie die Rechenzeiten, welche in den untersuchten Beispielen nicht weit von denen der klassischen lokalen Finiten Elemente entfernt sind, verifiziert werden.

Contents

Introduction and Basic Principles	3
1 Introduction, Motivation and Outline	3
1.1 Gradient Elasticity	4
1.2 Gradient Damage	7
1.3 Scope and Outline	8
2 Continuum Mechanical Fundamentals	11
2.1 Definitions	11
2.1.1 Tensor Operators	11
2.1.2 Differential Operators	13
2.1.3 Function Spaces and Norms	14
2.1.4 Important Identities	19
2.2 Finite Strain Kinematics and Stress Measures	19
2.3 Variational Principles	21
2.3.1 Time Discretization	21
2.3.2 Variation	22
2.3.3 Linearization	23
2.3.4 Example: Local Hyperelasticity	24
2.4 Fundamentals of Mixed Variational Formulations	24
2.4.1 Introduction to Mixed Variational Formulations	25
2.4.2 Definition of Stability	26
2.4.3 The Inf-Sup Condition	27
2.4.4 Brezzi's Splitting Theorem Applied to Three-Field Formulations	28
3 Fundamentals of the Finite Element Method	31
3.1 Fundamentals of Finite Element Interpolation Functions	31
3.1.1 Interpolation Problem, Degrees of Freedom and Shape Functions	31
3.1.2 Example: Lowest Order Raviart-Thomas Interpolation	33
3.2 Finite Element Parametrizations	35
3.2.1 Example: Raviart-Thomas Interpolation Over the Reference Element	39
3.3 Example: $P2$ -Discretization of the Elasticity Problem	42
3.3.1 Quadratic Nodal Lagrange Interpolation	42

3.3.2	Discrete Weak Form	43
3.3.3	Matrix Notation	44
I	Finite Element Formulations for Gradient Elasticity	47
4	Purely Displacement Based Formulation	49
4.1	The Gradient Elasticity Problem	49
4.2	Challenges of a C^1 Continuous Interpolation	50
4.2.1	Degrees of Freedom, Shape Functions and Interpolation Operator	51
4.2.2	Visualization of the Interelement Continuity	54
4.2.3	Finite Element Computation	57
4.2.4	Summary and Discussion of Challenges	60
5	Hu-Washizu Type Mixed FE for Gradient Elasticity	63
5.1	Straightforward Approach	63
5.1.1	Continuous Formulation	64
5.1.2	Discretizations	66
5.2	H-Div Λ -Formulation	69
5.2.1	Continuous Formulation	69
5.2.2	Discretization	70
5.3	Formulation with Symmetric Solution Fields	74
5.3.1	Continuous Formulation	74
5.3.2	Discretization	75
6	Rotation-Free Mixed FE for Gradient Elasticity	77
6.1	Continuous Formulation	77
6.1.1	Decomposed Lagrange Multiplier Method	77
6.1.2	Continuous Lagrangian of the RotFEM Approach	78
6.1.3	2D Variational Formulation	79
6.1.4	3D Variational Formulation	80
6.1.5	Stability of the Linearized Continuous Formulation	80
6.2	Finite Element Approximations	82
6.2.1	Interpolation Matrices Pre- and Postprocessing Step	82
6.2.2	Interpolation Matrices of the Main Step in 2D	83
6.2.3	Interpolation Matrices of the Main Step in 3D	84
6.2.4	Stability Analysis of the Finite Element Approximations	85
7	Numerical Studies for Gradient Elasticity	89
7.1	Constitutive Framework	89
7.2	Unit Cube Benchmark Problem	91
7.3	Cook's Problem	96

7.4	Plate With Hole	100
7.5	Summary	101
II	Finite Element Formulations for Gradient Damage	105
8	Introduction and Some Challenges	107
8.1	Local Damage Formulation	107
8.1.1	Mesh Dependency and Lack of Robustness	109
8.2	The Gradient Damage Problem	109
8.3	Some Challenges of Existing Gradient Damage Formulations	112
8.3.1	Penalty Formulation	112
8.3.2	Neighbored Element Formulation	115
9	An Efficient FE Formulation for Gradient Damage	119
9.1	The Proposed Approach	119
9.1.1	Continuous Formulation	119
9.1.2	Discretizations	122
9.1.3	Algorithmic Treatment	124
9.2	Numerical Results	126
9.2.1	Convergence Study	126
9.2.2	Comparative Study	129
9.2.3	Behavior Under Cyclic Loading	131
9.2.4	Element Erosion	133
9.2.5	Parameter Study	133
	Treatise Conclusion and Outlook	139
	Appendix	143
A	Continuous Expressions	143
A.1	Continuous Gradient Elasticity Formulations	143
A.1.1	Formulations Corresponding to Section 5.1.1	144
A.1.2	Formulations Corresponding to Section 5.2.1	145
A.1.3	Formulations Corresponding to Section 5.3.1	147
A.2	Continuous Proposed Gradient Damage Formulation	148
B	Discrete Expressions	149
B.1	Static Condensation	149
B.2	Interpolation Matrices of the RotFEM Approach	150
B.3	Details on the H-Div Λ Discretization	151

List of Figures	155
List of Tables	157
Bibliography	159
List of Publications	167

Introduction and Basic Principles

Chapter 1

Introduction, Motivation and Outline

Founded on NEWTON's [1687] laws of motion the essential ingredients of classical continuum-mechanical models are EULER's [1752] equation of motion, namely the balance of linear momentum and the balance of angular momentum combined with CAUCHY's [1823] notion of the stress tensor, some constitutive relations (starting with HOOKE's [1678] law) and the principle of local action (among some other principles, see e.g. the summary of ALTENBACH [2012]). To this day, most of the concurrent corresponding common finite element software tools that are used for the computation of structural mechanical problems are rooted in these classical CAUCHY-continuum (also referred to as 'local') models, since they have been found to align with a wide range of experimental findings. This holds true particularly for standard construction materials, which are predominantly analyzed under small strains, such as common steel alloys used in civil and mechanical engineering applications. Also, a variety of materials that, when in operation, experience significant deformations and exhibit nonlinear elastic behavior can be accurately modeled by classical nonlinear continuum approaches (under consideration of more advanced kinematics). However, classical continuum theories fail to provide satisfactory models for a diverse array of materials, including granular solids, rocks, bone, animal blood, liquid crystals, composite materials and various other types of amorphous materials. Specifically, when the size of the material heterogeneities or microstructure becomes relatively large compared to the overall size of the modeled geometry, the disparity between the outcomes derived from classical continuum mechanics and experimental results becomes significant. This issue becomes even more prevalent in the vicinity of cracks and sharp edges or corners, where stress gradients are considerably large. In addition to the aforementioned materials, discrepancies are also observed in multi-molecular bodies like polymers, where the presence of nonlocal intermolecular attractions plays a crucial role. Another example of applications in which these beforementioned size effects play a role is e.g. in special semiconductor components which reach overall sizes on the micro- or even nanoscale and even non-standard electromechanical coupling effects can be observed. Another class of materials that is of growing research interest is the class of architected, so-called metamaterials, in which through special design of the internal structure the components can be designed to have very specific characteristics interesting for various advanced applications. Here, obviously by design the internal structure has nonlocal effects on the material behavior, for which corresponding material models utilized for the simulation of such need to account for. Overall it can be stated that, while local models can satisfactorily capture the physical behavior of numerous materials in application, still many advanced materials can not be accurately modeled. This motivates for the introduction of more advanced continuum models (more details in the next sections) that are able to capture the effects that are missed by local formulations. Moreover,

in order to be able to use these models to numerically simulate real world application cases the development of corresponding reliable and efficient finite element schemes (such as e.g. those subject to the present contribution) is crucial and with regards to incorporation into commercial software still in its infancy.

1.1 Gradient Elasticity

A remedy to the shortcomings of local elastic continuum models are non-local formulations that can account for size effects through the addition of extra kinematic quantities that fill in the gap between the modeled geometry's scale and the microstructure's scale. Proposals that expand the classical Cauchy continuum correspondingly date back to the work of COSSERAT AND COSSERAT [1909], that incorporates micro-rotations and micro-torques into the continuum principles, resulting in the development of polar media. This concept was subsequently expanded to settle the micro-rotations within a more general framework of micro-deformations, see the landmark contributions of MINDLIN's [1964] theory of microstructure in elasticity and TOUPIN's [1964] theory of elasticity with couple stress. In this context, worth mentioning is also the related micromorphic approach of ERINGEN [1999, 2002] among various other related contributions. The gradient elasticity theory, which is subject to the present contribution, is located within the more general framework of MINDLIN [1964] and can be considered a special case of the micro-deformation theory, in which the latter are modeled in terms of the displacement gradients. This brings the advantage that the entire formulation can be postulated by only one kinematic variable, namely the displacements, while still providing the ability to constitute the full scale-dependent nonlocal relations through the incorporation of higher order gradients. A historic overview of the emergence of gradient elasticity formulations can be found in BERTRAM [2022], see also ASKES AND AIFANTIS [2011] which gives an overview of various contributions made in this field. Another variational framework, from which the strain gradient elasticity formulation is derived, can be found in ABALI ET AL. [2017]. A constitutive law for gradient elasticity featuring the general case of nonlinear kinematic descriptors is given by DELL'ISOLA ET AL. [2018] and the extension of the strain gradient elasticity approach to incorporate plasticity and damage can be found in PLACIDI ET AL. [2021] (among others). An active field of research in the realm of gradient elasticity models is the correct determination of the additional constitutive parameters appearing in the model. These parameters link the local elastic constitutive parameters to a characteristic length parameter that take into account the scale of material heterogeneities relative to the scale of the macroscopic mechanical fields. The works of ABALI [2018] and YANG ET AL. [2019] propose approaches for the determination of the parameters based on action principles and asymptotic analysis, respectively. Meanwhile, in REZAEI ET AL. [2024] a specific experimental procedure is proposed using the pull-out test of a rigid bar along the symmetry axis of a cylindrical probe to determine the characteristic length parameter. An additional benefit of the strain gradient formulation is the ability to avoid the occurrence of stress singularities at sharp edges of the modeled body. In these occurrences the local elasticity formulations even fail to predict physically accurate solutions at all (cf. REZAEI ET AL. [2022]) and may in addition lead to mesh sensitive corresponding numerical results. An additional area where higher order gradient formulations find application is in the representation of aforementioned unique electromechanical coupling effects (cf. SERRAO AND KOZINOV [2023] and TANNHÄUSER ET AL. [2024]) observed, for instance, in nanosized semiconductor components.

Finite Elements For Gradient Elasticity When it comes to finite element formulations for gradient elasticity, the main challenge lies in meeting the C^1 continuity requirement. This requirement necessitates not only the continuity of the primal solution variable (i.e., the displacements) but also the continuity of the gradient of the primal solution variable across element interfaces. Therefore, interpolation schemes that are fully C^1 continuous incorporate additional degrees of freedom associated with higher order derivatives along with an increased polynomial order of the interpolating functions. Hence, the interpolation becomes considerably more complex, posing a significant challenge in its implementation, particularly for three-dimensional domains. In the more simple 2D scenario, the lowest order fully C^1 continuous element is the well known triangular element of ARGYRIS AND SCHARPF [1968] (see also OKABE [1993]) and requires already a polynomial order of five and 21 degrees of freedom, which is relatively large yet still usable. Meanwhile, the lowest order tetrahedral counterpart as first proposed by ŽENIŠEK [1973] (see also LAI AND SCHUMAKER [2007] as well as section 4.2 of this contribution) demands a minimum ninth order polynomial interpolation and 220 degrees of freedom for a single displacement component. In addition, corresponding element matrices encounter the issue of having very high condition numbers, which further questions their usability. When using typical solvers only certain meshes with a few elements can yield results (cf. ZHANG [2008], see also the discussion in section 4.2 of this contribution). An additional difficulty arises from the presence of face and edge derivative degrees of freedom, making the element not belong to the family of affine elements and the transformation of the interpolation operator from the reference to the physical element not straightforward. Yet, some methods on kinematic transformations for complex tetrahedral interpolation schemes are proposed by KIRBY [2018]. Various tetrahedral extensions have been proposed based on the subdivision technique, which was initially introduced in the form of the Hsiegh-Clough-Tocher triangular finite element CLOUGH AND TOCHER [1965]. These extensions offer a reduced number of degrees of freedom and a lower polynomial interpolation order, while still maintaining full C^1 continuity. However, the reduced size of these elements comes at the expense of increased complexity, as the subdivision of the macro-element requires the definition of corresponding shape functions and compatibility conditions for each sub-element. Nevertheless, some of these reduced interpolation approaches do not have edge- and face-derivative degrees of freedom, allowing for affine transformations. Additionally, they possess reasonable matrix conditions and corresponding convergence studies (cf. WALKINGTON [2014]) are possible. For more detailed information, refer to ALFELD [1984], LAI AND SCHUMAKER [2007], and WALKINGTON [2014]. Furthermore, some C^1 problems can be accurately solved by employing displacement-based finite elements with simpler non-conforming approximation schemes. A prominent example is the triangular element of MORLEY [1968] designed for the biharmonic problem. However, when the weak form includes first order gradients in addition to second order gradients, such as in gradient elasticity, the Morley element fails to achieve convergence (cf. NILSSEN ET AL. [2000]). While the modification proposed by NILSSEN ET AL. [2000] offers a solution for the elliptic singular perturbation problem characterized by full first and second order gradients in the weak form, it does not extend to symmetric gradients as encountered in the gradient elasticity problem. Another non-conforming strategy is the so-called Hermite interpolation method introduced by CIARLET AND RAVIART [1972] (also discussed in TABATA AND UEDA [2009] and KIRBY [2018]). Although the Hermite interpolation approach ensures full C^1 continuity in one-dimensional space, the corresponding two and three-dimensional elements exhibit C^1 continuity solely at the vertices, rendering them incapable of consistently solving general C^1 problems (cf. KIRBY [2018]; see also section 4.2 in this work). A noteworthy finite element formulation for gradient elasticity based on a hexahedral Hermite interpolation scheme is given by PAPANICOLOPULOS ET AL. [2008], however a corresponding

discussion of the fulfillment of the necessary conditions for C^1 continuity (e.g. the unisolvency of the interpolation problem on the interface¹) is still missing. In recent times, researchers have shown interest in the use of isogeometric analysis (IGA) for addressing higher gradient formulations. References HUGHES ET AL. [2005], RUDRARAJU ET AL. [2014] and WANG ET AL. [2016] present IGA approaches for gradient elasticity, where the computational domain is partitioned into patches and spline interpolation functions of arbitrary polynomial order are utilized instead of traditional finite element triangulations. One of the key advantages of IGA formulations is the ability to achieve C^1 or even higher continuity without increasing the complexity of the formulation. However, a persistent technical challenge lies in handling gaps and overlaps that may arise when trimming geometries to approximate the physical geometry, as discussed in detail in MARUSSIG AND HUGHES [2018]. This challenge can be viewed as a limitation compared to conventional finite elements, which benefit from well-established automatic mesh generation techniques. A noteworthy contribution in the context of IGA and tetrahedral meshes is given by LAI AND SCHUMAKER [2007], where a general framework for spline-based interpolation schemes for triangular and tetrahedral meshes is given, however, resulting again in complex C^1 elements. Furthermore, the literature has presented a variety of non-standard methods. One innovative approach is provided by WRIGGERS AND HUDOBIVNIK [2023] and utilizes the virtual finite element method for C^1 -continuous interpolations. Another method, known as the C^0 interior penalty method, was first introduced by BRENNER AND SUNG [2005] and can be viewed as a specialized version of the discontinuous Galerkin method. In this technique, standard C^0 interpolation functions are employed to discretize the weak form's volume integrals. However, to ensure the desired continuity of displacement gradients across element interfaces, additional interface integrals are introduced incorporating the interface continuity through penalty terms. In VENTURA ET AL. [2021], the application of this method to gradient elasticity is discussed. Yet, numerical experiments have shown that satisfactory convergence is achieved only when using interpolation functions of third order or higher. Another strategy involves the utilization of mixed finite element formulations. A commonly employed method is akin to the variational principle of HU [1955] and WASHIZU [1955]. In this approach, a Lagrange multiplier term is introduced to establish the compatibility between the displacement gradient and a mixed solution variable, allowing for the use of simpler C^0 continuous interpolation functions (first small strain contributions were given by SHU ET AL. [1999](2D) and ZYBELL ET AL. [2012](3D)). Resulting from using only C^0 functions, corresponding interpolation functions necessitate for much fewer degrees of freedom than the C^1 schemes, while (provided the underlying variational formulation is consistent) maintaining full conformity with the original formulation. However, in the mentioned literature the fulfillment of the mixed stability conditions (see e.g. BOFFI ET AL. [2013], BRAESS [2007] and section 2.4 of this contribution) is missing leading to issues with respect to numerical robustness. Moreover, the introduction of additional mixed variables naturally leads to additional degrees of freedom and finding formulations incorporating discretization schemes that remain computationally cost-efficient remains an important research objective. Therefore, the first part of the present work contributes various mixed finite element formulations for gradient elasticity which incorporate shown to be stable pairings of interpolation functions promising for robust numerical behavior while maintaining relative cost efficiency through specific suitable approximation techniques.

¹A corresponding discussion can be found in section 4.2 of this contribution.

1.2 Gradient Damage

The degradation of stiffness and softening of engineering and biological materials resulting from the deterioration of the microstructure can be modeled using continuum damage formulations. These models incorporate a damage variable, the evolution of which is determined by specific constitutive relations. The progression of the damage variable leads to a decrease in the strain energy density, reflecting the material's softening behavior (cf. LEMAITRE [1984], LEMAITRE AND CHABOCHE [1990] and KACHANOV [1986] for small strains). Formulations for damage under finite strain conditions are presented in the works of MIEHE [1995] and MENZEL AND STEINMANN [2001] (also see BALZANI ET AL. [2006], BALZANI. ET AL. [2012] for applications in biological tissue damage modeling). While local damage schemes may provide accurate solutions for minor damage levels, the governing equations may lose ellipticity as damage intensifies. Consequently, in such scenarios, numerical solution algorithms may fail to converge, resulting in mesh-dependent outcomes due to the localization of numerical values of the damage variable. Hence, in order to address this concern, several regularization techniques have been developed, and the advancement of robust and computationally efficient numerical formulations remains an active area of research. One strategy involves the creation of a relaxed incremental stress potential, which transforms the original nonconvex problem into a convex one (cf. GÜRSES AND MIEHE [2011]) and thereby providing a variational framework which allows for mesh independent simulations. Additionally, the large strain approach proposed by BALZANI AND ORTIZ [2012] and SCHMIDT AND BALZANI [2016], as well as the application of MIEHE [2011] to multi-field dissipative problems, offer further insights into this matter. However, these relaxation schemes initially lacked the capability to accurately model strain-softening, resulting in limited attention. Nevertheless, recent advancements in extended formulations have demonstrated the ability to incorporate strain softening, as evidenced by the works of SCHWARZ ET AL. [2020] and KÖHLER AND BALZANI [2023]. Another method involves spatial regularization by incorporating gradients of either the damage variable or the quantities driving damage (cf. PEERLINGS ET AL. [1996], also refer to PLACIDI. ET AL. [2021] for a strain gradient damage formulation in materials with granular microstructure). In the former scenario, the introduction of the gradient enhancement term transforms the damage evolution equation from a local constant equation to a partial differential equation. This transition to higher regularity helps prevent the loss of ellipticity and enables the attainment of mesh-independent solutions.

Numerical Methods for Gradient Damage In local damage finite element formulations, a common approach is to interpolate the displacements the usual way with Lagrange basis functions and to incorporate the update condition of the damage variable in terms of a local history variable. Since the corresponding gradient damage update equation is not local anymore (i.e. gradient operators are present), a storage of the damage variable as local history variable in corresponding finite element subroutines is not possible anymore as the resolution of the gradients comes with additional continuity requirements. Moreover, a straightforward update scheme of the damage equation at the material point level as in local formulations is no longer feasible. Yet, if the partial differential equation governing the damage evolution is considered in strong form, updating at the material point level remains viable. Nonetheless, the field equation in this case involves the Laplace operator, making it challenging to devise suitable discretization schemes. The methodology proposed by JUNKER ET AL. [2019] presents a numerical scheme for small strains (also see VOGEL AND JUNKER [2019] for an extension to finite strains in JUNKER ET AL. [2022] as well as section 8.3 of this contribution).

A limitation of these methods is that due to the necessity of information exchange across elements, conventional element-internal material subroutines can not be used anymore, thereby complicating implementation. An alternative to address this limitation is to introduce a finite element formulation with an additional nodal solution variable to incorporate the gradient enhancement. One of the earlier contributions in this regard is the finite element formulation by PEERLINGS ET AL. [1996], where the damage update is influenced by an equivalent strain measure introduced as a mixed variable, resulting in a two-field mixed formulation. An alternative method is presented in LIEBE ET AL. [2001], DIMITRIJEVIC AND HACKL [2008] and the finite strain formulation WAFFENSCHMIDT ET AL. [2013]. In these approaches, the damage field itself is represented by an additional nodal variable, and its equivalence to the locally updated history parameter is enforced through a penalty constraint term. Corresponding solution schemes can be solved monolithically without the need for additional global iterations as necessary in staggered approaches such as e.g. the related phase field formulations² of MIEHE ET AL. [2010b,a], GERASIMOV AND DE LORENZIS [2019]. When dealing with penalty gradient damage finite element formulations, however, maintaining numerical robustness in the presence of severe damage poses a challenge. Furthermore, when choosing low numerical values of the penalty parameter, values of the additionally introduced relaxed variable may vary significantly from the damage variable as the constraint condition weakens for smaller values of the penalty parameter. In such cases, the stiffness contributions of certain elements may be significantly reduced, resulting in difficult global matrix conditions, which are further exacerbated when a penalty term is introduced. Hence, the second part of the present work (specifically chapter 9) presents a Lagrange multiplier based mixed finite element approach with interpolation functions that satisfy numerical stability criteria without requiring a penalty term enabling for robust solutions. Additionally, utilizing a discretization scheme that allows for static condensation minimizes the size of the global tangent matrix, prevents zero-valued diagonal submatrices, and achieves a positive definite symmetric global matrix.

1.3 Scope and Outline

The present work is structured as follows.

- Firstly, the introductory **chapter 2** provides an overview of some fundamental concepts and definitions within the realm of the continuous body and spaces that are relevant for this contribution. Note, that here besides the rather commonly known concepts of the first sections of this chapter specifically the section 2.4 aims to give a summary of the stability conditions that are relevant to the numerical analysis of mixed formulations of the succeeding chapters of the main parts of this work.
- The second introductory **chapter 3** then provides an overview over some fundamentals of finite element interpolations with special emphasis on the ingredients necessary for a conforming approximation scheme as well as kinematics with respect to the interpolation over reference elements.

The first main part of this work is concerned with finite elements for gradient elasticity, framed within the general kinematic framework of finite strains.

²Noteworthy contributions in the field of phase field modeling are also the earlier works of FRANCFORT AND MARIGO [1998], BOURDIN ET AL. [2000]. See also the approach MIEHE ET AL. [2016] for modeling ductile fracture at finite strains with plasticity. For a comparison between gradient damage and phase field formulations, refer to DE BORST AND VERHOESEL [2016].

- Therefore, in the starting **chapter 4** the original (meaning purely displacement based) gradient elasticity problem is postulated and then the challenges accompanying C^1 -conforming fully displacement based approximations are illustrated by means of the corresponding lowest order 3D formulation.
- Providing a remedy by allowing for simple C^0 approximations **chapters 5 and 6** present suitable mixed finite element formulations based on the three field mixed variational formulation and the rot-free mixed variational formulation respectively. Here, the continuous formulations as well as the corresponding suitable approximation functions are shown together with the fulfillment of stability conditions mentioned in chapter 2 allowing for consistent, robust and efficient corresponding computations.
- In order to verify and compare the stability, robustness and efficiency of the formulations of the preceding chapters **chapter 7** provides numerical results and corresponding discussions for various relevant benchmark problems together with the corresponding constitutive large strain gradient elastic framework.

The second main part of this work is concerned with finite elements for finite strain gradient damage.

- Therefore, **chapter 8** introduces the general concept of damage formulations, the gradient damage problem and illustrates challenges of some existing finite element formulations motivating for the formulation of the subsequent chapter.
- Lastly, in **chapter 9** an efficient Lagrange multiplier based mixed finite element formulation is presented in terms of the continuous formulation, corresponding discretizations and algorithmic treatment. The robustness, efficiency as well as applicability within various ranges of parameters and boundary condition is shown in various numerical tests.

Chapter 2

Continuum Mechanical Fundamentals

2.1 Definitions

This section gives an overview of general definitions for tensor- and differential operators as well as spaces and identities that are relevant for the content of the subsequent chapters of this contribution. On the presented fundamentals numerous literature exists. Some selected references are BRAESS [2007] and ALTENBACH [2012]. Note, that the manifold on which everything that follows is based is with \mathbf{R}^d the d -dimensional Euclidean space with the corresponding standard metric $\|(\bullet)\| = \sqrt{\sum_{i=1}^d (\bullet)_i^2}$ (where i are the vector components).

2.1.1 Tensor Operators

In order to be able to describe field functions such as e.g. stress and strain measures, the first ingredient is the notion of the tensor. Therefore, let $(\bullet) \in \mathbf{R}^{d^n}$ be some n -order Tensor function describing the map

$$(\bullet) : \mathbf{X} \rightarrow \mathbf{R}^{d^n} \quad (2.1)$$

where $\mathbf{X} \in \mathbf{R}^d$ denotes a Cartesian based position vector and $d \in \{2, 3\}$ is the space dimension. For any two tensors (\bullet) and (\blacksquare) of the same order n the scalar product (inner product) is defined by the map

$$(\bullet) \cdot (\blacksquare) : \mathbf{R}^{3^n} \times \mathbf{R}^{3^n} \rightarrow \mathbf{R} \quad (2.2)$$

and describes the sum in which each summand corresponds to each entry of (\bullet) multiplied with the corresponding entry of (\blacksquare) . The scalar product enables for the definition of the generalized Frobenius norm

$$\|(\bullet)\| = \sqrt{(\bullet) \cdot (\bullet)}. \quad (2.3)$$

On various occasions it is necessary to build the inner product only over some parts of two tensors $(\bullet) \in \mathbf{R}^{d^n}$ and $(\blacksquare) \in \mathbf{R}^{d^m}$, which now may be of different orders n and m , respectively. The corresponding operations are with

$$\begin{aligned} (\bullet) \cdot (\blacksquare) &: \mathbf{R}^{d^n} \times \mathbf{R}^{d^m} \rightarrow \mathbf{R}^{d^{(n+m-2)}} \\ (\bullet) : (\blacksquare) &: \mathbf{R}^{d^n} \times \mathbf{R}^{d^m} \rightarrow \mathbf{R}^{d^{(n+m-4)}} \\ (\bullet) \dot{ : } (\blacksquare) &: \mathbf{R}^{d^n} \times \mathbf{R}^{d^m} \rightarrow \mathbf{R}^{d^{(n+m-6)}} \end{aligned} \quad (2.4)$$

denoted as the standard simple, double and triple contraction, respectively. Of course, the contraction operators are only applicable to tensors of at least first, second and third order,

respectively, since the result must at least be a scalar quantity $\mathbf{R}^{d^0} = \mathbf{R}$. The exterior product (dyadic product) is denoted by

$$(\bullet) \otimes (\blacksquare) : \mathbf{R}^{d^n} \times \mathbf{R}^{d^m} \rightarrow \mathbf{R}^{d^{n+m}} \quad (2.5)$$

such that any tensor $\mathbb{A} \in \mathbf{R}^{d^n}$ can be written with

$$A_{i_1 \dots i_n} \mathbf{e}_{i_1} \otimes \dots \otimes \mathbf{e}_{i_n} \quad (2.6)$$

in terms of coefficients $A_{i_1 \dots i_n}$ and corresponding base vectors $\mathbf{e}_{i_1}, \dots, \mathbf{e}_{i_n}$, which throughout this contribution for the sake of simplicity are taken to be the Cartesian base vectors. The third important type of product is the three-dimensional cross product of tensors with vectors, reads

$$(\bullet) \times (\blacksquare) : \mathbf{R}^{3^n} \times \mathbf{R}^3 \rightarrow \mathbf{R}^{3^n} \quad (2.7)$$

and is applied row wise to tensor-valued functions. The following operators are concerned with tensors of specific order. In the case of a second order tensor $\mathbf{A} \in \mathbf{R}^{3 \times 3}$ and a vector $\mathbf{b} \in \mathbf{R}^3$ the coefficients of the cross product explicitly read

$$\mathbf{A} \times \mathbf{b} := \begin{bmatrix} A_{13}b_2 - A_{12}b_3 & A_{11}b_3 - A_{13}b_1 & A_{12}b_1 - A_{11}b_2 \\ A_{23}b_2 - A_{22}b_3 & A_{21}b_3 - A_{23}b_1 & A_{22}b_1 - A_{21}b_2 \\ A_{33}b_2 - A_{32}b_3 & A_{31}b_3 - A_{33}b_1 & A_{32}b_1 - A_{31}b_2 \end{bmatrix}. \quad (2.8)$$

Yet, in the planar case in line with the notation that is classically used e.g. when considering the mechanics of planar motion the vector product can be written as

$$\begin{bmatrix} a_1 \\ a_2 \\ 0 \end{bmatrix} \times \begin{bmatrix} b_1 \\ b_2 \\ 0 \end{bmatrix} = \begin{bmatrix} 0 \\ 0 \\ a_2b_1 - a_1b_2 \end{bmatrix}. \quad (2.9)$$

In what follows in the two-dimensional case for the cross product the reduced notation is used, resulting in the definition

$$\begin{bmatrix} a_1 \\ a_2 \end{bmatrix} \times \begin{bmatrix} b_1 \\ b_2 \end{bmatrix} = a_2b_1 - a_1b_2 \quad (2.10)$$

that reduces the tensorial order by one. Generalized to 2D tensors, it can be described by the map

$$(\bullet) \times (\blacksquare) : \mathbf{R}^{2^n} \times \mathbf{R}^2 \rightarrow \mathbf{R}^{2^{n-1}}. \quad (2.11)$$

Thus, explicitly in this case the coefficients of the cross product of a second order tensor $\mathbf{A} \in \mathbf{R}^{2 \times 2}$ and a vector $\mathbf{b} \in \mathbf{R}^2$ then read

$$\mathbf{A} \times \mathbf{s} := \begin{bmatrix} A_{12}b_1 - A_{11}b_2 \\ A_{22}b_1 - A_{21}b_2 \end{bmatrix}. \quad (2.12)$$

Introduce the symmetric operator acting on second order tensors by

$$\text{sym}(\bullet) := \frac{1}{2}((\bullet)^T + (\bullet)) \quad \forall (\bullet) \in \mathbf{R}^{3 \times 3}. \quad (2.13)$$

Further, denote $\mathbb{S} := \{(\bullet) \in \mathbf{R}^{3 \times 3} : \text{sym}(\bullet) = (\bullet)\}$ as the space of symmetric second order tensors. Analogously to (2.13) define the symmetric operator for the coefficients $(\bullet)_{ijk}$ of third order tensors (which appear typically in gradient elasticity formulations) as follows

$$\text{sym}(\bullet)_{ijk} := \frac{1}{2}((\bullet)_{jik} + (\bullet)_{ijk}) \quad \forall (\bullet) \in \mathbf{R}^{3 \times 3 \times 3}. \quad (2.14)$$

Any three-dimensional second order tensor together with some arbitrarily oriented unit vector \mathbf{n} can be decomposed as follows

$$(\bullet)^{(n)} := (\bullet) \cdot (\mathbf{n} \otimes \mathbf{n}) \quad \text{and} \quad (\bullet)^{(t)} := (\bullet) \cdot (\mathbf{1} - \mathbf{n} \otimes \mathbf{n}). \quad (2.15)$$

This becomes relevant (as will be introduced later) for the decomposition of tensors on some surface $\partial\mathcal{B}$ of some body $\mathcal{B} \in \mathbf{R}^3$ where \mathbf{n} is the vector normal to the surface. Then, $(\bullet)^{(n)}$ can be considered as the surface normal components of (\bullet) and $(\bullet)^{(t)}$ can be considered as surface tangential components of (\bullet) .

2.1.2 Differential Operators

For two and three space dimensions ($d \in \{2, 3\}$) and any n -th order tensor field $(\bullet) \in \mathbf{R}^{3^n}$ define the row-wise applied derivative operators

$$\nabla(\bullet) := \partial_j(\cdot)_{i_1 \dots i_n} \mathbf{e}_{i_1} \otimes \dots \otimes \mathbf{e}_{i_n} \otimes \mathbf{e}_j, \quad (2.16)$$

$$\text{Div}(\bullet) := \partial_{i_n}(\cdot)_{i_1 \dots i_n} \mathbf{e}_{i_1} \otimes \dots \otimes \mathbf{e}_{i_{n-1}}, \quad (2.17)$$

$$\text{Rot}(\bullet) := -\partial_j(\cdot)_{i_1 \dots i_n} \mathbf{e}_{i_1} \otimes \dots \otimes \mathbf{e}_{i_n} \times \mathbf{e}_j, \quad (2.18)$$

where \mathbf{e}_\bullet denote Cartesian base vectors and $(\cdot)_{i_1 \dots i_n}$ denote the tensor coefficients. In order to simplify notation in subsequent occurrences in which the individual indices of tensor quantities are mentioned, the coefficient notation is used and Cartesian base vectors are implied.

Remark 1. *In the literature sometimes the nabla operator which in the 3D case is defined by*

$$\nabla \dots := (\partial_1 \dots, \partial_2 \dots, \partial_3 \dots)^T \quad (2.19)$$

is utilized for the definitions for differential operators. The definitions (2.16)-(2.18) are then written as

$$\nabla(\bullet) := (\bullet) \otimes \nabla \quad \text{Div}(\bullet) := (\bullet) \cdot \nabla \quad \text{and} \quad \text{Rot}(\bullet) := (\bullet) \times \nabla$$

Recall that both in two and three dimensions the gradient increases the tensorial order by one while the divergence reduces the tensorial order by one. Meanwhile, the rotation in the 3D case maintains the tensorial order and in the 2D case with the definition (2.11) of the cross product reduces the tensorial order by one. Naturally, the gradient of any vector $(\bullet) \in \mathbf{R}^3$ yields a second order tensor. Thus, given the decomposition (2.15) define the surface normal and tangential gradient by

$$\begin{aligned} (\nabla(\bullet) \cdot \mathbf{n}) \otimes \mathbf{n} &= (\nabla \bullet)^{(n)} \equiv n_j D(\bullet_i) \\ \nabla_\Gamma(\bullet) &:= (\nabla \bullet)^{(t)} \equiv D_j(\bullet_i) \quad (\text{cf. MINDLIN [1964], pp.67}). \end{aligned} \quad (2.20)$$

Following therefrom, by means of the standard definition of the divergence being the trace of the gradient, the surface divergence is defined by

$$\text{Div}_\Gamma(\bullet) := \nabla_\Gamma(\bullet) : \mathbf{1} \equiv D_j(\bullet_j). \quad (2.21)$$

Now, let $\mathbf{H} \in H^1(\mathcal{B}; \mathbf{R}^{(d \times d)})$ be a second order tensor, for which a full gradient is computable. Then the row-wise applied rotation operator (2.18) can be expressed in terms of the gradient components by

$$\text{Rot } \mathbf{H} := \begin{bmatrix} (\nabla \mathbf{H})_{121} - (\nabla \mathbf{H})_{112} \\ (\nabla \mathbf{H})_{221} - (\nabla \mathbf{H})_{212} \end{bmatrix} \quad \text{for } d = 2 \quad (2.22)$$

and similarly for $d = 3$, the relation

$$\text{Rot } \mathbf{H} = \begin{bmatrix} (\nabla \mathbf{H})_{132} - (\nabla \mathbf{H})_{123} & (\nabla \mathbf{H})_{113} - (\nabla \mathbf{H})_{131} & (\nabla \mathbf{H})_{121} - (\nabla \mathbf{H})_{112} \\ (\nabla \mathbf{H})_{232} - (\nabla \mathbf{H})_{223} & (\nabla \mathbf{H})_{213} - (\nabla \mathbf{H})_{231} & (\nabla \mathbf{H})_{221} - (\nabla \mathbf{H})_{212} \\ (\nabla \mathbf{H})_{332} - (\nabla \mathbf{H})_{323} & (\nabla \mathbf{H})_{313} - (\nabla \mathbf{H})_{331} & (\nabla \mathbf{H})_{321} - (\nabla \mathbf{H})_{312} \end{bmatrix} \quad (2.23)$$

(cf. RIESELDMANN ET AL. [2021]).

Important Identities of Differential Operators In the following, various specific properties and identities of the previously introduced differential operators are summarized and will be used in later chapters. The following orthogonality relations hold:

$$\text{The gradient of a tensor is rotation-free: } \text{Rot}(\nabla(\bullet)) = \mathbf{0} \quad (2.24)$$

$$\text{The rotation of a tensor is divergence-free: } \text{Div}(\text{Rot}(\bullet)) = \mathbf{0} \quad (2.25)$$

Consequently, written in weak form the orthogonality (2.24) of rotations and gradients reads

$$\int_{\mathcal{B}} \text{Rot}(\bullet) \cdot \nabla(\blacksquare) \, dV = 0 \quad (2.26)$$

with (\bullet) and (\blacksquare) being some tensor functions of matching order. The Divergence theorem in its fundamental form reads

$$\int_{\partial \mathcal{B}} (\bullet) \cdot \mathbf{n} \, dA = \int_{\mathcal{B}} \text{Div}(\bullet) \, dV. \quad (2.27)$$

where \mathbf{n} denotes the unit normal vector pointing outwards of the boundary $\partial \mathcal{B}$ of the integrated domain. Applied to the inner product of two tensors (\bullet) and (\blacksquare) , where the first is one tensorial order higher than the former, the Divergence theorem can be rewritten to

$$\int_{\partial \mathcal{B}} (\bullet \cdot \mathbf{n}) \cdot (\blacksquare) \, dA = \int_{\mathcal{B}} \text{Div}(\bullet) \cdot (\blacksquare) + (\bullet) \cdot \nabla(\blacksquare) \, dV. \quad (2.28)$$

This identity is e.g. used to get from weak forms to the strong form of variational equations and vice versa. Note, that another corollary of the divergence theorem in the presence of the cross product of two vectors yields the following identity

$$\int_{\partial \mathcal{B}} (\bullet \times \blacksquare) \cdot \mathbf{n} \, dA = \int_{\mathcal{B}} (\bullet) \cdot \text{Rot}(\blacksquare) - \text{Rot}(\bullet) \cdot (\blacksquare) \, dV \quad (2.29)$$

which will be made use of in chapter 6.

2.1.3 Function Spaces and Norms

For the analysis of the stability and error convergence of formulations, a necessary ingredient is to classify the spaces and corresponding measures (norms) which the solution functions may belong to. Further details on the following can be found in BRAESS [2007] and BOFFI ET AL. [2013] (among others). Firstly, define the domain $\mathcal{B} \in \mathbb{R}^3$ as closed subset of the Euclidean space \mathbb{R}^3 , which in the continuum mechanical setting represents the solid body of interest. Here, the first space, on which subsequently defined spaces are based on is the so-called Lebesgue space of square integrable functions (i.e. L^2 -space) defined by

$$L^2(\mathcal{B}; \mathbb{R}^{3^n}) := \{(\bullet) \in \mathbb{R}^{3^n} : (\bullet) \text{ is square integrable over } \mathcal{B} \text{ with the finite norm } \|\bullet\|_{L^2}\} \quad (2.30)$$

and the respective measure is the Lebesgue measure (aka L^2 -norm)

$$\|\bullet\|_{L^2} := \left(\int_{\mathcal{B}} (\bullet) \cdot (\bullet) \, dV \right)^{\frac{1}{2}}. \quad (2.31)$$

Note, that the present definition constitutes a generalization to n -order tensors by means of the scalar product (2.2). The following L^2 sub-spaces contain functions for which various partial differentials must be computable and are called Hilbert spaces¹. Therefore, define the space

$$H^m(\mathcal{B}; \mathbf{R}^{3^n}) := \{(\bullet) \in L^2(\mathcal{B}; \mathbf{R}^{3^n}) : \nabla^i(\bullet) \in L^2(\mathcal{B}; \mathbf{R}^{3^{n+i}}) \text{ for } i = 1, \dots, m\} \quad (2.32)$$

of functions which are m times differentiable in any coordinate direction and corresponding gradients are square integrable over the body with the norm

$$\|\bullet\|_{H^m} := \left(\|\bullet\|_{L^2}^2 + \|\nabla(\bullet)\|_{L^2}^2 + \|\nabla^2(\bullet)\|_{L^2}^2 + \dots + \|\nabla^m(\bullet)\|_{L^2}^2 \right)^{\frac{1}{2}}. \quad (2.33)$$

Here, the notation $\nabla^i(\bullet)$ refers to the i -th order gradient with $\nabla^1(\bullet) := \nabla(\bullet)$ and $\nabla^2 := \nabla\nabla(\bullet)$ and so on. Thus, if a linearized variational formulation for example contains quadratic terms of second order gradients the corresponding suitable solution space is the H^2 -space, which is the case e.g. in the gradient elasticity formulation (cf. section 4.1). Furthermore, corresponding to each summand in (2.33) is defined the so-called seminorm $|(\bullet)|_{H^i} := \|\nabla^i(\bullet)\|_{L^2}$. Also, note the relation

$$H^m(\mathcal{B}; \mathbf{R}^{3^n}) \subset \dots \subset H^2(\mathcal{B}; \mathbf{R}^{3^n}) \subset H^1(\mathcal{B}; \mathbf{R}^{3^n}) \subset L^2(\mathcal{B}; \mathbf{R}^{3^n}) \quad (2.34)$$

meaning that all functions that belong to e.g. $H^2(\mathcal{B}; \mathbf{R}^{3^n})$ also belong to $H^1(\mathcal{B}; \mathbf{R}^{3^n})$ and so on. Meanwhile, the magnitude of the norm of any function $(\bullet) \in H^m(\mathcal{B}; \mathbf{R}^{3^n})$ is ordered by the sequence

$$\|\bullet\|_{L^2} \leq \|\bullet\|_{H^1} \leq \|\bullet\|_{H^2} \leq \dots \leq \|\bullet\|_{H^m}, \quad (2.35)$$

which becomes relevant for estimating upper and lower bounds for some inequalities introduced later on. So far, the spaces have been defined such that for the functions arbitrary values over the domain \mathcal{B} are possible. Yet, in boundary value problems often on some parts of the domain fixed values of the solution functions are prescribed. Therefore, picking up on the notation of BRAESS [2007] here, for those functions the most general definition of Lebesgue spaces with generalized Dirichlet boundary conditions is introduced. For that, define by

$$L_0^2(\mathcal{B}; \mathbf{R}^{3^n}) := \{(\bullet) \in L^2(\mathcal{B}; \mathbf{R}^{3^n}) : \text{each component of } (\bullet) \text{ is constant on some part of } \mathcal{B}\} \quad (2.36)$$

the L^2 space with generalized Dirichlet border. The generalized Dirichlet border can be e.g. a fixed mean integral $\int_{\mathcal{B}} (\bullet) \, dV = 0$, a subdomain of the boundary $(\bullet) = (\bullet)^*$ on $\Gamma \subseteq \partial\mathcal{B}$ or the entire boundary fixed. Note, that generally throughout what follows, functions with non-zero Dirichlet boundary conditions on subdomains are considered. There, following BRAESS [2007], p35 ff. and remark 6.1 problems with functions with non-zero boundary conditions can be transformed to problems with functions with zero-boundary conditions. Therefore, when in later chapters stability conditions (such as Brezzi's stability condition (cf. section 2.4)) are postulated for zero boundary conditions, they in general imply these conditions

¹Hilbert spaces are also referred to as Sobolev spaces. Here, the distinction is that Hilbert spaces are based on the L^2 -norm, whereas Sobolev spaces in general can be based on any L^p norm BRAESS [2007].

also for problems with non-zero boundary conditions as well. Define the Hilbert space with generalized Dirichlet boundary conditions by

$$H_0^m(\mathcal{B}; \mathbb{R}^{3^n}) := \{(\bullet) \in H^m(\mathcal{B}; \mathbb{R}^{3^n}) : \nabla^{i-1}(\bullet) \in L_0^2(\mathcal{B}; \mathbb{R}^{3^{n+i}}) \text{ for } i = 1, \dots, m\}. \quad (2.37)$$

Now, the subscript H_0 implies that the functions and all components of derivatives of one order lower than those over which the space is defined to take fixed values somewhere in \mathcal{B} . Here, it is noteworthy that in the case of Dirichlet conditions on the boundary only surface normal components of the higher gradients of the function need to additionally be fixed, since the fixed surface tangential components of gradients are implied by fixed values of the functions themselves. Thus, specifically in the case of Dirichlet boundary conditions for (2.37) the boundary conditions become

$$(\bullet)|_{\Gamma_1} = (\blacksquare)^*, \quad \nabla(\bullet)|_{\Gamma_2} \cdot \mathbf{n} = (\blacksquare)^{**}, \quad \nabla^{m-1}(\bullet)|_{\Gamma_m} \odot \underbrace{(\mathbf{n} \otimes \dots \otimes \mathbf{n})}_{(m-1) \text{ times}} = (\blacksquare)^{* \dots *},$$

where Γ_i are some subsets of the boundary, $(\blacksquare)^*$, $(\blacksquare)^{**}$, ... refer to some prescribed functions and \odot denotes the $m - 1$ -order contraction. That is, e.g. in the case of Dirichlet boundary conditions for the first and second order case the definitions

$$H_0^1(\mathcal{B}; \mathbb{R}^{3^n}) := \{(\bullet) \in H^1(\mathcal{B}; \mathbb{R}^{3^n}) : (\bullet)|_{\Gamma_1} = (\blacksquare)^*\} \quad (2.38)$$

$$H_0^2(\mathcal{B}; \mathbb{R}^{3^n}) := \{(\bullet) \in H^2(\mathcal{B}; \mathbb{R}^{3^n}) : (\bullet)|_{\Gamma_1} = (\blacksquare)^*, \nabla(\bullet)|_{\Gamma_2} \cdot \mathbf{n} = (\blacksquare)^{**}\} \quad (2.39)$$

follow. Analogous to the H^1 -space containing first order gradients, the spaces

$$H(\text{Div}; \mathcal{B}; \mathbb{R}^{3^n}) := \{(\bullet) \in L^2(\mathcal{B}; \mathbb{R}^{3^n}) : \text{Div}(\bullet) \in L^2(\mathcal{B}; \mathbb{R}^{3^{(n-1)}})\} \quad (2.40)$$

$$H(\text{Rot}; \mathcal{B}; \mathbb{R}^{3^n}) := \{(\bullet) \in L^2(\mathcal{B}; \mathbb{R}^{3^n}) : \text{Rot}(\bullet) \in L^2(\mathcal{B}; \mathbb{R}^{3^n})\} \quad (2.41)$$

contain functions with first order divergences and rotations, respectively, with the corresponding norms

$$\|\bullet\|_{H(\text{Div})} := \left(\|(\bullet)\|_{L^2}^2 + \|\text{Div}(\bullet)\|_{L^2}^2 \right)^{\frac{1}{2}} \quad (2.42)$$

$$\|\bullet\|_{H(\text{Rot})} := \left(\|(\bullet)\|_{L^2}^2 + \|\text{Rot}(\bullet)\|_{L^2}^2 \right)^{\frac{1}{2}}. \quad (2.43)$$

Note, that adding the index H_0 in the case of the present $H(\text{Div})$ and $H(\text{Rot})$ spaces refers to generalized Dirichlet boundary conditions in the same manner as discussed before.

Commuting Diagram A useful sequence in order to illustrate some relations between differential operators and spaces relevant for the stability analysis of formulations is the following commuting diagram also known as the De Rham complex (cf. BOFFI ET AL. [2013])

$$H^1(\mathcal{B}) \xrightarrow{\nabla} H(\text{Rot}; \mathcal{B}; \mathbb{R}^3) \xrightarrow{\text{Rot}} H(\text{Div}; \mathcal{B}; \mathbb{R}^3) \xrightarrow{\text{Div}} L^2(\mathcal{B}). \quad (2.44)$$

Here, it is worth noting that the image of the differential operators is the kernel of the corresponding next space in the sequence, meaning that e.g. the gradient applied to H^1 -functions yields rotation-free functions living in $H(\text{Rot}; \mathcal{B}; \mathbb{R}^3)$. The rotation applied to functions in the latter space yields divergence-free functions living in $H(\text{Div}; \mathcal{B}; \mathbb{R}^3)$ and finally the divergence applied to functions in the latter space yields functions in L^2 . Further reading on commuting diagrams and their use for the construction of mixed finite element formulations besides

BOFFI ET AL. [2013] can be found in the generalizing framework of ARNOLD ET AL. [2006]. See also the elasticity complex and based thereon formulations of ARNOLD AND WINTHER [2002] and ARNOLD ET AL. [2008]. With the definitions (2.16)-(2.18) the commuting diagram extends naturally to higher order tensors. Note, that in the two-dimensional case with the 2D rotation operator defined by (2.18) and (2.12) the commuting diagram simplifies to

$$H^1(\mathcal{B}) \xrightarrow{\nabla} H(\text{Rot}; \mathcal{B}; \mathbb{R}^2) \xrightarrow{\text{Rot}} L^2(\mathcal{B}) \quad (2.45)$$

(cf. SCHÖBERL [2009]). Furthermore, by means of the 3D commuting diagram (2.44) the following scheme indicates suitable Hilbert spaces for the following L^2 pairings including differential operators:

$$\begin{aligned} \int_{\mathcal{B}} (\bullet) \cdot \nabla(\blacksquare) \, dV &\rightarrow (\bullet) \in H(\text{Rot}^0; \mathcal{B}; \mathbb{R}^{3^{n+1}}) \quad \text{and} \quad (\blacksquare) \in H^1(\mathcal{B}; \mathbb{R}^{3^n}), \\ \int_{\mathcal{B}} (\bullet) \cdot \text{Rot}(\blacksquare) \, dV &\rightarrow (\bullet) \in H(\text{Div}^0; \mathcal{B}; \mathbb{R}^{3^n}) \quad \text{and} \quad (\blacksquare) \in H(\text{Rot}; \mathcal{B}; \mathbb{R}^{3^n}), \\ \int_{\mathcal{B}} (\bullet) \cdot \text{Div}(\blacksquare) \, dV &\rightarrow (\bullet) \in L^2(\mathcal{B}; \mathbb{R}^{3^{n-1}}) \quad \text{and} \quad (\blacksquare) \in H(\text{Div}; \mathcal{B}; \mathbb{R}^{3^n}), \end{aligned} \quad (2.46)$$

where $H(\text{Rot}^0; \mathcal{B}; \mathbb{R}^{3^n})$ and $H(\text{Div}^0; \mathcal{B}; \mathbb{R}^{3^n})$ are defined by

$$H(\text{Rot}^0; \mathcal{B}; \mathbb{R}^{3^n}) := \{(\bullet) \in H(\text{Rot}; \mathcal{B}; \mathbb{R}^{3^n}) : \text{Rot}(\bullet) = \mathbf{0}\} \quad \text{and} \quad (2.47)$$

$$H(\text{Div}^0; \mathcal{B}; \mathbb{R}^{3^n}) := \{(\bullet) \in H(\text{Div}; \mathcal{B}; \mathbb{R}^{3^n}) : \text{Div}(\bullet) = \mathbf{0}\}. \quad (2.48)$$

Dual Spaces and Double Pairings Another pairing occurring in later introduced formulations is the simple L^2 pairing $\int_{\mathcal{B}} (\bullet) \cdot (\blacksquare) \, dV$, where (\blacksquare) belongs to $(\blacksquare) \in H^1(\mathcal{B}; \mathbb{R}^{3^n})$. Then, provided no other restrictions with respect to differentiability of (\bullet) (i.e. no other occurrences of derivatives of (\bullet) in the formulation) are present for (\bullet) the dual space is defined by

$$H^{-1}(\mathcal{B}; \mathbb{R}^{3^n}) := \{(\bullet) \in \mathbb{R}^{3^n} \text{ with the norm } \|\bullet\|_{H^{-1}} \text{ defined } \forall (\blacksquare) \in H^1(\mathcal{B}; \mathbb{R}^{3^n})\} \quad (2.49)$$

and the norm defined as

$$\|\bullet\|_{H^{-1}} := \sup_{(\blacksquare) \in H_0^1(\mathcal{B}; \mathbb{R}^{3^n}) \setminus \{0\}} \frac{\int_{\mathcal{B}} (\bullet) \cdot (\blacksquare) \, dV}{\|(\blacksquare)\|_{H^1}} \quad (\text{cf. BRAESS [2007], p.117, def 3.1}) \quad (2.50)$$

Further, note the relations

$$\begin{aligned} H^1(\mathcal{B}; \mathbb{R}^{3^n}) &\subset H(\text{Div}; \mathbb{R}^{3^n}) \subset L^2(\mathcal{B}; \mathbb{R}^{3^n}) \subset H^{-1}(\mathcal{B}; \mathbb{R}^{3^n}) \quad \text{and} \\ \|\bullet\|_{H^{-1}} &\leq \|\bullet\|_{L^2} \leq \|\bullet\|_{H(\text{Div})} \leq \|\bullet\|_{H^1}, \end{aligned} \quad (2.51)$$

which will also become relevant for the determination of bounds of inequality conditions (e.g. the inf-sup condition) discussed later on. Similarly, the H^1 -space is embedded with $H^1(\mathcal{B}; \mathbb{R}^{3^n}) \subset H(\text{Rot}; \mathbb{R}^{3^n})$ in the $H(\text{Rot})$ -space and thus, every element of H^1 is also an element of $H(\text{Rot})$ (this is relevant to the formulation of chapter 6). In some instances in the case of mixed formulations also double pairings, meaning that one function is paired with two different functions, are possible. Here, the concept of defining therefore suitable spaces is exemplified by means of one specific for this contribution relevant example. Consider the example

$$\int_{\mathcal{B}} (\bullet) \cdot \mathbf{H} + \text{Div}(\bullet) \cdot \mathbf{u} \, dV \quad (2.52)$$

with $\mathbf{H} \in H^1(\mathcal{B}; \mathbb{R}^{3 \times 3})$ and $\mathbf{u} \in L^2(\mathcal{B}; \mathbb{R}^3)$. In the case of the second pairing, for the function (\bullet) the divergence must be computable and paired with L^2 . Meanwhile, due to the first pairing the function (\bullet) must also be considered as dual to a H^1 -function, that is, being an element of the space H^{-1} . Therefore, define the solution space specifically matching the present scenario (cf. also the formulation of section 5.2.1 as well as the alternative formulation of RIESELDMANN ET AL. [2021]) by

$$H^{-1}(\text{Div}; \mathcal{B}; \mathbb{R}^{3 \times 3}) := \{\mathbf{\Lambda} \in H^{-1}(\mathcal{B}; \mathbb{R}^{3 \times 3}) : \text{Div } \mathbf{\Lambda} \in L^2(\mathcal{B}; \mathbb{R}^3)\} \quad (2.53)$$

with the norm

$$\|(\bullet)\|_{H^{-1}(\text{Div})} := \left(\|(\bullet)\|_{H^{-1}}^2 + \|\text{Div}(\bullet)\|_{L^2}^2 \right)^{\frac{1}{2}}. \quad (2.54)$$

Helmholtz Decomposition Consider the three-dimensional second order tensor field $\mathbf{\Lambda} \in L^2(\mathcal{B}; \mathbb{R}^{3 \times 3})$. The theorem of HELMHOLTZ [1858] (see also SCHEDENSACK [2015]) states that $\mathbf{\Lambda}$ can be expressed as a superposition

$$\mathbf{\Lambda} = \mathbf{\Lambda}_G + \mathbf{\Lambda}_R \quad (2.55)$$

of an irrotational (rotation-free) field $\mathbf{\Lambda}_G$ and a solenoidal (divergence-free) field $\mathbf{\Lambda}_R$. Consequently, with (2.24) and (2.25) the two parts can be expressed by gradient and rotation functions respectively:

$$\mathbf{\Lambda}_R = \text{Rot } \mathbf{\Phi} \quad \text{and} \quad \mathbf{\Lambda}_G = -\nabla \mathbf{g}, \quad (2.56)$$

with $\mathbf{g} \in H_0^1(\mathcal{B}; \mathbb{R}^3)$ being a vector-valued function and $\mathbf{\Phi} \in H_0(\text{Div}^0; \mathcal{B}; \mathbb{R}^{3 \times 3})$ being the space for tensor-valued L^2 functions with vanishing divergence and normal boundary conditions; see subsection 6.1.5 for details. Note, that the decomposition has been initially postulated for vector fields but with the tensorial definition of the differential operators it applies naturally to arbitrary tensorial orders $n \geq 1$. Here it is formulated in terms of second order tensors matching the use case in chapter 6. Note also, that whenever in some integral expression (i.e. variational formulation) $\mathbf{\Lambda}$ is replaced by the expressions (2.56) containing first derivatives, it becomes necessary to fix \mathbf{g} and $\mathbf{\Phi}$ by means of some generalized Dirichlet conditions to maintain unisolvency.

Functions Appearing in Integral Terms on the Boundary of \mathcal{B} : In case a variational formulation has surface integrals such as e.g. the integral including the surface tractions of the classical elasticity problem for the corresponding functions, specific spaces are defined. These definitions account for the relation between the functions in the volume of the body and the surface. For any function \mathbf{u} defined over the body \mathcal{B} define the corresponding space of surface functions

$$H^{1/2}(\Gamma; \mathbb{R}^3) := \{\mathbf{v} \in L^2(\Gamma; \mathbb{R}^3) : \exists \mathbf{u} \in H^1(\mathcal{B}; \mathbb{R}^3) \text{ with } \mathbf{v} = \mathbf{u}|_\Gamma\} \quad (2.57)$$

$$H^{3/2}(\Gamma; \mathbb{R}^3) := \{\mathbf{v} \in H^1(\Gamma; \mathbb{R}^3) : \exists \mathbf{u} \in H^2(\mathcal{B}; \mathbb{R}^3) \text{ with } \mathbf{v} = \mathbf{u}|_\Gamma \text{ and } \nabla \mathbf{v} \cdot \mathbf{n} = \nabla \mathbf{u} \cdot \mathbf{n}|_\Gamma\} \quad (2.58)$$

being with $\mathbf{v} \in L^2(\Gamma; \mathbb{R}^3)$ square integrable over the surface. The dual spaces corresponding to (2.57) and (2.58) are given by

$$H^{-1/2}(\Gamma; \mathbb{R}^3) := \{\mathbf{t} \in L^2(\Gamma; \mathbb{R}^3) : \exists \mathbf{f}_P \in \mathcal{P} \text{ with } \mathbf{t} = \mathbf{f}_P\} \quad (2.59)$$

$$H^{-3/2}(\Gamma; \mathbb{R}^3) := \{\mathbf{r} \in L^2(\Gamma; \mathbb{R}^3) : \exists \mathbf{f}_G \in \mathcal{G} \text{ with } \mathbf{r} = \mathbf{f}_G\} \quad (2.60)$$

where $f_{\mathcal{P}}$ and $f_{\mathcal{G}}$ refer to some functions of the traction duals accounting for the surface equations specific to the formulation². The spaces \mathcal{P} and \mathcal{G} denote some suitable spaces specific to the formulation. Further details on Hilbert spaces on the boundary are given BRAESS [2007], see also SCHEDENSACK [2015]. Note, that the space definitions of the present subsection are given only for the sake of completeness and do not appear in any subsequent analysis.

2.1.4 Important Identities

This subsection provides a summary of some identities, that are in the literature of the numerical analysis of finite elements repeatedly referred to. Firstly, introduce the notations

$$(\bullet) \lesssim (\blacksquare) := (\bullet) \leq c (\blacksquare) \quad \text{and} \quad (\bullet) \gtrsim (\blacksquare) := (\bullet) \geq c (\blacksquare),$$

which refer to an inequality where $c \in \mathbf{R}^+ \setminus \{0\}$ is a positive constant and is hidden within the operators \lesssim and \gtrsim . The so called *triangular inequality*, which applies to sums and therefore also to integrals, reads

$$\left| \sum_i (\bullet)_i \right| \leq \sum_i |(\bullet)| \quad \text{and} \quad \left| \int_{\mathcal{B}} (\bullet) \, dV \right| \leq \int_{\mathcal{B}} |(\bullet)| \, dV. \quad (2.61)$$

The *Poincaré(-Friedrich) inequality* applied to L^2 spaces is given by

$$\|(\bullet)\|_{L^2} \lesssim \|\nabla(\bullet)\|_{L^2} \quad \forall (\bullet) \in H_0^1(\mathcal{B}) \quad (2.62)$$

where $H_0^1(\mathcal{B})$ refers to the H^1 -space of functions with generalized Dirichlet condition, as discussed in section 2.1.3. Note, that the Poincaré inequality holds for any L^p -space, however only the L^2 space is of relevance within this contribution. *Korn's inequality* is defined as

$$\|\nabla(\bullet)\|_{L^2}^2 \lesssim \|\text{sym } \nabla(\bullet)\|_{L^2} \quad \forall (\bullet) \in H_0^1(\mathcal{B}; \mathbf{R}^3), \quad (2.63)$$

where (\bullet) has some Dirichlet boundary which is larger than a point. Lastly, the *Cauchy-Schwarz inequality* applied to L^2 spaces is defined as

$$\left| \int_{\mathcal{B}} (\bullet) \cdot (\blacksquare) \, dV \right|^2 \leq \|(\bullet)\|_{L^2}^2 \|(\blacksquare)\|_{L^2}^2 \quad \text{ie.} \quad \left| \int_{\mathcal{B}} (\bullet) \cdot (\blacksquare) \, dV \right| \leq \|(\bullet)\|_{L^2} \|(\blacksquare)\|_{L^2} \quad (2.64)$$

2.2 Finite Strain Kinematics and Stress Measures

The present section provides an overview of the notations and kinematic relations describing the motions and deformations of the continuum mechanical body of interest. Further reading can be found in the books of ALTENBACH [2012] and WRIGGERS [2008] (among other contributions). Therefore, following the commonly used kinematic framework, it can be distinguished between the body in reference undeformed condiguration \mathcal{B} and in the current/actual deformed configuration \mathcal{S} . There exists a bijective function $\chi := \chi(\mathbf{X}, t)$, which maps with

$$\chi : \mathcal{B} \rightarrow \mathcal{S} \quad (2.65)$$

²In the case of local elasticity that is the Cauchy theorem and in the case of gradient elasticity that is the corresponding first and second order surface traction equation.

for any $t \in \hat{t} := [t_0, t_{\text{end}}]$ in the considered time interval \hat{t} any point in the coordinates \mathbf{X} of the body \mathcal{B} in reference configuration to a point of the body \mathcal{S} in the actual configuration with the relations

$$\mathbf{x} = \chi(\mathbf{X}, t) \quad \text{and} \quad \mathbf{X} = \chi^{-1}(\mathbf{x}, t). \quad (2.66)$$

where \mathbf{x} are coordinates of the body in the actual configuration. Throughout this contribution the coordinates \mathbf{X} of the reference configuration are used and the material time derivative is denoted as

$$(\dot{\bullet}) := \frac{\partial(\bullet)}{\partial t} \left(= \frac{\partial(\bullet) \circ \chi^{-1}}{\partial t} + \frac{\partial(\bullet)}{\partial \mathbf{x}} \cdot \frac{\partial \mathbf{x}}{\partial t} \right) \quad (2.67)$$

where (\bullet) : denotes any n -tensor valued function. The displacement function $\mathbf{u} : (\mathcal{B} \times \hat{t}) \rightarrow \mathbb{R}^3$ is given through the relation $\mathbf{x} = \mathbf{X} + \mathbf{u}$ and the deformation gradient reads

$$\mathbf{F} := \frac{\partial \mathbf{x}}{\partial \mathbf{X}} = \mathbf{1} + \nabla \mathbf{u}. \quad (2.68)$$

The Green Lagrange nonlinear strain tensor is defined as

$$\mathbf{E}(\nabla \mathbf{u}) = \frac{1}{2}(\mathbf{C} - \mathbf{1}) = \frac{1}{2}((\nabla \mathbf{u})^T \cdot \nabla \mathbf{u} + \nabla \mathbf{u} + (\nabla \mathbf{u})^T). \quad (2.69)$$

In what follows all body, surface and line integrals are posed in terms of the body in reference configuration. Therefore, to make notation more simple the subscript of \mathbf{n}_0 referring to the reference configuration will be omitted and in what follows the normal vector with respect to the reference configuration is simply denoted by \mathbf{n} and the tangential vector is denoted by \mathbf{s} . Following ALTENBACH [2012] (p. 81) the kinematic relations between volume, surface and line increments is given by

$$dv = \det \mathbf{F} \, dV, \quad (2.70)$$

$$d\mathbf{a} = \det \mathbf{F} \mathbf{F}^{-T} \cdot d\mathbf{A} \quad \text{and} \quad (2.71)$$

$$d\mathbf{x} = \mathbf{F} \cdot d\mathbf{X}, \quad (2.72)$$

respectively. Further, $(\bullet)^{-T} := ((\bullet)^T)^{-1}$ denotes the inverse of a transposed second order tensor and the vector valued surface and line differentials can equivalently be written as $d\mathbf{A} = \mathbf{n} \, dA$ and $d\mathbf{X} = \mathbf{s} \, dX$. The response of any body loaded with external forces is an internal state of stress. The symmetric local stress tensor $\boldsymbol{\sigma} \in L^2(\mathcal{S}; \mathbb{S})$ related to the current configuration, \mathcal{S} is commonly referred to as the true stress tensor and in the case of classical elasticity called the Cauchy stress tensor. Based on the previous relation (2.71) integrating the Cauchy stress over the Neumann surface $\partial \mathcal{S}_\sigma$ in the current configuration yields the relation

$$\int_{\partial \mathcal{S}_\sigma} \boldsymbol{\sigma} \cdot d\mathbf{a} = \int_{\Gamma_N} \underbrace{\det \mathbf{F} \mathbf{F}^{-1} \cdot \boldsymbol{\sigma}}_{:= \mathbf{P}} \cdot d\mathbf{A},$$

where Γ_N corresponds to the corresponding Neumann surface in reference configuration and \mathbf{P} denotes the first Piola Kirchhoff stress tensor. The relations

$$\mathbf{P} = (\det \mathbf{F}) \mathbf{F}^{-1} \cdot \boldsymbol{\sigma} \quad \text{and} \quad \boldsymbol{\sigma} = (\det \mathbf{F})^{-1} \mathbf{F} \cdot \mathbf{P} \quad (2.73)$$

are referred to as *pull back* of the Cauchy stress tensor and *push forward* of the first Piola Kirchhoff stress tensor, respectively. At this point it is already worth mentioning the analogy to the later discussed finite element kinematics of section 3.2. For the sake of completeness, note the relation

$$\mathbf{S} = \mathbf{F}^{-1} \cdot \mathbf{P} \quad \text{with} \quad \mathbf{P} \in L^2(\mathcal{B}; \mathbb{R}^{3 \times 3}) \quad (2.74)$$

between the first and symmetric second order Piola Kirchhoff tensor $\mathbf{S} \in L^2(\mathcal{B}; \mathbb{S})$. For further fundamental continuum mechanical concepts and notions such as e.g. balance- and constitutive equations as well as principles of material theory, the reader is referred to ALTENBACH [2012] (among other basic literature).

2.3 Variational Principles

This section summarizes the well known main principles of the calculus of variations, which are used in the context of the formulations presented in this contribution. Therefore, first a generic example potential is introduced by which in the following the steps of time discretization, variation and linearization are illustrated. Further reading in the context of variational calculus can be found, e.g. in FOX [1987] and GELFAND AND FOMIN [2000]. Let $\mathbf{v} := \mathbf{v}(\mathbf{X}, t)$, $\mathbf{w}_1 := \mathbf{w}_1(\mathbf{X}, t)$ and $\mathbf{w}_2 := \mathbf{w}_2(\mathbf{X}, t)$ be sets of arbitrary-order tensor-valued functions of time and space, which map with $\mathbf{v} : (\mathcal{B}, \hat{t}) \rightarrow \mathcal{V}$, $\mathbf{w}_1 : (\mathcal{B}, \hat{t}) \rightarrow \mathcal{W}$ and $\mathbf{w}_2 : (\Gamma_N, \hat{t}) \rightarrow \mathcal{W}_2$ a point from the considered space-time domain (\mathcal{B}, \hat{t}) (and the boundary-time subdomain (Γ_N, \hat{t}) with $\Gamma_N \subseteq \partial\mathcal{B}$) into some function space \mathcal{V} , \mathcal{W}_1 and \mathcal{W}_2 . Further, let $f := f(\mathbf{v}, \partial_{X_i}\mathbf{v}, \dots, \partial_t\mathbf{v}, \dots, \mathbf{w}_1)$ denote a *functional* of \mathbf{v} and \mathbf{w}_1 and (in the most generous case) its space- and time derivatives up to an arbitrary order defined over the domain (\mathcal{B}, \hat{t}) and $g := (\mathbf{v}|_{\Gamma_N}, \dots, \mathbf{w}_2)$ denote a functional of the functions $\mathbf{v}|_{\Gamma_N}$ (and derivatives) and \mathbf{w}_2 evaluated on some boundary subdomain $(\Gamma_N \cap \partial\mathcal{B}, \hat{t})$ ³. In order to fix ideas and keep notation simple a functional f is considered, which may depend on first order time- and space-derivatives⁴. Yet, the corresponding following concepts of variation and linearization apply analogously to any set of functional arguments. Furthermore, the global functional also referred to as (pseudo)-potential is defined by the functional f and g integrated over the domains

$$\Pi := \int_{\hat{t}} \left(\int_{\mathcal{B}} f(\mathbf{v}, \dot{\mathbf{v}}, \nabla\mathbf{v}, \mathbf{w}_1) \, dV + \int_{\Gamma_N} g(\mathbf{v}|_{\Gamma_N}, \mathbf{w}_2) \, dA \right) dt \quad (2.75)$$

where we denote by $\mathbf{v} \in \mathcal{V}$ the *solution* functions and denote by $\mathbf{w}_1 \in \mathcal{W}_1$ and $\mathbf{w}_2 \in \mathcal{W}_2$ the fields of *external loads*. Then, according to the variational principle of least action developed in the late 1700s by Leibniz, Euler, Lagrange and others (for an overview see PULTE [1989]) among all possible arguments of f , we seek for given $\mathbf{w}_1 \in \mathcal{W}_1$ and $\mathbf{w}_2 \in \mathcal{W}_2$ those functions over the domain \mathcal{B} and \hat{t} that stationarize⁵ the action integral

$$\Pi \Rightarrow \underset{\mathbf{v}}{\text{stat}} \quad (2.76)$$

2.3.1 Time Discretization

Integrals such as (2.75) can usually not be solved analytically and need to be spatially discretized (by e.g. finite element approaches, of which the fundamentals are presented in detail in the next chapter 3) and solved with numerical solution schemes such as the well known Newton's method. Since in the general case the formulation is nonlinear in the solution fields and external loads, the system is therefore linearized and the stationary point is computed by iteratively solving the linear system. However, obviously due to the nonlinearity of the functional response, iterative solution schemes such as Newton's method usually fail to find the solution or provide inaccurate solutions when the entire time domain \hat{t} is analyzed at once. Therefore, the time domain $\hat{t} = [t_0, t_{\text{end}}]$ is divided into discrete time increments and (2.75)

³In the most general case, for each component of \mathbf{w}_2 and corresponding derivative components, the subdomain can be a different subset of the boundary $\partial\mathcal{B}$.

⁴Typically, continuum mechanical models, which aim to incorporate inertial effects and the dynamic behavior of the system, include second order time derivatives. These are, however, not part of the present study. Time derivatives of first order usually appear in formulations incorporating viscose or dissipative effects and corresponding potential functions are considered pseudo potentials. Formulations including the first order time derivative will appear in the gradient damage chapters 8 and 9 of this contribution.

⁵That is, depending on the problem seeking a minimum, maximum or saddle point.

can be written as the sum of integrals over each time increment

$$\int_{\hat{t}} (\bullet) \, dV = \int_{t_0}^{t_1} (\bullet) \, dV + \dots + \int_{t_n}^t (\bullet) \, dV + \dots + \int_{t_{\text{end}-1}}^{t_{\text{end}}} (\bullet) \, dV. \quad (2.77)$$

Now, for any time step $[t_n, t]$ the corresponding summand in (2.77) depends both on solution quantities of t and quantities of the previous time steps. The stationary point (2.76) is sought subsequently for each time increment $[t_n, t]$ given the solution of the previous time steps. Note, that applying the stationary operator to each summand of (2.77) yields the same results as applying the stationary operator to (2.75), because (2.77) and (2.75) are equivalent. For the discretization of the time integrals numerous approaches of various complexity (e.g. the method of NEWMARK [1959] for formulations including second order time derivatives) can be employed (see also BELYTSCHKO [1986]). In the formulations of the present contribution, no time derivatives higher than first order turn up. Therefore, with the first order time discretization

$$(\dot{\bullet}) \approx \frac{(\bullet) - (\bullet)_n}{t - t_n} \quad (2.78)$$

the integrals in (2.77) depend only on current quantities t and quantities of the previous time step⁶ t_n and the following Backward-Euler numerical time integration can be used:

$$\int_{t_n}^t (\bullet) \, dV \approx ((\bullet) - (\bullet)_n)(t - t_n) \quad (2.79)$$

Thus, in the time-incremental setting for each time step $[t_n, t]$ we seek for given $\mathbf{w}_1 \in \mathcal{W}_1$ and $\mathbf{w}_2 \in \mathcal{W}_2$ the solution $\mathbf{v} \in \mathcal{V}$ such that the integral

$$\Pi := \int_{\mathcal{B}} f(\mathbf{v}, \nabla \mathbf{v}, \mathbf{w}_1, \mathbf{v}_n) \, dV + \int_{\Gamma_N} g(\mathbf{v}|_{\Gamma_N}, \mathbf{w}_2) \, dA \Rightarrow \underset{\mathbf{v}}{\text{stat.}} \quad (2.80)$$

becomes stationary. In consequence, within the framework of the incremental load step solution procedure the stationary point of (2.75) can be computed by the sequence of stationary points of the integral of (2.80) also known as the load step solution procedure.

2.3.2 Variation

According to the principle of calculus of variations, the stationary point $\mathbf{v} \in \mathcal{V}$ of (2.80) is the point at which the Gateaux derivative

$$\frac{D}{D\epsilon} \left(\int_{\mathcal{B}} f(\mathbf{v} + \epsilon \delta \mathbf{v}, \nabla \mathbf{v} + \epsilon \nabla \delta \mathbf{v}, \mathbf{w}_1, \mathbf{v}_n) \, dV + \int_{\Gamma_N} g(\mathbf{v}|_{\Gamma_N} + \epsilon \delta \mathbf{v}|_{\Gamma_N}, \mathbf{w}_2) \, dA \right) \Big|_{\epsilon=0} = 0 \quad (2.81)$$

over all functional arguments becomes zero in the limit of the parametrization $\epsilon \rightarrow 0$ with $\delta \mathbf{v}$ and $\delta \mathbf{v}|_{\Gamma_N}$ being arbitrary variations of the solution functions. Further, introduce the boundary domain $\Gamma_D^{(i)} \subseteq \partial \mathcal{B}$ with $\Gamma_D^{(i)} \cap \Gamma_N^{(i)} = \emptyset$ and $\Gamma_D^{(i)} \cup \Gamma_N^{(i)} = \partial \mathcal{B}$ complementary to $\Gamma_N^{(i)}$ on which components $v_i = v_i^*$ of the function values themselves can be prescribed. For the sake of simplicity, in what follows the assumption is made that the boundary decompositions coincide for all components i and without loss of generality, the following concepts can be applied to arbitrary boundary decompositions. The boundary conditions $v_i|_{\Gamma_D} = v_i^*|_{\Gamma_D}$ are denoted *Dirichlet boundary conditions* with the corresponding variations $\delta v_i|_{\Gamma_D} = 0$ being zero. Moreover, the surface integrals containing the functions $\mathbf{w}_2 \in \mathcal{W}_2$ are denoted *Neumann*

⁶In the case of higher order time derivatives this is generally not the case cf. BELYTSCHKO [1986].

boundary conditions, which include also the free boundary on which \mathbf{w}_2 is zero. Note, that following a more strict notation in the potential expressions the solution functions would have to be denoted differently (e.g. $\tilde{\mathbf{v}}$) in order to account for the fact that the potential formulation does not display the solution yet. However, for the sake of simplicity in what follows the simplified notation as presented before is used. The Gateaux differential (2.81) is equivalent to the following variational equation

$$\delta_{\mathbf{v}}\Pi := \int_{\mathcal{B}} \partial_{\mathbf{v}}f \cdot \delta\mathbf{v} + \partial_{\nabla\mathbf{v}}f \cdot \nabla\delta\mathbf{v} \, dV + \int_{\Gamma_N} \partial_{\mathbf{v}}g|_{\Gamma_N} \cdot \delta\mathbf{v}|_{\Gamma_N} \, dA = 0 \quad (2.82)$$

of which both the first and second integral expressions must independently be zero. The present representation (2.82) of the problem denotes the weak form since only first order gradients appear, although the corresponding set of local equations are of second order: By application of the divergence theorem (2.28) and inserting $\delta\mathbf{u}|_{\Gamma_D} = \mathbf{0}$ the following strong form

$$\int_{\mathcal{B}} \partial_{\mathbf{v}}f \cdot \delta\mathbf{v} - \text{Div} \partial_{\nabla\mathbf{v}}f \cdot \delta\mathbf{v} \, dV + \int_{\Gamma_N} (\partial_{\nabla\mathbf{v}}f \cdot \mathbf{n})|_{\Gamma_N} \cdot \delta\mathbf{u}|_{\Gamma_N} + \partial_{\mathbf{v}}g|_{\Gamma_N} \cdot \delta\mathbf{v}|_{\Gamma_N} \, dA = 0 \quad (2.83)$$

can be obtained incorporating with $\text{Div} \partial_{\nabla\mathbf{v}}f(\dots, \nabla\mathbf{v}, \dots)$ second order derivatives. In finite element formulations, the weak form represents the more favorable display format, since interpolation schemes including only first order derivatives are more simple than those incorporating second order derivatives. We note that both integrals in (2.83) must independently be zero due to the following reason: The equation needs to hold for any $\delta\mathbf{u}$ and $\delta\mathbf{u}|_{\Gamma_N}$. Thus, it must hold for the choice $\delta\mathbf{u}|_{\Gamma_N} = \mathbf{0}$ on Γ_N (which does not imply $\delta\mathbf{u} = \mathbf{0}$ in \mathcal{B}). Therefore, the local equation

$$\partial_{\mathbf{v}}f - \text{Div} \partial_{\nabla\mathbf{v}}f = 0 \quad (2.84)$$

must always hold. Reversely, since (2.83) must always be zero even with (2.84) for any $\mathbf{v}|_{\Gamma_N}$ the surface equation

$$\partial_{\nabla\mathbf{v}}f \cdot \mathbf{n} + \partial_{\mathbf{v}}g = 0 \quad \text{on } \Gamma_N \quad (2.85)$$

must hold as well. In what follows, again for the sake of readability throughout this contribution, the subscript $(\bullet)|_{\Gamma_N}$ is omitted from occurrences of solution variables in surface integral expressions.

2.3.3 Linearization

In general, the functionals are nonlinear in their respective arguments. Linearizations of the formulations are presented in various occurrences throughout this contribution, both in the continuous and in the following discrete settings that incorporate the finite element discretizations of the weak forms. Therefore, by means of the previous example (2.82) the concept of linearization is briefly illustrated here. Applying the Taylor series expansion up to first order around the solution functions yields for (2.82)

$$\text{Lin}[\delta_{\mathbf{v}}\Pi] = \int_{\mathcal{B}} \partial_{\mathbf{v}}f|_i \cdot \delta\mathbf{v} + \partial_{\nabla\mathbf{v}}f|_i \cdot \nabla\delta\mathbf{v} + (\partial_{\mathbf{v}}\partial_{\nabla\mathbf{v}}f|_i : \Delta\mathbf{v}) \cdot \nabla\delta\mathbf{u} \, dV + \int_{\Gamma_N} \partial_{\mathbf{v}}g|_i \cdot \delta\mathbf{v} \, dA. \quad (2.86)$$

where $f|_i$ is short for $f(\mathbf{v}|_i, \nabla\mathbf{v}|_i, \mathbf{w}_1, \mathbf{v}_n)$ and $g|_i$ analogously and the index i refers to the value at the point around which the Taylor series is developed. Here, to keep the expression simple $\mathbf{v} \in \mathbf{R}^3 \cap \mathcal{V}$ is assumed to be a vector and f and g are assumed to be linear in \mathbf{v} , thus, having no second derivatives (also known as tangent operators). Furthermore, in the formulations of

this contributions i corresponds to the previous Newton iteration and $\Delta \mathbf{v} = \mathbf{v} - \mathbf{v}_i$ denotes the solution increment for which the linear problem $\text{Lin}[\delta_{\mathbf{v}}\Pi] = 0$ needs to be solved for each iteration. Finally, by defining bilinear and linear forms

$$\begin{aligned} a(\delta \mathbf{v}, \Delta \mathbf{v}) &:= \int_{\mathcal{B}} (\partial_{\mathbf{v}} \partial_{\mathbf{v}} f|_i : \Delta \mathbf{v}) \cdot \nabla \delta \mathbf{u} \, dV \\ l(\delta \mathbf{v}) &:= - \int_{\mathcal{B}} \partial_{\mathbf{v}} f|_i \cdot \delta \mathbf{v} + \partial_{\nabla \mathbf{v}} f|_i \cdot \nabla \delta \mathbf{v} \, dV - \int_{\Gamma_{\text{N}}} \partial_{\mathbf{v}} g|_i \cdot \delta \mathbf{v} \, dA, \end{aligned} \quad (2.87)$$

respectively, the linear problem in abstract notation can be denoted as follows. For given $\mathbf{w}_1 \in \mathcal{W}_1$, $\mathbf{w}_2 \in \mathcal{W}_2$ and $\mathbf{v}|_i \in \mathcal{V}$ find $\Delta \mathbf{v} \in \mathcal{V}$ such that

$$\text{Lin}[\delta_{\mathbf{v}}\Pi] = 0 \quad \Leftrightarrow \quad a(\delta \mathbf{v}, \Delta \mathbf{v}) = l(\delta \mathbf{v}) \quad (2.88)$$

holds for all $\delta \mathbf{v} \in \mathcal{V}$.

2.3.4 Example: Local Hyperelasticity

The most classical example in which the variational principles are applied in the continuum mechanical context is the elasticity problem, for which f and g are defined as

$$f(\mathbf{u}, \nabla \mathbf{u}, \mathbf{f}) := \psi(\mathbf{C}(\mathbf{F})) - \mathbf{f} \cdot \mathbf{u} \quad \text{and} \quad g(\mathbf{u}, \mathbf{t}) := \mathbf{t} \cdot \mathbf{u} \quad (2.89)$$

where ψ is the volume specific strain energy, \mathbf{F} is the deformation gradient (2.68), $\mathbf{u} \in H_0^1(\mathcal{B}; \mathbb{R}^3)$ are the displacements with the Dirichlet conditions $\mathbf{u} = \mathbf{u}^*$ on Γ_{D} , $\mathbf{f} \in H^{-1}(\mathcal{B}; \mathbb{R}^3)$ is a volume load and $\mathbf{t} \in H^{-1/2}(\Gamma_{\text{N}}, \mathbb{R}^3)$ are surface tractions. The variational equation then reads

$$\int_{\mathcal{B}} \mathbf{P} \cdot \delta \mathbf{F} - \mathbf{f} \cdot \delta \mathbf{u} \, dV - \int_{\Gamma_{\text{N}}} \mathbf{t} \cdot \delta \mathbf{u} \, dA = 0 \quad (2.90)$$

where $\mathbf{P} := \partial_{\mathbf{F}} \psi$ denotes the first order Piola-Kirchhoff stress tensor (cf. section 2.2). From the variational equation, the balance of linear momentum

$$- \text{Div } \mathbf{P} = \mathbf{f} \quad (2.91)$$

corresponding to (2.84) and the Cauchy equation

$$\mathbf{P} \cdot \mathbf{n} = \mathbf{t} \text{ on } \Gamma_{\text{N}} \quad (2.92)$$

corresponding to (2.85) can be identified.

2.4 Fundamentals of Mixed Variational Formulations

In this section, some fundamental aspects around the concept of stability within the context of mixed finite element formulations are summarized. Baseline contributions in the analysis of stability of (mixed) finite element formulations were made by LAX AND MILGRAM [1954], LADYZHENSKAYA [1969], BABUŠKA [1973], BREZZI [1974] and FORTIN [1977]. Further, comprehensive overviews can be found e.g. in the books of BRENNER AND SCOTT [1994], BRAESS [2007] and particularly BOFFI ET AL. [2013]. Among others, descriptive content on this topic can also be found in the dissertations of SCHEDENSACK [2015] (from the field of numerical mathematics) and VIEBAHN [2019] (from the field of computational mechanics).

2.4.1 Introduction to Mixed Variational Formulations

The following concepts of analytically predicting the stability of formulations are framed within the abstract notation, including bilinear and linear forms. In order to make concepts clear for the linear elasticity problem, specific examples of the different mixed variational approaches are given. Starting point is the primal, purely displacement based variational formulation. Here, to keep notation short and therefore assuming pure Dirichlet conditions, the corresponding elastic potential reads

$$\Pi_u := \int_{\mathcal{B}} \frac{1}{2} \nabla^s \mathbf{u} : \mathbb{C} : \nabla^s \mathbf{u} - \mathbf{f} \cdot \mathbf{u} \, dV \quad (2.93)$$

where \mathbb{C} denotes the linear elastic tangent operator and $\nabla^s := \text{sym}(\nabla)$ the symmetric gradient operator. Following therefrom, the linear problem seeks $\mathbf{u} \in H_0^1(\mathcal{B}; \mathbb{R})$ for all $\mathbf{f} \in H^{-1}(\mathcal{B}; \mathbb{R}^3)$ and $\mathbf{u}^*|_{\Gamma_D}$ such that

$$a(\delta \mathbf{u}, \mathbf{u}) = l(\delta \mathbf{u}) \quad (2.94)$$

holds for all $\delta \mathbf{u} \in H_0^1(\mathcal{B}; \mathbb{R}^3)$ and the bilinear and linear form is defined as

$$a(\delta \mathbf{u}, \mathbf{u}) := \int_{\mathcal{B}} \nabla^s \delta \mathbf{u} : \mathbb{C} : \nabla^s \mathbf{u} \, dV \quad \text{and} \quad l(\delta \mathbf{u}) := \int_{\mathcal{B}} \mathbf{f} \cdot \delta \mathbf{u} \, dV. \quad (2.95)$$

Now, an example for a mixed variational formulation incorporating two solution variables can be found following the concepts of HELLINGER [1913] and REISSNER [1950]. The corresponding following formulation can be found in VIEBAHN ET AL. [2018] and reads

$$\Pi_{\text{HR}} := \int_{\mathcal{B}} \frac{1}{2} \boldsymbol{\sigma} : \mathbb{C}^{-1} : \boldsymbol{\sigma} + \text{Div} \boldsymbol{\sigma} \cdot \mathbf{u} + \mathbf{f} \cdot \mathbf{u} \, dV \quad (2.96)$$

and \mathbb{C}^{-1} is called compliance tensor. The corresponding linear variational problem seeks for given $\mathbf{f} \in L^2(\mathcal{B}; \mathbb{R}^3)$ and the Dirichlet condition $\boldsymbol{\sigma} \cdot \mathbf{n} = \mathbf{t}$ on Γ_N the solution $(\boldsymbol{\sigma}, \mathbf{u}) \in H(\text{Div}; \mathcal{B}; \mathbb{S}) \times L^2(\mathcal{B}; \mathbb{R}^3)$ such that

$$\begin{aligned} a(\delta \boldsymbol{\sigma}, \boldsymbol{\sigma}) + b(\delta \boldsymbol{\sigma}, \mathbf{u}) &= 0 \\ b(\boldsymbol{\sigma}, \delta \mathbf{u}) &= -l(\delta \mathbf{u}) \end{aligned} \quad (2.97)$$

holds for all $(\delta \boldsymbol{\sigma}, \delta \mathbf{u}) \in H(\text{Div}; \mathbb{S}) \times L^2(\mathcal{B}; \mathbb{R}^3)$. Here, the bilinear and linear forms are defined as

$$\begin{aligned} a(\delta \boldsymbol{\sigma}, \boldsymbol{\sigma}) &:= \int_{\mathcal{B}} \delta \boldsymbol{\sigma} : \mathbb{C}^{-1} : \boldsymbol{\sigma} \, dV \quad \text{and} \\ b(\delta \boldsymbol{\sigma}, \mathbf{u}) &:= \int_{\mathcal{B}} \text{Div} \delta \boldsymbol{\sigma} \cdot \mathbf{u} \, dV \end{aligned} \quad (2.98)$$

and $l(\delta \mathbf{u})$ defined the same as in (2.95). Note, that in the case where the original problem (2.94) consists of a pure Dirichlet boundary (ie. $\Gamma_N = \emptyset$), for the present two-field problem the entire boundary $\partial \mathcal{B}$ is of homogeneous Neumann type (cf. CARSTENSEN ET AL. [2019], see also VIEBAHN [2019]). For the given example $\boldsymbol{\sigma}$ denotes the *primal variable* and \mathbf{u} , which has the function of a Lagrange multiplier, is denoted as *constraining variable* in the present case ensuring that the balance of linear momentum formulated in terms of the primal variable $\boldsymbol{\sigma}$ is fulfilled. The second, constraining term in (2.96) accounts for the coupling of the two solution variables and enforces some constraint on the primal variable.

The third example corresponds to formulations incorporating three solution variables based on the variational principles of HU [1955] and WASHIZU [1955]. For the present problem, the corresponding formulation can be found in ZIENKIEWICZ AND TAYLOR [2000]. The potential reads

$$\Pi_{\text{HW}} := \int_{\mathcal{B}} \frac{1}{2} \boldsymbol{\varepsilon} : \mathbb{C} : \boldsymbol{\varepsilon} + \boldsymbol{\sigma} \cdot (\boldsymbol{\varepsilon} - \nabla^s \mathbf{u}) - \mathbf{f} \cdot \mathbf{u} \, dV \quad (2.99)$$

and in the present local linear elasticity case the solution of the corresponding linear variational equation can be sought in the spaces $(\mathbf{u}, \boldsymbol{\varepsilon}, \boldsymbol{\sigma}) \in H_0^1(\mathcal{B}; \mathbf{R}) \times L^2(\mathcal{B}; \mathbb{S}) \times L^2(\mathcal{B}; \mathbb{S})$ so that for given $\mathbf{f} \in H^{-1}(\mathcal{B}; \mathbf{R}^3)$ and $\mathbf{u}^*|_{\Gamma_D}$ the equations

$$\begin{aligned} b_2(\boldsymbol{\sigma}, \delta \mathbf{u}) &= l(\delta \mathbf{u}) \\ a(\delta \boldsymbol{\varepsilon}, \boldsymbol{\varepsilon}) + b_1(\delta \boldsymbol{\varepsilon}, \boldsymbol{\sigma}) &= 0 \\ b_2(\delta \boldsymbol{\sigma}, \mathbf{u}) + b_1(\boldsymbol{\varepsilon}, \delta \boldsymbol{\sigma}) &= 0 \end{aligned} \quad (2.100)$$

hold for all $(\delta \mathbf{u}, \delta \boldsymbol{\varepsilon}, \delta \boldsymbol{\sigma}) \in H_0^1(\mathcal{B}; \mathbf{R}) \times L^2(\mathcal{B}; \mathbb{S}) \times L^2(\mathcal{B}; \mathbb{S})$. The corresponding definitions of the bilinear and linear forms read

$$\begin{aligned} a(\delta \boldsymbol{\varepsilon}, \boldsymbol{\varepsilon}) &:= \int_{\mathcal{B}} \delta \boldsymbol{\varepsilon} : \mathbb{C} : \boldsymbol{\varepsilon} \, dV \\ b_1(\delta \boldsymbol{\varepsilon}, \boldsymbol{\sigma}) &:= \int_{\mathcal{B}} \boldsymbol{\sigma} \cdot \delta \boldsymbol{\varepsilon} \, dV \\ b_2(\boldsymbol{\sigma}, \delta \mathbf{u}) &:= - \int_{\mathcal{B}} \boldsymbol{\sigma} \cdot \nabla^s \delta \mathbf{u} \, dV \end{aligned} \quad (2.101)$$

and $l(\delta \mathbf{u})$ unchanged from the previous cases. In the context of local linear elasticity, the introduction of mixed solution variables is motivated by providing formulations that avoid locking in the case of nearly incompressible material behavior (see e.g. ZIENKIEWICZ AND TAYLOR [2000] and many other contributions).

2.4.2 Definition of Stability

In the following, the conditions of LAX AND MILGRAM [1954] are introduced, which are necessary conditions for the primal variational formulation but also for some of the bilinear forms of the mixed variational formulations in order to produce stable solutions. In the context of primal variational formulations, the terminology stability refers to existence of a solution and uniqueness of such. In the context of mixed variational formulations, the term stability additionally includes the consistency of the mixed solution with the solution of the original problem. In the discrete finite element setting, the term stability translates to rank sufficiency of the tangent matrix of the corresponding linear system of equations (cf. section 3.3.3) and robustness of the corresponding numerical solution procedure. Note, that the following concepts of stability only refer to linear systems.

Boundedness and Coercivity: The theorem of LAX AND MILGRAM [1954] states that a problem with one primal solution variable (\mathbf{u} in the case of problem (2.94)) is stable if the bilinear form is *bounded* and *coercive*. Boundedness is given if the condition

$$|a(\delta \mathbf{u}, \mathbf{u})| \lesssim \|\mathbf{u}\|_{\mathcal{U}} \|\delta \mathbf{u}\|_{\mathcal{U}} \quad \forall \mathbf{u}, \delta \mathbf{u} \in \mathcal{U} \quad (2.102)$$

is fulfilled, where \mathcal{U} denotes the solution space of \mathbf{u} and $\|\bullet\|_{\mathcal{U}}$ its corresponding norm. In the present context of linear operators, the term boundedness is equivalent with the term

continuity (cf. BRAESS [2007]). Meanwhile, coercivity is given if the condition

$$a(\mathbf{u}, \mathbf{u}) \gtrsim \|\mathbf{u}\|_{\mathcal{U}}^2 \quad \forall \mathbf{u} \in \mathcal{U} \quad (2.103)$$

is fulfilled. Provided the bilinear form is elliptic, the terms coercivity and ellipticity are interchangeable (cf. BRAESS [2007], p. 37). In the present notation, a positive constant $c \in \mathbb{R}^+ \setminus \{0\}$ is hidden within the operators \lesssim and \gtrsim (cf. definitions of section 2.1). A geometric interpretation of a coercive bilinear form can be given by the observation that the slope of the functional value of the operator can only grow as the values of its arguments increase. A bilinear form that, as in the linear elasticity example (2.94) consists of a quadratic functional of symmetric gradients and solution space $H_0^1(\mathcal{B}; (\mathbb{R}^3))$ fulfills the boundedness and coercivity condition. Here, (denoted by the subscript 0) it is important that the solution space has a compact support (in other words, some generalized Dirichlet condition). Corresponding proofs can be found in BRAESS [2007].

2.4.3 The Inf-Sup Condition

In the case of two-field formulations such as (2.97) due to the existence of the second bilinear form b the previously stated Lax-Milgram stability conditions are no longer sufficient (ARNOLD [1990]). Now, in order to prove the uniqueness and existence of a solution LADYZHENSKAYA [1969], BABUŠKA [1973] and BREZZI [1974] showed that another necessary condition is the inf-sup condition (also known as LBB condition) applied to the bilinear form of the constraint term.

For the Hellinger Reissner formulation (2.97) the condition corresponding to the continuous formulation reads:

$$\sup_{\boldsymbol{\sigma} \in H(\text{Div}; \mathcal{B}; \mathbb{S}) \setminus \{0\}} \frac{b(\boldsymbol{\sigma}, \mathbf{u})}{\|\boldsymbol{\sigma}\|_{H(\text{Div})}} \gtrsim \|\mathbf{u}\|_{L^2} \quad \forall \mathbf{u} \in L^2(\mathcal{B}; \mathbb{R}^3) \quad (2.104)$$

Investigations with respect to the stability of problem (2.97) incorporating with $\boldsymbol{\sigma} \in H(\text{Div}; \mathcal{B}; \mathbb{S})$ symmetric solution fields can e.g. be found in ARNOLD AND WINTHER [2002] and ARNOLD ET AL. [2008].

Remark 2. *Note, that the terminology 'inf-sup' condition stems from the fact that (2.104) can equivalently be written as follows:*

$$\inf_{\mathbf{u} \in L^2(\mathcal{B}; \mathbb{R}^3) \setminus \{0\}} \sup_{\boldsymbol{\sigma} \in H(\text{Div}; \mathcal{B}; \mathbb{S}) \setminus \{0\}} \frac{b(\boldsymbol{\sigma}, \mathbf{u})}{\|\boldsymbol{\sigma}\|_{H(\text{Div})} \|\mathbf{u}\|_{L^2}} \geq c$$

Continuous and Discrete Inf-Sup Condition: For a stable finite element formulation, the inf-sup condition needs to be fulfilled both for the continuous formulation (infinite dimensional solution space as presented here) as well as for the discretized formulation (finite dimensional solution space). The criterion of FORTIN [1977] (see also BRAESS [2007], section 4.8) links the continuous inf-sup condition to the discrete inf-sup condition and can be often times applied to prove the discrete inf-sup stability. Further, for a finite element formulation for which the discrete inf-sup stability is fulfilled, the corresponding submatrix \mathbf{B} of (2.105) possesses always non-zero singular values and thus making the global matrix \mathbf{K} invertible (provided \mathbf{A} is also non-singular, which is linked to the ellipticity and continuity condition of a).

Remark 3. Generally, the global tangent matrix corresponding to the discretization of any two field variational formulation with the structure of the left-hand side as in the example (2.97) has the saddle point form

$$\mathbf{K} := \begin{bmatrix} \mathbf{A} & \mathbf{B}^T \\ \mathbf{B} & \mathbf{0} \end{bmatrix}, \quad (2.105)$$

where the coefficients of the submatrix \mathbf{A} are derived from the bilinear form $a(\boldsymbol{\sigma}^h, \delta\boldsymbol{\sigma}^h)$ and the coefficients of the submatrix \mathbf{B}^T and \mathbf{B} are derived from the discretized bilinear form $b(\delta\boldsymbol{\sigma}^h, \mathbf{u}^h)$ and $b(\boldsymbol{\sigma}^h, \delta\mathbf{u}^h)$, respectively. Here, \mathbf{u}^h and $\boldsymbol{\sigma}^h$ are assumed to be suitable discretizations of (2.97). More details with respect to finite element discretizations are given in chapter 3

Brezzi's Conditions for the Stability for Two-Field Formulations: As postulated by BREZZI AND FORTIN [1991], Proposition 1.1, for quadratic problems under linear constraints the following set of stability conditions needs to be fulfilled.

Boundedness of the bilinear forms (continuity): Similar to the previous subsection, the boundedness condition needs to be fulfilled to both bilinear forms. Thus, for (2.97) follows:

$$\begin{aligned} |a(\delta\boldsymbol{\sigma}, \boldsymbol{\sigma})| &\lesssim \|\boldsymbol{\sigma}\|_{H(\text{Div})} \|\delta\boldsymbol{\sigma}\|_{H(\text{Div})} \quad \forall \delta\boldsymbol{\sigma}, \boldsymbol{\sigma} \in H(\text{Div}; \mathcal{B}; \mathbb{S}) \\ |b(\boldsymbol{\sigma}, \mathbf{u})| &\lesssim \|\boldsymbol{\sigma}\|_{H(\text{Div})} \|\mathbf{u}\|_{L^2} \quad \forall \mathbf{u} \in L^2(\mathcal{B}; \mathbb{R}^3), \forall \boldsymbol{\sigma} \in H(\text{Div}; \mathcal{B}; \mathbb{S}) \end{aligned} \quad (2.106)$$

Coercivity (ellipticity): The coercivity condition applies to the quadratic term including the primal variable (first bilinear form) under the condition that the constraint term is fulfilled. Here, the latter is the case if $\boldsymbol{\sigma}$ belongs to the kernel space $\mathcal{Z}(\boldsymbol{\sigma}) := \{\delta\boldsymbol{\sigma} \in H(\text{Div}; \mathcal{B}; \mathbb{S}) : b(\delta\boldsymbol{\sigma}, \delta\mathbf{u}) = 0 \forall \delta\mathbf{u} \in L^2(\mathcal{B}; \mathbb{R}^3)\}$, which includes all functions $\boldsymbol{\sigma}$ for which the second term in (2.97)₁ vanishes. The coercivity/ellipticity condition for the given example then reads:

$$a(\boldsymbol{\sigma}, \boldsymbol{\sigma}) \gtrsim \|\boldsymbol{\sigma}\|_{H(\text{Div})}^2 \quad \forall \boldsymbol{\sigma} \in \mathcal{Z}(\boldsymbol{\sigma}) \quad (2.107)$$

Inf-sup condition: Finally, the Brezzi's conditions for the present two-field formulations are fulfilled if a finite element formulation fulfills together with the boundedness conditions (2.106) and the coercivity condition (2.107) the inf-sup condition (2.104).

2.4.4 Brezzi's Splitting Theorem Applied to Three-Field Formulations

In the case of Hu-Washizu type formulations the situation becomes more complicated as in formulations there are now two constraint terms. Nevertheless, corresponding stability analysis exists as well and is shortly summarized in this subsection. The following is based on BREZZI AND FORTIN's [1991], splitting Theorem 1.1 (see also SCHEDENSACK [2015], Theorem 2.8) generalized to three field formulations of the present type (cf. SCHEDENSACK [2015], Proposition 5.1, see also RIESELNANN ET AL. [2021], Lemma 1, where the splitting theorem was applied in the context of gradient elasticity formulations). Considered is a mixed three-field formulation of the type of the example (2.100) written now in terms of some generic solution variables in line with notations of subsequent proposed formulations:

$$\begin{aligned} a(\delta\mathbf{H}, \mathbf{H}) + b_1(\delta\mathbf{H}, \boldsymbol{\Lambda}) &= l_H(\delta\mathbf{H}) \\ b_1(\mathbf{H}, \delta\boldsymbol{\Lambda}) + b_2(\delta\boldsymbol{\Lambda}, \mathbf{u}) &= l_\Lambda(\delta\boldsymbol{\Lambda}) \\ b_2(\boldsymbol{\Lambda}, \delta\mathbf{u}) &= l_u(\delta\mathbf{u}), \end{aligned} \quad (2.108)$$

where $b_1(\mathbf{H}, \boldsymbol{\Lambda})$ and $b_2(\boldsymbol{\Lambda}, \mathbf{u})$ are bilinear forms of two constraint terms with some Lagrange multiplier variables $\boldsymbol{\Lambda} \in \mathcal{L}$ and $\mathbf{u} \in \mathcal{U}$ and \mathcal{U} and \mathcal{L} being some corresponding Sobolev

spaces. Analogous to the previous section, the kernel space of functions $\mathbf{\Lambda}$ that fulfill the constraint term $b_2(\mathbf{\Lambda}, \delta \mathbf{u}) = 0$ and the space of functions $\mathbf{H} \in \mathcal{H}$ that fulfill the constraint term $b_1(\mathbf{H}, \delta \mathbf{\Lambda})$ is defined by

$$\mathcal{Z}(\mathbf{\Lambda}) := \{\mathbf{\Lambda} \in \mathcal{L} : b_2(\delta \mathbf{\Lambda}, \delta \mathbf{u}) = 0 \ \forall \delta \mathbf{u} \in \mathcal{U}\} \quad \text{and} \quad (2.109)$$

$$\mathcal{Z}(\mathbf{H}) := \{\mathbf{H} \in \mathcal{H} : b_1(\delta \mathbf{H}, \delta \mathbf{\Lambda}) = 0 \ \forall \delta \mathbf{\Lambda} \in \mathcal{Z}(\mathbf{\Lambda})\} \quad (2.110)$$

respectively. Now, provided $a(\delta \mathbf{H}, \mathbf{H})$ is elliptic in the kernel space $\mathbf{H}, \delta \mathbf{H} \in \mathcal{Z}(\mathbf{H})$ and all bilinear forms are continuous, the formulation (2.108) has a unique solution if the following two inf-sup conditions hold:

$$\sup_{\mathbf{\Lambda} \in \mathcal{L} \setminus \{0\}} \frac{b_2(\mathbf{\Lambda}, \mathbf{u})}{\|\mathbf{\Lambda}\|_{\mathcal{L}}} \gtrsim \|\mathbf{u}\|_{\mathcal{U}} \quad \forall \mathbf{u} \in \mathcal{U} \quad (2.111)$$

$$\sup_{\mathbf{H} \in \mathcal{H} \setminus \{0\}} \frac{b_1(\mathbf{H}, \mathbf{\Lambda})}{\|\mathbf{H}\|_{\mathcal{H}}} \gtrsim \|\mathbf{\Lambda}\|_{\mathcal{L}} \quad \forall \mathbf{\Lambda} \in \mathcal{Z}(\mathbf{\Lambda}). \quad (2.112)$$

The splitting theorem is applied in the analysis of formulations appearing in this contribution in section 5.2.1 and chapter 6.

Chapter 3

Fundamentals of the Finite Element Method

3.1 Fundamentals of Finite Element Interpolation Functions

For the finite element method the considered body \mathcal{B} is subdivided into a finite number of elements T , which for what follows are mainly taken to be tetrahedra and in some occurrences hexahedra. Yet, the following notations refer to tetrahedral elements. The corresponding discretized mesh is denoted by \mathcal{T} with $T \in \mathcal{T} \subseteq \mathcal{B}$. The set of 4 faces $F \in \mathcal{F}_T$ of one element is denoted by \mathcal{F}_T , the set of 6 edges $E \in \mathcal{E}_T$ of one element is denoted by \mathcal{E}_T and the set of 4 vertices $V \in \mathcal{V}_T$ of one element is denoted by \mathcal{V}_T . In this section, some generic aspects of the construction of conforming finite element interpolation schemes are discussed. The theoretical aspects are showcased by means of the tetrahedral interpolation method based on RAVIART AND THOMAS [1977]. Note, that all subsequent conforming discretizations throughout this contributions fit within the following framework, yet, especially the full C^1 continuous formulation of section 4.2 picks up on the following fundamentals.

3.1.1 Interpolation Problem, Degrees of Freedom and Shape Functions

For the following, firstly one single element T is considered. Let $u \in \mathcal{U}(T)$ be a function that is to be interpolated and $\mathcal{U}(T)$ be the corresponding Sobolev space defined over the element. The element-interpolation operator $Iu : \mathcal{U}(T) \rightarrow P(T)$ maps the function u into the space $P(T)$ of polynomials defined over the element. For each element, the interpolation operator can be expressed as linear combination

$$Iu = \sum_{I=1}^n d_I(u) N_I := \sum_{I=1}^n d_I(u(\mathbf{X})) N_I(\mathbf{X}) \quad (3.1)$$

of n degrees of freedom $d_I(u)$, which are in general functionals of the solution function and basis functions N_I , which are in general functions of the physical coordinates \mathbf{X} . Degrees of freedom and basis functions can be scalar-, vector- or tensor-valued. Following the standard finite element approach, the biorthogonality condition

$$d_J(N_I) = \delta_{IJ} \quad \text{for } I, J \in \{1, \dots, n\} \quad (3.2)$$

states that the evaluation of each basis function needs to be one for the evaluation of the corresponding degree of freedom and zero for all other degrees of freedom and leads to a set

of equations from which the basis functions of any specific finite element formulation can be computed. In what follows, (3.2) is referred to as interpolation problem. Moreover, provided the interpolation problem is unisolvent from the biorthogonality the following two properties follow automatically:

$$d_I(u) = d_I(Iu) \quad \text{and} \quad Iu = IIu. \quad (3.3)$$

CIARLET's Definition of the Finite Element and Conditions for Conformity According to CIARLET [1978] (see also NEDÉLEC [1986]) a finite element can be defined by the following:

- The domain T , i.e. a tetrahedron in the present case
- A space $P(T)$ of polynomials $N_I : T \rightarrow P(T)$ with n -coefficients (ie. $P(T)$ has the dimension n).
- The set of n degrees of freedom, which are linear functionals $d_I : \mathcal{U}(T) \rightarrow \mathbb{R}$ acting on P .

Obviously, the first necessary condition for conformity is that the polynomial space $P(T)$ is a subspace of the continuous solution space $\mathcal{U}(T)$ so that the image of the interpolation operator is still an element of the solution space with

$$Iu : \mathcal{U}(T) \rightarrow P(T) \subseteq \mathcal{U}(T). \quad (3.4)$$

Secondly, the interpolation problem (3.2) needs to be unisolvent meaning that the number of polynomial coefficients, which is also referred to as dimension of the polynomial space $\dim P(T)$, must be the same as the number of degrees of freedom and the set of equations resulting from (3.2) needs to be linearly independent. So far, considerations were only restricted to one element. Since, in general, the body \mathcal{B} of interest is discretized into multiple elements making up the mesh \mathcal{T} with $T \in \mathcal{T} \subseteq \mathcal{B}$ consider now the set of interpolation operators $\bigcup_{T \in \mathcal{T}} Iu|_T \in P(\mathcal{T})$ consisting of all element-wise defined interpolation operators and $P(\mathcal{T})$ is the corresponding space of piecewise defined polynomials. Clearly, for a globally conforming interpolation scheme the piecewise polynomial space needs to be with

$$P(\mathcal{T}) \subseteq \mathcal{U}(\mathcal{B}) \quad (3.5)$$

a subspace of the global solution space $\mathcal{U}(\mathcal{B})$. According to the finite element theory, this is the case (given the first and second condition is fulfilled) if the traces (cf. table 3.1) of interpolation operators of two neighboring elements across the element interface are equivalent. The latter condition is fulfilled if the dimension of the trace of the polynomial space is equivalent to the number of degrees of freedom that evaluate the corresponding trace at one element face. In section 3.1.2 the concept is illustrated by means of the example of the Raviart-Thomas interpolation scheme.

Setup for Tangent Matrices and Residuals Of course, in general the finite element method does not seek to interpolate a given solution but to compute an approximation of the a priori unknown solution for some boundary value problem. Therefore, in the weak form (such as e.g. (2.90)) describing the boundary value problem, the unknown solution functions and test functions are replaced by the approximation functions

$$u^h = \sum_{I=1}^n d_I N_I \quad \text{and} \quad \delta u^h = \sum_{I=1}^n \delta d_I N_I \quad (3.6)$$

Sobolev Space	Integral Theorem	Trace(s) on ∂T
$H^1(T)$	$\int_T \nabla(\bullet) \, dV = \int_{\partial T} (\bullet) \, dA$	(\bullet)
$H(\text{Div}; T; \mathbb{R}^3)$	$\int_T \text{Div}(\blacksquare) \, dV = \int_{\partial T} (\blacksquare) \cdot \mathbf{n} \, dA$	$(\blacksquare) \cdot \mathbf{n}$
$H(\text{Rot}; T; \mathbb{R}^3)$	$\int_T \text{Rot}(\blacksquare) \, dV = \int_{\partial T} (\blacksquare) \times \mathbf{n} \, dA$	$(\blacksquare) \times \mathbf{n}$
$H^2(T)$	$\int_T \nabla \nabla(\bullet) \, dV = \int_{\partial T} \nabla(\bullet) \cdot \mathbf{n} \, dA$	$\nabla(\bullet) \cdot \mathbf{n}$

Table 3.1: Overview of traces of some selected Sobolev spaces and corresponding integral theorems. Here, (\bullet) denote scalar-valued functions and (\blacksquare) denote vector-valued functions. Integral theorems can be found in ALTENBACH [2012] and are corollaries of the divergence theorem (2.27).

and corresponding derivative occurrences, where the degrees of freedom are the unknowns. Therefrom, as in detail described in the subsequent section 3.3, the tangent matrices and residuals can be derived by means of which the finite element problem can be solved for the degrees of freedom.

3.1.2 Example: Lowest Order Raviart-Thomas Interpolation

In the following, the $H(\text{Div}; \mathcal{B}; \mathbb{R}^3)$ -conforming tetrahedral interpolation scheme of NEDÈLEC [1980] is presented in order to showcase the previously discussed conditions for conforming interpolation schemes. Since the tetrahedral interpolation scheme is based on the method of RAVIART AND THOMAS [1977], in what follows it is referred to as Raviart-Thomas interpolation. The vector function to be interpolated is considered to be in $\mathbf{u} \in H(\text{Div}; \mathcal{B}; \mathbb{R}^3)$.

Conformity of the Interpolation Space on one Element For now, the considered domain is one tetrahedron. The lowest order Raviart-Thomas polynomial space defined over the tetrahedron reads

$$RT0(T; \mathbb{R}^3) := \left\{ \mathbf{N}_{\text{ansatz}}^{(RT0)} = \begin{bmatrix} a \\ b \\ c \end{bmatrix} + d \begin{bmatrix} X \\ Y \\ Z \end{bmatrix} \quad \text{with } a, b, c, d \in \mathbb{R} \right\}, \quad (3.7)$$

where $\mathbf{N}_{\text{ansatz}}^{(RT0)}$ denotes the vector-valued polynomial basis and a, b, c and d some real valued coefficients. To improve readability for all subsequent occurrences throughout this and the next section, the superscript $(RT0)$ will be omitted. By taking the divergence $\text{Div} \mathbf{N}_{\text{ansatz}} = 3d$, which obviously holds for all elements of the space and therefore one can write $\text{Div}(RT0(T; \mathbb{R}^3)) = P0(T)$, it becomes clear that the result is a multiple of the constant function $d \in P0(T)$ which is L^2 -integrable showcasing that the $RT0$ -space is $H(\text{Div})$ -conforming. The basis functions describe the map

$$\mathbf{N}_I : T \rightarrow RT0(T; \mathbb{R}^3) \subseteq H(\text{Div}; T; \mathbb{R}^3). \quad (3.8)$$

As a result, it becomes clear that, provided the degrees of freedom map with

$$d_I : H(\text{Div}; T; \mathbf{R}^3) \rightarrow \mathbf{R} \quad (3.9)$$

the function to be interpolated to real scalar values, the interpolation operator

$$I\mathbf{u} = \sum_{I=1}^n d_I(\mathbf{u}) \mathbf{N}_I \quad \text{maps with} \quad I\mathbf{u} : H(\text{Div}; T; \mathbf{R}^3) \rightarrow RT0(T; \mathbf{R}^3) \subseteq H(\text{Div}; T; \mathbf{R}^3) \quad (3.10)$$

$\mathbf{u} \in H(\text{Div}; T; \mathbf{R}^3)$ conformingly to the polynomial subspace $I\mathbf{u} \in RT0(T; \mathbf{R}^3) \subseteq H(\text{Div}; T; \mathbf{R}^3)$. It remains to be shown that the degrees are such that (3.9) holds, the interpolation problem is unisolvent and the interface condition holds.

Degrees of Freedom and Unisolvency The degrees of freedom of any k -order Raviart-Thomas interpolation are defined by face- and volume moments

$$d_I = \int_{F_I} (\bullet) \cdot \mathbf{n} v \, dA \quad \forall v \in P_{k-1} \quad (3.11)$$

$$d_I = \int_T (\bullet) \cdot \mathbf{v} \, dV \quad \forall \mathbf{v} \in P_{k-2} \quad (3.12)$$

respectively, where in the lowest order case with $\mathbf{v} = \mathbf{0}$ no volume moments are present and with $v = 1$ associated to each face is one face moment, giving a total of 4 degrees of freedom. Clearly, (3.9) holds, since the integrals result in some real scalar function values. Moreover, the number of polynomial coefficients that is $\dim(RT0(T; \mathbf{R}^3)) = 4$ is the same as the number of degrees of freedom and the interpolation problem (3.2) is unisolvent. It remains to show the interface condition for global conformity.

Fulfillment of the Global Conformity Condition Next to the conformity on one element as discussed before, a necessary condition for conformity over the full discretized body \mathcal{T} (with $T \in \mathcal{T} \subseteq \mathcal{B}$) is the continuity of the trace of the interpolation operator across the interface of neighboring elements. In the present case, that is continuity of the normal direction $I\mathbf{u} \cdot \mathbf{n}$ (cf. table 3.1). The proof of the interface continuity condition for the 3D case can be found in NEDÉLEC [1980], following theorem 3. The corresponding necessary condition, namely the unisolvency of the interpolation problem reduced to the interface, can also be shown by the following argumentation. Obviously, the number of degrees of freedom that correspond to the normal direction at the face is per definition one. It remains to show that the dimension of the trace of the polynomial space $RT0(T; \mathbf{R}^3)$ reduced to the face is also one, making the interpolation scheme unisolvent for the trace at the interface. Therefore, consider some shape function $\mathbf{N}_1 \in RT0(T; \mathbf{R}^3)$ that fulfills the biorthogonality condition (3.2). By using the divergence theorem, the following relation can be obtained:

$$\int_T \text{Div}(\mathbf{N}_1) \, dV = \sum_{I=1}^4 \int_{F_I} \mathbf{N}_1 \cdot \mathbf{n} \, dA \quad (3.13)$$

Meanwhile, computing the divergence $\text{Div}(\mathbf{N}_1) = d_1$ ¹, inserting into the left-hand side of (3.13) and considering the biorthogonality on the right-hand side of (3.13) (resulting in all summands except for one to be zero) leads to

$$\int_T d_1 \, dV = \int_{F_1} \mathbf{N}_1 \cdot \mathbf{n} \, dA, \quad (3.14)$$

¹Here, d_1 denotes the fourth coefficient of the ansatz and is assumed to include the factor 3

which illustrates that the dimension of the trace of the polynomial space reduced to the face with $\dim(RT0(T; \mathbf{R}^3)|_F \cdot \mathbf{n}) = 1$ is also one, since on the left-hand side there is one coefficient d_1 .

Now, with the unisolvency of the problem at the interface the last remaining step in order to ensure global continuity is to ensure that the normal vectors of two neighboring elements are defined in the same direction. To illustrate this issue, consider the interpolation operators of two neighboring elements $I^{T_1}\mathbf{u}$ and $I^{T_2}\mathbf{u}$ and denote the shared interface by F . As stated before, due to the biorthogonality the interpolation operator reduced to the face consists of the corresponding face degree of freedom and reads

$$I^{T_1}\mathbf{u}|_F = \int_F \mathbf{u} \cdot \mathbf{n}_1 \, dA \quad \text{and} \quad I^{T_2}\mathbf{u}|_F = \int_F \mathbf{u} \cdot \mathbf{n}_2 \, dA$$

where \mathbf{n}_1 and \mathbf{n}_2 are the per definition outward pointing surface normal vectors with the relation $\mathbf{n}_1 = -\mathbf{n}_2$. Thus, without modification the difference

$$I^{T_1}\mathbf{u}|_F - I^{T_2}\mathbf{u}|_F = \int_F \mathbf{u} \cdot \mathbf{n}_1 + \mathbf{u} \cdot \mathbf{n}_1 \, dA \neq 0 \quad \dagger$$

is not zero. Therefore, in order to achieve equivalence the normal vectors have to be defined globally². Replacing \mathbf{n}_1 and \mathbf{n}_2 by the globally defined normal vector $\mathbf{n}_F = \mathbf{n}_1 = -\mathbf{n}_2$ leads to the relation

$$I^{T_1}\mathbf{u}|_F - I^{T_2}\mathbf{u}|_F = \int_F \mathbf{u} \cdot \mathbf{n}_F - \mathbf{u} \cdot \mathbf{n}_F \, dV = 0, \quad (3.15)$$

which fulfills the global continuity condition. Finally, given the interface condition in the present example the space that consists of polynomials belonging to $RT0(T; \mathbf{R}^3)$ defined piecewise for all elements $T \in \mathcal{T} \subseteq \mathcal{B}$ of the mesh can be postulated by $RT0(\mathcal{T}; \mathbf{R}^3)$ with $RT0(\mathcal{T}; \mathbf{R}^3) \subseteq H(\text{Div}; \mathcal{B}; \mathbf{R}^3)$. Note, that by following the previously discussed scheme but instead of the ansatz space (3.7) using now full vector valued $P1$ polynomials (possessing 12 coefficients) and defining three dofs per face one arrives at the $H(\text{Div})$ -conforming (BDM) finite element scheme of BREZZI ET AL. [1985]. Furthermore, when incorporating edge moments as degrees of freedom and using polynomial ansatz spaces for which rotations are computable by analogous considerations one arrives at the $H(\text{Rot})$ -conforming elements of NEDÉLEC [1980] and NEDÉLEC [1986] referred to as edge elements of first and second kind, respectively. Similarly to the difference between the RTk and BDM elements is that Nedelec's edge element of first and second kind are based on reduced (in the lowest order case 6 dimensional) vs full (in the lowest order case 12 dimensional) vector valued polynomials. Note, that the use of the $P1(T) \subset H^1(T)$ polynomial space is still conforming in both cases due to the relation $H^1(T; \mathbf{R}^3) \subset H(\text{Div}; T; \mathbf{R}^3)$ and $H^1(T; \mathbf{R}^3) \subset H(\text{Rot}; T; \mathbf{R}^3)$ (cf. (2.51) ff).

3.2 Finite Element Parametrizations

Generally, in order to keep the computational effort of the assembly procedure minimal, finite element interpolation functions are constructed once for the *reference element* and are then with isomorphic maps transformed to the actual element of the physical mesh. Therefore, this section summarizes the fictitious kinematic relations between the reference element and

²In implementations used throughout this contribution the global sign of \mathbf{n} is determined by the sign of the scalar product of $\mathbf{n}_1 \cdot (1, 0, 0)^T$ with the unit Cartesian direction and a sequence of alternative choices ($\mathbf{n}_1 \cdot (0, 1, 0)^T$ or $\mathbf{n}_1 \cdot (0, 0, 1)^T$) in the case any of the scalar products are zero.

the physical element that are made use of throughout this contribution. In some instances, analogies to the finite strain kinematics, in which the deformation describes an isomorphic map between the body in the initial configuration to the body in the deformed configuration, become apparent. Analogously to (2.65) introduce the bijective function $\phi := \phi(\Xi)$, which maps with

$$\phi : T^R \rightarrow T \quad (3.16)$$

any point $\Xi = [\xi, \eta, \zeta]^T$ in the coordinates of the reference element T^R to a point $\mathbf{X} = [X, Y, Z]^T$ of the physical element in the initial configuration. The set of vertex nodes of the reference tetrahedron reads $\mathcal{V}_T(T_R) = \{[1, 0, 0]^T, [0, 1, 0]^T, [0, 0, 1]^T, [0, 0, 0]^T\}$. Usually, the map (3.16) is described by parameterizing the physical elements with the help of nodal physical coordinate values and corresponding Lagrange interpolation functions formulated in terms of the reference coordinates. Thus, the notations

$$\mathbf{X}(\Xi) = \phi(\Xi) \quad \text{and} \quad \Xi(\mathbf{X}) = \phi^{-1}(\mathbf{X}) \quad (3.17)$$

are introduced, where the parametrization is given by

$$\mathbf{X}(\Xi) = \sum_{I=1}^n \mathbf{X}_I N_I(\Xi), \quad (3.18)$$

n is the number of nodes, \mathbf{X}_I denote the nodal coordinates and N_I denote the corresponding Lagrange function. Specific formulas for the computation and examples of nodal Lagrange shape functions can be found in ZIENKIEWICZ AND TAYLOR [2000]. The gradient

$$\mathbf{J} := \frac{\partial \mathbf{X}(\Xi)}{\partial \Xi} \quad (3.19)$$

of the parametrization with respect to the reference coordinates is called Jacobian and $\det \mathbf{J}$ denotes its determinant. In the case of interpolation schemes, where the parametrization is identical to the interpolation of the degrees of freedom, the transformation is called *isoparametric*. In this case, given the interpolation order is higher than linear, curvilinear elements can be mapped with the isoparametric concept providing more favorable approximation properties for geometries with curved boundaries (cf. BABUŠKA AND PITKÄRANTA [1990]). In the case of linear parametrizations the map is referred to as affine transformation, (3.18) is identical to

$$\mathbf{X}(\Xi) = \mathbf{J} \cdot \Xi + \mathbf{X}_4, \quad (3.20)$$

the Jacobian is constant, and the elements are referred to as straight-edge elements. In the case of the affine transformation, the inverse map can be simply computed by $\Xi = \mathbf{J}^{-1}(\mathbf{X} - \mathbf{X}_4)$.

Kinematics of Differential Operators With (3.18) gradients can be computed with the usual relation

$$\nabla(\bullet) = \partial_{\Xi}(\bullet) \cdot \mathbf{J}^{-1}. \quad (3.21)$$

For the sake of completeness, note also the relations for the divergence and rotation operators

$$\text{Div}(\bullet) = (\det \mathbf{J})^{-1} \text{Div}_{\Xi}(\det \mathbf{J} \mathbf{J}^{-1} \cdot (\bullet)) \quad \text{and} \quad \text{Rot}(\bullet) = (\det \mathbf{J})^{-1} \mathbf{J} \cdot \text{Rot}_{\Xi}(\mathbf{J}^T \cdot (\bullet)), \quad (3.22)$$

respectively (cf. SCHÖBERL [2009], lemma 14).

Kinematics of Integral Operators Analogous to the kinematic relations (2.70)-(2.72) between line-, surface- and volume increments of the initial and the deformed configuration presented in section 2.2 the following relations for the mapping from the reference to the physical element hold:

$$dV = \det \mathbf{J} dV^R, \quad d\mathbf{A} = \det \mathbf{J} \mathbf{J}^{-T} \cdot d\mathbf{A}^R \quad \text{and} \quad d\mathbf{X} = \mathbf{J} \cdot d\mathbf{X}^R, \quad (3.23)$$

where with $d\mathbf{A} = \mathbf{n} dA$ the vector \mathbf{n} is orthogonal to the surface increment and with $d\mathbf{X} = \mathbf{s} dX$ the vector \mathbf{s} is tangential to $d\mathbf{X}$. Now, let $(\bullet) \in \mathbb{R}^3$ be some vector function. With the relations (3.23) integrals over physical domains can be expressed in terms of integrals over corresponding reference domains by

$$\int_T (\bullet) dV = \int_{T^R} (\bullet) \det \mathbf{J} dV^R, \quad (3.24)$$

$$\int_F (\bullet) \cdot d\mathbf{A} = \int_{F^R} \det \mathbf{J} (\bullet) \cdot d\mathbf{A}^R \cdot \mathbf{J}^{-1} = \int_{F^R} \det \mathbf{J} (\mathbf{J}^{-1} \cdot (\bullet)) \cdot \mathbf{n}^R dA^R \quad \text{and} \quad (3.25)$$

$$\int_E (\bullet) \cdot d\mathbf{X} = \int_{E^R} (\bullet) \cdot \mathbf{J} \cdot d\mathbf{X}^R = \int_{E^R} (\mathbf{J}^T \cdot (\bullet)) \cdot \mathbf{s}^R dX^R. \quad (3.26)$$

From the face integral relation (3.25) the co- and contravariant *Piola transformation* (cf. BENTLEY [2017])

$$(\det \mathbf{J}) \mathbf{J}^{-1} \cdot (\bullet) \quad \text{and} \quad (\det \mathbf{J})^{-1} \mathbf{J} \cdot (\bullet), \quad (3.27)$$

can be derived, which is used when mapping interpolation operators that contain face integrals as degrees of freedom (cf. the following section 3.2.1). Analogously, from the edge integral relation (3.26) the co- and contravariant transformation

$$\mathbf{J}^T \cdot (\bullet) \quad \text{and} \quad \mathbf{J}^{-T} \cdot (\bullet), \quad (3.28)$$

can be derived, which is used when mapping interpolation operators that contain edge integrals as degrees of freedom such as the first and second type of edge elements of NEDELEC [1980] and NEDELEC [1986], respectively. In some occurrences in the following the covariant transformations are also referred to as *pull back* operation and the contravariant transformation is referred to as *push forward* operation in order to provide analogy to the finite strain kinematics 2.2³. Furthermore, note that in the case of straight edge elements due to \mathbf{J} being constant the following relations between reference and physical element volume V and V_R and triangular surface areas A and A_R hold:

$$V = \det \mathbf{J} V^R \quad (3.29)$$

$$A \mathbf{n}|_A = \det \mathbf{J} (A^R \mathbf{n}|_{A^R}) \mathbf{J}^{-1}. \quad (3.30)$$

³That is, analogously to the finite strain kinematics, assuming that in the 'forward' state is the physical space and the 'backward' state is the reference space. Note, that this notation might differ from other notations in the mathematical community (e.g. KIRBY [2018]) in which the 'forward' state is considered to be the reference space.

Surface and Edge Parameterizations Also, for the sake of completeness note, that the element faces and edges can be parametrized analogously to (3.18) by

$$\mathbf{X}(s, t) : F_R \rightarrow T \quad \text{with} \quad \mathbf{X}(s, t) = \sum_{I=1}^n \mathbf{X}_I^{(F)} N_I^{(2D)}(s, t) \quad (3.31)$$

$$\mathbf{X}(s) : E_R \rightarrow T \quad \text{with} \quad \mathbf{X}(s) = \sum_{I=1}^n \mathbf{X}_I^{(E)} N_I^{(1D)}(s) \quad (3.32)$$

$$\Xi(s, t) : F_R \rightarrow T_R \quad \text{with} \quad \Xi(s, t) = \sum_{I=1}^n \Xi_I^{(F)} N_I^{(2D)}(s, t), \quad (3.33)$$

where in (3.31) and (3.33) s and t denote the coordinates of the reference triangle with the vertices $\mathcal{V}_F(F_R) = \{[1, 0]^T, [0, 1]^T, [0, 0]^T\}$ and in (3.32) s denotes the coordinate of the reference line with the vertices $\mathcal{V}_E(E_R) = \{1, 0\}$. Meanwhile, n are the number of nodes corresponding to the Lagrange interpolation scheme, T_R , F_R and E_R denote the reference tetrahedron, triangle and line, respectively and \mathbf{X}_I denote the physical coordinates of the nodes of the tetrahedron, $\mathbf{X}_I^{(F)}$ denote the physical coordinates of the tetrahedron that lie on the I -th surface triangle, $\Xi_I^{(F)}$ denote the reference coordinates that lie on the I -th surface triangle of the reference tetrahedron and $N_I^{(2D)}(s, t)$ denote the corresponding 2D-Lagrange shape functions of the reference triangle. With (3.33) the physical coordinates can also be written as the composition $\mathbf{X}(\Xi(s, t)) := \mathbf{X}(\Xi) \circ \Xi(s, t) : F_R \rightarrow T$ combining (3.18) and (3.33). Then, again for the sake of completeness note, that gradients can be computed by $\nabla(\bullet) = \partial_{\Xi(s, t)}(\bullet) \cdot \mathbf{J}^{-1}(s, t)$, where $\mathbf{J}(s, t) := \partial_{\Xi(s, t)} \mathbf{X}(\Xi(s, t))$ denotes the Jacobian of the transformation and is a function of s and t . The computation of volume gradients in terms of surface parameters becomes necessary e.g. when imposing higher order continuity conditions through element interface integrals in discontinuous Galerkin approaches (see e.g. BRENNER AND SUNG [2005]) or when implementing higher order surface boundary conditions (cf. RIESELNANN ET AL. [2024]). Moreover, with the expression

$$\det \mathbf{J}_A(s, t) := \left\| \frac{\partial \mathbf{X}(s, t)}{\partial s} \times \frac{\partial \mathbf{X}(s, t)}{\partial t} \right\| \quad (3.34)$$

the surface unit normal vector can be computed by

$$\mathbf{n}(s, t) := \frac{1}{\det \mathbf{J}_A} \left(\frac{\partial \mathbf{X}(s, t)}{\partial s} \times \frac{\partial \mathbf{X}(s, t)}{\partial t} \right). \quad (3.35)$$

At this point it is worth pointing out that $\det \mathbf{J}_A(s, t)$ is not to be confused with $\det \mathbf{J}(s, t)$ as they are different quantities: \mathbf{J} refers to the Jacobian linking the volume gradients whereas $\det \mathbf{J}_A$ is a surface derivative quantity. In the case of straight edge elements, that is affine transformations, the parameterization is given by

$$\begin{aligned} \mathbf{X}(s, t) &= \mathbf{X}_2 s + \mathbf{X}_3 t + \mathbf{X}_1 (1 - s - t) \\ &= \mathbf{X}_1 + (\mathbf{X}_2 - \mathbf{X}_1) s + (\mathbf{X}_3 - \mathbf{X}_1) t \end{aligned} \quad (3.36)$$

which corresponds to an interpolation with linear Lagrange shape functions where \mathbf{X}_i denote the 3D coordinate values of the vertex nodes enclosing the triangle. It becomes clear that higher order parameterization schemes can be obtained analogously with higher order Lagrange functions interpolating the corresponding higher order set of nodal coordinates \mathbf{X}_i . In the linear case with (3.36) the computation of the normal vector simplifies to

$$\mathbf{n} := \frac{1}{\det \mathbf{J}_A} (\mathbf{X}_2 - \mathbf{X}_1) \times (\mathbf{X}_3 - \mathbf{X}_1) \quad \text{with} \quad \det \mathbf{J}_A := \|(\mathbf{X}_2 - \mathbf{X}_1) \times (\mathbf{X}_3 - \mathbf{X}_1)\| \quad (3.37)$$

and the relation $\det \mathbf{J}_A = 2A$ holds, where A denotes the area of the surface triangle. Similarly, the edge tangent vectors can be computed by

$$\mathbf{s}(s) := \left\| \frac{\partial \mathbf{X}(s)}{\partial s} \right\|^{-1} \frac{\partial \mathbf{X}(s)}{\partial s} \quad \text{and} \quad \mathbf{s} := \frac{\mathbf{X}_2 - \mathbf{X}_1}{\|\mathbf{X}_2 - \mathbf{X}_1\|} \quad (3.38)$$

for curves and straight lines, respectively. In the latter, \mathbf{X}_1 and \mathbf{X}_2 denote the coordinates of the enclosing vertex nodes with the linear parameterization $\mathbf{X}(s) = \mathbf{X}_2 s + \mathbf{X}_1(1-s)$ ($= \mathbf{X}_1 + s(\mathbf{X}_2 - \mathbf{X}_1)$). Explicit expressions of Lagrange shape functions can be found e.g. in ZIENKIEWICZ AND TAYLOR [2000].

Kinematics for Numerical Integration With the previously discussed volume, surface and edge parameterizations numerical integration schemes such as the Gauss quadrature can be used. Therefore, the integrals (3.24)-(3.26) expressed in parameter form read

$$\int_T (\bullet) \, dV = \int_0^1 \int_0^{1-\xi} \int_0^{1-\xi-\eta} (\bullet) \det \mathbf{J} \, d\zeta \, d\eta \, d\xi \quad (3.39)$$

$$\int_F (\bullet) \cdot d\mathbf{A} = \int_0^1 \int_0^{1-s} (\bullet) \cdot \mathbf{n} \det \mathbf{J}_A \, dt \, ds \quad (3.40)$$

$$\int_E (\bullet) \cdot d\mathbf{X} = \int_0^1 (\bullet) \cdot \mathbf{s} \|\partial_s \mathbf{X}(s)\| \, ds \quad (3.41)$$

and \mathbf{n} and \mathbf{t} defined in (3.35) and (3.38), respectively. Clearly, in the case of $(\bullet) \in \mathbf{R}^{3^n}$ being a vector or higher tensorial quantity (3.39) results in a quantity of the same tensorial order whereas (3.40) and (3.41) yields a quantity of order $n-1$. In the case of $(\bullet) \in \mathbf{R}$ being scalar valued instead of (3.40) and (3.41) the surface and edge integral relations

$$\begin{aligned} \int_F (\bullet) \, dA &= \int_0^1 \int_0^{1-s} (\bullet) \det \mathbf{J}_A \, dt \, ds \\ \int_E (\bullet) \, dX &= \int_0^1 (\bullet) \|\partial_s \mathbf{X}(s)\| \, ds \end{aligned} \quad (3.42)$$

hold. Based on (3.39)-(3.42) corresponding Gauss integration schemes can be used in order to evaluate the integrals numerically. Further reading with respect to Gauss quadrature rules also for tetrahedra and triangles and specific quadrature point and weight factor values can be found in ZIENKIEWICZ AND TAYLOR [2000] and SOLIN ET AL. [2004]. The high order quadrature points used in section 4.2 of this contribution are based on the rules of GRUNDMANN AND MÖLLER [1978].

Finally, note that the size of the element becomes relevant in the analysis of interpolation and discretization errors and is defined by

$$h := \max_{T \in \mathcal{T}} (\text{diam}(T)), \quad (3.43)$$

where $\text{diam}(T)$ defines the maximum distance between two vertices of one element. For example, the reference tetrahedron with the vertex set $v(T_R) = \{[1, 0, 0]^T, [0, 1, 0]^T, [0, 0, 1]^T, [0, 0, 0]^T\}$ has the diameter $\text{diam}(T_R) = \sqrt{2}$.

3.2.1 Example: Raviart-Thomas Interpolation Over the Reference Element

In this subsection the example of section 3.1.2, namely the lowest order Raviart-Thomas interpolation is picked up again in order to showcase the method of solving the interpolation

problem once for the reference element and postulating the physical interpolation operator by means of the Piola transformation. The latter is possible, since the lowest order Raviart-Thomas interpolation belongs to the affine family and the interpolation problem is invariant with respect to the transformation. This means there exists a push forward operation which when applied to the interpolation operator obtained by solving the interpolation problem (3.2) on the reference element yields exactly the interpolation operator obtained by solving the interpolation problem (3.2) on the physical element. As a result, the interpolation problem (3.45) is independent of any transformation to the physical element. The following considerations illustrate this characteristic and show the corresponding steps in the derivation of the push forward operator that is the Piola transformation. Analogous steps can be followed in order to derive transformation operators for other finite element interpolation schemes that belong to the affine family (see e.g. the Hermite interpolation scheme of section 4.2.2). Yet, for some elements the interpolation problem is not independent of the transformation as they do not belong to the affine family (cf. the C^1 interpolation of section 4.2.1). By means of (3.25) the face moment degrees of freedom of (3.11) can be formulated in terms of the reference element, which in the lowest order case read with $v = 1$:

$$d_I = \int_{F_I^R} \underbrace{(\det \mathbf{J} \mathbf{J}^{-1} \cdot (\bullet))}_{:= (\bullet)^R} \cdot \mathbf{n}^R \, dA^R \quad (3.44)$$

where $(\bullet)^R : T^R \rightarrow H(\text{Div}; T^R; \mathbf{R}^3)$ denotes the function pulled back to the reference space. Define the reference degree of freedom function $d_I^R : H(\text{Div}; T^R; \mathbf{R}^3) \rightarrow \mathbf{R}$ with $d_I^R := \int_{F_I^R} (\bullet)^R \cdot \mathbf{n}^R \, dA^R$. The interpolation problem on the reference element then reads

$$d_I^R(\mathbf{N}_J^R) = \delta_{IJ}, \quad (3.45)$$

where the previously introduced $(\bullet)^R$ is replaced by the reference basis functions $\mathbf{N}_I^R(\Xi) : T^R \rightarrow RT0(T^R; \mathbf{R}^3) \subseteq H(\text{Div}; T^R; \mathbf{R}^3)$ with $RT0(T^R; \mathbf{R}^3)$ defined by (3.7) but with physical coordinates replaced by reference coordinates. The solution of (3.45) leads in the present case to the explicit expressions

$$\mathbf{N}_1^R = 2 \begin{bmatrix} \xi \\ \eta \\ \zeta \end{bmatrix}, \quad \mathbf{N}_2^R = 2 \begin{bmatrix} \xi \\ \eta \\ \zeta - 1 \end{bmatrix}, \quad \mathbf{N}_3^R = 2 \begin{bmatrix} \xi \\ \eta - 1 \\ \zeta \end{bmatrix} \quad \text{and} \quad \mathbf{N}_4^R = 2 \begin{bmatrix} \xi - 1 \\ \eta \\ \zeta \end{bmatrix} \quad (3.46)$$

where the ordering 1 – 4 is associated to the faces of the unit tetrahedron with the normal vectors

$$\mathbf{n}_1^R = \frac{1}{\sqrt{3}} \begin{bmatrix} 1 \\ 1 \\ 1 \end{bmatrix}, \quad \mathbf{n}_2^R = \begin{bmatrix} 0 \\ 0 \\ -1 \end{bmatrix}, \quad \mathbf{n}_3^R = \begin{bmatrix} 0 \\ -1 \\ 0 \end{bmatrix} \quad \text{and} \quad \mathbf{n}_4^R = \begin{bmatrix} -1 \\ 0 \\ 0 \end{bmatrix} \quad (3.47)$$

(cf. BENTLEY [2017] see also SCHWARZ [2009]). Furthermore, the solution (3.46) of the interpolation problem leads to the interpolation operator

$$I^R \mathbf{u}^R = \sum_{I=1}^4 d_I^R \mathbf{N}_I^R \quad (3.48)$$

describing the map $I^R \mathbf{u}^R : H(\text{Div}; T^R; \mathbf{R}^3) \rightarrow RT0(T^R; \mathbf{R}^3) \subseteq H(\text{Div}; T^R; \mathbf{R}^3)$, which, however, when defined piecewise for each element does not lead to a conforming discretization yet since the normal continuity condition is not fulfilled. Therefore, the aim is now to find

the suitable transformation to $I^R \mathbf{u}^R$ such that it is equivalent to the conforming physical interpolation operator $I\mathbf{u}$ of (3.10). Firstly, we note that by the definition of the interpolation problem the relation

$$\delta_{IJ} = \int_{F_I} \mathbf{N}_J \cdot d\mathbf{A} = \int_{F_I^R} \mathbf{N}_J^R \cdot d\mathbf{A}^R \quad (3.49)$$

holds, where the left hand side expression is the physical interpolation problem and the right-hand side is the reference interpolation problem. Now, inserting the inverse of the relation (3.25) $\int_{F_I^R} (\bullet)^R \cdot d\mathbf{A}^R = \int_{F_I} ((\det \mathbf{J})^{-1} \mathbf{J} \cdot (\bullet)) \cdot d\mathbf{A}$ into the right-hand side of (3.49) yields

$$\int_{F_I} \mathbf{N}_J \cdot d\mathbf{A} = \int_{F_I} ((\det \mathbf{J})^{-1} \mathbf{J} \cdot \mathbf{N}_J^R) \cdot d\mathbf{A}$$

which holds only true if the relation

$$\mathbf{N}_J = (\det \mathbf{J})^{-1} \mathbf{J} \cdot \mathbf{N}_J^R \quad (3.50)$$

holds. The relation (3.50) describes the push forward operation by which the reference basis functions \mathbf{N}_J^R corresponding to face moment degrees of freedom of the Raviart-Thomas interpolation scheme can be transformed to the physical basis functions \mathbf{N}_J . Together with (3.44), which formulates the physical degrees of freedom in terms of the reference face integrals and the therefrom resulting relation

$$d_I = \int_{F_I^R} (\bullet)^R \cdot d\mathbf{A}^R = \int_{F_I} (\bullet) \cdot d\mathbf{A} \quad (3.51)$$

the physical interpolation operator can be written as

$$\begin{aligned} I\mathbf{u} &= \sum_{I=1}^4 d_I(\mathbf{u}) \mathbf{N}_I = \sum_{I=1}^4 \int_{F_I^R} (\det \mathbf{J} \mathbf{J}^{-1} \cdot \mathbf{u}) \cdot d\mathbf{A}^R (\det \mathbf{J})^{-1} \mathbf{J} \cdot \mathbf{N}_I^R \\ &= \sum_{I=1}^4 d_I(\mathbf{u}) (\det \mathbf{J})^{-1} \mathbf{J} \cdot \mathbf{N}_I^R \\ &= (\det \mathbf{J})^{-1} \mathbf{J} \cdot I^R \mathbf{u} \end{aligned} \quad (3.52)$$

where in the last step the push forward operator has been factored out of the sum, showing that for the lowest order Raviart-Thomas scheme the interpolation problem is independent with respect to transformations.

Remark 4. *Note, that the relation (3.52) holds also in the case of higher order parametrizations with non-constant Jacobians. See e.g. BERTRAND AND STARKE [2016] where a parametrization approach incorporating curvilinear elements applied to the lowest order Raviart-Thomas interpolation is presented. Yet, in the case of higher order Raviart-Thomas (and for that matter higher order Nédelec's-edge) interpolation schemes, pushing forward operations on the interpolation operator are not as straightforward, since due to the appearance of volume moments for the different basis functions different push forward operators apply so that the last step in (3.52) is not directly possible. Nevertheless, the higher order schemes still belong to the affine family as in general it is possible to solve the interpolation problem on the reference elements and transform it to the physical space (see also BENTLEY [2017]). Analogous characteristics are also present for the Hermite interpolation scheme, in which different kinematic relations apply to the gradient dof basis functions than to the nodal dof basis functions (cf. section 4.2.2).*

Setup for the Implementation of Tangent- and Stiffness Matrices Picking up on the considerations made in sections 3.1.1 and 3.1.2 for the example of the lowest order Raviart-Thomas interpolation and taking into account the direction of the normal vectors yields for the approximation functions

$$\mathbf{u}^h = \sum_I^4 \mathbf{sgn}(\mathbf{n}_I) d_I \mathbf{N}_I = \sum_I^4 \mathbf{sgn}(\mathbf{n}_I) d_I (\det \mathbf{J})^{-1} \mathbf{J} \cdot \mathbf{N}_I^R. \quad (3.53)$$

Resulting therefrom with (3.22) the approximation of the divergence reads

$$\text{Div } \mathbf{u}^h = \sum_I^4 \mathbf{sgn}(\mathbf{n}_I) d_I \text{Div } \mathbf{N}_I = \sum_I^4 \mathbf{sgn}(\mathbf{n}_I) d_I (\det \mathbf{J})^{-1} \text{Div}_{\Xi} \mathbf{N}_I^R, \quad (3.54)$$

where the simplification

$$\text{Div}_{\Xi}((\det \mathbf{J}) \mathbf{J}^{-1} \cdot \mathbf{N}_I) = \text{Div}_{\Xi}((\det \mathbf{J}) (\det \mathbf{J})^{-1} \mathbf{J}^{-1} \cdot \mathbf{J} \cdot \mathbf{N}_I^R) = \text{Div}_{\Xi} \mathbf{N}_I^R$$

was used. Here, as discussed in section 3.1.2 in order to ensure global continuity, the normal vectors appearing in the dof functions need to be defined globally. Therefore, from an implementation point of view, since the dofs are unknown, this fact is accounted for by adding a sign operator such as e.g.

$$\mathbf{sgn}(\mathbf{n}_I) := \begin{cases} \mathbf{sgn}(\mathbf{n}_I \cdot (1, 0, 0)^T) & \text{if } \mathbf{n}_I \cdot (1, 0, 0)^T \neq 0 \\ \mathbf{sgn}(\mathbf{n}_I \cdot (0, 1, 0)^T) & \text{if } \mathbf{n}_I \cdot (1, 0, 0)^T = 0 \text{ and } \mathbf{n}_I \cdot (0, 1, 0)^T \neq 0 \\ \mathbf{sgn}(\mathbf{n}_I \cdot (0, 0, 1)^T) & \text{if } \mathbf{n}_I \cdot (1, 0, 0)^T = 0 \text{ and } \mathbf{n}_I \cdot (0, 1, 0)^T = 0 \end{cases} \quad (3.55)$$

to each summand.

3.3 Example: $P2$ -Discretization of the Elasticity Problem

This section aims to illustrate the finite element procedure by means of the simple, well known local elasticity example. First, the suitable interpolation scheme that is conforming with the nonlinear continuous formulation is postulated. Then the corresponding approximation functions with unknown degrees of freedom are introduced. Finally, the tangent and residual matrix- and vector quantities are defined, which correspond to the global linearized system of equations. Starting point is the continuous nonlinear local elasticity problem given by the weak form (2.90) with the solution space $\mathbf{u} \in H_0^1(\mathcal{B}; \mathbf{R}^3)$ where $\mathbf{u} = [u_1, u_2, u_3]^T$ is the displacement vector.

3.3.1 Quadratic Nodal Lagrange Interpolation

Since in the case of nodal Lagrange interpolations of vector- or tensor-valued quantities all components are interpolated with the same scalar-valued basis functions, for the sake of simplicity throughout this subsection we concentrate on a scalar valued interpolation Iu where $u \in H^1(\mathcal{B}; \mathbf{R})$ can be any of the three vector components of \mathbf{u} . Furthermore, the example of the quadratic Lagrange interpolation is chosen, since generally in the case of elasticity it is well known to provide convergence results that are more favorable compared to the linear interpolation. Therefore, define on one element the quadratic polynomial space

$$P2(T; \mathbf{R}) := \{N_I \text{ is a quadratic polynomial}\} \quad (3.56)$$

for which on T clearly a gradient is computable and therefore fulfilling the conformity condition $P2(T; \mathbf{R}) \subseteq H^1(T; \mathbf{R})$. The degrees of freedom, basis functions and interpolation operator of the nodal Lagrange interpolation describe the following maps

$$d_I : H^1(T; \mathbf{R}) \rightarrow \mathbf{R} \quad (3.57)$$

$$N_I : T \rightarrow P2(T; \mathbf{R}) \subseteq H^1(T; \mathbf{R}) \quad (3.58)$$

$$Iu : H^1(T; \mathbf{R}) \rightarrow P2(T; \mathbf{R}) \subseteq H^1(T; \mathbf{R}). \quad (3.59)$$

Here, the degrees of freedom are simply the functions evaluated at the nodes, which are in the present case the four vertex nodes and the six mid-edge nodes, making up a total of 10 nodes. Since quadratic trivariate polynomials have with $\dim P2(T; \mathbf{R}) = 10$ coefficients, the interpolation problem is unisolvent. The trace of the H^1 -space is the function value itself (cf. table 3.1) on the surface. Thus, for global conformity the element interface condition manifests in the condition that the dimension of (3.56) reduced to some interface triangle (i.e. $\dim P2(T; \mathbf{R})|_F = \dim P2^{(2D)}(F; \mathbf{R}) = 6$) must be the same as the number of nodes present at that triangle. Since the triangular face of the nodal $P2$ element is enclosed by 3 vertex nodes and 3 mid-edge nodes, the number of nodes at the face is the same as $\dim P2(T; \mathbf{R})|_F = 6$ making the scheme unisolvent at the interface and therefore C^0 continuous and H^1 -conforming. Moreover, in the case of nodal Lagrange elements with the relations

$$d_I(\bullet) = (\bullet)|_I \quad \text{and} \quad \delta_{IJ} = N_J|_I = N_J^R|_I \quad (3.60)$$

the transformation of the reference interpolation to the physical interpolation operator is trivial since the resulting interpolation operators

$$Iu = \sum_{I=1}^{10} d_I N_I = \sum_{I=1}^{10} d_I N_I^R = I^R u \quad (3.61)$$

are equivalent (cf. SCHÖBERL [2009]). The specific expressions of the nodal shape functions N_I^R can be found e.g. in ZIENKIEWICZ AND TAYLOR [2000]. Error estimators and expected rates of convergence of the nodal Lagrange interpolation scheme can be found eg. in BRAESS [2007]. Based on (3.61) the vector-valued approximation functions read

$$\mathbf{u}^h = \begin{bmatrix} u_1 \\ u_2 \\ u_3 \end{bmatrix} = \sum_{I=1}^{10} \begin{bmatrix} d_I^{(u_1)} N_I \\ d_I^{(u_2)} N_I \\ d_I^{(u_3)} N_I \end{bmatrix} = \sum_{I=1}^{10} \mathbf{d}_I N_I = \sum_{I=1}^{10} \mathbf{d}_I N_I^R \quad (3.62)$$

with $\mathbf{d}_I := [d_I^{(u_1)}, d_I^{(u_2)}, d_I^{(u_3)}]^T$. Furthermore, with the kinematic gradient relation (3.21) the approximation of the displacement gradients reads

$$\nabla \mathbf{u}^h = \sum_{I=1}^{10} \mathbf{d}_I \otimes \nabla N_I = \sum_{I=1}^{10} \mathbf{d}_I \otimes \nabla_{\Xi} N_I^R \cdot \mathbf{J}^{-1}. \quad (3.63)$$

Note, that throughout this contribution, the kinematic relation (3.63) is used for the implementation of all subsequent occurrences of gradient approximations by nodal Lagrange interpolations.

3.3.2 Discrete Weak Form

Following the common Bubnov-Galerkin approach, in which in the weak form both solution functions and test functions are approximated by the same interpolation scheme⁴, insert-

⁴Contrary to that is the Petrov-Galerkin approach, in which the test functions may be composed of a different interpolation scheme (see e.g. ERN AND GUERMOND [2004]).

ing the discrete approximation functions into (2.90) yields the discrete weak form. Moreover, by means of the finite element procedure the domain is subdivided into the tetrahedral mesh \mathcal{T} and the discrete problem seeks $\mathbf{u} \in P2(\mathcal{T}; \mathbf{R}^3) \cap H_0^1(\mathcal{B}; \mathbf{R}^3)$ for given $(\mathbf{u}^*, \mathbf{f}, \mathbf{t}) \in H^{1/2}(\Gamma_D; \mathbf{R}^3) \times H^{-1}(\mathcal{B}; \mathbf{R}^3) \times H^{-1/2}(\Gamma_N; \mathbf{R}^3)$ (which are the prescribed displacements, volume loads and surface tractions) such that

$$\sum_{T \in \mathcal{T}} \int_T \partial_{\nabla \mathbf{u}^h} \psi(\nabla \mathbf{u}^h) \cdot \nabla \delta \mathbf{u}^h - \mathbf{f} \cdot \delta \mathbf{u}^h \, dV - \sum_{F \in \mathcal{F}_T \cap \Gamma_N} \int_F \mathbf{t} \cdot \delta \mathbf{u}^h \, dA = 0 \quad (3.64)$$

holds for all $\delta \mathbf{u}^h \in P2(\mathcal{T}; \mathbf{R}^3) \cap H_0^1(\mathcal{B}; \mathbf{R}^3)$. The discrete problem can equivalently be formulated in terms of the minimization problem

$$\begin{aligned} \Pi^h &\Rightarrow \min_{\mathbf{u}^h \in P2(\mathcal{T}; \mathbf{R}^3) \cap H_0^1(\mathcal{B}; \mathbf{R}^3)} \quad \text{with} \\ \Pi^h &:= \sum_{T \in \mathcal{T}} \int_T \psi(\nabla \mathbf{u}^h) \, dV + \Pi_{\text{ext}}^h. \end{aligned} \quad (3.65)$$

where the discretized external potential is given by

$$\Pi_{\text{ext}}^h := - \sum_{T \in \mathcal{T}} \int_T \mathbf{f} \cdot \mathbf{u}^h \, dV - \sum_{F \in \mathcal{F}_T \cap \Gamma_N} \int_F \mathbf{t} \cdot \mathbf{u}^h \, dA \quad (3.66)$$

3.3.3 Matrix Notation

In the case of the present example, each element has a set of $3 \times 10 = 30$ degrees of freedom, which can be described in terms of the vector

$$\underline{\mathbf{d}} := [d_1^{(u_1)}, d_1^{(u_2)}, \dots, d_{10}^{(u_2)}, d_{10}^{(u_3)}]^T. \quad (3.67)$$

Furthermore, introduce the global set of degrees of freedom

$$\underline{\mathbf{D}} = \bigcup_{T \in \mathcal{T}} \underline{\mathbf{d}}_T \quad (3.68)$$

where the operator

$$\bigcup_{T \in \mathcal{T}} (\bullet)_T \quad (3.69)$$

denotes the union of all elements of the mesh \mathcal{T} . Here, to provide some context, it appears worth mentioning that in the present standard continuous interpolation approach two neighboring elements share the same degrees of freedom on the interface. This is in contrary to so called discontinuous Galerkin (DG) approaches, in which each element has an independent set of degrees of freedom and the continuity is enforced by additional surface terms (See e.g. the nonlinear elasticity formulations of TEN EYCK AND LEW [2000] and BAYAT ET AL. [2019] among many other DG-contributions for various applications). Since the approximation operators (3.62) and (3.63) are (by definition of the finite element approach) linear in the degrees of freedom, finding the dofs that correspond to the minimizer \mathbf{u}^h of Π^h is equivalent to finding the root of the tangent vector

$$\underline{\mathbf{0}} = \frac{\partial \Pi^h}{\partial \underline{\mathbf{D}}} =: \underline{\mathbf{R}}(\underline{\mathbf{D}}), \quad (3.70)$$

which is typically referred to as *global residual vector*. In other words, the finite element solution of the problem (3.65) corresponds to the solution of problem (3.70). Yet, in general, as in the present example of finite strain hyperelasticity the problem (3.70) is nonlinear in $\underline{\mathbf{D}}$ since the strain energy function ψ can be an arbitrary function of $\mathbf{C}(\nabla \mathbf{u}^h)$.⁵ Therefore,

⁵The classic Neo-Hooke hyperelastic strain energy function e.g. contains logarithmic components.

in order to find the root, linearization based numerical solution schemes such as the Newton scheme are utilized. The corresponding linearized problem seeks $\Delta \underline{\mathbf{D}}$ such that

$$\text{Lin}[\underline{\mathbf{R}}] = \underline{\mathbf{R}}|_i + \underline{\mathbf{K}}|_i \Delta \underline{\mathbf{D}} = \underline{\mathbf{0}} \quad (3.71)$$

holds for each iteration i . Here, $\underline{\mathbf{K}} := \frac{\partial \underline{\mathbf{R}}}{\partial \underline{\mathbf{D}}}$ usually is referred to as *global tangent matrix*, $(\bullet)|_i$ denotes values of the previous iteration and $\Delta \underline{\mathbf{D}} = \underline{\mathbf{D}} - \underline{\mathbf{D}}|_i$ refers to the solution increment.

Assembly Operator An alternative notation can be given when taking into account the contributions of the individual *element tangent matrices* and *element residual vectors* defined by

$$\underline{\mathbf{r}} := \frac{\partial \Pi^h|_T}{\partial \underline{\mathbf{d}}} \quad \text{and} \quad \underline{\mathbf{k}} := \frac{\partial \underline{\mathbf{r}}}{\partial \underline{\mathbf{d}}}, \quad (3.72)$$

respectively. Within the so-called assembly procedure, a connectivity operator assigns to each element vector- and matrix index of $\underline{\mathbf{r}}$ and $\underline{\mathbf{k}}$ a corresponding global index. Thereby, the connectivity map is based on the order in which with (3.69) the element degrees of freedom are placed in the global degree of freedom vector. Thus, the linearized problem (3.71) can be written as

$$\text{Lin}[\underline{\mathbf{R}}] = \mathbf{A}_{T \in \mathcal{T}} \left(\underline{\mathbf{k}}_i \Delta \underline{\mathbf{d}} + \underline{\mathbf{r}}_i \right) = \underline{\mathbf{0}}, \quad (3.73)$$

where $\Delta \underline{\mathbf{d}}$ refers to the increment $\Delta \underline{\mathbf{d}} = \underline{\mathbf{d}} - \underline{\mathbf{d}}_i$ and the assembly operator

$$\mathbf{A}_{T \in \mathcal{T}} (\bullet)_T \quad (3.74)$$

corresponds to the sum of all element vector- and matrix entries under consideration of the global connectivity.

Part I

Finite Element Formulations for Gradient Elasticity

Chapter 4

Purely Displacement Based Formulation

4.1 The Gradient Elasticity Problem

In the following, the gradient elasticity approach introduced by MINDLIN [1964] and TOUPIN [1964] is presented in the notation of the nonlinear finite strain kinematic framework (cf. DELL'ISOLA ET AL. [2018]). Therefore, the hyperelastic strain energy, which in classical formulations is a function of the deformation gradient $\mathbf{F} := \mathbf{1} + \nabla \mathbf{u}$, is enriched by a non-local contribution including the second order deformation gradient

$$\psi := \psi^{\text{loc}}(\mathbf{F}) \quad (\text{classical elasticity}) \quad \Rightarrow \quad \psi := \psi^{\text{loc}}(\mathbf{F}) + \psi^{\text{nloc}}(\mathbf{F}, \nabla \mathbf{F}) \quad (\text{gradient elasticity}). \quad (4.1)$$

A brief discussion of the fulfillment of material objectivity and isotropy condition for the strain energy function follows in section 7.1. Within the second gradient framework for each coordinate direction i the boundary of \mathcal{B} is decomposed in the following way:

$$\begin{aligned} \partial \mathcal{B}^{(i)} &= \Gamma_{\text{N}}^{(i)} \cup \Gamma_{\text{D}}^{(i)} & \text{with} & \quad \Gamma_{\text{N}}^{(i)} \cap \Gamma_{\text{D}}^{(i)} = \emptyset & \text{and} \\ \partial \mathcal{B}^{(i)} &= \Gamma_{\text{M}}^{(i)} \cup \Gamma_{\text{H}}^{(i)} & \text{with} & \quad \Gamma_{\text{M}}^{(i)} \cap \Gamma_{\text{H}}^{(i)} = \emptyset. \end{aligned} \quad (4.2)$$

with $\Gamma_{\text{D}}^{(i)}$ and $\Gamma_{\text{N}}^{(i)}$ being the standard Dirichlet- and Neumann boundaries with prescribed $u_i = u_i^*$ and t_i , respectively, whereas $\Gamma_{\text{H}}^{(i)}$ and $\Gamma_{\text{M}}^{(i)}$ are second-order Dirichlet- and Neumann boundaries with prescribed $(\nabla \mathbf{u} \cdot \mathbf{n})_i = h_i^*$ and r_i , respectively. $\Upsilon_{\text{N}}^{(i)} = \partial \mathcal{B}^{(i)} \cap \Gamma_{\text{N}}^{(i)}$ is the set of edges $\partial \mathcal{B}^{(i)}$ on the first order Neumann boundary $\Gamma_{\text{N}}^{(i)}$ on which additional line tractions l_i can be prescribed. Followingly, the total elastic potential of the body \mathcal{B} in reference configuration is defined by

$$\Pi := \underbrace{\int_{\mathcal{B}} \psi(\mathbf{F}, \nabla \mathbf{F}) \, dV}_{\Pi_{\text{int}}} - \underbrace{\int_{\mathcal{B}} \mathbf{u} \cdot \mathbf{f} \, dV - \int_{\Gamma_{\text{N}}^{(i)}} u_i t_i \, dA - \int_{\Gamma_{\text{M}}^{(i)}} (\nabla \mathbf{u} \cdot \mathbf{n})_i r_i \, dA - \int_{\Upsilon_{\text{N}}^{(i)}} u_i l_i \, dS}_{\Pi_{\text{ext}}}, \quad (4.3)$$

where Π_{int} denotes the internal elastic potential and Π_{ext} denotes the potential due to external loads¹. The gradient elasticity boundary value problem can be formulated as the following

¹In general, the components of first and second order Dirichlet boundaries do not necessarily need to coincide and consequently neither do the components of the first and second order Neumann boundaries.

minimization problem. For given $\mathbf{f}, \mathbf{t}, \mathbf{r}$ and \mathbf{l} find the minimizer $\mathbf{u} \in \mathcal{U}$ of the total potential

$$\Pi \Rightarrow \min_{\mathbf{u}} \quad (4.4)$$

where Π is the total potential (4.3). Here, due to the appearance of second order gradients the solution space \mathcal{U} defined by

$$\mathcal{U} := \{\mathbf{u} \in H^2(\mathcal{B}, \mathbb{R}^3) : u_i = u_i^* \text{ on } \Gamma_D^{(i)} \text{ and } (\nabla \mathbf{u} \cdot \mathbf{n})_i = h_i \text{ on } \Gamma_H^{(i)}\} \quad (4.5)$$

is a H^2 sub-space, which requires conforming discretizations to be C^1 continuous (cf. BRAESS [2007]). The challenges connected to direct C^1 continuous finite elements are discussed in section 4.2. The corresponding set of Euler-Lagrange equations obtained by variation of (4.3) with respect to \mathbf{u} and integrating by parts can be found in (cf. MINDLIN [1964], p.69). The corresponding weak form is given in appendix A.1.

4.2 Challenges of a C^1 Continuous Interpolation

In the following the lowest order conforming C^1 continuous interpolation scheme that is suitable for 3D tetrahedral meshes is discussed as an example, showcasing the increased complexity compared to Lagrange interpolations and resulting therefrom some numerical challenges. The following approach was first introduced by ŽENIŠEK [1973] (see also LAI AND SCHUMAKER [2007]) and is considered the 3D-analogue to the C^1 continuous triangular element of ARGYRIS AND SCHARPF [1968] (see also OKABE [1993]). A summary of various other existing C^1 continuous approaches is given in the introduction of chapter 1. First, in what follows, a summary of the necessary conditions for C^1 continuity is given. Then, in section 4.2.1 the degrees of freedom of the present P9-C1 interpolation are summarized, the corresponding interpolation problem for the computation of the shape function coefficients is discussed and the interpolation operator is presented. Based thereon, in a numerical test, the interpolation power of the approach is shown. In section 4.2.2 the fulfillment of the interelement continuity condition for the P9-C1 element is discussed and visualized with counter examples of the P3-Hermite and P2-Lagrange interpolation schemes, which fail to fulfill this condition. The discussion is followed by an example finite element computation in section 4.2.3, which unveils the numerical issues the P9-C1 element is challenged with.

Necessary Conditions for C^1 Continuity In order to obtain a full C^1 continuous 3D finite element scheme, which conformingly interpolates the field $u \in H^2(\mathcal{B})$ the following requirements are necessary (cf. BRAESS [2007], LAI AND SCHUMAKER [2007]):

- On one element the polynomial space $P(T) \subseteq H^2(T)$ must be a subspace of the desired H^2 - Sobolev space.
- For unisolvency of the interpolation problem (3.2) the number of degrees of freedom n and the dimension of the polynomial space $\dim P$ must coincide ($\dim P = n$).

Thus, formally the surface integrals should read $\sum_{(i) \in \{1,2,3\}} \int_{\Gamma^{(i)}} (\bullet) \, dA$, where $\Gamma \in \{\Gamma_N, \Gamma_M\}$ denotes the boundary type, i is the vector component, for which each sub-surface integral is considered independently and $\sum_{(i) \in \{1,2,3\}}$ denotes the sum of the three surface-subdomain integrals. Throughout this contribution, however for the sake of readability for the surface integrals the short notation $\int_{\Gamma^{(i)}} (\bullet) \, dA := \sum_{(i) \in \{1,2,3\}} \int_{\Gamma^{(i)}} (\bullet) \, dA$, is used. The same holds for the edge integrals.

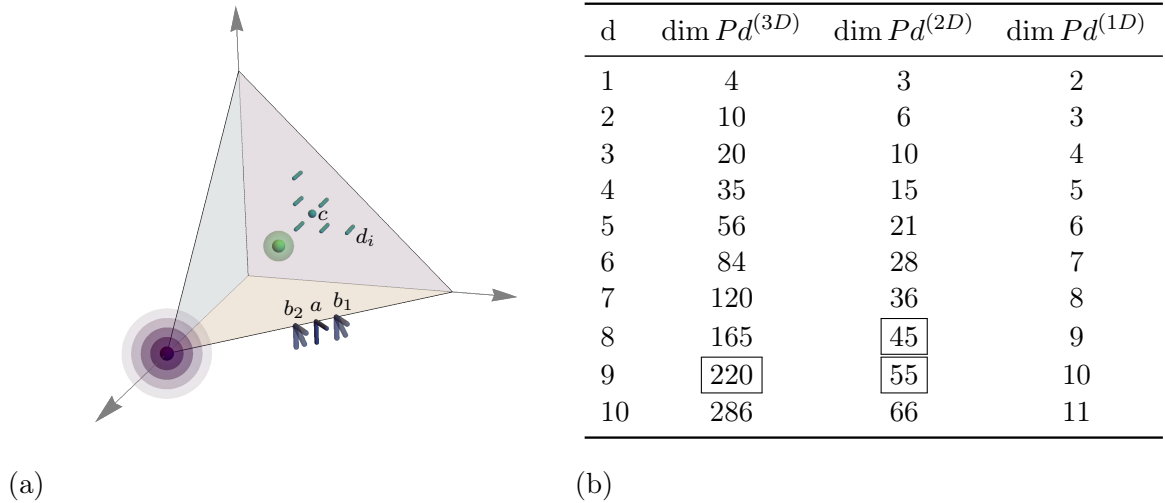


Figure 4.1: (a) Visualization of the degrees of freedom of the P9-C1-Element. Here, for the sake of clearness, the degrees of freedom (dofs) of only one exemplary vertex, face and edge are visualized. The element has with 35 dofs at each vertex, 8 dofs at each edge, 7 dofs at each face and 4 dofs in the center node a total of 220 dofs. (b) List of dimensions of spaces of d -order polynomials from 3D to 1D (note the relations (4.8)).

- Interface continuity condition: On the interface $F = \partial T_1 \cap \partial T_2$ between two elements T_1 and T_2 both the interpolated solution variable Iu and its normal gradient $\nabla(Iu) \cdot \mathbf{n}$ needs to be continuous. From the condition, the continuity of the full gradient across the interface follows also, since the continuity of Iu automatically implies continuity of the surface tangential direction of the gradient.
- Unisolvency of the interpolation problem reduced to the face: The polynomial space $\dim P|_F$ reduced to the face must have the same dimension as the number of degrees of freedom (dofs) and surface tangential derivative components of the dofs at the face (C^0 -continuity condition). In addition, the dimension of the polynomial space one order lower than P reduced to the face must have the same dimension as the number of normal derivative components of the dofs at the face (C^1 -continuity condition). If the present unisolvency is fulfilled, the interface continuity condition is fulfilled.

The lowest order polynomial space for which an interpolation scheme that fulfills the conditions can be constructed (and gets by without element subdivision) is of order $P9$ (cf. LAI AND SCHUMAKER [2007]). Details on the implementation of the corresponding interpolation scheme first introduced by ŽENIŠEK [1973] are presented in the following. In the subsequent subsections, the interpolation scheme is denoted as P9-C1-element. The following illustrated implementations are based on straight edge kinematics and the extension to kinematics with suitable isoparametric curvilinear elements is left for the future.

4.2.1 Degrees of Freedom, Shape Functions and Interpolation Operator

Consider a single element T in physical space. By choosing a $P9$ polynomial space, the degrees of freedom and the corresponding shape functions describe the following mappings

$$d_I : P9(T) \rightarrow \mathbf{R} \quad \text{and} \quad N_I : T \rightarrow P9(T) \quad (4.6)$$

Clearly, since a $P9$ -polynomial defined over the element is 9 times continuously differentiable the polynomial space $P9(T) \subseteq H^2(T)$ is a subspace of the desired $H^2(T)$ Sobolev space, fulfilling the first of the beforementioned conditions. In order to ensure unisolvency of the interpolation problem (3.2), since trivariate $P9$ -polynomials have 220 independent coefficients ($\dim P9 = 220$), logically the present element needs to have 220 degrees of freedom. In the following, the specific functionals of all the degrees of freedom (visualized in figure 4.1(a)) are listed. The vertex degrees of freedom are given by

$$d_1 - d_{140} : \quad (\bullet)|_V, \nabla(\bullet)|_V, \nabla^2(\bullet)|_V, \nabla^3(\bullet)|_V, \nabla^4(\bullet)|_V \quad \text{for } V \in \mathcal{V}_T. \quad (4.7)$$

Here, the function values and Cartesian derivatives up to order 4 are considered. The symmetry conditions of higher derivatives (i.e. $\partial_{XY} = \partial_{YX}$ in the second order case) yield for the orders 2-4 for each vertex 6, 10 and 15 independent derivatives, respectively giving in total 35 dofs at each vertex. Note, that the sequence is equivalent to the third column of table (b) in figure 4.1. Here, by counting and simple comparison, it can easily be verified that the following relations hold:

$$\begin{aligned} \Delta \dim P^{(3D)} &\equiv \dim P^{(2D)} \equiv \dim \nabla^d(\bullet) & \text{and} \\ \Delta \dim P^{(2D)} &\equiv \dim P^{(1D)} \equiv \dim \nabla_{(2D)}^d(\bullet) \end{aligned} \quad (4.8)$$

Where $\Delta \dim P^{(3D)}$ denotes the number of additional polynomial coefficients that are added by going from one degree to the next. The edge degrees of freedom read

$$\begin{aligned} d_{141} - d_{188} : \quad & \nabla(\bullet)|_E^a \cdot \mathbf{e}_1, \nabla(\bullet)|_E^a \cdot \mathbf{e}_2, \nabla^2(\bullet)|_E^{b_i} : (\mathbf{e}_1 \otimes \mathbf{e}_1), \nabla^2(\bullet)|_E^{b_i} : (\mathbf{e}_1 \otimes \mathbf{e}_2), \\ & \nabla^2(\bullet)|_E^{b_i} : (\mathbf{e}_2 \otimes \mathbf{e}_2) \quad \text{for } i \in \{1, 2\} \quad \text{and } E \in \mathcal{E}_T \end{aligned} \quad (4.9)$$

where \mathbf{e}_1 and \mathbf{e}_2 denote vectors orthogonal to the edge vector \mathbf{s} defined by (3.38). Note that in order to ensure that the dofs are defined uniformly for adjacent elements the orientation of \mathbf{e}_1 and \mathbf{e}_2 has to be defined globally². The face degrees of freedom are defined by

$$d_{189} - d_{216} : \quad (\bullet)|_F^c, \nabla(\bullet)|_F^{d_i} \cdot \mathbf{n} \quad \text{for } i \in \{1, \dots, 6\} \quad \text{and } F \in \mathcal{F}_T \quad (4.10)$$

where \mathbf{n} denotes the face normal vector based on definition (3.37). Here, however, analogous to the Raviart-Thomas discretization (cf. sections 3.1.2 and 3.2.1) (and to the preceding definition of \mathbf{e}_1 and \mathbf{e}_2) in order ensure global continuity between elements the direction of \mathbf{n} needs to be defined globally. Finally, the internal degrees of freedom associated to the center node of the element are given by:

$$d_{216} - d_{220} : \quad (\bullet)|_C, \nabla(\bullet)|_C \quad (4.11)$$

where $(\bullet)|_C$ denotes the value evaluated at the center of the element. The $P9$ -polynomial ansatz reads

$$N_{\text{ansatz}}^{(P9)} = a_1 \gamma_1^9 + a_2 \gamma_1^8 \gamma_2 + \dots + a_{220} \gamma_4^9, \quad (4.12)$$

where the polynomial is written in terms of the four barycentric coordinates γ_i and is called Bernstein polynomials (B-polynomial) (cf. LAI AND SCHUMAKER [2007])³. Inserting (4.12)

²In the present implementation, \mathbf{e}_1 and \mathbf{e}_2 are defined by the cross product of \mathbf{s} with the Cartesian unit directions (i.e. $\mathbf{e}_1 = \mathbf{s} \times (1, 0, 0)^T$ $\mathbf{e}_2 = \mathbf{s} \times (0, 1, 0)^T$ and a sequence of alternative choices in case any of the cross products yield the zero vector)

³Alternatively, the ansatz with a polynomial representation in terms of the trivariate coordinates $N_{\text{ansatz}}^{\text{Bernstein}} = b_1 + b_2 X + \dots + b_{220} Z^9$ makes no difference conceptually and can be used as well. However, the use of Bernstein polynomials makes the computation of coefficients more simple (cf. LAI AND SCHUMAKER [2007]).

into the biorthogonality condition (3.2) yields for the computation of e.g. the second shape function $I = 2$ a linear equation system, which can be written as

$$\underline{d}(\underline{c}) = \underline{M}\underline{c} = [0, 1, 0, \dots]^T \quad \text{with } \underline{M} := \partial_{\underline{c}}\underline{d} \quad (4.13)$$

and $\underline{c}_2 = [a_1, \dots, a_{220}]^T \in \mathbb{R}^{220}$ denoting the vector of coefficients corresponding to the second shape function, the right-hand side given by the vector $[0, 1, \dots, 0]^T \in \mathbb{R}^{220}$ and

$$\underline{d}(\underline{c}) = [d_1(N_{\text{ansatz}}^{(P9)}), \dots, d_{220}(N_{\text{ansatz}}^{(P9)})]^T \in \mathbb{R}^{220}$$

denoting the vector of values of degrees of freedom resulting from inserting (4.12) into the functionals (4.7)-(4.11). Note, that the system of equations is linear since the polynomials are a linear combination of the coefficients and the degrees of freedom are linear functionals. The entire matrix $\underline{C} = (\underline{c}_1 | \underline{c}_2 | \dots | \underline{c}_{220}) \in \mathbb{R}^{220 \times 220}$ (where the columns correspond to the different shape functions and the rows correspond to the different coefficients) of 48400 coefficients of all shape functions can be computed by inverting \underline{M} :

$$\underline{M}\underline{C} = \underline{1} \quad \Leftrightarrow \quad \underline{C} = \underline{M}^{-1} \quad (4.14)$$

where the right-hand side $\underline{1} \in \mathbb{R}^{220 \times 220}$ is the unity matrix representing the right-hand side of the biorthogonality condition (3.2). Note, that following LAI AND SCHUMAKER [2007] the shape function coefficients of the 220 by 220 matrix can be computed successively with explicit formulas and by solving sub-equation systems, since especially in the case of the Bernstein polynomial representation some of the degrees of freedom (namely the vertex degrees of freedom) depend exclusively on subsets of \underline{c} leading to a decoupled, cheaper set of equations. Nevertheless, for the computation of the 220×220 coefficients for one element alone, an extensive amount of formulas and equation systems has to be solved. Moreover, another drawback of the present element is, that due to the existence of degrees of freedom associated to directional derivatives on the edges and faces, the P9-C1 element does not belong to the family of affine elements anymore. Correspondingly, a computation of the shape functions once and a mapping between the reference- and the physical tetrahedron (analogous to the Piola transformation in the case of Raviart-Thomas elements cf. section 3.2.1) is not possible. Note, however, that e.g. for the more simple also not affine Argyris triangle the theory of quasi affine elements (CIARLET [1978]) can be applied for corresponding transformations (see also BRAESS [2007]). In this context noteworthy is also the contribution of KIRBY [2018], where a general procedure including matrix operators acting on the basis functions has been proposed e.g. for the Argyris triangle and the triangle of MORLEY [1968]. In the case of the present P9-C1 element, after the mesh is generated, in a preprocessing step the shape function coefficients are computed explicitly for each element. With the computed shape functions, the interpolation operator for interpolation of the field $u \in H^2(B)$ reads

$$Iu = \sum_I^{220} d_I(u) N_I \quad (4.15)$$

where Iu is defined piecewise for each element.

In what follows, the interpolation power of the P9-C1 scheme is tested. Therefore, let $u \in C^9 \subseteq H^2(\mathcal{B})$ be the smooth field

$$u = (X(1-X)Y(1-Y)Z(1-Z))^2, \quad (4.16)$$

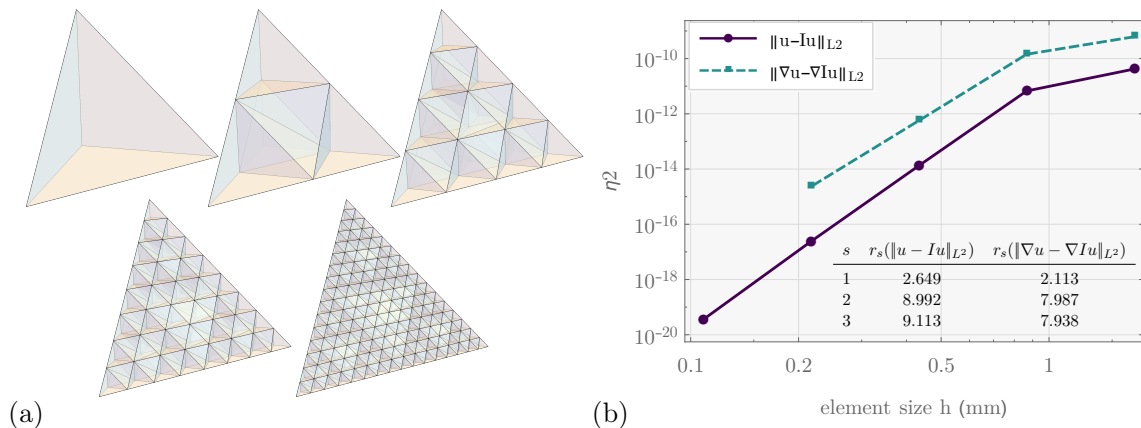


Figure 4.2: Convergence results of the interpolation problem for the P9-C1 element. (a) shows the refinement sequence of the considered mesh. (b) shows the convergence of the interpolation errors $\|u - Iu\|_{L^2}$ and $\|\nabla u - \nabla Iu\|_{L^2}$ ⁵ and corresponding rates of convergence in the table.

which is at least 9 times continuously differentiable. Given in LAI AND SCHUMAKER [2007], Theorem 18.5 the optimal rates of convergence of the interpolation error of the n -th derivative can be computed by

$$\|\nabla^n(u - Iu)\|_{L^2} \lesssim h^{10-n} \|\nabla^9 u\|_{L^2}. \quad (4.17)$$

Starting from the tetrahedron with the vertex nodes $\{(1, 0, 0), (0, 1, 0), (0, 0, 1)\}$ (cf. image of figure 4.2(a)) in a uniform refinement sequence visualized in the subsequent images the L^2 -norms of the interpolation errors $\|u - Iu\|_{L^2}$ and $\|\nabla u - \nabla Iu\|_{L^2}$ are plotted in figure 4.2 (b). As shown in the corresponding table in the same figure, within the considered refinement steps rates of convergence close to the optimal rates can be observed. Here, the convergence rates r are computed by

$$r_s(\bullet) = \frac{\ln((\bullet)_{s-1}) - \ln((\bullet)_s)}{\ln(h_{s-1}) - \ln(h_s)}, \quad (4.18)$$

where s refers to the refinement step, h to the element size (3.43) and (\bullet) denotes the error measure (cf. GALLISTL [2017]).

4.2.2 Visualization of the Interelement Continuity

In the preceding subsection, the computation of the shape functions has been discussed so far without addressing the interface condition mentioned in the beginning of this section. While the interface continuity condition is in general not a necessary condition to produce converging results for the interpolation problem, it is very much a necessary condition in order to produce consistent results for actual finite element computations. Therefore, in what follows, it is illustrated how the P9-C1 formulation fulfills the condition that ensures C^1 continuity, while e.g. the comparative $P3$ Hermite approach does not and corresponding solutions of finite element problems that require C^1 continuity fail to converge. Firstly, for the P9-C1 element the fulfillment of the unisolvency condition necessary for C^0 continuity stated at the beginning of this section is discussed by counting for one element face F the degrees of freedom associated to the function values themselves and the degrees of freedom

⁵Note, that for the present implementation, the computation of the results of the last refinement step of the gradient of the interpolation error was not possible within feasible computing times and are therefore omitted.

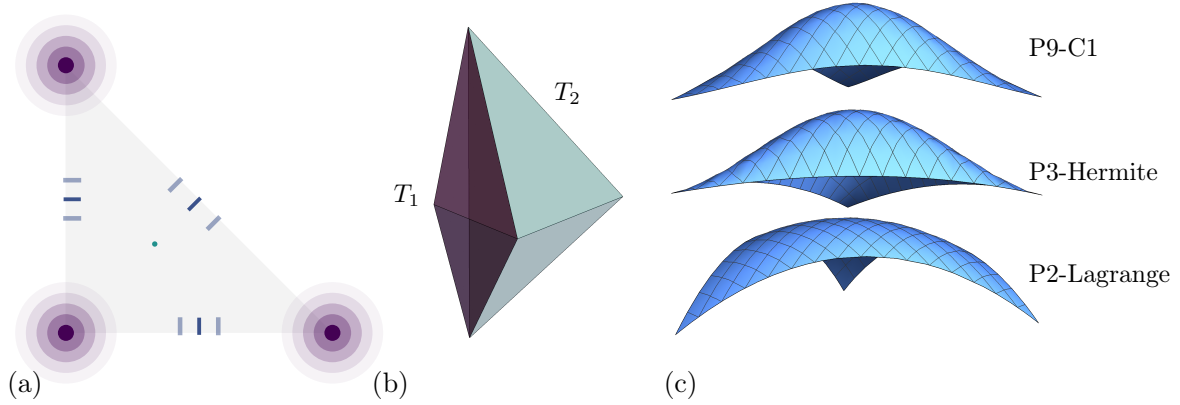


Figure 4.3: (a) Visualization of the face tangential components of the degrees of freedom of the P9-C1 element. (b) Two arbitrary tetrahedral elements with shared face $F = \partial T_1 \cap \partial T_2$. (c) Visualization of the surface parametrizations of the interpolation operators $I^{(T_1)}u|_F(s, t)$ and $I^{(T_2)}u|_F(s, t)$ with u given in (4.16). Clearly, since the elements are C^0 continuous, the interpolation operators for both elements yield the same results.

associates to derivatives that have a surface tangential component. The number of dofs that are function values themselves are 1 at each vertex and 1 at the midface node. The number of surface tangential components of the gradient dofs of the vertex are for first gradients 2, for second gradients 3, for third gradients 4 and for fourth gradients 5 giving with the 1 function value itself a total of 15 degrees of freedom at each vertex. Independent of the order of the derivative the edge degrees of freedom have only one surface tangential component and that is normal to the edge (cf. figure 4.3(a)), since the edge degrees of freedom have per definition (4.9) no component tangential to the edge. The remaining surface normal face degrees of freedom are not considered, since they are orthogonal to the tangential direction. Thus, the total count of dofs restricted to the surface tangential direction is

$$\underbrace{3 \times 15}_{\mathcal{V}_F} + \underbrace{1}_{\mathcal{F}_F} + \underbrace{3 \times 3}_{\mathcal{E}_F} = 55 = \dim P9(F), \quad (4.19)$$

which is equivalent to the dimension of the corresponding 2D polynomial space $\dim P9(F)$ (cf. figure 4.1(b)) and the unisolvency condition is fulfilled. In order to visualize the interface continuity, the example interface of two arbitrary elements (cf. figure 4.3(b)) is considered. Associated to that is figure 4.3(c), in which the surface parametrization (cf. section 3.2) of the operators $I^{(T_1)}u|_F(s, t)$ and $I^{(T_2)}u|_F(s, t)$ is visualized. It becomes clear that due to the C^0 continuity, the results of both $Iu|_{\partial T_1 \cap F}(s, t)$ and $Iu|_{\partial T_2 \cap F}$ coincide.

The C^1 continuity condition can be illustrated analogously to the previous considerations. Here, the derivative degrees of freedom of the P9-C1 element that have a surface normal direction need to be considered. A corresponding illustration is given in figure 4.4(a). This yields at the vertex node a count of 1 for the first derivative, 2 for the second derivative, 3 for the third derivative and 4 for the fourth derivative, adding up to 10 per vertex node. Note, that, e.g. in the case of second derivatives the mixed directions $\nabla(\bullet)|_V : (\mathbf{n} \otimes \mathbf{s})$ need to be accounted for. Therefore, it has a count of 2 and analogously consideration lead to the counts for the higher derivative orders. Analogous to the previous consideration are the edge degrees of freedom. That is, independent of the derivative order, each node produces a count of 1 since the edge tangential direction is per definition zero. Finally, the face dofs are the first normal derivative dofs themselves, producing a count of 1 at each node. In summary,

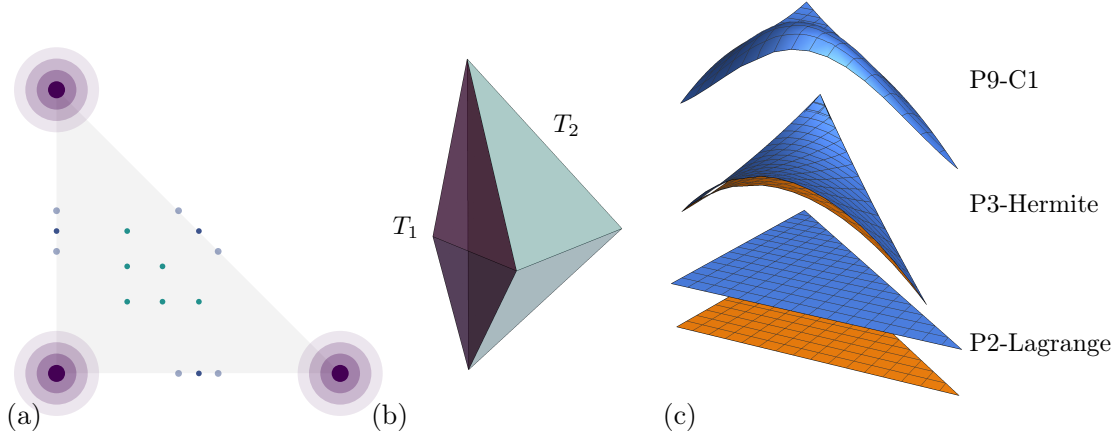


Figure 4.4: (a) Visualization of the face normal derivative components of the degrees of freedom of the P9-C1 element. (b) Two arbitrary tetrahedral elements with shared face $F = \partial T_1 \cap \partial T_2$. (c) Visualization of the surface parametrizations of the arbitrary derivative direction ∂_X of the element interpolation operators $\partial_X I^{(T_1)} u|_F(s, t)$ and $\partial_X I^{(T_2)} u|_F(s, t)$ with u given in (4.16). Here, it becomes visible that at the interface the gradients of the element interpolation operators of the P2-Lagrange and the P3-Hermite element yield different results, whereas the C^1 continuous P9-C1 element yields coinciding results.

the total count can be written as

$$\underbrace{3 \times 10}_{\mathcal{V}_F} + \underbrace{6 \times 1}_{\mathcal{F}_F} + \underbrace{3 \times 3}_{\mathcal{E}_F} = 45 = \dim P8(F) \quad (4.20)$$

which is equivalent to the dimension of the 2D polynomial space $\dim P8(F)$ (cf. figure 4.1(b)) fulfilling the unisolvency condition resulting together with the previously discussed condition in a full C^1 continuous approximation. The corresponding values of the first Cartesian component of the gradient of the interpolation operator $\partial_X I^{(T_1)} u|_F(s, t)$ and $\partial_X I^{(T_2)} u|_F(s, t)$ at the interface F of the two elements are visualized in figure 4.4(c). Here, it becomes visible that for the present P9-C1 element, the gradients of both interpolation operators coincide. Note, that, since the face normal direction of F in the present example is not the X -direction the arbitrary gradient component ∂_X moreover visualizes, that the continuity not only applies to the normal direction but also (due to the C^0 continuity) to any direction. Meanwhile, it becomes visible that the comparative Lagrange and Hermite elements, which do not fulfill normal gradient unisolvency condition (cf. following discussion), produce results that are not coinciding.

Comparative Elements To provide a comparison, the interface conditions for the P3-Hermite element are briefly discussed in the following. The degrees of freedom of the Hermite element are the function values at the vertices and the midface nodes as well as the first derivatives at the vertex nodes, giving a total of 20 dofs. The C^0 continuity for the Hermite element can be illustrated by the following expression

$$\underbrace{3 \times 3}_{\mathcal{V}_F} + \underbrace{1}_{\mathcal{F}_F} + = 10 = \dim P3(F) \quad (4.21)$$

as the tangential components of the derivative degrees of freedom are 2 for each vertex, giving with the function values a count of 3. The P3-Hermite element however fails to pass the C^1

continuity condition, since the vertex derivative degrees of freedom restricted to the surface normal direction yield a count of 1 for each vertex:

$$\underbrace{3 \times 1}_{\mathcal{V}_F} = 3 \stackrel{\neq}{=} 6 = \dim P2(F), \quad (4.22)$$

whereas the required number of dofs for unisolvency is given by $\dim P2(F) = 6$ ⁶. The violated C^1 continuity manifests in the deviations of the gradients (i.e. $\partial_X I^{(T_1)} u|_F(s, t) \neq \partial_X I^{(T_2)} u|_F(s, t)$) of the interpolation values across the surface of two neighboring elements (cf. figure 4.4(c)). For the P2 Lagrange element, showing the violation of the unisolvency condition in face normal direction is trivial, since no derivative degrees of freedom exist.

4.2.3 Finite Element Computation

While as shown in the preceding sections the P9-C1 formulation exhibits high order interpolation power and provides full C^1 continuity, its applicability as finite element approach is faced with significant numerical challenges that are illustrated in the following. Therefore, the following fourth order elliptic boundary value problem as a simplification of the gradient elasticity problem is considered: For a given volume load f find u such that

$$c_1 \operatorname{Div} \operatorname{Div} \nabla^2 u - c_2 \operatorname{Div} \nabla u = f \text{ in } \mathcal{B} \quad \text{and} \quad u = \nabla u \cdot \mathbf{n} = 0 \text{ on } \partial \mathcal{B} \quad (4.23)$$

with the constants $c_1 \in \{1, 0\}$ and $c_2 \in \{0, 1\}$ enabling to switch from the biharmonic problem with $(c_1, c_2) = (1, 0)$ to the Laplace problem with $(c_1, c_2) = (0, 1)$. Here, problem (4.23) is considered instead of the gradient elasticity problem as it is already sufficient to showcase the relevant issues of the discussed formulations. Moreover, in the case of gradient elasticity solutions can not be obtained at all since the issues shown in the following become even more severe. The potential of the discrete displacement based formulation corresponding to problem (4.23) reads

$$\Pi^h = \sum_{T \in \mathcal{T}} \int_{\mathcal{B}} \frac{c_1}{2} \nabla^2 u^h \cdot \nabla^2 u^h + \frac{c_2}{2} \nabla u^h \cdot \nabla u^h - f u^h \, dV. \quad (4.24)$$

where the interpolation functions u^h and corresponding gradients are defined for each element T of the mesh \mathcal{T} and read

$$u^h|_T = \sum_I^{220} d_I N_I \quad \text{and} \quad \nabla u^h|_T = \sum_I^{220} d_I \nabla N_I \quad \text{and} \quad \nabla^2 u^h|_T = \sum_I^{220} d_I \nabla^2 N_I \quad (4.25)$$

The expressions corresponding to the comparative P3-Hermite and P2-Lagrange elements are the same but instead of (4.25) with the respective interpolation functions inserted into (4.24). By defining a global vector \underline{D} as the union of all element degrees of freedom the

⁶A similar observation can be made for the hexahedral element of PAPANICOLOPULOS ET AL. [2008] mentioned in the introductory chapter 1 of this contribution. The formulation is based on tri-cubic polynomials with 64 coefficients. Since the proposed dofs of the entire element count 64 the interpolation problem is unisolvent. However, the polynomial space when reduced to the interface has the dimension 16, which does not appear to match the number of tangential components of the degrees of freedom at the interface. A similar observation can be made when comparing the dimension of the first derivative of the polynomial space reduced to the face (that is 9) to the number of normal derivative components of the degrees of freedom. Yet, interestingly, for the benchmark tests chosen in PAPANICOLOPULOS ET AL. [2008] the formulation appears to yield converging results.

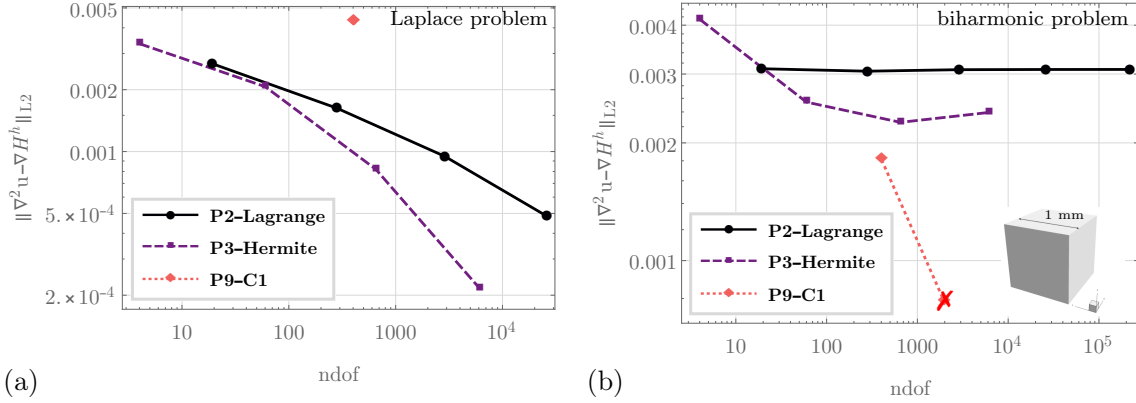


Figure 4.5: Unit cube convergence results of the C^1 continuous P9-C1 element compared to the non- C^1 continuous P3-Hermite and P2-Lagrange element for (a) the first order Laplace problem and for (b) the second order biharmonic problem. As expected in the case of the first order problem the results of the local elements converge and diverge in the case of the second order problem. Meanwhile, the results of the P9-C1 element appear to converge in the case of the biharmonic problem for the first refinement step. However, due to bad conditions of the global tangent matrix, the linear solver fails to produce solutions for finer meshes. The largest possible refinement steps are marked with a red cross.

corresponding tangent matrices are defined by $\underline{\mathbf{R}} = \partial_{\underline{\mathbf{D}}}\Pi^h$ and $\underline{\mathbf{K}} = \partial_{\underline{\mathbf{D}}}\underline{\mathbf{R}}$, respectively, resulting in the following global linear system

$$\underline{\mathbf{K}}\underline{\mathbf{D}} = -\underline{\mathbf{R}}, \quad (4.26)$$

of which the solution inserted into (4.25) yields the finite element solution u^h approximating the exact solution u to problem (4.23).

Unit Cube Test For what follows, again the constructed solution (4.16) is considered as reference. Due to its definition, u and ∇u take the value zero at the points 0 and 1, respectively in each coordinate direction. Therefore, the unit cube $\mathcal{B} = [1, 0] \times [1, 0] \times [1, 0] \text{ mm}^3$ is a suited geometry to for a boundary value problem that is set up to have u as analytical solution and the Dirichlet boundary condition $u = \nabla u \cdot \mathbf{n} = 0$ on $\partial\mathcal{B}$ (where \mathbf{n} is the outward pointing unit vector normal to the surface). See also section 7.2, where the unit cube geometry is also used for finite strain gradient elasticity benchmark testing. The corresponding right-hand side f is computed by inserting u into equation (4.23). Now, the consistency and the approximation power of the present formulations can be evaluated by discretization of the geometry, applying the volume load condition f and Dirichlet boundary condition and computing the finite element solution u^h . Then, the finite element solutions are compared to the exact solutions in terms of the L^2 error measure $\|\nabla^2 u - \nabla^2 u^h\|_{L^2}$. To evaluate the rates of convergence, the meshes are refined uniformly and results of the error are plotted for each refinement step. The corresponding plots are shown in figure 4.5. Here, the results of plots (a) correspond with $(c_1, c_2) = (0, 1)$ to the first order Laplace problem and those of plots (b) correspond with $(c_1, c_2) = (1, 0)$ to the second order biharmonic problem. Note, that in the case of the first order Laplace problem, prescribing $\nabla u \cdot \mathbf{n}$ on $\partial\mathcal{B}$ is not necessary but possible since the gradient of the reference solution is zero on the boundary anyway. The Dirichlet boundary conditions are imposed by fixing all degrees of freedom on the boundary that correspond to the function values and additionally in the case of the biharmonic problem

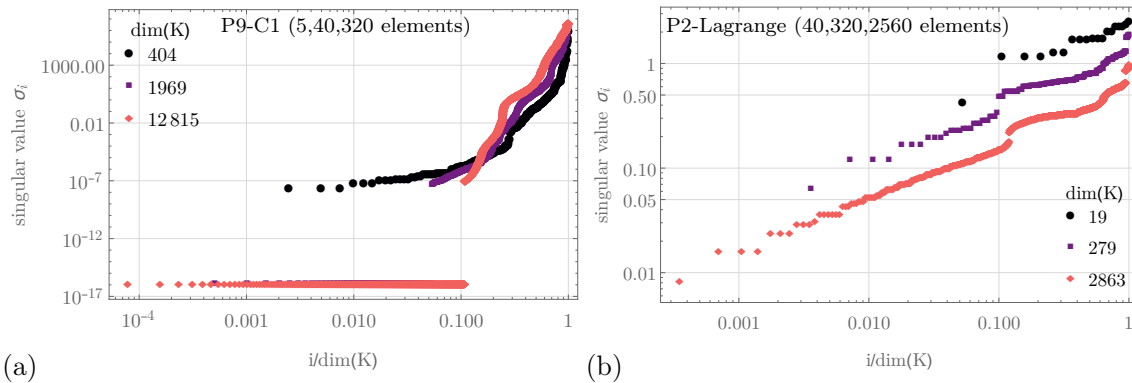


Figure 4.6: Singular value spectra for various mesh refinements of (a) the P9-C1 element compared to the P2-Lagrange element (b) and parameters corresponding to the biharmonic problem. In figure (a) the deterioration of the lower end of the singular value spectrum for the P9-C1 element becomes visible. Some of the lower singular values even take values below computer precision. Remarkably, even though already for the second refinement step some singular values of the P9-C1 element were below computer precision the PARDISO solver was able to compute a solution (cf. figure 4.5 (b)).

and the P9-C1 and the P3-Hermite element that correspond to the derivatives of first order. As expected in the case of the first order problem the results of the P3-Hermite and the P2-Lagrange elements converge and the results of the same elements clearly diverge in the case of the second order problem due to the non-existing C^1 continuity. Meanwhile, the results of the P9-C1 element appear to converge in the case of the biharmonic problem for the first refinement step. However, for the P9-C1 element only results of very low refinement stages are computable as the linear system of equations becomes unsolvable for standard linear solvers⁷ at higher refinements. The last refinement step before the issue occurs is marked with a red cross. Here, while in the present studies in the case of the biharmonic problem two refinement steps are computable, in the case of the Laplace problem not even more than one step is computable. And that is despite the fact that in the present study, the first refinement step consists of only one element patch with five elements. Thus, the considerable element size of the P9-C1 element becomes clear as it even with consideration of the Dirichlet conditions for one element patch in the first step already exhibits 404 degrees of freedom. Meanwhile, the P3-Hermite element has in the first refinement step less 4 degrees of freedom that are not fixed. Since in the case of the P2-Lagrange element for only one element patch there is nothing to calculate since all dofs are prescribed, the results shown start with the smallest mesh consisting of 40 elements.

The failure of the linear solver to produce solutions can be explained by the fact that the condition number $\kappa = \max(\sigma_i)/\min(\sigma_i)$ of the global tangent matrix quickly grows to infinity as the mesh gets finer. A corresponding study is presented in figure 4.6 (a), where the singular values of the tangent matrix \underline{K} are plotted for each mesh refinement step. While in theory the tangent matrices of the P9-C1 element are not singular, it can be seen from plot (a) that at the third refinement the lowest singular values are sink below computer precision (see also the discussion of ZHANG [2008]), whereas in the comparative plot (b) showing the singular values of the P2-Lagrange element the lower ends of the singular value spectra remain well above computer precision. For the present studies for the P9-C1 element a numerical

⁷For the present study, the AceGen/AceFEM software package and the PARDISO linear solver were used.

integration scheme incorporating 126 Gauss points (cf. GRUNDMANN AND MÖLLER [1978], see also SOLIN ET AL. [2004]) has been used as for a further increase of Gauss integration points no improvement of the results was observed.

4.2.4 Summary and Discussion of Challenges

In the preceding, it was shown that the P9-C1 element has optimal interpolation power and fulfills the C^1 continuity condition, making it fully $H^2(\mathcal{B})$ conforming and in theory suitable for the solution of gradient elasticity problems. Yet, due to its complexity it faces some numerical challenges summarized as follows:

- The number of degrees of freedom is very large and a total of 48400 shape function coefficients of one element alone makes the computation of shape functions already a numerically challenging task. Moreover, the condition number of the global stiffness matrix is due to the different orders of magnitude of shape function coefficients very high and grows at extremely high rates as the mesh gets finer. In consequence, conventional linear solvers quickly reach their limits in the ability to compute a solution as the lowest singular values of the global stiffness matrix fall below computer accuracy, as shown in the present numerical studies (see also results of ZHANG [2008]).
- Due to the existence of face normal and edge tangential derivatives the element does not belong to the affine family and operators mapping the interpolation functions of the reference element to interpolation functions of the physical element do not get by without distorting the derivative directions. Nevertheless, as discussed in ZHANG [2008] the P9-C1 element can be considered as almost affine making -analogous to the case of the Argyris triangle (cf. discussion of BRAESS [2007])- in principle, the application of corresponding mapping operators possible without loss of optimal convergence rates. Yet, so far the introduction of specific mapping operators as done e.g. by KIRBY [2018] for the Argyris triangle is missing in the literature. For present implementations coefficients have to be computed in a preprocessing step, increasing the computing time since for each element 48400 coefficients have to be computed.
- Since the interpolation space is P_9 , in order to ensure no decrease of convergence rates in the case of geometries and boundary conditions with corresponding curvature (cf. BABUŠKA AND PITKÄRANTA [1990]) a P_9 -parametrization of corresponding curvilinear elements would be the necessary choice, for which again implementation appears to be cumbersome and numerical integration expensive.

Numerous approaches exist in the literature proposing formulations that get by with less challenging sets of element degrees of freedom. A possible approach is the use of the so-called macro element technique and the use of reduced polynomial spaces as proposed by WALKINGTON [2014] following the approach for triangular elements of CLOUGH AND TOCHER [1965]. There, through element subdivision and incorporating special polynomial spaces which have a reduced order at the element faces, the corresponding interpolation scheme gets by with P_5 polynomials and derivative degrees of freedom similar to the Argyris triangle⁸, yet at the cost of increased complexity due to additional compatibility conditions that the shape functions of the sub-elements need to fulfill. Moreover, by even further subdividing the element interpolations with only P_2 polynomials and only 16 degrees of freedom is possible but with the

⁸Namely, up to second order gradients at the vertices, normal derivatives at the midface nodes and field values at the element center node giving a total of 45 degrees of freedom.

downside of having to subdivide the element into 24 sub-elements and impose an even larger number of internal compatibility conditions making an implementation even more challenging (cf. WALKINGTON [2014]). Among other approaches (cf. introduction of chapter 1) another much simpler remedy is the use of mixed formulations, in which through modification of the underlying continuous variational formulations additional solution variables are introduced enabling for much simpler C^0 continuous interpolation schemes. Various corresponding formulations that are suitable for gradient elasticity are subject of the present contribution and discussed in the following chapters.

Chapter 5

Mixed Finite Elements for Gradient Elasticity Based on the Hu-Washizu Variational Principle

In order to circumvent the challenges connected to conforming C^1 continuous interpolations illustrated in chapter 4 and other purely displacement based approaches discussed in chapter 1 a remedy allowing for simple C^0 continuous interpolation functions are three field mixed formulations akin to the Hu-Washizu variational principle. The present chapter discusses several such mixed three field finite element formulations for gradient elasticity both in the continuous setting as well as corresponding suitable approximation schemes: Firstly, section 5.1 presents the three field formulation of RIESELMANN ET AL. [2019] extended by the so called rot-rot stabilization to account for any kind of nonlocal strain energy. Then in section 5.2 a modification of the formulation is proposed allowing for L^2 and $H(\text{Div})$ approximation functions of which the corresponding pairing is known to be stable, while being applicable to any kind of nonlocal gradient elastic model. Moreover, the approximation scheme of ARNOLD AND BREZZI [1985] together with a volume bubble approximation of the mixed variable is proposed enabling static condensation and a relatively low number of global degrees of freedom. Lastly, section 5.3 introduces the finite strain extension of the small strain gradient elasticity formulation of RIESELMANN ET AL. [2024], which incorporates symmetric solution variables reducing the number of degrees of freedom and allowing for a formulation suitable for nonlocal energies of the strain gradient type without the need for the rot-rot stabilization parameter.

5.1 Straightforward Approach

In the following, a finite element approach for gradient elasticity based on RIESELMANN ET AL. [2019] (see also the small strain contributions of SHU ET AL. [1999] and ZYBELL ET AL. [2012]) is presented

5.1.1 Continuous Formulation

Starting point of the straightforward approach enabling the use of C^0 continuous interpolation functions is the following Lagrangian

$$\Pi_{\text{H1}} := \int_{\mathcal{B}} \psi^{\text{loc}}(\nabla \mathbf{u}) + \psi^{\text{nloc}}(\mathbf{H}, \nabla \mathbf{H}) + \boldsymbol{\Lambda} \cdot (\mathbf{H} - \nabla \mathbf{u}) \, dV + \Pi_{\text{ext}} + \Pi_{\Gamma} + \Pi_{\text{rot}}, \quad (5.1)$$

where \mathbf{H} is a mixed variable associated to the displacement gradient and $\boldsymbol{\Lambda}$ is the Lagrange multiplier variable. The corresponding saddle point problem seeks for given external loads (Π_{ext} defined in (4.3)) the functions $(\mathbf{u}, \mathbf{H}, \boldsymbol{\Lambda}) \in H_0^1(\mathcal{B}; \mathbb{R}^3) \times H_0^1(\mathcal{B}; \mathbb{R}^{3 \times 3}) \times H^{-1}(\mathcal{B}; \mathbb{R}^{3 \times 3})$ so that

$$\Pi_{\text{H1}} \Rightarrow \underset{\mathbf{u}, \mathbf{H}, \boldsymbol{\Lambda}}{\text{stat}} \quad (5.2)$$

becomes stationary. Here, the Lagrange multiplier term

$$\Pi_{\text{lag}} := \int_{\mathcal{B}} \boldsymbol{\Lambda} \cdot (\mathbf{H} - \nabla \mathbf{u}) \, dV \quad (5.3)$$

enforces compatibility of the mixed variable $\mathbf{H} = \nabla \mathbf{u}$ associated to the displacement gradient.

Treatment of Boundary Conditions Meanwhile, the term

$$\Pi_{\Gamma} = \int_{\partial \mathcal{B}} (\bar{\mathbf{G}} \cdot \mathbf{n}) \cdot (\nabla \mathbf{u} - \mathbf{H}) \, dA \quad (5.4)$$

ensures consistency with the surface terms of the original formulation (4.4) ($\bar{\mathbf{G}} := \partial_{\nabla \mathbf{H}} \psi$ denotes the higher order stress tensor in terms of \mathbf{H}). The kinematics for the discretization of the surface integrals are given in section 3.2 and further details on the implementation can be found in RIESELDMANN ET AL. [2024], where also corresponding numerical studies investigate the influence of Π_{Γ} under special boundary conditions. Note, that there, the surface integral terms in Π_{Γ} are introduced for the small strain analogon to the reduced formulation of section 5.3. Here, for the sake of simplicity and since the numerical examples throughout this contribution consider problems in which the addition of Π_{Γ} is not necessary¹ in the subsequent discretizations (5.4) is not considered. The components i of the first order Dirichlet conditions are given by

$$(\mathbf{u} = \mathbf{u}^*)_i^* \quad \text{and} \quad ((\mathbf{H})^{(t)} = \nabla_{\Gamma} \mathbf{u}^*)_i \quad \text{on} \quad \Gamma_{\text{D}}^{(i)}, \quad (5.5)$$

where $(\bullet)^{(t)}$ refers with definition (2.15) to the surface tangential components of (\bullet) . Meanwhile, the components i that belong to the second order Dirichlet boundary of the original problem are given through:

$$(\mathbf{H} \cdot \mathbf{n} = \nabla \mathbf{u} \cdot \mathbf{n} = \mathbf{h}^*)_i \quad \text{on} \quad \Gamma_{\text{H}}^{(i)} \quad (5.6)$$

Here, prescribing $(\mathbf{H})_i^{(t)}$ on $\Gamma_{\text{D}}^{(i)}$ and $(\nabla \mathbf{u} \cdot \mathbf{n})_i$ on $\Gamma_{\text{H}}^{(i)}$ is not strictly necessary, since the information of the prescriptors is already given via $(\nabla_{\Gamma} \mathbf{u} = \nabla_{\Gamma} \mathbf{u}^*)_i$ (implicitly imposed via $(\mathbf{u} = \mathbf{u}^*)_i$ on $\Gamma_{\text{D}}^{(i)}$ and $(\mathbf{H} \cdot \mathbf{n} = \mathbf{h}^*)_i$ on $\Gamma_{\text{H}}^{(i)}$ and coupled to the other field via the Lagrange multiplier term. More details on the variational equations are given in appendix A.1 where also the equivalence of the variational problem corresponding to (5.2) with the original variational equation (4.4) is shown.

¹The consideration of Π_{Γ} is not necessary, because on the boundary of the present problems there are either Dirichlet conditions or $(\mathbf{G} \cdot \mathbf{n})_i$ is taken to be zero.

Rot-Rot Stabilization In the potential (5.1) the additional rot-rot stabilization term

$$\Pi_{\text{rot}} := \int_{\mathcal{B}} \frac{\alpha}{2} \text{Rot } \mathbf{H} \cdot \text{Rot } \mathbf{H} \, dV \quad (5.7)$$

as proposed for the formulation of RIESELDMANN ET AL. [2021] (see also chapter 6) with the scalar numerical parameter $\alpha \in \mathbb{R}^+$ ensures unisolvency in the case of non-local strain energies which are formulated solely in terms of symmetric functions of \mathbf{H} (eg. $\psi^{\text{nloc}} := \psi^{\text{nloc}}(\mathbf{E}, \nabla \mathbf{E})$ with the Green Lagrange tensor $\mathbf{E} := \frac{1}{2}(\mathbf{H}^T \cdot \mathbf{H} + \mathbf{H}^T + \mathbf{H})$, cf. section 7.1). In the following discussion, this type of non-local energy is referred to as symmetric energy. In this case without the addition of Π_{rot} corresponding discrete residual equations for the 9 nodal degrees of freedom of \mathbf{H} yield only 6 linearly independent equations and the corresponding element sub-tangent matrices $\underline{\mathbf{k}}_{\mathbf{H}}$ (cf. following section 5.1.2) lose rank sufficiency, which is a crucial condition for stability.

In the following it is shown that the loss of linear independence is inherent already to the present continuous formulation and how this fact translates to any corresponding discrete system. Consider the symmetric energy function $\psi = \psi(\mathbf{E}, \nabla \mathbf{E})$ with E_{kl} being the components of the beforementioned Green-Lagrange tensor \mathbf{E} with the symmetry relations $E_{kl} = E_{lk}$ and $E_{lm,n} = E_{ml,n}$ (and therefore symmetric stress quantities $S_{kl} := \partial_{E_{kl}} \psi = \partial_{E_{lk}} \psi = S_{lk}$ and $B_{lmn} := \partial_{E_{lm,n}} \psi = \partial_{E_{ml,n}} \psi = B_{mln}$). Then, due to the symmetries, the following relations hold

$$\begin{aligned} \frac{\partial \psi}{\partial H_{ij}} &= \frac{\partial \psi}{\partial E_{kl}} \frac{\partial E_{kl}}{\partial H_{ij}} = \frac{\partial \psi}{\partial E_{kl}} \frac{\partial E_{kl}}{\partial H_{ji}} = \frac{\partial \psi}{\partial H_{ji}} \\ \frac{\partial \psi}{\partial H_{ij,k}} &= \frac{\partial \psi}{\partial E_{lm,n}} \frac{\partial E_{lm,n}}{\partial H_{ij,k}} = \frac{\partial \psi}{\partial E_{lm,n}} \frac{\partial E_{lm,n}}{\partial H_{ji,k}} = \frac{\partial \psi}{\partial H_{ji,k}} \end{aligned} \quad (5.8)$$

showcasing that differentiation with respect to H_{ij} and H_{ji} as well as $H_{ij,k}$ and $H_{ji,k}$ yields the same result, respectively. As a consequence, without the rot-rot stabilization any residual expressions

$$r_{d_{H_{ij}}} = \sum_{T \in \mathcal{T}} \int_T \frac{\partial \psi(H_{ij}^h, H_{ij,k}^h)}{\partial d_{H_{ij}}} \, dV \quad \text{and} \quad r_{d_{H_{ji}}} = \sum_{T \in \mathcal{T}} \int_T \frac{\partial \psi(H_{ij}^h, H_{ij,k}^h)}{\partial d_{H_{ji}}} \, dV, \quad (5.9)$$

that correspond to differentiation of the global functional with respect to the discrete degrees of freedom $d_{H_{ij}}$ and $d_{H_{ji}}$, respectively must be equivalent ($r_{d_{H_{ij}}} = r_{d_{H_{ji}}}$) for any nodal interpolation scheme $H_{ij}^h = \sum_I d_I^{(H_{ij})} N_I$ and $H_{ij,k}^h = \sum_I d_I^{(H_{ij})} (N_I)_{,k}$ leading to linearly dependent equations.

Now, in the following, it is illustrated how adding the rot-rot stabilization restores the linear independence of the discrete residual equations. By simply comparing the components of $\text{Rot } \mathbf{H}^h$ given by (2.23) one can easily verify that the rotation operator with

$$(\text{Rot } \mathbf{H}^h)_{ij} \neq (\text{Rot } \mathbf{H}^h)_{ji} \quad (5.10)$$

is not symmetric. As a consequence, following an analogous argumentation as before the residual components under consideration of the rot-rot stabilization become

$$\tilde{r}_{d_{H_{ij}}} = r_{d_{H_{ij}}} + \frac{\partial \Pi_{\text{rot}}^h}{\partial d_{H_{ij}}} \quad \text{and} \quad \tilde{r}_{d_{H_{ji}}} = r_{d_{H_{ji}}} + \frac{\partial \Pi_{\text{rot}}^h}{\partial d_{H_{ji}}} \quad (5.11)$$

and are with

$$r_{d_{H_{ij}}} = r_{d_{H_{ji}}} \quad \text{and} \quad \frac{\partial \Pi_{\text{rot}}^h}{\partial d_{H_{ij}}} \neq \frac{\partial \Pi_{\text{rot}}^h}{\partial d_{H_{ji}}} \quad (5.12)$$

not equivalent anymore, and the therefrom arising problem of linear dependency disappears.

Remark 5. Note, that in the present formulation the issue applies only to the non-local contribution ψ^{nlloc} since the local contribution is a functional of $\nabla \mathbf{u}$. Yet, the preceding discussion of the necessity of the rot-rot stabilization is applicable analogously in subsequently introduced formulations of which the entire strain energy (not only the non-local part) might be functions of \mathbf{H} and $\nabla \mathbf{H}$, since (5.8)-(5.12) hold without loss of generalization in that case.

Furthermore, it is worth noting that the addition of (5.7) does not alter the solution to the continuous formulation since the function \mathbf{H} that satisfies the constraint (5.3) is rotation-free anyway (cf. discussion in appendix A.1.1). Yet, in the discrete setting, where the mesh resolution is not infinite, the constraint Π_{lag} is not fully converged and the rot-rot stabilization leads to a set of linearly independent equations that is superposed with the originally linearly dependent equations leading to a solvable system. Moreover, since as the mesh gets finer due to the convergence of the constraint $\mathbf{H}^h = \nabla \mathbf{u}^h$ and thereby implied $\text{Rot } \mathbf{H}^h = \mathbf{0}$ converging towards zero (again, cf. appendix A.1.1, see also results of figure 7.4) the amount by which Π_{rot} deviates the solution from the original solution also converges towards zero. Note also RIESELDMANN ET AL. [2021] proof of proposition 1 (see also chapter 6), where continuity and coercivity is shown for the linearized version of the energy symmetric in \mathbf{H} with added rot-rot stabilization. This implies the same characteristics for the bilinear form of the present formulation that corresponds to the sub-matrix $\underline{\mathbf{k}}_H$ (cf. next section 5.1.2) in the discrete setting.

5.1.2 Discretizations

In the following, the interpolation functions and corresponding degrees of freedom for a tetrahedral finite element discretization $T \in \mathcal{T}$ of the body \mathcal{B} are presented and corresponding expressions of the element tangent matrices and residuals are given. Since the solution variables \mathbf{u} and \mathbf{H} belong to the standard H^1 -Sobolev spaces, Lagrange interpolation functions can be used. With $\boldsymbol{\Lambda} \in H^{-1}(\mathcal{B}; \mathbb{R}^{3 \times 3}) \supseteq L^2(\mathcal{B}; \mathbb{R}^{3 \times 3}) \supseteq H^1(\mathcal{B}; \mathbb{R}^{3 \times 3})$ for the Lagrange multiplier variable both piecewise constant and Lagrange interpolation functions are conforming choices.

Proposed $P2_u$ - $P1B_H$ - $P0_\Lambda$ Interpolation The discrete displacements $\mathbf{u}^h \in H_0^1(\mathcal{B}; \mathbb{R}^3) \cap P2(\mathcal{T}; \mathbb{R}^3)$ and the corresponding deformation gradients \mathbf{F}^h interpolated over the tetrahedron $T \in \mathcal{T}$ read

$$\mathbf{u}^h|_T = \sum_{I=1}^{10} \mathbf{d}_I^{(u)} N_I^{(P2)} \quad \text{and} \quad \mathbf{F}^h|_T = \sum_{I=1}^{10} \mathbf{d}_I^{(u)} \otimes \nabla N_I^{(P2)} + \mathbf{1} \quad (5.13)$$

with $N_I^{(P2)} : T \rightarrow H^1(T) \cap P2(T)$ being the quadratic tetrahedral Lagrange interpolation functions and $\mathbf{d}_I^{(u)} = (d_I^{(u_1)}, d_I^{(u_2)}, d_I^{(u_3)})^T$ denoting the standard degrees of freedom $d_I^{(u_i)} : H^1(\mathcal{B}) \rightarrow \mathbb{R}$ giving the values of the components u_i at the corresponding nodes. A necessary condition for rank sufficiency of the resulting finite element tangent matrix is the count criterion, requiring for any possible mesh configuration that the number of degrees of freedom of \mathbf{H}^h is larger than the number of degrees of freedom of the Lagrange multiplier $\boldsymbol{\Lambda}^h$. Thus, for the interpolation of the mixed variable with $\mathbf{H}^h \in H_0^1(\mathcal{B}; \mathbb{R}^{3 \times 3}) \cap (P1(\mathcal{T}; \mathbb{R}^{3 \times 3}) \oplus B4(\mathcal{T}; \mathbb{R}^{3 \times 3}))$ a composition of P1-linear Lagrange functions and the volume bubble Lagrange function is

used (cf. BOFFI ET AL. [2013]):

$$\mathbf{H}^h|_T = \sum_{I=1}^4 \mathbf{d}_I^{(H)} N_I^{(P1)} + \mathbf{d}_B^{(H)} N_B^{(P4)} \quad \text{and} \quad \nabla \mathbf{H}^h|_T = \sum_{I=1}^4 \mathbf{d}_I^{(H)} \otimes \nabla N_I^{(P1)} + \mathbf{d}_B^{(H)} \otimes \nabla N_B^{(P4)} \quad (5.14)$$

whereas the approximation $\text{Rot } \mathbf{H}^h$ of $\text{Rot } \mathbf{H}$ appearing in Π_{rot} is given by evaluating (2.23) in terms of $\nabla \mathbf{H}^h$. Here, $N_I^{(P1)} : T \rightarrow H^1(T) \cap P1(T)$ denote the linear Lagrange interpolation functions and $d_I^{(H_{ij})} : H^1(\mathcal{B}) \rightarrow \mathbf{R}$ denote the components of the degrees of freedom corresponding to the vertex nodes I . Meanwhile, $d_B^{(H_{ij})} : H^1(\mathcal{B}) \rightarrow \mathbf{R}$ denote the components of the degrees of freedom of the element center node and the corresponding shape function $N_B^{(P4)} : T \rightarrow H^1(T) \cap P4(T)$ is given by the quartic Lagrange function $N_B^{(P4)} = 1/256\gamma_1\gamma_2\gamma_3\gamma_4$, where γ_i denote the barycentric coordinates of the tetrahedron. The shape function $N_B^{(P4)}$ takes the value 1 at the center node and is zero valued at the boundary of the tetrahedron and therefore referred to as ‘‘volume bubble’’ function. Further reading with respect to the volume bubble enrichment can be found in BOFFI ET AL. [2013] and BRAESS [2007]. The Lagrange multiplier $\mathbf{\Lambda}^h \in H^{-1}(\mathcal{B}; \mathbf{R}^{3 \times 3}) \cap P0(\mathcal{T}; \mathbf{R}^{3 \times 3})$ is interpolated element-wise constant as

$$\mathbf{\Lambda}^h|_T = \mathbf{d}^{(\Lambda)} N^{(P0)}, \quad (5.15)$$

where $d^{(\Lambda_{ij})} : H^{-1}(\mathcal{B}) \rightarrow \mathbf{R}$ denotes the element-constant degrees of freedom and $N^{(P0)} = 1$ is the corresponding (trivial) basis function. The vector- and tensor valued degrees of freedom consist of the entries

$$\mathbf{d}_I^{(u)} := \begin{bmatrix} d_{u_1} \\ d_{u_2} \\ d_{u_3} \end{bmatrix}_I, \quad \mathbf{d}_{I/B}^{(H)} := \begin{bmatrix} d^{H_{11}} & d^{H_{12}} & d^{H_{13}} \\ d^{H_{21}} & d^{H_{22}} & d^{H_{23}} \\ d^{H_{31}} & d^{H_{32}} & d^{H_{33}} \end{bmatrix}_{I/B} \quad \text{and} \quad \mathbf{d}^{(\Lambda)} := \begin{bmatrix} d_{\Lambda_{11}} & d_{\Lambda_{12}} & d_{\Lambda_{13}} \\ d_{\Lambda_{21}} & d_{\Lambda_{22}} & d_{\Lambda_{23}} \\ d_{\Lambda_{31}} & d_{\Lambda_{32}} & d_{\Lambda_{33}} \end{bmatrix} \quad (5.16)$$

Altogether, assigned to one element are 30 nodal displacement degrees of freedom (as usual per P2-Lagrange displacement elements) and 36 displacement gradient degrees of freedom. Moreover, the condensable degrees of freedom assigned to the element center are 9 displacement degrees of freedom and 9 Lagrange multiplier degrees of freedom, leaving a total of 66 global element degrees of freedom. In the numerical tests of chapter 7 the discretization scheme is referred to as P2 \mathbf{u} -P1B \mathbf{H} -P0 $\mathbf{\Lambda}$ -element. Explicit expressions of the Lagrange shape functions can e.g. be found in ZIENKIEWICZ AND TAYLOR [2000]. The discrete Lagrangian reads

$$\Pi_{\text{H1}}^h = \sum_{T \in \mathcal{T}} \left(\int_T \psi^{\text{loc}}(\nabla \mathbf{u}^h) + \psi^{\text{nloc}}(\mathbf{H}^h, \nabla \mathbf{H}^h) + \mathbf{\Lambda}^h \cdot (\mathbf{H}^h - \nabla \mathbf{u}^h) \, dV \right) + \Pi_{\text{ext}}^h + \Pi_{\text{rot}}^h \quad (5.17)$$

Note, that in what follows, no additional higher surface tractions \mathbf{r} or line tractions \mathbf{l} (cf. section 4.1) are considered and therefore, the discrete external potential of the form given by (3.66) is used. The expression for Π_{rot}^h is obtained by replacing in (5.7) $\text{Rot } \mathbf{H}$ by $\text{Rot } \mathbf{H}^h$.

Matrix Notation and Static Condensation The following presents expressions corresponding to the element degrees of freedom and residual vectors, the element tangent matrix of the P2 \mathbf{u} -P1B \mathbf{H} -P0 $\mathbf{\Lambda}$ formulation. The vectors of the various element degrees of freedom

are defined as

$$\begin{aligned}
\mathbf{d}_u &:= [d_1^{(u_1)}, d_1^{(u_2)}, \dots, d_{10}^{(u_2)}, d_{10}^{(u_3)}]^T \\
\mathbf{d}_H &:= [\mathbf{d}_{H_I}^T, \mathbf{d}_{H_B}^T]^T \quad \text{with} \quad \begin{cases} \mathbf{d}_{H_I} := [d_1^{(H_{11})}, d_1^{(H_{12})}, \dots, d_4^{(H_{32})}, d_4^{(H_{33})}]^T \\ \mathbf{d}_{H_B} := [d_B^{(H_{11})}, d_B^{(H_{12})}, \dots, d_B^{(H_{32})}, d_B^{(H_{33})}]^T \end{cases} \\
\mathbf{d}_\Lambda &:= [d_{\Lambda_{11}}, d_{\Lambda_{12}}, \dots, d_{\Lambda_{32}}, d_{\Lambda_{33}}]^T \\
\mathbf{d} &:= [\mathbf{d}_u^T, \mathbf{d}_H^T, \mathbf{d}_\Lambda^T]^T
\end{aligned} \tag{5.18}$$

From differentiation of the discrete Lagrangian (5.17) the following element residual and tangent matrix components associated to the different solution fields can be derived:

$$\begin{aligned}
\mathbf{r}_u &:= \frac{\partial \Pi^h|_T}{\partial \mathbf{d}_u} & \mathbf{k}_u &:= \frac{\partial \mathbf{r}_u}{\partial \mathbf{d}_u} & \mathbf{k}_{uH} &:= \frac{\partial \mathbf{r}_u}{\partial \mathbf{d}_H} = \mathbf{0} & \mathbf{k}_{u\Lambda} &:= \frac{\partial \mathbf{r}_u}{\partial \mathbf{d}_\Lambda} \\
\mathbf{r}_H &:= \frac{\partial \Pi^h|_T}{\partial \mathbf{d}_H} & \mathbf{k}_{Hu} &:= \frac{\partial \mathbf{r}_H}{\partial \mathbf{d}_u} = \mathbf{0} & \mathbf{k}_H &:= \frac{\partial \mathbf{r}_H}{\partial \mathbf{d}_H} & \mathbf{k}_{H\Lambda} &:= \frac{\partial \mathbf{r}_H}{\partial \mathbf{d}_\Lambda} \\
\mathbf{r}_\Lambda &:= \frac{\partial \Pi^h|_T}{\partial \mathbf{d}_\Lambda} & \mathbf{k}_{\Lambda u} &:= \frac{\partial \mathbf{r}_\Lambda}{\partial \mathbf{d}_u} = (\mathbf{k}_{u\Lambda})^T & \mathbf{k}_{\Lambda H} &:= \frac{\partial \mathbf{r}_\Lambda}{\partial \mathbf{d}_H} = (\mathbf{k}_{H\Lambda})^T & \mathbf{k}_{H\Lambda} &:= \frac{\partial \mathbf{r}_\Lambda}{\partial \mathbf{d}_\Lambda} = \mathbf{0}
\end{aligned} \tag{5.19}$$

The global residual $\mathbf{R}_{H1} := \frac{\partial \Pi_{H1}^h}{\partial \mathbf{D}}$ corresponds to the stationary point of Π_{H1}^h with the global solution vector $\mathbf{D} := \bigcup_{T \in \mathcal{T}} \mathbf{d}_T$. Linearization leads to the following system of equations to be solved by the iterative solution procedure:

$$\text{Lin}[\mathbf{R}_{H1}] = \mathbf{A}_{T \in \mathcal{T}} \left(\begin{bmatrix} \mathbf{k}_u & \mathbf{0} & \mathbf{k}_{u\Lambda} \\ \mathbf{0} & \mathbf{k}_H & \mathbf{k}_{H\Lambda} \\ \mathbf{k}_{\Lambda u} & \mathbf{k}_{\Lambda H} & \mathbf{0} \end{bmatrix}_i \begin{bmatrix} \Delta \mathbf{d}_u \\ \Delta \mathbf{d}_H \\ \Delta \mathbf{d}_\Lambda \end{bmatrix} + \begin{bmatrix} \mathbf{r}_u \\ \mathbf{r}_H \\ \mathbf{r}_\Lambda \end{bmatrix}_i \right) = \mathbf{0}, \tag{5.20}$$

where the assembly operator given in (3.74) and $[\bullet]_i$ denotes the matrix values corresponding to the previous iteration. Following the steps for the static condensation of the internal degrees of freedom (cf. appendix B.1) yields the reduced system

$$\boxed{\mathbf{A}_{T \in \mathcal{T}} \left(\begin{bmatrix} \mathbf{k}_u^{**} & \mathbf{k}_{uH}^{**} \\ \mathbf{k}_{Hu}^{**} & \mathbf{k}_H^{**} \end{bmatrix}_i \begin{bmatrix} \Delta \mathbf{d}_u \\ \Delta \mathbf{d}_H \end{bmatrix} + \begin{bmatrix} \mathbf{r}_u^{**} \\ \mathbf{r}_H^{**} \end{bmatrix}_i \right) = \mathbf{0}.} \tag{5.21}$$

Alternative P2-P2-P1 Interpolation While the displacement interpolation remains unchanged from (5.14) for the alternative P2_u-P2_H-P1_Λ formulation $\mathbf{H}^h \in (H^1(\mathcal{B}; \mathbf{R}^{3 \times 3}) \cap P2(\mathcal{T}; \mathbf{R}^{3 \times 3}))$ is interpolated with quadratic Lagrange polynomials and $\mathbf{\Lambda}^h \in (H^1(\mathcal{B}; \mathbf{R}^{3 \times 3}) \cap P1(\mathcal{T}; \mathbf{R}^{3 \times 3})) \subseteq H^{-1}(\mathcal{B}; \mathbf{R}^{3 \times 3})$ with linear Lagrange polynomials:

$$\mathbf{H}^h|_T = \sum_{I=1}^{10} \mathbf{d}_I^{(H)} N_I^{(P2)}, \quad \nabla \mathbf{H}^h|_T = \sum_{I=1}^{10} \mathbf{d}_I^{(H)} \otimes \nabla N_I^{(P2)} \quad \text{and} \quad \mathbf{\Lambda}^h|_T = \sum_{I=1}^4 \mathbf{d}_I^{(\Lambda)} N_I^{(P1)} \tag{5.22}$$

Yet, for the present interpolation scheme, no degrees of freedom can be condensed and the corresponding tangent matrix remains the saddle point structure (5.39). Moreover, the element is with 156 global degrees of freedom significantly more expensive. Nevertheless, due to the higher polynomial order of the interpolation functions of \mathbf{H}^h for some boundary value problems an improved convergence behavior compared to the P2_u-P1B_H-P0_Λ is possible (cf. numerical results of section 7.2).

5.2 H-Div Λ -Formulation

This section introduces a novel approach which is based on a simple modification of the three field formulation of the previous section 5.1. By making use of the divergence theorem the formulation yields a displacement Lagrange multiplier pairing $(\int_{\mathcal{B}} \text{Div } \mathbf{\Lambda} \cdot \mathbf{u} \, dV)$ for which the inf-sup stability is well known in other contexts and some hints on the mathematical stability in the present context are given as well (together with robust numerical results, cf. chapter 7). Moreover, since now the second constraint term fulfills the inf-sup condition, it becomes possible to formulate the entire strain energy (local and nonlocal part) in terms of \mathbf{H} . This was not possible in the formulation of the previous section 5.1. Moreover, for the corresponding $H(\text{Div}; \mathcal{B}; \mathbf{R}^{3 \times 3})$ conforming discretization of the Lagrange multiplier the hybridization approach of ARNOLD AND BREZZI [1985] is used, which together with the volume bubble discretization of \mathbf{H}^h enables for static condensation. In what follows the formulation is presented in the continuous setting with some hints on the inf-sup stability followed by the discretization approach together with corresponding matrix expressions. Numerical results showing the stability and cost efficiency compared to other approaches are given in the following chapter 7.

5.2.1 Continuous Formulation

Starting from the potential (5.1), replacing the displacement gradients in the local part $\psi^{\text{loc}}(\nabla \mathbf{u}) \rightarrow \psi^{\text{loc}}(\mathbf{H})$ of the strain energy by the mixed variable \mathbf{H} and applying the divergence theorem to the term $-\int_{\mathcal{B}} \mathbf{\Lambda} \cdot \nabla \mathbf{u} \, dV$ yields the formulation

$$\Pi_{\text{H2}} := \int_{\mathcal{B}} \psi(\mathbf{H}, \nabla \mathbf{H}) + \mathbf{\Lambda} \cdot \mathbf{H} + \text{Div } \mathbf{\Lambda} \cdot \mathbf{u} \, dV - \int_{\partial \mathcal{B}} (\mathbf{\Lambda} \cdot \mathbf{n}) \cdot \mathbf{u} \, dA + \Pi_{\text{ext}} + \Pi_{\Gamma} + \Pi_{\text{rot}} \quad (5.23)$$

which is the basis for the present approach. Clearly, since both sides of the equation of the divergence theorem are equivalent, the formulation (5.23) still enforces the constraint $\nabla \mathbf{u} = \mathbf{H}$. Thus, showing that variation of (5.23) is identical to variation of (5.1) and therefore identical to the original problem (4.4) is straightforward (cf. appendix A.1.2). In consequence, unchanged from the formulation of section 5.1 remains the observation that $\text{Rot } \mathbf{H} = \mathbf{0}$ holds (cf. discussion of appendix A.1.1). Therefore, as in section 5.1.1 the addition of the rot-rot stabilization Π_{rot} does not change the problem (see also study of figure 7.4). The solution in the stationary point of (5.23) can now be found in the spaces $(\mathbf{u}, \mathbf{H}, \mathbf{\Lambda}) \in \mathcal{U} \times \mathcal{H} \times \mathcal{L}$ defined as

$$\begin{aligned} \mathcal{U} &:= \{\mathbf{u} \in L_0^2(\mathcal{B}; \mathbf{R}^3)\} \\ \mathcal{H} &:= \{\mathbf{H} \in H_0^1(\mathcal{B}; \mathbf{R}^{(3 \times 3)})\} \\ \mathcal{L} &:= \{\mathbf{\Lambda} \in H^{-1}(\text{Div}; \mathcal{B}; \mathbf{R}^{3 \times 3})\} \end{aligned} \quad (5.24)$$

(definitions of spaces given in section 2.1.3). The Dirichlet boundary conditions remain unchanged from section 5.1. The corresponding variational equations and bilinear forms of the linearization are given in appendix A.1.2. Note, that as in the previous section, the further treatment of Π_{Γ} is left for the future. Yet, it is noteworthy that by the volume interpolation of \mathbf{u}^h with Crouzeix-Raviart functions (cf.(5.32)) the interpolation of $\nabla \mathbf{u}^h \cdot \mathbf{n}$ appearing in Π_{Γ} is also possible.

Hints on the Stability of the Continuous Formulation: The following section provides some considerations regarding the mathematical stability conditions (cf. section 2.4) of the linearization of the variational equation corresponding to (5.23) with Dirichlet boundary conditions. The corresponding expressions leading to the definitions of the following bilinear- and linear forms can be found in appendix A.1.2. The extension of Brezzi's conditions to the non-linear case is to the best of the authors knowledge a research issue that has not been solved. Nevertheless, the following considerations on the linear system might give hints towards the stability of the present formulation. Variation and linearization of (9.2) yields the following problem to be solved in each iteration: For the given external loads and residual values from the previous iteration find the solution increments $(\Delta \mathbf{u}, \Delta \mathbf{H}, \Delta \Lambda) \in \mathcal{U} \times \mathcal{H} \times \mathcal{L}$ such that

$$\begin{aligned} b_2(\Delta \Lambda, \delta \mathbf{u}) &= l_u(\delta \mathbf{u}) \\ a(\delta \mathbf{H}, \Delta \mathbf{H}) + b_1(\delta \mathbf{H}, \Delta \Lambda) &= l_H(\delta \mathbf{H}) \\ b_2(\delta \Lambda, \Delta \mathbf{u}) + b_1(\Delta \mathbf{H}, \delta \Lambda) &= l_\Lambda(\delta \Lambda) \end{aligned} \quad (5.25)$$

holds for all $\mathcal{U} \times \mathcal{H} \times \mathcal{L}$. The problem (5.25) is of the same structure as (2.108), therefore Brezzi's splitting theorem is applicable and the following inf-sup conditions need to be fulfilled.

$$\sup_{\Lambda \in \mathcal{L} \setminus \{0\}} \frac{b_2(\Lambda, \mathbf{u})}{\|\Lambda\|_{\mathcal{L}}} \gtrsim \|\mathbf{u}\|_{L^2} \quad \forall \mathbf{u} \in \mathcal{U} \quad (5.26)$$

$$\sup_{\mathbf{H} \in \mathcal{H} \setminus \{0\}} \frac{b_1(\mathbf{H}, \Lambda)}{\|\mathbf{H}\|_{\mathcal{H}}} \gtrsim \|\Lambda\|_{\mathcal{L}} \quad \forall \Lambda \in \mathcal{Z}(\Lambda). \quad (5.27)$$

where the kernel space (cf. section 2.4.4) is defined as $\mathcal{Z}(\Lambda) := \{\delta \Lambda \in \mathcal{L} : b_2(\delta \Lambda, \delta \mathbf{u}) = 0 \forall \delta \mathbf{u} \in L^2(\mathcal{B}; \mathbb{R}^3)\}$. Appendix A.1.2 presents some findings of preceding contributions that strongly suggest the fulfillment of the inf-sup condition. The inf-sup stability together with the ellipticity and continuity of a which is shown in the proof of proposition 1 of RIESSELMANN ET AL. [2021] (see also section 6.1) proofs that (5.25) has a unique solution.

5.2.2 Discretization

The following discusses the interpolation functions that are used for the discretization of the present approach. Firstly it can be noted, that while the Lagrange interpolation of \mathbf{H}^h can remain unchanged from section 5.1, a suitable choice for \mathbf{u}^h and Λ^h would now be the interpolation approach of RAVIART AND THOMAS [1977] (discussed in section 3.1.2 of this contribution), since with $RT0(\mathcal{T}; \mathbb{R}^{3 \times 3}) \subseteq H(\text{Div}; \mathcal{B}; \mathbb{R}^{3 \times 3}) \subseteq H^{-1}(\text{Div}; \mathcal{B}; \mathbb{R}^{3 \times 3}) =: \mathcal{L}$ the Raviart-Thomas space $RT0$ is conforming with the present solution space \mathcal{L} . The corresponding displacement interpolation would with $\mathbf{u}^h \in P0(\mathcal{T}; \mathbb{R}^3) \subseteq \mathcal{U}$ be piecewise constant. However, to further increase efficiency and to obtain displacement degrees of freedom that live on the element boundary and therefore simplifying the incorporation of the displacement Dirichlet conditions the $H(\text{Div})$ -conforming hybridization approach of ARNOLD AND BREZZI [1985] is used in the following. The idea is to instead of choosing Raviart-Thomas functions for Λ^h and therefore incorporating the necessary condition of normal continuity across element interfaces directly, instead interpolate Λ^h elementwise discontinuous and enforce the normal continuity with Lagrange multipliers living on the element faces. As a result, when using the volume bubble interpolation of \mathbf{H}^h as before, the Lagrange multiplier degrees of freedom can be statically condensed again yielding a reduced element tangent matrix. Moreover, in the present case the Lagrange multiplier degrees of freedom are in the limit equivalent to the displacement values of the mid-face nodes (cf. ARNOLD AND BREZZI [1985], Theorem 1.4) and

can therefore be taken as displacement degrees of freedom enabling for a direct incorporation of the displacement boundary conditions. Since in the present case interpolation functions appear that are not higher than linear on edges and faces, for the approximation of the element geometry and corresponding kinematics straight edge elements used in the following. The discretization of $\mathbf{H}^h \in \mathcal{H} \cap (P1(\mathcal{T}; \mathbf{R}^{3 \times 3}) \oplus B4(\mathcal{T}; \mathbf{R}^{3 \times 3}))$ and its gradient is identical to (5.14).

Discretization of $\mathbf{\Lambda}$: Recall that $T \in \mathcal{T}$ denotes a tetrahedron as an element of the mesh \mathcal{T} and $F \in \mathcal{F}$ denotes a triangle as an element of the set of all faces \mathcal{F} within the mesh. Further, let \mathcal{F}_T denote the set of faces of one element T . The discretization of $\mathbf{\Lambda}^h$ follows the approach described in GALLISTL [2017], Remark 7 based on ARNOLD AND BREZZI [1985]. Namely, $\mathbf{\Lambda}^h \in (\mathcal{L} \cap P_0(\mathcal{T}; \mathbf{R}^{3 \times 3}))$ is sought to consist of elementwise constant functions

$$\mathbf{\Lambda}^h|_T = \mathbf{d}^{(\Lambda)} N^{(P0)} \quad (\text{here: } N^{(P0)} = 1) \quad (5.28)$$

and the second constraint term is approximated by the following (for details on the derivation, see appendix B.3)

$$\int_{\mathcal{B}} \text{Div } \mathbf{\Lambda} \cdot \mathbf{u} \, dV \rightarrow - \sum_{T \in \mathcal{T}} \sum_{I \in \mathcal{F}_T \setminus \partial \mathcal{B}} \mathbf{\Lambda}^h|_T \cdot \mathbf{n}|_{A_I} \cdot \mathbf{d}_I^{(u)} A_I, \quad (5.29)$$

where A_I is the area of each element face I , $\mathbf{n}|_{A_I}$ is the corresponding outwards pointing unit normal vector defined by (3.37) and $\mathcal{F}_T \setminus \partial \mathcal{B}$ denotes the set of element faces that are within the body (and not on the boundary). Thus, each face A_I in (5.29) is the interface of two neighboring elements. Evaluating one summand of (5.29) at one such example interface I yields the term

$$(\mathbf{\Lambda}^h|_{T_1} \mathbf{n}|_{A_I}^{(T_1)} - \mathbf{\Lambda}^h|_{T_2} \mathbf{n}|_{A_I}^{(T_2)}) \cdot \mathbf{d}_I^{(u)} A_I. \quad (5.30)$$

Note, that the second term gets the negative sign through the relation $\mathbf{n}|_{A_I}^{(T_2)} = -\mathbf{n}|_{A_I}^{(T_1)}$. From (5.30) it can be seen that $\mathbf{d}_I^{(u)}$ act as Lagrange multipliers constraining the continuity of $\mathbf{\Lambda}^h$ in normal direction across two interfaces. Thus, due to the opposing signs of the normal vectors of two adjacent elements (5.29) ensures normal continuity across all interfaces of \mathcal{T} within the body. In appendix B.3 it is shown that (5.29) is equivalent to the Raviart-Thomas discretization.

Remark on Notation: Note, that in line with the notation common for other discontinuous approaches (references mentioned in chapter 1) (5.29) can alternatively be written as the single sum over all element interfaces as

$$\sum_{T \in \mathcal{T}} \sum_{I \in \mathcal{F}_T \setminus \partial \mathcal{B}} \mathbf{\Lambda}^h|_T \cdot \mathbf{n}|_{A_I} \cdot \mathbf{d}_I^{(u)} A_I = - \sum_{F \in \mathcal{F} \setminus \partial \mathcal{B}} \int_F \llbracket \mathbf{\Lambda}^h \cdot \mathbf{n}_F \rrbracket \cdot \mathbf{d}_F^{(u)} \, dA, \quad (5.31)$$

where $\llbracket \bullet \rrbracket_F$ denotes the difference (5.30) of the neighboring quantities and due to the straight-edge kinematics and $\mathbf{\Lambda}^h$ and $\mathbf{d}_F^{(u)}$ being constant the integral expression is interchangeable with the expression $\llbracket \mathbf{\Lambda}^h \cdot \mathbf{n}_F \rrbracket \cdot \mathbf{d}_F^{(u)} A_F$.

Discretization of \mathbf{u} : As shown in ARNOLD AND BREZZI [1985], theorem 1.4 the Lagrange multipliers $\mathbf{d}_I^{(u)}$ living on the mid-face nodes \mathcal{F}_T are a piecewise constant approximation of \mathbf{u} . Therefore, in order to provide integrability over the element volume, which is needed for the

evaluation of the volume loads and the evaluation of the L^2 -displacement-error, the following linear interpolation is used for bu \mathbf{u}^h

$$\mathbf{u}^h = \sum_{I \in \mathcal{F}_T} \mathbf{d}_I^{(u)} N_I^{(\text{CR})} \quad \text{and} \quad \nabla \mathbf{u}^h = \sum_{I \in \mathcal{F}_T} \mathbf{d}_I^{(u)} \otimes \nabla N_I^{(\text{CR})} \quad (5.32)$$

where $N_I^{(\text{CR})}$ denote the shape functions corresponding to the method of CROUZEIX AND RAVIART [1973], given on the reference tetrahedron by

$$N_I^{(\text{CR})}(\boldsymbol{\xi}^R) \in \{-2 + 3\xi + 3\eta + 3\zeta, 1 - 3\zeta, 1 - 3\eta, 1 - 3\xi\} \quad (5.33)$$

With the L^2 -integrability given through interpolation (5.32) follows $\mathbf{u}^h \in \mathcal{U}$. Here, it is worth noting that the Crouzeix-Raviart interpolation is non-conforming with H^1 since it is only continuous at the midpoints of the element faces. Yet, with $\mathbf{u}^h \in L_0^2(\mathcal{B}; \mathbb{R}^3) = \mathcal{U}$ being in the larger L^2 -space the interpolation is conforming in the present case. A noteworthy contribution in this context is the work of MARINI [1985] showing that at the lowest order the solution of the mixed method of RAVIART AND THOMAS [1977] can be obtained from the solution of the P1-nonconforming method.

Discretization of the boundary: The discretization (5.29) can also without the need for any modifications be used for the discretization of the surface term in (5.23) by defining (5.29) also on the element faces that live on the surface $\partial\mathcal{B}$:

$$- \int_{\partial\mathcal{B}} (\boldsymbol{\Lambda} \cdot \mathbf{n}) \cdot \mathbf{u} \, dA \rightarrow - \sum_{T \in \mathcal{T}} \sum_{I \in \mathcal{F}_T \cap \partial\mathcal{B}} \boldsymbol{\Lambda}^h|_T \cdot \mathbf{n}|_{A_I} \cdot \mathbf{d}_I^{(u)} A_I, \quad (5.34)$$

where now $\mathcal{F}_T \cap \partial\mathcal{B}$ denotes the element faces on the boundary of the domain. Here, since on the boundary $\partial\mathcal{B}$ the difference (5.30) reduces to a single term, the expression does not act as constraint term enforcing continuity, but simply as discrete boundary surface term, through which the boundary conditions can be incorporated. The Dirichlet boundary conditions e.g. are incorporated the usual way by prescribing the corresponding values for $\mathbf{d}_I^{(u)}$ on Γ_D . By combining (5.29) and (5.34) one can define

$$\Pi_{\Lambda n}^h := - \sum_{T \in \mathcal{T}} \sum_{I \in \mathcal{F}_T} \boldsymbol{\Lambda}^h|_T \cdot \mathbf{n}|_{A_I} \cdot \mathbf{d}_I^{(u)} A_I, \quad (5.35)$$

corresponding to the discretization of $\int_{\mathcal{B}} \text{Div } \boldsymbol{\Lambda} \cdot \mathbf{u} \, dV - \int_{\partial\mathcal{B}} (\boldsymbol{\Lambda} \cdot \mathbf{n}) \cdot \mathbf{u} \, dA$.

Discrete Lagrangian Finally, inserting the discretization functions into the potential (5.23) yields the discrete expression

$$\Pi_{\text{H2}}^h = \sum_{T \in \mathcal{T}} \left(\int_T \psi(\mathbf{H}^h, \nabla \mathbf{H}^h) + \boldsymbol{\Lambda}^h \cdot \mathbf{H}^h \, dV \right) + \Pi_{\Lambda n}^h + \Pi_{\text{ext}}^h + \Pi_{\text{rot}}^h \quad (5.36)$$

A visualization of the degrees of freedom of the present interpolation scheme is given in figure. The entries of the nodal degree of freedom vectors $\mathbf{d}_I^{(u)}$ and matrices $\mathbf{d}_{I/B}^{(H)}$ and $\mathbf{d}^{(\Lambda)}$ are unchanged from (5.16). The present discrete formulation is in following numerical tests denoted by $\text{CR}_{\mathbf{u}}\text{-P1B}_{\mathbf{H}}\text{-P0}_{\boldsymbol{\Lambda}}$. The present formulation is with $4 \times 9 + 4 \times 3 = 48$ global degrees of freedom smaller as e.g. the $P3$ -Lagrange element and the $P3$ -Hermite element, both of which have 60 degrees of freedom and are only suitable for local problems. Interestingly, the global degrees of freedom of the $\text{CR}_{\mathbf{u}}\text{-P1B}_{\mathbf{H}}\text{-P0}_{\boldsymbol{\Lambda}}$ formulation are the same as the degrees of freedom of the $P3$ -Hermite element.

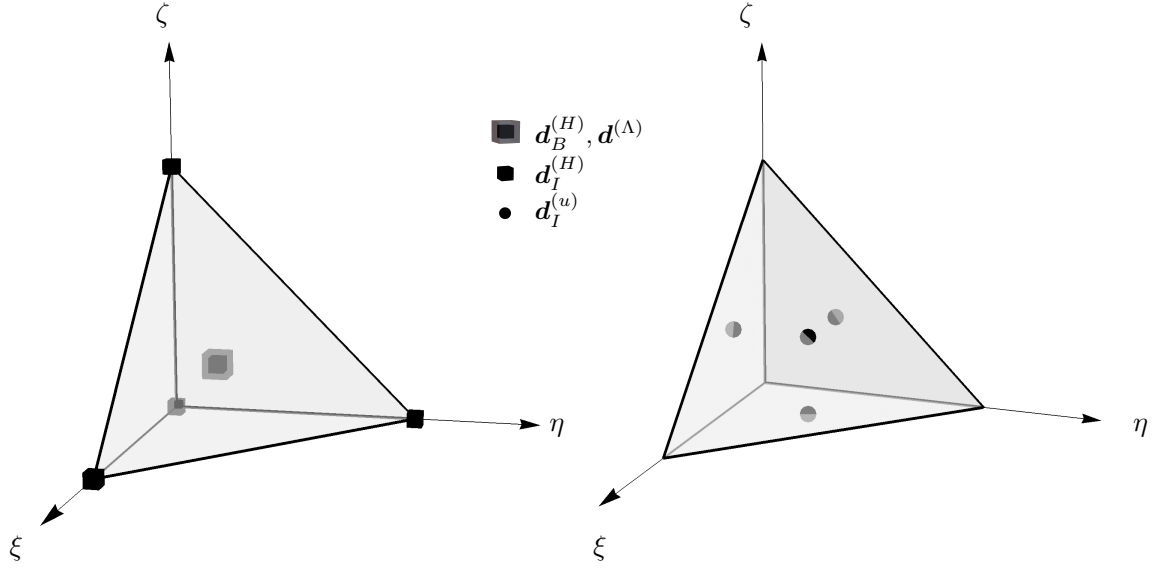


Figure 5.1: Visualization of the degrees of freedom on the reference tetrahedron corresponding to the $\text{CR}_u\text{-P1B}_H\text{-P0}_\Lambda$ formulation

Matrix Notation and Static Condensation The expressions related to the degrees of freedom and residual vectors, as well as the element tangent matrix of the $\text{CR}_u\text{-P1B}_H\text{-P0}_\Lambda$ formulation, are provided below. The definitions of the element degrees of freedom are unchanged from (5.18) with the exception of the displacement degrees of freedom now given by

$$\underline{\mathbf{d}}_u := [d_1^{(u_1)}, d_1^{(u_2)}, \dots, d_4^{(u_2)}, d_4^{(u_3)}]^T \quad (5.37)$$

Further, also the notation for expressions of the element residual and tangent matrix components derived from differentiation of (5.36) are unchanged from (5.19) the only difference now being that in the present case the sub-matrix

$$\underline{\mathbf{k}}_u := \frac{\partial \underline{\mathbf{r}}_u}{\partial \underline{\mathbf{d}}_u} = \underline{\mathbf{0}} \quad (5.38)$$

is zero. Analogously to section 5.1.2 the global residual $\underline{\mathbf{R}}_{\text{H2}} := \frac{\partial \Pi_{\text{H2}}^h}{\partial \underline{\mathbf{D}}}$ corresponds to the stationary point of Π_{H2}^h and the global solution vector reads $\underline{\mathbf{D}} := \bigcup_{T \in \mathcal{T}} \underline{\mathbf{d}}_T$. The system of equations to be solved by the iterative solution procedure obtained by linearization reads:

$$\text{Lin}[\underline{\mathbf{R}}_{\text{H2}}] = \mathbf{A} \left(\begin{bmatrix} \underline{\mathbf{0}} & \underline{\mathbf{0}} & \underline{\mathbf{k}}_{u\Lambda} \\ \underline{\mathbf{0}} & \underline{\mathbf{k}}_H & \underline{\mathbf{k}}_{H\Lambda} \\ \underline{\mathbf{k}}_{\Lambda u} & \underline{\mathbf{k}}_{\Lambda H} & \underline{\mathbf{0}} \end{bmatrix}_i \begin{bmatrix} \Delta \underline{\mathbf{d}}_u \\ \Delta \underline{\mathbf{d}}_H \\ \Delta \underline{\mathbf{d}}_\Lambda \end{bmatrix} + \begin{bmatrix} \underline{\mathbf{r}}_u \\ \underline{\mathbf{r}}_H \\ \underline{\mathbf{r}}_\Lambda \end{bmatrix}_i \right) = \underline{\mathbf{0}}, \quad (5.39)$$

where again $[\bullet]_i$ denotes the matrix values corresponding to the previous iteration the assembly operator is defined by (3.74). Due to the fact that \mathbf{H} is enriched with the volume bubble function associated to the element center node as well as the piecewise constant interpolation of Λ^h , the local degrees of freedom can be condensed giving the following reduced system (cf. appendix B.1)

$$\mathbf{A} \left(\begin{bmatrix} \underline{\mathbf{k}}_u^{**} & \underline{\mathbf{k}}_{uH}^{**} \\ \underline{\mathbf{k}}_{Hu}^{**} & \underline{\mathbf{k}}_H^{**} \end{bmatrix}_i \begin{bmatrix} \Delta \underline{\mathbf{d}}_u \\ \Delta \underline{\mathbf{d}}_H \end{bmatrix} + \begin{bmatrix} \underline{\mathbf{r}}_u^{**} \\ \underline{\mathbf{r}}_H^{**} \end{bmatrix}_i \right) = \underline{\mathbf{0}} \quad (5.40)$$

5.3 Formulation with Symmetric Solution Fields

Since the local and non-local strain energy functions of common strain gradient elasticity models (see e.g. MINDLIN [1964]) and corresponding finite strain extensions (see e.g. DELL'ISOLA ET AL. [2018]) can be formulated solely in terms of symmetric strain tensor quantities and their gradient, the present section presents a modification of the approach of section 5.1 in which instead of the full gradient a symmetric mixed solution variables and corresponding symmetric compatibility condition is introduced. Furthermore, the following formulation is the large strain analogon to the small strain gradient elasticity formulation of RIESELMANN ET AL. [2024].

5.3.1 Continuous Formulation

The Lagrangian of the present formulation reads

$$\Pi_{\text{H3}} := \int_{\mathcal{B}} \psi^{\text{loc}}(\nabla \mathbf{u}) + \psi^{\text{nlloc}}(\mathbf{E}, \nabla \mathbf{E}) + \boldsymbol{\Sigma} \cdot (\mathbf{E} - \mathbf{E}(\nabla \mathbf{u})) \, dV + \Pi_{\text{ext}} + \Pi_{\Gamma}^{\text{s}} \quad (5.41)$$

where $\mathbf{E} \in H_0^1(\mathcal{B}; \mathbb{S})$ denotes the mixed variable, $\boldsymbol{\Sigma} \in H^{-1}(\mathcal{B}; \mathbb{S})$ the Lagrange multiplier enforcing compatibility and $\mathbf{E}(\nabla \mathbf{u})$ is the Green Lagrange nonlinear strain tensor (2.69) formulated in terms of the displacements $\mathbf{u} \in H_0^1(\mathcal{B}; \mathbb{R}^3)$. Refer to section 2.1 in which \mathbb{S} is defined as the space of symmetric second order tensors. The surface term that analogous to (5.4) ensures consistency with the surface terms of the original formulation (4.4) (cf. appendix A.1.3) reads

$$\Pi_{\Gamma}^{\text{s}} := \int_{\partial \mathcal{B}} (\bar{\mathbf{B}} \cdot \mathbf{n}) : (\mathbf{E}(\nabla \mathbf{u}) - \mathbf{E}) \, dA \quad (5.42)$$

with the symmetric higher order stress tensor $\bar{\mathbf{B}} := \partial_{\nabla \mathbf{E}} \psi$ defined in terms of the mixed variable \mathbf{E} . Again, in what follows the addition of Π_{Γ}^{s} is not necessary since either Dirichlet conditions are considered or $(\mathbf{G} \cdot \mathbf{n})_i = (\mathbf{F} \cdot \mathbf{B} \cdot \mathbf{n})_i$ is taken to be zero. Further details on the kinematic relations of the higher order strain and stress tensors can be found in section 7.1. For a detailed discussion on implementation and numerical influence of the corresponding formulation in the case of linear strain gradient elasticity, see RIESELMANN ET AL. [2024]. Note, that formulation (5.41) is applicable to strain gradient type elasticity models (see discussion of 7.1) and gets by without the additional rot-rot term (5.7) that was present in formulations of the previous sections. The first order Dirichlet conditions are imposed as in the previous section through the displacements $\mathbf{u} = \mathbf{u}^*$ on Γ_{D} .

Meanwhile, for the incorporation including the second order Dirichlet boundary a direct incorporation via the mixed variable \mathbf{E} is possible in the case of coinciding first and second order Dirichlet conditions by

$$\mathbf{E} = \mathbf{E}(\nabla_{\Gamma} \mathbf{u}^*, \mathbf{h}^*) \text{ on } \Gamma_{\text{D}} \cap \Gamma_{\text{H}}, \quad (5.43)$$

where through the decomposition (2.20) by inserting $\nabla \mathbf{u} = \nabla_{\Gamma} \mathbf{u}^* + \mathbf{h}^* \otimes \mathbf{n}$ into the Green Lagrange strain tensor both the first and second order Dirichlet functions \mathbf{u}^* and \mathbf{h}^* are included. In general, in the case where (5.43) is not applicable², following the small strain formulation of RIESELMANN ET AL. [2024] based on the method of NITSCHKE [1971] (see also

²That is, in the case of higher order Dirichlet conditions on boundary subdomains $\Gamma_{\text{H}} \not\subseteq \Gamma_{\text{D}}$ that do not belong to the first order Dirichlet boundary.

J. AND STENBERG [1995]) a possible way to incorporate the higher order Dirichlet boundary could be adding the surface integral

$$\Pi_{\text{H3}} \leftarrow \Pi_{\text{H3}} + \int_{\Gamma_{\text{H}}} (\mathbf{F} \cdot \bar{\mathbf{B}}) : (\mathbf{n} \otimes \mathbf{n}) \cdot (\nabla \mathbf{u} \cdot \mathbf{n}) + \frac{\beta}{2} (\nabla \mathbf{u} \cdot \mathbf{n})^2 \, dA, \quad (5.44)$$

where β is some penalty parameter. A corresponding implementation for the present large strain case is left for the future.

5.3.2 Discretization

The continuous solution spaces of the present formulations are analogous to the formulation of section 5.1 with the only difference being that in the present case symmetric tensors are considered. Thus, the corresponding discrete solution spaces read

$$\begin{aligned} \mathbf{u}^h &\in H_0^1(\mathcal{B}; \mathbf{R}^3) \cap P2(\mathcal{T}; \mathbf{R}^3) \\ \mathbf{E}^h &\in H_0^1(\mathcal{B}; \mathbb{S}) \cap P1(\mathcal{T}; \mathbb{S}) \oplus B4(\mathcal{T}; \mathbb{S}) \\ \boldsymbol{\Sigma}^h &\in H^{-1}(\mathcal{B}; \mathbb{S}) \cap P0(\mathcal{T}; \mathbb{S}) \end{aligned} \quad (5.45)$$

and the same Lagrange interpolation functions as in section 5.1 are used. Only the nodal degree of freedom vectors $\mathbf{d}_I^{(E)}$ and $\mathbf{d}^{(\Sigma)}$ are defined differently, since they now contain only six independent degrees of freedom instead of nine. The corresponding symmetric degree of freedom matrices read

$$\mathbf{d}_{I/B}^{(E)} := \begin{bmatrix} d_{E_1} & d_{E_6} & d_{E_5} \\ & d_{E_2} & d_{E_4} \\ \text{sym.} & & d_{E_3} \end{bmatrix}_{I/B} \quad \text{and} \quad \mathbf{d}^{(\Sigma)} := \begin{bmatrix} d_{\Sigma_1} & d_{\Sigma_6} & d_{\Sigma_5} \\ & d_{\Sigma_2} & d_{\Sigma_4} \\ \text{sym.} & & d_{\Sigma_3} \end{bmatrix} \quad (5.46)$$

where the order of the individual degrees of freedom follows the Voigt notation. In what follows the present discrete formulation is denoted by $P2_{\mathbf{u}}\text{-}P1B_{\mathbf{E}}\text{-}P0_{\boldsymbol{\Sigma}}$ and exhibits 30 nodal displacement degrees of freedom and 24 nodal degrees of freedom associated to \mathbf{E}^h . The discrete Lagrangian on which the following implementations and numerical evaluations are based on reads:

$$\boxed{\Pi_{\text{H3}}^h = \sum_{T \in \mathcal{T}} \left(\int_T \psi^{\text{loc}}(\nabla \mathbf{u}^h) + \psi^{\text{nloc}}(\mathbf{E}^h, \nabla \mathbf{E}^h) + \boldsymbol{\Sigma}^h \cdot (\mathbf{E}^h - \mathbf{E}(\nabla \mathbf{u}^h)) \, dV \right) + \Pi_{\text{ext}}^h} \quad (5.47)$$

Matrix Notation and Static Condensation The vectors of the various element degrees of freedom of the $P2_{\mathbf{u}}\text{-}P1B_{\mathbf{E}}\text{-}P0_{\boldsymbol{\Sigma}}$ element are defined as

$$\begin{aligned} \underline{\mathbf{d}}_{\mathbf{u}} &:= [d_1^{(u_1)}, d_1^{(u_2)}, \dots, d_{10}^{(u_2)}, d_{10}^{(u_3)}]^T \\ \underline{\mathbf{d}}_{\mathbf{E}} &:= [\underline{\mathbf{d}}_{E_I}^T, \underline{\mathbf{d}}_{E_B}^T]^T \quad \text{with} \quad \begin{cases} \underline{\mathbf{d}}_{E_I} := [d_1^{(E_1)}, d_1^{(E_2)}, \dots, d_4^{(E_5)}, d_4^{(E_6)}]^T \\ \underline{\mathbf{d}}_{E_B} := [d_B^{(E_1)}, d_B^{(E_2)}, \dots, d_B^{(E_5)}, d_B^{(E_6)}]^T \end{cases} \\ \underline{\mathbf{d}}_{\boldsymbol{\Sigma}} &:= [d_{\Sigma_1}, d_{\Sigma_2}, \dots, d_{\Sigma_5}, d_{\Sigma_6}]^T \\ \underline{\mathbf{d}} &:= [\underline{\mathbf{d}}_{\mathbf{u}}^T, \underline{\mathbf{d}}_{\mathbf{E}}^T, \underline{\mathbf{d}}_{\boldsymbol{\Sigma}}^T]^T \end{aligned} \quad (5.48)$$

The definition of the element residual and tangent matrices is analogous to (5.19). Again analogous to the previous formulations, with the global solution vector $\underline{\mathbf{D}} := \bigcup_{T \in \mathcal{T}} \underline{\mathbf{d}}_T$ the

global residual $\underline{\mathbf{R}}_{\text{H3}} := \frac{\partial \Pi_{\text{H3}}^h}{\partial \underline{\mathbf{D}}}$ corresponds to the stationary point of Π_{H3}^h and Linearization yields following system of equations:

$$\text{Lin}[\underline{\mathbf{R}}_{\text{H3}}] = \mathbf{A}_{T \in \mathcal{T}} \left(\begin{bmatrix} \underline{\mathbf{k}}_u & \mathbf{0} & \underline{\mathbf{k}}_{u\Sigma} \\ \mathbf{0} & \underline{\mathbf{k}}_E & \underline{\mathbf{k}}_{E\Sigma} \\ \underline{\mathbf{k}}_{\Sigma u} & \underline{\mathbf{k}}_{\Sigma E} & \mathbf{0} \end{bmatrix}_i \begin{bmatrix} \Delta \underline{\mathbf{d}}_u \\ \Delta \underline{\mathbf{d}}_E \\ \Delta \underline{\mathbf{d}}_\Sigma \end{bmatrix} + \begin{bmatrix} \underline{\mathbf{r}}_u \\ \underline{\mathbf{r}}_E \\ \underline{\mathbf{r}}_\Sigma \end{bmatrix}_i \right) = \mathbf{0}, \quad (5.49)$$

Following the steps for the static condensation of the internal degrees of freedom (cf. appendix B.1) yields the reduced system

$$\mathbf{A}_{T \in \mathcal{T}} \left(\begin{bmatrix} \underline{\mathbf{k}}_u^{**} & \underline{\mathbf{k}}_{uE}^{**} \\ \underline{\mathbf{k}}_{Eu}^{**} & \underline{\mathbf{k}}_E^{**} \end{bmatrix}_i \begin{bmatrix} \Delta \underline{\mathbf{d}}_u \\ \Delta \underline{\mathbf{d}}_E \end{bmatrix} + \begin{bmatrix} \underline{\mathbf{r}}_u^{**} \\ \underline{\mathbf{r}}_E^{**} \end{bmatrix}_i \right) = \mathbf{0} \quad (5.50)$$

to be solved at each iteration of the Newton-Raphson solution procedure.

Alternative P2-P2-P1 Interpolation Analogous to the alternative formulation of section 5.1 the present alternative formulation incorporates the discretization

$$\begin{aligned} \mathbf{u}^h &\in H_0^1(\mathcal{B}; \mathbf{R}^3) \cap P2(\mathcal{T}; \mathbf{R}^3) \\ \mathbf{E}^h &\in H_0^1(\mathcal{B}; \mathbb{S}) \cap P2(\mathcal{T}; \mathbb{S}) \\ \Sigma^h &\in H^{-1}(\mathcal{B}; \mathbb{S}) \cap P1(\mathcal{T}; \mathbb{S}) \end{aligned} \quad (5.51)$$

The interpolation functions are analogous to those of the alternative P2-P2-P1 formulation of section 5.1 with the only difference being that in the present case, again the symmetric degree of freedom matrices (5.48) are used. The alternative symmetric formulation is in what follows, denoted by P2_u-P2_E-P1_Σ element.

Chapter 6

Rotation-Free Mixed Finite Elements for Gradient Elasticity

This chapter presents the finite strain mixed finite element approach of RIESELMANN ET AL. [2021] (see also the related contributions RIESELMANN ET AL. [2022], RIESELMANN ET AL. [2021b], RIESELMANN ET AL. [2019b] and RIESELMANN ET AL. [2019c]), in which, through a rot-free constraint, the displacement and displacement gradient solution variables appear in a decoupled set of variational equations promising increased computational efficiency while fulfilling the stability conditions allowing for numerically robust computations. In section 6.1, the continuous variational setting is discussed, while section 6.2 focuses on suitable finite element interpolations and the corresponding set of discrete matrix-vector notations at the element level. The proposed approaches are further supported by a stability analysis of the small strain counterparts in section 6.1.5 and section 6.2.4 for the continuous and discrete settings, respectively.

6.1 Continuous Formulation

This section covers the continuous formulation of the RotFEM approach of RIESELMANN ET AL. [2021]. Therefore, the assumption is made that the body \mathcal{B} has a finite size and is simply connected with a connected essential boundary Γ_D .

6.1.1 Decomposed Lagrange Multiplier Method

Starting point is the Hu-Washizu type Lagrangian similar to the approaches of chapter 5, which in the strain energy function includes solely first order gradients, allowing for C^0 continuous finite elements. Therefore, the total elastic potential (4.3) is reformulated into the Lagrangian

$$\Pi_H := \int_{\mathcal{B}} \psi(\mathbf{H}, \nabla \mathbf{H}) \, dV + \Pi_{\text{ext}} + \Pi_{\text{lag}} \quad (6.1)$$

where ψ denotes the gradient enhanced strain energy (4.1). Here, ψ is a functional of the displacement gradient variable \mathbf{H} , compatibility with the displacement \mathbf{u} is enforced by the

constraint term $\Pi_{\text{lag}} = \int_{\mathcal{B}} \mathbf{\Lambda} \cdot (\mathbf{H} - \nabla \mathbf{u}) \, dV$ given by (5.3). The potential Π_{ext} of external loads remains a functional of the displacements and is unchanged from (4.3). Now, a key feature of the following approach is the decomposition of the Lagrange multiplier $\mathbf{\Lambda} = -\nabla \mathbf{g} + \text{Rot } \mathbf{\Phi}$ according to relations (2.55) and (2.56) into a gradient and a rotation enabling the decoupling of the displacements. Thereby, by making use of the divergence theorem (2.29) the original constraint (5.3) can be written as

$$\Pi_{\text{R,lag}} = \int_{\mathcal{B}} \left(\nabla \mathbf{g} \cdot (\nabla \mathbf{u} - \mathbf{H}) + \mathbf{\Phi} \cdot \text{Rot } \mathbf{H} \right) \, dV. \quad (6.2)$$

Note the exclusion of $\nabla \mathbf{u}$ in the second term of (6.2), since the scalar product of rot and gradient tensor functions vanishes with (2.26). The second term of (6.2) can be interpreted as constraint term enforcing \mathbf{H} to be rot-free, which is a necessary condition for gradient functions.

Remark 6. *In the scenario where the nonlocal contribution of the strain energy density disappears ($\psi^{\text{nl}} = 0$), $\mathbf{\Lambda}$ can be identified as the first Piola Kirchhoff stress tensor \mathbf{P} , and $-\nabla \mathbf{g} + \text{Rot } \mathbf{\Phi}$ can be interpreted as the respective split of the latter. This verification can be done through the Euler-Lagrange equations obtained by varying (6.1) based on the Hu-Washizu variational principle.*

Rot-Rot Stabilization In order to take into account the case in which the nonlocal contribution becomes small, the stabilization term Π_{rot} (5.7) discussed in section 5.1.1 is added to (6.1). By incorporating this augmentation term, the problem retains its well-posedness even when the nonlocal contribution approaches zero. Additionally, the inf-sup stability condition is satisfied. The problem (6.1) remains unaffected by the stabilization term because the solution fulfills $\delta_{\mathbf{H}} \Pi_{\text{rot}} = 0$ (see also the discussion of section 5.1.1). An analysis showing the coercivity and continuity of the corresponding relevant bilinear form of the linearized system is given in section 6.1.5.

6.1.2 Continuous Lagrangian of the RotFEM Approach

Under consideration of the previously discussed decomposition the Lagrangian of the current approach which in what follows will be referred to as RotFEM approach reads

$$\Pi_{\text{R}} := \int_{\mathcal{B}} \left(\psi(\mathbf{H}, \nabla \mathbf{H}) + \nabla \mathbf{g} \cdot (\nabla \mathbf{u} - \mathbf{H}) + \mathbf{\Phi} \cdot \text{Rot } \mathbf{H} \right) \, dV + \Pi_{\text{ext}} + \Pi_{\text{rot}} \quad (6.3)$$

The corresponding problem seeks for given volume loads and surface tractions the functions $(\mathbf{u}, \mathbf{H}, \mathbf{\Phi}, \mathbf{g}) \in H_0^1(\mathcal{B}; \mathbf{R}^d) \times H_0^1(\mathcal{B}; \mathbf{R}^{d \times d}) \times \mathcal{Q} \times H_0^1(\mathcal{B}; \mathbf{R}^d)$ such that

$$\Pi_{\text{R}} \Rightarrow \underset{\mathbf{u}, \mathbf{H}, \mathbf{\Phi}, \mathbf{g}}{\text{stat}} \quad (6.4)$$

becomes stationary. Here, the definition of the Lagrange multiplier space

$$\mathcal{Q} := \left\{ \begin{array}{ll} \mathbf{\Phi} \in L^2(\mathcal{B}; \mathbf{R}^2) : \int_{\mathcal{B}} \mathbf{\Phi} \, dV = \mathbf{0} & \text{for } d = 2 \\ \mathbf{\Phi} \in H(\text{Div}; \mathcal{B}; \mathbf{R}^{3 \times 3}) : \text{Div } \mathbf{\Phi} = \mathbf{0} \text{ and } \mathbf{\Phi} \cdot \mathbf{n} = \mathbf{0} \text{ on } \Gamma_{\text{D}} & \text{for } d = 3 \end{array} \right\} \quad (6.5)$$

depends on the space dimension $d \in \{2, 3\}$, since the Rot-operator has different characteristics in 2D than it has in 3D. Namely, in the first case it yields L^2 -vector functions and in the second case it yields divergence-free second order tensor functions (see also the corresponding legs of the commuting diagrams (2.44) and (2.45)).

Treatment of Boundary Conditions The Dirichlet boundary conditions read as follows

$$\begin{aligned} \mathbf{u} = \mathbf{u}^* , \quad \mathbf{H} \times \mathbf{n} = \nabla \mathbf{u}^* \times \mathbf{n} , \quad \Phi \cdot \mathbf{n} = \mathbf{0} , \quad \mathbf{g} = \mathbf{0} \quad & \text{on } \Gamma_{\text{D}} \quad \text{and} \\ \mathbf{H} \cdot \mathbf{n} = \mathbf{h}^* \quad & \text{on } \Gamma_{\text{H}} \end{aligned} \quad (6.6)$$

Note, that in contrary to the boundary conditions of the three field formulations discussed in section 5.1.1, where prescribing besides the displacements the tangential direction of \mathbf{H} was not strictly necessary, in the present formulation it is crucial for stability to prescribe both the values for \mathbf{u} and the tangential components of \mathbf{H} with $\mathbf{H} \times \mathbf{n}$ on the boundary Γ_{D} . Moreover, the Dirichlet boundary needs to be connected. The reason therefore is discussed in the following section. Note further, that analogous to the formulations of chapter 5 adding Π_{Γ} (5.4) to Π_{R} might improve rates of convergence for the special the case of non-homogeneous higher order contributions of the Neumann boundaries (cf. sections 5.1.1 and A.1, see also RIESELMANN ET AL. [2024]). Yet, for the sake of simplicity it is omitted, since it is expected to only become relevant in the case of the rather special boundary configuration, where individual vector components of the boundary are of first order Neumann and second order Dirichlet type (cf. RIESELMANN ET AL. [2024]).

6.1.3 2D Variational Formulation

In the two-dimensional case $d = 2$ with definitions (2.18) and (2.12) $\text{Rot } \mathbf{H}$ simplifies to the vector

$$\text{Rot } \mathbf{H} = \begin{bmatrix} \partial_1 H_{12} - \partial_2 H_{11} \\ \partial_1 H_{22} - \partial_2 H_{21} \end{bmatrix}. \quad (6.7)$$

Thus, in this case the Lagrange multiplier Φ also needs to be only vector-valued and fulfills the inf-sup stability condition (cf. (6.22) in section 6.1.5 of this chapter) without further restrictions with respect to differential operations as it is in the 2D case simply an element of the Sobolev space $\Phi \in L_0^2(\mathcal{B}; \mathbb{R}^2)$ (cf. definition (6.5)). The weak form corresponding to (6.4) reads

$$\delta_{\mathbf{u}} \Pi = 0 = \int_{\mathcal{B}} \nabla \delta \mathbf{u} \cdot \nabla \mathbf{g} \, dV + \delta \Pi^{\text{ext}}, \quad (6.8)$$

$$\delta_{\mathbf{H}} \Pi = 0 = \int_{\mathcal{B}} (\delta \mathbf{H} \cdot \mathbf{P} + \nabla \delta \mathbf{H} \cdot \mathbf{G} + \text{Rot } \delta \mathbf{H} \cdot \Phi + \alpha \text{Rot } \delta \mathbf{H} \cdot \text{Rot } \mathbf{H} - \delta \mathbf{H} \cdot \nabla \mathbf{g}) \, dV, \quad (6.9)$$

$$\delta_{\Phi} \Pi = 0 = \int_{\mathcal{B}} \delta \Phi \cdot \text{Rot } \mathbf{H} \, dV, \quad (6.10)$$

$$\delta_{\mathbf{g}} \Pi = 0 = \int_{\mathcal{B}} \nabla \delta \mathbf{g} \cdot (\nabla \mathbf{u} - \mathbf{H}) \, dV. \quad (6.11)$$

The system of equations from (6.8) to (6.11) illustrates the division of the second-order weak form (A.2) into a series of first-order equations. This method was, before being introduced for the gradient elasticity problem in RIESELMANN ET AL. [2021], initially proposed for polyharmonic problems in GALLISTL [2017] and is also based on initial concepts introduced in ORTIZ AND MORRIS [1988] in the context of discretizing Kirchhoff's equations of thin plate bending using C^0 finite elements. Within the present equation framework, the displacement function \mathbf{u} is decoupled from (6.9) and (6.10), which in what follows is referred to as main problem. The displacements are solely present in the straightforward Laplace-type equations (6.8) and (6.11), which in what follows are denoted as the pre- and post-processing steps, respectively. The fact that the displacements are decoupled from the main problem (6.9)

(6.10) provides sub-problems that are reduced in complexity, promising increased efficiency and robustness. Yet, for the incorporation of the essential boundary condition, special care has of ensuring that the information regarding the prescribed displacements enters the main problem. Therefore, it becomes clear that prescribing $\mathbf{H} \times \mathbf{n} = \nabla \mathbf{u}^* \times \mathbf{n}$ on Γ_D is crucial in order to accord to the main problem the necessary boundary information. The stability of the linearized version of the present formulation is presented in subsection 6.1.5 and propositions 1 and 2.

6.1.4 3D Variational Formulation

In the three-dimensional case ($d = 3$), to fulfill the inf-sup condition (6.22) (cf. section 6.1.5), the Lagrange multiplier $\Phi \in \mathcal{Q}$ (with \mathcal{Q} defined in (6.5)) needs to be divergence-free with vanishing boundary trace $\Phi \cdot \mathbf{n} = \mathbf{0}$ on Γ_D . Therefore, in this case, the second constraint term

$$\Pi_R \leftarrow \Pi_R + \Pi_{\text{div}} \quad \text{with} \quad \Pi_{\text{div}} := \int_{\mathcal{B}} \boldsymbol{\mu} \cdot \text{Div } \Phi \, dV \quad (6.12)$$

is added to (6.3) in order to weakly impose the divergence-free condition, where $\boldsymbol{\mu}$ is a vector-valued, second Lagrange multiplier sought in the space $\boldsymbol{\mu} \in L_0^2(\mathcal{B}; \mathbf{R}^3)$ where $\boldsymbol{\mu}$ is fixed by the mean integral value $\int_{\mathcal{B}} \boldsymbol{\mu} \, dV = \mathbf{0}$. Similar to the previous case, together with (6.12), the weak form corresponding to the extended Lagrangian (6.12) now reads

$$\delta_{\mathbf{H}} \Pi = 0 = \int_{\mathcal{B}} (\delta \mathbf{H} \cdot \mathbf{P} + \nabla \delta \mathbf{H} \cdot \mathbf{G} + \text{Rot } \delta \mathbf{H} \cdot \Phi + \alpha \text{Rot } \delta \mathbf{H} \cdot \text{Rot } \mathbf{H} - \delta \mathbf{H} \cdot \nabla \mathbf{g}) \, dV, \quad (6.13)$$

$$\delta_{\Phi} \Pi = 0 = \int_{\mathcal{B}} (\delta \Phi \cdot \text{Rot } \mathbf{H} + \text{Div } \delta \Phi \cdot \boldsymbol{\mu}) \, dV, \quad (6.14)$$

$$\delta_{\boldsymbol{\mu}} \Pi = 0 = \int_{\mathcal{B}} \delta \boldsymbol{\mu} \cdot \text{Div } \Phi \, dV, \quad (6.15)$$

with the spaces for \mathbf{u} , \mathbf{g} and \mathbf{H} unchanged and $\delta_{\mathbf{u}} \Pi$ and $\delta_{\mathbf{g}} \Pi$ according to (6.8) and (6.11). See propositions 1, 2 and 3 in the following subsection 6.1.5 stating the stability of the linearized version of the present formulation.

6.1.5 Stability of the Linearized Continuous Formulation

In this section, the stability of the proposed approach in the linearized framework is discussed. The proofs for the propositions, lemmas, and corollaries presented in this section can be found in the appendix of RIESELMANN ET AL. [2021]. With pure Dirichlet boundary conditions, linearization of the variational equation (A.2) corresponding to the original problem yields the problem

$$a(\nabla \delta \mathbf{u}, \nabla \mathbf{u}) = l(\delta \mathbf{u}) \quad \text{for all } \delta \mathbf{u} \in \mathcal{U}. \quad (6.16)$$

for which the small displacement increments $\mathbf{u} \in \mathcal{U}$ are sought for all $\delta \mathbf{u} \in \mathcal{U}$ and given right-hand side. The bilinear and linear forms a and l are defined by (A.5) and original solution space with pure Dirichlet boundary is defined as

$$\mathcal{U} := \{\mathbf{u} \in H_0^2(\mathcal{B}; \mathbf{R}^3) : \mathbf{u}|_{\partial \mathcal{B}} = \mathbf{0} \text{ and } \nabla \mathbf{u} \cdot \mathbf{n}|_{\partial \mathcal{B}} = \mathbf{0}\}. \quad (6.17)$$

Define the spaces

$$\mathcal{G} := \{\mathbf{g} \in H_0^1(\mathcal{B}; \mathbf{R}^d) : \mathbf{g}|_{\partial \mathcal{B}} = \mathbf{0}\} \quad \text{and} \quad \mathcal{V} := \{\mathbf{H} \in H_0^1(\mathcal{B}; \mathbf{R}^{d \times d}) : \mathbf{H}|_{\partial \mathcal{B}} = \mathbf{0}\} \quad (6.18)$$

With \mathcal{Q} defined by (6.5) define the bilinear form $b : \mathcal{V} \times \mathcal{Q} \rightarrow \mathbf{R}$ by

$$b(\delta\mathbf{H}, \delta\Phi) := \langle \text{Rot } \delta\mathbf{H}, \delta\Phi \rangle. \quad (6.19)$$

(note the L^2 scalar product definition (A.1)). Now, introducing the bilinear form with added stabilization term $\tilde{a} : \mathcal{V} \times \mathcal{V} \rightarrow \mathbf{R}$ by

$$\tilde{a}(\mathbf{H}, \delta\mathbf{H}) := a(\mathbf{H}, \delta\mathbf{H}) + \alpha \langle \text{Rot } \mathbf{H}, \text{Rot } \delta\mathbf{H} \rangle. \quad (6.20)$$

where a is defined by (A.5) and the original arguments $\nabla\delta\mathbf{u}$ and $\nabla\mathbf{u}$ have been replaced by $\delta\mathbf{H}$ and \mathbf{H}). Note, that (6.20) is equivalent to the first bilinear form of (A.12) of the H-Div Λ approach (cf. section 5.2.1). The small strain-analogue to (6.9) seeks $(\mathbf{H}, \Phi) \in \mathcal{V} \times \mathcal{Q}$ for a given $\mathbf{g} \in \mathcal{G}$ such that

$$\begin{aligned} \tilde{a}(\mathbf{H}, \delta\mathbf{H}) + b(\delta\mathbf{H}, \Phi) &= \langle \nabla\mathbf{g}, \delta\mathbf{H} \rangle \\ b(\mathbf{H}, \delta\Phi) &= 0 \end{aligned} \quad (6.21)$$

holds for all $(\delta\mathbf{H}, \delta\Phi) \in \mathcal{V} \times \mathcal{Q}$. It is now shown that (6.21) is stable and robust for a vanishing nonlocal contribution $c_1 \rightarrow 0$, where $c_1 > 0$ refers to the constant nonlocal parameter which the tangent operator \mathbb{L} defined in appendix A.1 is a positive linear function of. The robustness is proven with respect to the following energy norm on \mathcal{V} that depends on the nonlocal contribution,

$$\|\delta\mathbf{H}\| := (c_1 \|\nabla\delta\mathbf{H}\|_{L^2(\mathcal{B})}^2 + \alpha \|\text{Rot } \delta\mathbf{H}\|_{L^2(\mathcal{B})}^2 + \|\mathbb{C}^{1/2} \text{sym } \delta\mathbf{H}\|_{L^2(\mathcal{B})}^2)^{1/2}.$$

The unique existence of solutions to (6.9) with stabilization in the linear case is postulated by the subsequent proposition.

Proposition 1. *Let $\max\{\alpha, c_1\} > c > 0$ and $\max\{\alpha, c_1\} < C < \infty$. There exists a unique solution $(\mathbf{H}, \Phi) \in \mathcal{V} \times \mathcal{Q}$ to the problem (6.21). (RIESELNANN ET AL. [2021])*

For the proof of (1) the inf-sup condition

$$\sup_{\mathbf{H} \in \mathcal{V} \setminus \{0\}} \frac{b(\mathbf{H}, \Phi)_{L^2(\mathcal{B})}}{\|\mathbf{H}\|} \gtrsim \|\Phi\|_{L^2(\mathcal{B})} \quad (6.22)$$

needs is the main ingredient. The proof of (6.22) and (1) is given in RIESELNANN ET AL. [2021].

Remark 7. *It should be noted that Proposition 1 still holds true even if the stabilization term is not included in the bilinear form. In other words, if \tilde{a} is replaced by a in (6.21). This is due to the fact that functions in the kernel of b are divergence-free and a is coercive on this kernel. However, this property no longer holds for the discretization process, hence the inclusion of the stabilization term. See also the discussion regarding the rot-rot stabilization of section 5.1.1.*

The subsequent proposition asserts that the reformulated problem is indeed synonymous with the original problem.

Proposition 2. *If $\mathbf{u} \in \mathcal{U}$ is a solution of the original problem (6.16) then there exists $\Phi \in \mathcal{Q}$ and $\mathbf{g} \in \mathcal{G}$ such that $(\mathbf{u}, \nabla\mathbf{u}, \Phi, \mathbf{g}) \in \mathcal{G} \times \mathcal{V} \times \mathcal{Q} \times \mathcal{G}$ solves (6.8), (6.21) and (6.11). On the other hand, if $(\mathbf{u}, \mathbf{H}, \Phi, \mathbf{g}) \in \mathcal{G} \times \mathcal{V} \times \mathcal{Q} \times \mathcal{G}$ solves (6.8), (6.21) and (6.11), then \mathbf{u} solves (6.16). (RIESELNANN ET AL. [2021])*

Stability of the 3D Variational Formulation With Two Lagrange Multipliers It is now shown that in the linearized framework the solution of the 3D variational formulation (6.13) through (6.15) coincides with the solution of the original problem. Define the spaces of the Lagrange multipliers

$$\tilde{\mathcal{Q}} := \{\Phi \in H(\text{Div}; \mathcal{B}; \mathbf{R}^{3 \times 3}) : \Phi \cdot \mathbf{n}|_{\partial \mathcal{B}} = \mathbf{0}\} \quad \text{and} \quad \mathcal{M} := L_0^2(\mathcal{B}, \mathbf{R}^3). \quad (6.23)$$

The linearized version of equations (6.13), (6.14), and (6.15) can be expressed as the following problem. Find $(\mathbf{H}, \Phi, \mu) \in \mathcal{V} \times \tilde{\mathcal{Q}} \times \mathcal{M}$ such that

$$\begin{aligned} \tilde{a}(\mathbf{H}, \delta \mathbf{H}) + b(\delta \mathbf{H}, \Phi) &= \langle \nabla \mathbf{g}, \delta \mathbf{H} \rangle \\ b(\mathbf{H}, \delta \Phi) + \langle \text{Div} \delta \Phi, \mu \rangle &= 0 \\ \langle \text{Div} \Phi, \delta \mu \rangle &= 0 \end{aligned} \quad (6.24)$$

holds for all $(\delta \mathbf{H}, \delta \Phi, \delta \mu) \in \mathcal{V} \times \tilde{\mathcal{Q}} \times \mathcal{M}$.

The following states the continuous stability of (6.24), meaning it has a unique solution and the solution is consistent with the solution to the problem (6.21) (where in the 3D case the divergence-free condition is explicitly implied by definition of \mathcal{Q}).

Proposition 3. *Let $\max\{\alpha, c_1\} > c > 0$ and $\max\{\alpha, c_1\} < C < \infty$. There exists a unique solution to (6.24). Furthermore, if $(\mathbf{H}, \Phi, \mu) \in \mathcal{V} \times \tilde{\mathcal{Q}} \times \mathcal{M}$ is a solution to (6.24), then $(\mathbf{H}, \Phi) \in \mathcal{V} \times \mathcal{Q}$ is a solution to (6.21). On the other hand, if $(\mathbf{H}, \Phi) \in \mathcal{V} \times \mathcal{Q}$ is a solution to (6.21), then there exists $\mu \in \mathcal{M}$ such that $(\mathbf{H}, \Phi, \mu) \in \mathcal{V} \times \tilde{\mathcal{Q}} \times \mathcal{M}$ is a solution to (6.24). (RIESELDMANN ET AL. [2021])*

Proposition 3 together with Proposition 2 implies that (6.8), (6.24) and (6.11) are equivalent to (6.16).

6.2 Finite Element Approximations

In line with discretizations of previously discussed formulations of this contribution for the finite element approximation, a partition of \mathcal{B} into a set of simplices $T \in \mathcal{T}$ is considered, where \mathcal{F} is the set of corresponding element faces. According to the standard continuous Galerkin approach, the solution variables and test functions in the continuous weak forms discussed in section 6.1 are substituted with piecewise polynomial functions outlined in the subsequent subsections. Additionally, matrix vector representations for the discretized weak forms are provided.

6.2.1 Interpolation Matrices Pre- and Postprocessing Step

Let $\underline{\mathbf{d}}_u$ and $\underline{\mathbf{d}}_g$ denote element vectors of the nodal degrees of freedom for the preprocessing and postprocessing problems (6.8) and (6.11). The corresponding vector-matrix interpolation operators read

$$\underline{\mathbf{u}}^h = \underline{\mathbf{N}}_u \underline{\mathbf{d}}_u, \quad \delta \underline{\mathbf{u}}^h = \underline{\mathbf{N}}_u \delta \underline{\mathbf{d}}_u, \quad \nabla \underline{\mathbf{u}}^h = \underline{\mathbf{B}}_u \underline{\mathbf{d}}_u, \quad \nabla \delta \underline{\mathbf{u}}^h = \underline{\mathbf{B}}_u \delta \underline{\mathbf{d}}_u, \quad (6.25)$$

$$\underline{\mathbf{g}}^h = \underline{\mathbf{N}}_u \underline{\mathbf{d}}_g, \quad \delta \underline{\mathbf{g}}^h = \underline{\mathbf{N}}_u \delta \underline{\mathbf{d}}_g, \quad \nabla \underline{\mathbf{g}}^h = \underline{\mathbf{B}}_u \underline{\mathbf{d}}_g, \quad \nabla \delta \underline{\mathbf{g}}^h = \underline{\mathbf{B}}_u \delta \underline{\mathbf{d}}_g, \quad (6.26)$$

where $\underline{\mathbf{N}}_u$ and $\underline{\mathbf{B}}_u$ represent suitable finite element interpolation matrices containing standard Lagrange shape functions (suitable choices of interpolation orders given in table 6.1 and 6.2)

and corresponding derivatives (cf. appendix B.2 for details on the matrix notation). By incorporating equations (6.25) and (6.26) into equations (6.8) and (6.11), one arrives at the subsequent matrix equations:

$$\delta_{\mathbf{u}}\Pi^h = \sum_{T \in \mathcal{T}} \delta \underline{\mathbf{d}}_u^T \left(\underbrace{\int_T \underline{\mathbf{B}}_u^T \underline{\mathbf{B}}_u \, dV \, \underline{\mathbf{d}}_g}_{\mathbf{k}_u} - \underbrace{\int_T \underline{\mathbf{N}}_u^T \underline{\mathbf{f}} \, dV - \int_{\delta T} \underline{\mathbf{N}}_u^T \underline{\mathbf{t}} \, dA}_{\mathbf{r}_u^{\text{ext}}} \right) = 0 \quad \text{and} \quad (6.27)$$

$$\delta_g \Pi^h = \sum_{T \in \mathcal{T}} \delta \underline{\mathbf{d}}_g^T \left(\underbrace{\int_T \underline{\mathbf{B}}_u^T \underline{\mathbf{B}}_u \, dV \, \underline{\mathbf{d}}_u}_{\mathbf{k}_u} - \underbrace{\int_T \underline{\mathbf{B}}_u^T \underline{\mathbf{N}}_H \underline{\mathbf{d}}_H^{\text{ext}} \, dV}_{\mathbf{r}_H^{\text{ext}}} \right) = 0, \quad (6.28)$$

where $\underline{\mathbf{d}}_H^{\text{ext}}$ denotes the element vector of nodal degrees of freedom that correspond to $\underline{\mathbf{H}}^h$ computed in the previous step. Note, that the pre- and postprocessing steps are linear. Therefore, even in the finite deformation regime, there is no need for further linearization of equations (6.27) and (6.28).

6.2.2 Interpolation Matrices of the Main Step in 2D

The matrix interpolation operators (cf. appendix B.2) introduced for the discretization of the weak form (6.9) are as follows.

$$\begin{aligned} \underline{\mathbf{H}}^h &= \underline{\mathbf{N}}_H \underline{\mathbf{d}}_H, & \nabla \underline{\mathbf{H}}^h &= \underline{\mathbf{B}}_H \underline{\mathbf{d}}_H, & \text{Rot } \underline{\mathbf{H}}^h &= \underline{\mathbf{R}}_H \underline{\mathbf{d}}_H, \\ \delta \underline{\mathbf{H}}^h &= \underline{\mathbf{N}}_H \delta \underline{\mathbf{d}}_H, & \nabla \delta \underline{\mathbf{H}}^h &= \underline{\mathbf{B}}_H \delta \underline{\mathbf{d}}_H, & \text{Rot } \delta \underline{\mathbf{H}}^h &= \underline{\mathbf{R}}_H \delta \underline{\mathbf{d}}_H. \end{aligned} \quad (6.29)$$

The variable \mathbf{H} is sought in the space $\mathbf{H} \in H_0^1(\mathcal{B}; \mathbb{R}^{d \times d})$, leading to the use of Lagrange interpolation functions and derivatives in the matrices $\underline{\mathbf{N}}_H$ and $\underline{\mathbf{B}}_H$, respectively. The construction of the rotation operator matrix $\underline{\mathbf{R}}_H$ is discussed in appendix B.2. In the case of two dimensions, the Lagrange multiplier $\Phi \in L^2$ is discretized using interpolation functions given by

$$\underline{\Phi}^h = \underline{\mathbf{N}}_\Phi \underline{\mathbf{d}}_\Phi \quad \text{and} \quad \delta \underline{\Phi}^h = \underline{\mathbf{N}}_\Phi \delta \underline{\mathbf{d}}_\Phi. \quad (6.30)$$

In the analysis of section 6.2.4 in 2D it has been established that any combination of interpolation functions that is stable for the Stokes problem (as discussed in BOFFI ET AL. [2013]) can be considered as a suitable choice for the approximations $\underline{\mathbf{H}}^h$ and $\underline{\Phi}^h$. As a result, the MINI interpolation scheme here denoted by P1 \mathbf{B}_H -P1 Φ and the Taylor-Hood interpolation schemes here denoted by P2 \mathbf{B}_H -P1 Φ and P3 \mathbf{B}_H -P2 Φ are proposed (cf. table 6.1, details in section 6.2.4). In the MINI interpolation scheme, $\underline{\mathbf{N}}_H$ comprises of linear Lagrange shape functions that correspond to the vertex nodes of the linear $P1$ -triangle, as well as the cubic Lagrange shape function that corresponds to the interior node of the cubic $P3$ -triangular element. The latter is also known as the volume bubble function (as discussed in section 6.2.4, cf. also the analogous 3D quintic volume bubble function of the formulations of chapter 5). The discretization of (6.29) and (6.30) is given by

$$\delta_{\mathbf{H}} \Pi^h = \sum_{T \in \mathcal{T}} \delta \underline{\mathbf{d}}_H^T \left(\underbrace{\int_T \frac{\partial \psi(\underline{\mathbf{d}}_H)}{\partial \underline{\mathbf{d}}_H} + \alpha \underline{\mathbf{R}}_H^T \underline{\mathbf{R}}_H \underline{\mathbf{d}}_H \, dV}_{\mathbf{r}_H(\underline{\mathbf{d}}_H)} + \underbrace{\int_T \underline{\mathbf{R}}_H^T \underline{\mathbf{N}}_\Phi \, dV \, \underline{\mathbf{d}}_\Phi}_{\mathbf{k}_{H\Phi}} - \underbrace{\int_T \underline{\mathbf{N}}_H^T \underline{\mathbf{B}}_u \underline{\mathbf{d}}_g^{\text{ext}} \, dV}_{\mathbf{r}_g^{\text{ext}}} \right), \quad (6.31)$$

$$\delta_\Phi \Pi^h = \sum_{T \in \mathcal{T}} \delta \underline{\mathbf{d}}_\Phi^T \left(\underbrace{\int_T \underline{\mathbf{N}}_\Phi^T \underline{\mathbf{R}}_H \, dV \, \underline{\mathbf{d}}_H}_{\mathbf{k}_{\Phi H}} \right), \quad (6.32)$$

Element name	$\underline{\mathbf{H}}^h$	$\underline{\Phi}^h$	$\underline{\mathbf{g}}^h/\underline{\mathbf{u}}^h$
P1 $\underline{\mathbf{B}}_H$ -P1 $\underline{\Phi}$ (MINI)	lin.(vertex), cubic (intern.) (4)	linear (3)	quadratic (6)
P2 $\underline{\mathbf{H}}_H$ -P1 $\underline{\Phi}$ (Taylor-Hood)	quadratic (6)	linear (3)	cubic (10)
P3 $\underline{\mathbf{H}}_H$ -P2 $\underline{\Phi}$ (Taylor-Hood)	cubic (10)	quadratic (6)	quartic (15)

Table 6.1: Overview of the 2D finite element interpolation schemes used. Each scheme is accompanied by the number of interpolation nodes, which is indicated within parentheses. The pre- and postprocessing elements are named $P2_{\mathbf{g},\mathbf{u}}$, $P3_{\mathbf{g},\mathbf{u}}$ and $P4_{\mathbf{g},\mathbf{u}}$. The order of this listing corresponds to the order of the elements appearing in the table.

where $\underline{\mathbf{k}}_{H\Phi} = \underline{\mathbf{k}}_{\Phi H}^T$ represents the element submatrix corresponding to the rot-free constraint condition, whereas $\underline{\mathbf{r}}_g^{\text{ext}}$ depicts the nodal load vector with $\underline{\mathbf{d}}_g^{\text{ext}}$ obtained from the solution of the preprocessing step (6.27). Generally, the strain energy function ψ is nonlinear in $\underline{\mathbf{H}}^h$ and $\nabla \underline{\mathbf{H}}^h$, making it nonlinear in $\underline{\mathbf{d}}_H$ as well. Therefore, the solution is obtained using the incremental Newton-Raphson load step solution procedure, which involves linearizing (6.31). The linearized discrete problem can be expressed as follows:

$$\text{Lin}[\delta_{\underline{\mathbf{H}}}\Pi^h + \delta_{\underline{\Phi}}\Pi^h] = \sum_{T \in \mathcal{T}} \begin{bmatrix} \delta \underline{\mathbf{d}}_H \\ \delta \underline{\mathbf{d}}_{\Phi} \end{bmatrix}^T \left(\begin{bmatrix} \underline{\mathbf{k}}_H & \underline{\mathbf{k}}_{H\Phi} \\ \underline{\mathbf{k}}_{\Phi H} & 0 \end{bmatrix} \begin{bmatrix} \Delta \underline{\mathbf{d}}_H \\ \Delta \underline{\mathbf{d}}_{\Phi} \end{bmatrix} + \begin{bmatrix} \underline{\mathbf{r}}_H(\underline{\mathbf{d}}_H) + \underline{\mathbf{r}}_g^{\text{ext}} \\ 0 \end{bmatrix} \right) = 0, \quad (6.33)$$

In the above equations, $\Delta \underline{\mathbf{d}}_H$ and $\Delta \underline{\mathbf{d}}_{\Phi}$ represent the increments of the nodal solution vectors, while $\underline{\mathbf{d}}_H$ represents the nodal solution from the previous step. The element tangent submatrix $\underline{\mathbf{k}}_H$ is given by:

$$\underline{\mathbf{k}}_H = \frac{\partial \underline{\mathbf{r}}_H(\underline{\mathbf{d}}_H)}{\partial \underline{\mathbf{d}}_H} = \int_T \left(\frac{\partial^2 \psi(\underline{\mathbf{d}}_H)}{\partial \underline{\mathbf{d}}_H^2} + \alpha \underline{\mathbf{R}}_H^T \underline{\mathbf{R}}_H \right) dV. \quad (6.34)$$

The second term in the equation represents the discretization of the rot-rot stabilization term. Finally, as usual, the integrals over the element are evaluated numerically using Gauss quadrature of the reference element (cf. section 3.2).

6.2.3 Interpolation Matrices of the Main Step in 3D

In order to obtain a stable discrete set of equations in three dimensions, the Lagrange multiplier is discretized conforming to the $H(\text{Div})$ -Sobolev space (cf. section 6.1.5). Consequently, the lowest order Raviart-Thomas interpolation method (cf. chapter 3) is employed for $\underline{\Phi}^h$. Through the use of suitable interpolation operator matrices, approximations can be written as

$$\begin{aligned} \underline{\Phi}^h &= \underline{\mathbf{S}}_{\Phi} \underline{\mathbf{d}}_{\Phi}, & \text{Div } \underline{\Phi}^h &= \underline{\mathbf{D}}_{\Phi} \underline{\mathbf{d}}_{\Phi}, \\ \delta \underline{\Phi}^h &= \underline{\mathbf{S}}_{\Phi} \delta \underline{\mathbf{d}}_{\Phi}, & \text{Div } \delta \underline{\Phi}^h &= \underline{\mathbf{D}}_{\Phi} \delta \underline{\mathbf{d}}_{\Phi}, \end{aligned} \quad (6.35)$$

where $\underline{\mathbf{S}}_{\Phi}$ and $\underline{\mathbf{D}}_{\Phi}$ contain the Raviart-Thomas shape functions and their respective divergences. Appendix B.2 provides information regarding the construction of $\underline{\mathbf{S}}_{\Phi}$ and $\underline{\mathbf{D}}_{\Phi}$. Since the second Lagrange multiplier $\underline{\mu}^h$ appearing in (6.14) and (6.15) is sought in the space $L_0^2(\mathcal{B}; \mathbb{R}^3)$, a piecewise constant approximation is used. Define the corresponding interpolation matrices $\underline{\mathbf{N}}_{\mu}$ (cf appendix B.2) by

$$\underline{\mu}^h = \underline{\mathbf{N}}_{\mu} \underline{\mathbf{d}}_{\mu} \quad \text{and} \quad \delta \underline{\mu}^h = \underline{\mathbf{N}}_{\mu} \delta \underline{\mathbf{d}}_{\mu}. \quad (6.36)$$

An outline of the Lagrange- and Raviart-Thomas interpolation schemes utilized to satisfy the stability conditions of section 6.2.4 is presented in table 6.2. In the interpolation of $\underline{\mathbf{H}}^h$, the

Variable name	Interpolation scheme	Interpolation type
$\underline{\mathbf{H}}^h$	linear (vertex), cubic (midface) (8)	Lagrange
$\underline{\Phi}^h$	linear in face normal direction (midface) (4)	Raviart-Thomas
$\underline{\mu}^h$	constant (internal node) (1)	Piecewise constant
$\underline{\mathbf{u}}^h/\underline{\mathbf{g}}^h$	quadratic (10)	Lagrange

Table 6.2: Overview of the 3D finite element interpolation schemes (P1FB $\underline{\mathbf{H}}$ -RT0 $\underline{\Phi}$ -P0 $\underline{\mu}$). For each scheme, the number of interpolation nodes is given in parantheses. The pre- and postprocessing elements are denoted by $P2_{\mathbf{g},\mathbf{u}}$.

matrix $\underline{\mathbf{N}}_H$ is composed of the linear Lagrange shape functions corresponding to the four vertex nodes of the (linear) $P1$ -tetrahedron and the cubic Lagrange shape functions corresponding to the four midface nodes of the (cubic) $P3$ -tetrahedral element. In section 6.2.4, the latter are denoted as cubic face bubble functions (cf. also GALLISTL [2017]). Analogously to the discretization procedure discussed in the previous section, with (6.29), (6.35) and (6.36) the following linearized system corresponding to the discretization of (6.13) through (6.15) is obtained:

$$\text{Lin}[\delta_{\underline{\mathbf{H}}}\Pi^h + \delta_{\underline{\Phi}}\Pi^h] = \sum_{T \in \mathcal{T}} \begin{bmatrix} \delta \underline{\mathbf{d}}_H \\ \delta \underline{\mathbf{d}}_{\Phi} \\ \delta \underline{\mathbf{d}}_{\mu} \end{bmatrix}^T \left(\begin{bmatrix} \underline{\mathbf{k}}_H & \underline{\mathbf{k}}_{H\Phi} & 0 \\ \underline{\mathbf{k}}_{\Phi H} & 0 & \underline{\mathbf{k}}_{\Phi\mu} \\ 0 & \underline{\mathbf{k}}_{\mu\Phi} & 0 \end{bmatrix} \begin{bmatrix} \Delta \underline{\mathbf{d}}_H \\ \Delta \underline{\mathbf{d}}_{\Phi} \\ \Delta \underline{\mathbf{d}}_{\mu} \end{bmatrix} + \begin{bmatrix} \underline{\mathbf{r}}_H(\bar{\underline{\mathbf{d}}}_H) + \underline{\mathbf{r}}_g^{\text{ext}} \\ 0 \\ 0 \end{bmatrix} \right) = 0. \quad (6.37)$$

The element tangent submatrices $\underline{\mathbf{k}}_{\Phi\mu} = \underline{\mathbf{k}}_{\mu\Phi}^T$ and $\underline{\mathbf{k}}_{H\Phi} = \underline{\mathbf{k}}_{\Phi H}^T$, which correspond to the rot-constraint and the div-constraint, respectively, are given by

$$\underline{\mathbf{k}}_{\Phi\mu} = \underline{\mathbf{k}}_{\mu\Phi}^T = \int_T \underline{\mathbf{D}}_{\Phi}^T \underline{\mathbf{N}}_{\mu} \, dV \quad \text{and} \quad (6.38)$$

$$\underline{\mathbf{k}}_{H\Phi} = \underline{\mathbf{k}}_{\Phi H}^T = \int_T \underline{\mathbf{R}}_H^T \underline{\mathbf{S}}_{\Phi} \, dV. \quad (6.39)$$

In the following, the discretization scheme (6.37) is denoted by P1FB $\underline{\mathbf{H}}$ -RT0 $\underline{\Phi}$ -P0 $\underline{\mu}$ and in the 3D numerical tests of chapter 7 it is referred to as RotFEM approach.

6.2.4 Stability Analysis of the Finite Element Approximations

In this section the stability of the finite element approximation schemes discussed in the previous sections is stated. Proofs of the propositions and lemmas of this section can be found in RIESELDMANN ET AL. [2021].

Stability of the 2D Finite Element Approximations In the 2D scenario ($d = 2$) any finite element combination that exhibits stability for the Stokes equations can be considered an appropriate choice for discretizing (6.9) and (6.10). This assertion is validated by the following proposition.

Proposition 4. *Let $c_1 > 0$, $\max\{\alpha, c_1\} > c > 0$ and $\max\{\alpha, c_1\} < C < \infty$. If $\mathcal{V}^h \times \mathcal{Q}^h$ is a stable finite element pair for the Stokes equations, then $\mathcal{V}^h \times \mathcal{Q}^h$ is a stable pairing for the discretization of (6.21) for $d = 2$. Therefore, there exists a unique solution $(\underline{\mathbf{H}}^h, \underline{\Phi}^h) \in$*

$\mathcal{V}^h \times \mathcal{Q}^h$ of the discretization with

$$\begin{aligned} & \| \mathbf{H} - \mathbf{H}^h \| + \| \Phi - \Phi^h \|_{L^2(\mathcal{B})} \\ & \lesssim \inf_{(\delta \mathbf{H}^h, \delta \Phi^h) \in \mathcal{V}^h \times \mathcal{Q}^h} \| \mathbf{H} - \delta \mathbf{H}^h \| + \| \Phi - \delta \Phi^h \|_{L^2(\mathcal{B})} \end{aligned} \quad (6.40)$$

where $(\mathbf{H}, \Phi) \in \mathcal{V} \times \mathcal{Q}$ is the solution to problem (6.21) (RIESELDMANN ET AL. [2021]).

Denote the discrete spaces corresponding to the MINI element (P1B \mathbf{H} -P1 Φ) by

$$\mathcal{V}_M^h := \mathcal{V} \cap P1(\mathcal{T}; \mathbf{R}^{2 \times 2}) \oplus B3(\mathcal{T}, \mathbf{R}^{2 \times 2}), \quad (6.41)$$

$$\mathcal{Q}_M^h := \mathcal{Q} \cap P1(\mathcal{T}; \mathbf{R}^2). \quad (6.42)$$

Here, $B3(\mathcal{T}, \mathbf{R}^{2 \times 2})$ is the space of cubic bubble functions defined on the triangle (cf. BRAESS [2007]). The discretization of (6.21) then seeks $(\mathbf{H}^h, \Phi^h) \in \mathcal{V}_M^h \times \mathcal{Q}_M^h$ such that (6.21) is solved for all test functions $(\delta \mathbf{H}^h, \delta \Phi^h) \in \mathcal{V}_M^h \times \mathcal{Q}_M^h$. The inf-sup condition for the Stokes equations BOFFI ET AL. [2013], theorem 8.8.1 together with proposition 4 proves the stability of this discretization and therefore, a unique solution exists and the error satisfies (6.40). The Taylor-Hood finite element subspaces (cf. BRAESS [2007]) are

$$\mathcal{V}_{\text{TH}}^h := \mathcal{V} \cap Pk + 1(\mathcal{T}; \mathbf{R}^{2 \times 2}) \quad \text{and} \quad \mathcal{Q}_{\text{TH}}^h := \mathcal{Q} \cap Pk(\mathcal{T}; \mathbf{R}^2) \quad \text{for } k \geq 1 \quad (6.43)$$

and the discrete problem seeks $(\mathbf{H}^h, \Phi^h) \in \mathcal{V}_{\text{TH}}^h \times \mathcal{Q}_{\text{TH}}^h$ such that (6.21) is solved for all $(\delta \mathbf{H}^h, \delta \Phi^h) \in \mathcal{V}_{\text{TH}}^h \times \mathcal{Q}_{\text{TH}}^h$. Again, the inf-sup condition for the Stokes equations BOFFI ET AL. [2013] together with proposition 4 proves that this defines a stable discretization. For $k = 1$ and $k = 2$ respectively, the corresponding finite elements are referred to by P2 \mathbf{H} -P1 Φ and P3 \mathbf{H} -P2 Φ in the following (see also table 6.1). Numerical tests verifying the postulated stability and rates of convergence independent on the magnitude of the nonlocal contribution for the 2D RotFEM formulation can be found in RIESELDMANN ET AL. [2021].

Stability of the 3D Finite Element Approximations As discussed in section 6.1.5, for $d = 3$ the Lagrange multiplier $\Phi \in \mathcal{Q}$ is required to be divergence-free. Thus, the formulation from section 6.1.4 with an additional Lagrange multiplier enforcing the divergence-free condition weakly is employed with the following discrete subspaces:

$$\mathcal{V}^h := \mathcal{V} \cap P1(\mathcal{T}; \mathbf{R}^{3 \times 3}) \oplus B3(\mathcal{F}, \mathbf{R}^{3 \times 3}), \quad (6.44)$$

$$\mathcal{Q}^h := \tilde{\mathcal{Q}} \cap RT0(\mathcal{T}; \mathbf{R}^{3 \times 3}) \quad \text{and} \quad (6.45)$$

$$\mathcal{M}^h := \mathcal{M} \cap P0(\mathcal{T}; \mathbf{R}^3). \quad (6.46)$$

Here, $B3(\mathcal{F}, \mathbf{R}^3)$ denotes the space of cubic face bubble functions vanishing on the element edges. Furthermore, $RT0(\mathcal{T}; \mathbf{R}^3)$ is the finite element space of RAVIART AND THOMAS [1977] introduced in section 3.1.2. The discretization of the modified problem (6.24) seeks $(\mathbf{H}^h, \Phi^h, \mu^h) \in \mathcal{V}^h \times \mathcal{Q}^h \times \mathcal{M}^h$ such that (6.24) is solved for all test functions $(\delta \mathbf{H}^h, \delta \Phi^h, \delta \mu^h) \in \mathcal{V}^h \times \mathcal{Q}^h \times \mathcal{M}^h$. This linear problem corresponds to the P1FB \mathbf{H} -RT0 Φ -P0 μ discretization of section 6.2.3 and is referred to as RotFEM formulation in subsequent tests of chapter 7. The subsequent proposition states the stability of this discretization method.

Proposition 5. *Let $c_1 > 0$, $\max\{\alpha, c_1\} > c > 0$ and $\max\{\alpha, c_1\} < C < \infty$. The discretization of (6.24) with the above choice of spaces has a unique solution $(\mathbf{H}^h, \Phi^h, \mu^h) \in \mathcal{V}^h \times \mathcal{Q}^h \times \mathcal{M}^h$ satisfying*

$$\begin{aligned} & \| \mathbf{H} - \mathbf{H}^h \| + \| \Phi - \Phi^h \|_{L^2(\mathcal{B})} \\ & \lesssim \inf_{(\delta \mathbf{H}^h, \delta \Phi^h) \in \mathcal{V}^h \times (\mathcal{Q}^h \cap \mathcal{Q})} \| \mathbf{H} - \delta \mathbf{H}^h \| + \| \Phi - \delta \Phi^h \|_{L^2(\mathcal{B})}, \end{aligned}$$

where $(\mathbf{H}, \Phi) \in \mathcal{V} \times \mathcal{Q}$ is the solution to (6.21) (RIESELMANN ET AL. [2021]).

Corresponding numerical results for the 3D RotFEM formulation verifying the postulated stability and convergence are given in the next chapter 7, where also an assessment of the performance of the present approach compared to the approaches of chapter 5 is given for various benchmark problems.

Chapter 7

Numerical Studies Comparing the Gradient Elasticity Formulations

This chapter presents numerical results and corresponding discussions for various relevant benchmark problems aiming to verify and compare the stability, robustness and efficiency of the formulations proposed in the preceding chapters 5 and 6. Therefore, firstly the nonlinear constitutive framework is introduced in section 7.1, followed by the numerical studies on various benchmark tests (section 7.2-7.4). Finally, an overview of the results and a concluding discussion is given in section 7.5. For the numerical results the AceFEM/AceGen software package was used. In all tests loads were applied with a linear increasing parametrization, solutions were obtained with the Newton-Raphson solution procedure and the PARDISO linear solver. Note, that for the evaluation of computing times in order to account for fluctuations of computer operations multiple computations were done and the average computing time was taken. Computations were performed on a local workstation.

7.1 Constitutive Framework

This section shortly presents the constitutive framework of gradient elasticity for the general nonlinear case at finite deformations and finite strains. First, briefly some aspects of isotropy and objectivity in the gradient elasticity context are discussed. Further, some relevant aspects of the higher gradient kinematics are provided. Finally, the specific strain energy functions that are used in the following numerical tests are presented. More details on the topic can be found in TRIANTAFYLIDIS AND AIFANTIS [1986], WRIGGERS [2008], DELL'ISOLA ET AL. [2018], MÜNCH AND NEFF [2018] and BERTRAM [2022].

A Note on Objectivity and Isotropy of the Strain Energy Function In the case of non-local strain energies a straightforward application of the local isotropy condition $\psi(\mathbf{F}, \nabla \mathbf{F}) = \psi(\mathbf{F}\mathbf{Q}, \nabla(\mathbf{F}\mathbf{Q}))$ and objectivity condition $\psi(\mathbf{F}, \nabla \mathbf{F}) = \psi(\mathbf{Q}\mathbf{F}, \nabla(\mathbf{Q}\mathbf{F}))$ can be considered too strict if with $\mathbf{Q} = \mathbf{Q}(\mathbf{X})$ arbitrary differentiable orthogonal 2nd order tensors are considered. This is due to the fact that with the matrix $\mathbf{Q}(\mathbf{X})$ not being constant inhomogeneous rotations need to be accounted for in the aforementioned conditions, which

contradicts the notion of rigid body motions¹ (MÜNCH AND NEFF [2018]). Therefore, MÜNCH AND NEFF [2018] introduce for isotropy and objectivity conditions constant rotations $\mathbf{Q} = \bar{\mathbf{Q}}$ and corresponding energies are called right global $SO(3)$ -invariant (isotropic) and left global $SO(3)$ -invariant (objective) (While local $SO(3)$ -invariance denotes the fulfillment of the before mentioned conditions when considering $\mathbf{Q} = \mathbf{Q}(\mathbf{X})$). As a result it can be distinguished between two sets of strain energies:

$$\mathcal{I}^{II} := \{\psi = \psi^{\text{loc}}(\mathbf{C}) + \psi^{\text{nlloc}}(\nabla \mathbf{C})\} \quad (7.1)$$

$$\mathcal{I}^I := \{\psi = \psi^{\text{loc}}(\mathbf{C}) + \psi^{\text{nlloc}}(\mathbf{F}^T \nabla \mathbf{F}) : \psi \notin \mathcal{I}^{II}\} \quad (7.2)$$

of which \mathcal{I}^{II} is both left- and right local and global $SO(3)$ -invariant and \mathcal{I}^I is left- and right global $SO(3)$ -invariant. In what follows, $\psi^I \in \mathcal{I}^I$ is referred to as type- I nonlocal energy and $\psi^{II} \in \mathcal{I}^{II}$ is referred to as type- II nonlocal energy. Note, that the present notation is in analogy to the small strain setting of MINDLIN's type I ($\psi := \psi(\boldsymbol{\varepsilon}, \nabla \nabla \mathbf{u})$) and type II ($\psi := \psi(\boldsymbol{\varepsilon}, \nabla \boldsymbol{\varepsilon})$) models. In both cases the following first and second order stress tensors are defined as

$$\mathbf{P} := \partial_{\mathbf{F}} \psi = \partial_{\nabla \mathbf{u}} \psi \quad \text{and} \quad \mathbf{G} := \partial_{\nabla \mathbf{F}} \psi = \partial_{\nabla \nabla \mathbf{u}} \psi \quad (7.3)$$

$$\mathbf{S} := \partial_{\mathbf{E}} \psi \quad \text{and} \quad \mathbf{B} := \partial_{\nabla \mathbf{E}} \psi \quad (7.4)$$

where \mathbf{P} and \mathbf{S} correspond to the first and second Piola Kirchhoff stress tensors, respectively and \mathbf{G} and \mathbf{B} are their higher order counterparts. Here, it is worth noting that in the nonlinear gradient elasticity framework both \mathbf{P} and \mathbf{S} have non-local contributions (cf. DELL'ISOLA ET AL. [2018]) Further reading on finite strain gradient elasticity models in the context of invariance conditions can be found in TRIANTAFYLIDIS AND AIFANTIS [1986], DELL'ISOLA ET AL. [2018] and BERTRAM [2022].

Remarks on the Kinematics of the Higher Gradient Quantities The nonlocal parts of the proposed mixed finite element formulations are either functions of $\nabla \mathbf{H}^h (= \nabla \mathbf{F}^h)$ or $\nabla \mathbf{E}^h (= 1/2 \nabla \mathbf{C}^h)$. Therefore, in the following, the applicability of the formulations to either type- I or type- II material models are discussed. While with the conversion formula

$$\nabla \mathbf{C} = \nabla(\mathbf{F}^T \cdot \mathbf{F}) = (F_{ai} F_{aj})_{,k} = F_{ai,k} F_{aj} + F_{ai} F_{aj,k} \quad (7.5)$$

$\nabla \mathbf{C}$ can directly be expressed in terms of $\nabla \mathbf{F}$ and \mathbf{F} the reverse case is with $\mathbf{F} = \mathbf{F}^{-T} \cdot \mathbf{C}$, $\mathbf{F}^T = \mathbf{C} \cdot \mathbf{F}^{-1}$ and

$$\nabla \mathbf{F} = \nabla(\mathbf{F}^{-T} \cdot \mathbf{C}) = ((\mathbf{F}^{-T})_{ia} C_{aj})_{,k} = (\mathbf{F}^{-T})_{ia,k} C_{aj} + (\mathbf{F}^{-T})_{ia} C_{aj,k} \quad (7.6)$$

not straightforward in the sense, that $\nabla \mathbf{F}$ can not be expressed solely in terms of \mathbf{C} and $\nabla \mathbf{C}$. Thus, for the formulations P2 \mathbf{u} -P1B \mathbf{E} -P0 Σ and P2 \mathbf{u} -P1B \mathbf{E} -P0 Σ with symmetric mixed solution variables (cf. section 5.3), if strain energies of type- I are to be used, the nonlocal parts of the strain energy can not exclusively be expressed in terms of the mixed variable \mathbf{E}^h and $\nabla \mathbf{E}^h$ and has with $\nabla \mathbf{F}^{-T}(\nabla \mathbf{u}^h)$ a second gradient contribution. In consequence, the standard Lagrange interpolations of \mathbf{u}^h are in this special case non-conforming and corresponding numerical results can not be expected to converge (cf. results of figure 7.3). This makes the P2 \mathbf{u} -P1B \mathbf{E} -P0 Σ and P2 \mathbf{u} -P1B \mathbf{E} -P0 Σ formulations rather suitable for type- II energies (such as the common strain gradient elasticity model). Since reversely with (7.5) $\nabla \mathbf{C}^h$ can

¹In the local case, the discussion about differentiability of \mathbf{Q} does not occur since the terms $\nabla(\mathbf{Q}\mathbf{F})$ and $\nabla(\mathbf{F}\mathbf{Q})$ are not present.

solely be expressed in terms of \mathbf{H}^h and $\nabla\mathbf{H}^h$ the formulations with full gradients as mixed solution variables have no restriction with respect to applicability to the type of strain energy function.

Analogously to the kinematic relation of the first order stress tensor

$$\mathbf{P} = \mathbf{F} \cdot \mathbf{S} \quad (7.7)$$

for the higher order stress tensors the following kinematic relation can be postulated:

$$\mathbf{G} = \mathbf{F} \cdot \mathbf{B} \quad (7.8)$$

The relation can be verified by application of the chain rule

$$\mathbf{G} := \frac{\partial\psi}{\partial\nabla\mathbf{F}} = \underbrace{\frac{\partial\psi}{\partial\nabla\mathbf{E}}}_{:=\mathbf{B}} \cdot \frac{\partial\nabla\mathbf{E}}{\partial\nabla\mathbf{F}} = \mathbf{B} \cdot \frac{\partial\mathbf{F}^T \cdot \nabla\mathbf{F}}{\partial\nabla\mathbf{F}} = \mathbf{B} \cdot (\mathbf{F}^T \cdot \overset{6}{\mathbb{I}}) = \mathbf{F} \cdot \mathbf{B}, \quad (7.9)$$

where $\overset{6}{\mathbb{I}}$ denotes the sixth order identity tensor. Here, it is worth pointing out that, with $\nabla\mathbf{E} = 1/2\nabla\mathbf{C}$ the relation (7.5) simplifies to $\nabla\mathbf{E} = \mathbf{F}^T \cdot \nabla\mathbf{F}$ only due to the symmetry $B_{ijk} = B_{jik}$. In the general case, when $\nabla\mathbf{E}$ is not paired with a tensor exhibiting symmetry of first and second index (7.5) can not be further simplified.

Models Used in the Following Tests The template finite strain gradient elastic energy functions (based on TRIANTAFYLLIDIS AND AIFANTIS [1986] and MÜNCH AND NEFF [2018]) used throughout the following tests read

$$\psi^I = \psi^{\text{loc}}(\mathbf{C}) + \frac{\mu l^2}{2} (\mathbf{F}^T \cdot \nabla\mathbf{F}) \cdot (\mathbf{F}^T \cdot \nabla\mathbf{F}) \quad (7.10)$$

$$\psi^{II} = \psi^{\text{loc}}(\mathbf{C}) + \frac{\mu l^2}{8} \nabla\mathbf{C} \cdot \nabla\mathbf{C} = \psi^{\text{loc}}(\mathbf{C}) + \frac{\mu l^2}{2} \nabla\mathbf{E} \cdot \nabla\mathbf{E} \quad (7.11)$$

with the kinematic relation $\nabla\mathbf{C} = 2\nabla\mathbf{E}$. In what follows, for the local part of the strain energy function the Neo-Hooke energy (cf. WRIGGERS [2008])

$$\psi^{\text{loc}}(\mathbf{C}) := \frac{\mu}{2}(I_1 - 3) + \frac{\lambda}{4}(J^2 - 1) - \frac{\lambda}{2} \ln J - \mu \ln J \quad (7.12)$$

is considered with $I_1 = \text{tr}(\mathbf{F}^T \cdot \mathbf{F})$, $J = \det \mathbf{F}$ and the Lamé parameters $\lambda = E\nu/((1+\nu)(1-2\nu))$ and $\mu = E/(2(1+\nu))$. Throughout the tests of this section the numerical values of the local elasticity parameter are set to $E = 1000$ MPa and $\nu = 0.3$.

7.2 Unit Cube Benchmark Problem

In order to assess the convergence behavior of the proposed formulations for this first boundary value problem the unit cube geometry $\mathcal{B} = [0, 1] \times [0, 1] \times [0, 1]$ mm³ (cf. figure 7.1 (a)) is considered. The domain has the pure Dirichlet condition $\mathbf{u} = \nabla\mathbf{u} \cdot \mathbf{n} = \mathbf{0}$ on the whole boundary $\partial\mathcal{B}$. A reference body force \mathbf{f} is computed analytically by making use of the balance of linear momentum of the gradient elasticity problem

$$-\text{Div } \mathbf{P} + \text{Div Div } \mathbf{G} = \mathbf{f}. \quad (7.13)$$

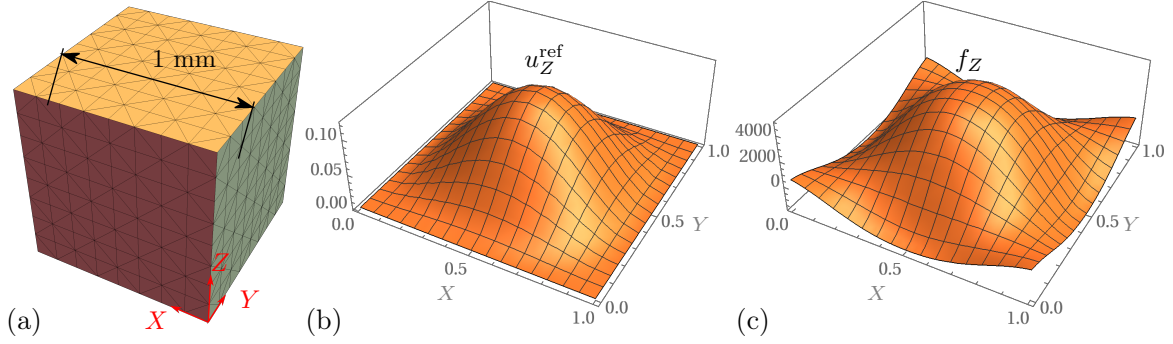


Figure 7.1: (a) Example mesh including reference coordinate system and dimension of the unit cube problem. (b) Visualization of the Z -component of the constructed reference solution evaluated at $Z = 0.5$ mm. (c) Z -component of the right-hand side of the balance of linear momentum (7.13) computed analytically from the reference solution u_Z^{ref} . Here, the strain energy (7.11) and a nonlocal parameter value $l = 0.1$ mm was used to compute \mathbf{f} .

Therefore, a constructed smooth reference solution

$$\mathbf{u}^{\text{ref}} = [0, 0, \beta(X(1-X)Y(1-Y)Z(1-Z))^2]^T, \quad (7.14)$$

is inserted in terms of corresponding derivatives appearing in \mathbf{P} and \mathbf{G} into (7.13). Here, $\beta = 500 \text{ mm}^{-11}$ is a scaling factor in order to arrive at larger displacements activating nonlinearities. Visualizations of the reference displacement and corresponding body force are given in figure 7.1. Due to the pure Dirichlet boundary the Neumann surface equations corresponding to problem (4.4) (cf. explicit equations (A.3) in appendix A.1) are not present. Therefore, \mathbf{u}^{ref} is also the analytical solution to the global problem (4.4) where \mathbf{f} is the external load. Thus, applying the volume load values of \mathbf{f} as external load at the Gauss points of the corresponding finite element problem the FE-solution \mathbf{u}^h of a consistent formulation is expected to in the limit of infinite mesh resolution coincide with the reference solution \mathbf{u}^{ref} . Hence, by comparing the FE solutions $\mathbf{u}^h, \mathbf{H}^h$ (and \mathbf{E}^h) to the reference solution \mathbf{u}^{ref} the yields exact L^2 -error norms

$$\|\mathbf{u}^{\text{ref}} - \mathbf{u}^h\|_{L^2}, \quad \|\nabla \mathbf{u}^{\text{ref}} - \mathbf{H}^h\|_{L^2} \quad \text{and} \quad \|\mathbf{E}(\nabla \mathbf{u}^{\text{ref}}) - \mathbf{E}^h\|_{L^2}, \quad (7.15)$$

where volume integrals of (7.15) are computed by imposing the values of the reference displacements and corresponding derivatives at the Gauss points. For the following studies, the structured meshes of the unit cube geometry (cf. figure 7.1) are uniformly refined. In addition to the error values (7.15) the corresponding rates of convergence are given with the relation $(\bullet) \propto h^r$, where $h := \max_{T \in \mathcal{T}}(\text{diam}(T))$ is an element size measure and (\bullet) denotes the error measure. The convergence rates r are computed with the formula (4.18).

Results of the Convergence Study The first convergence study of figure 7.2 shows the results of all proposed formulations for a study with a nonlocal parameter value of $l = 0.1$ mm and the type-II nonlocal model. The rot-rot parameters used for this and following tests are given in table 7.1. In (a) the L^2 errors of displacement are shown whereas in (b) the L^2 errors of the mixed variables (that is \mathbf{H}^h for the formulations incorporating full gradients and \mathbf{E}^h for the formulations $\text{P2}_u\text{-P2}_E\text{-P1}_\Sigma$ and $\text{P2}_u\text{-P1B}_E\text{-P0}_\Sigma$) are presented. It becomes clear that all formulations converge. Moreover, since the solution is a high order polynomial, for the present problem the formulations $\text{P2}_u\text{-P2}_H\text{-P1}_\Lambda$ and $\text{P2}_u\text{-P2}_E\text{-P1}_\Sigma$ that use quadratic instead

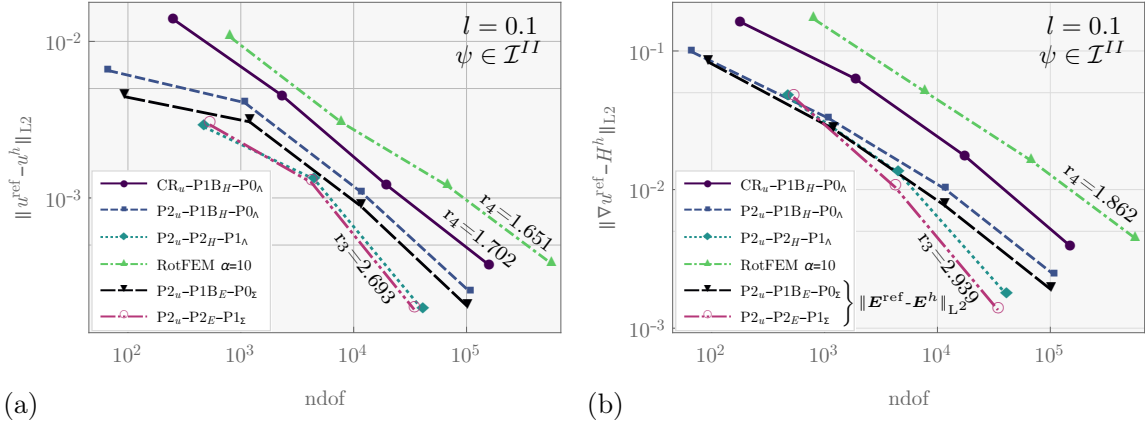


Figure 7.2: Unit Cube convergence results of the proposed formulations for a nonlocal parameter value of $l = 0.1$ mm and the type-II nonlocal model. In (a) the L^2 errors of displacement are shown whereas in (b) the L^2 errors of the mixed variables (that is \mathbf{H}^h for the formulations incorporating full gradients and \mathbf{E}^h for the formulations P2 $_u$ -P2 $_E$ -P1 $_\Sigma$ and P2 $_u$ -P1B $_E$ -P0 $_\Sigma$) are shown. It can be observed that all formulations converge. Due to the smoothness of the solution in the present problem, the results of the formulations incorporating quadratic instead of linear interpolation of the mixed variable are slightly superior.

of linear interpolation functions yield superior rates of convergence. Yet, in subsequent studies it will be shown that these elements require significantly larger computing times. Moreover, for problems in which the solution is not smooth, the superior convergence behavior vanishes (cf. results of section 7.4). The subsequent plots of figure 7.3 show results of an analogous study, but with a problem now based on a type-I strain energy function instead of a type-II strain energy function. While for the elements incorporating full gradients as mixed solution variable the convergence results remain qualitatively unchanged, it becomes visible that the results of the P2 $_u$ -P2 $_E$ -P1 $_\Sigma$ and P2 $_u$ -P1B $_E$ -P0 $_\Sigma$ fail to converge towards the reference solution. As discussed in section 7.1 for the type-I strain energy (7.10) since $\nabla \mathbf{F}^h$ can not solely be expressed in terms of \mathbf{E}^h and $\nabla \mathbf{E}^h$ (cf. section 7.1) the latter formulations incorporate higher order displacement gradients $\nabla \mathbf{F}^{-T}(\nabla \mathbf{u}^h)$ and are thus not suitable for these models. Note, however, that the type-I energy model constitutes rather a special case and type-II models (including the linear strain gradient elasticity model of MINDLIN [1964]) can be considered as more common. Nevertheless, in what follows, whenever the numerical test incorporates the type-I strain energy function (7.10) the not suitable elements P2 $_u$ -P2 $_E$ -P1 $_\Sigma$ and P2 $_u$ -P1B $_E$ -P0 $_\Sigma$ will not be considered. The plots of figure 7.4 visualize the convergence of the L^2 -norm of the rotation $\|\text{Rot } \mathbf{H}^h\|_{L^2}$. Shown are the results of all formulations incorporating the full gradient \mathbf{H}^h as mixed solution variable. Here, figure 7.4(a) corresponds to the study of figure 7.3 and figure 7.4(b) corresponds to the study of figure 7.2. It becomes visible that for all formulations and both types of nonlocal model the rotation of the mixed variable \mathbf{H}^h converges towards zero, which is in correspondence to the characteristic of gradient fields $\mathbf{H}^h \approx \nabla \mathbf{u}^{\text{ref}} \in H^1(\text{Rot}^0; \mathcal{B}; \mathbf{R}^{3 \times 3})$ (cf. identity (2.24)). The superior convergence behavior of the P2 $_u$ -P2 $_H$ -P1 $_\Lambda$ -element is in line with the results of the previous figures and can be attributed to the high smoothness of the solution of the present problem.

Results of the Parameter Study The parameter study of figures 7.5 and 7.6 aim to investigate the influence of the numerical value of the nonlocal parameter l for type-I and type-II problems, respectively. The results of figure 7.5 (a) and (c) present the convergence of the

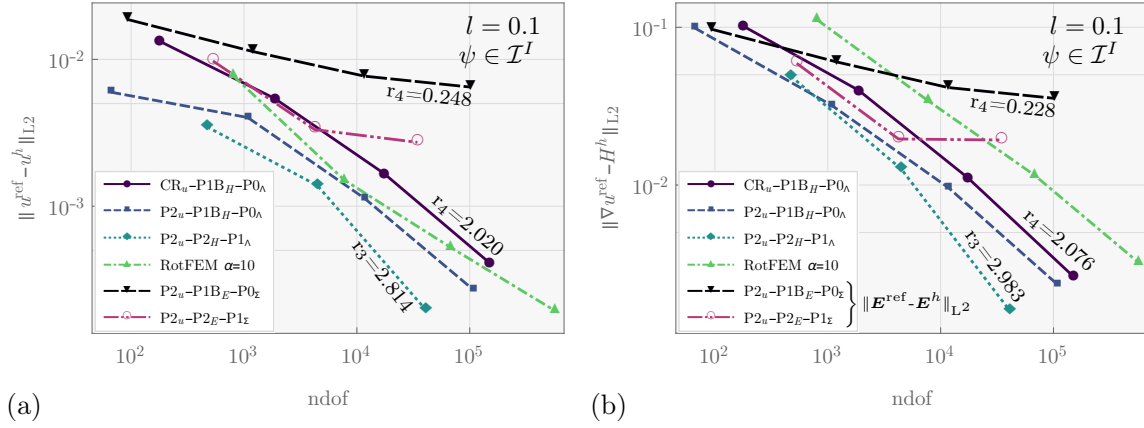


Figure 7.3: Unit Cube convergence results of the proposed formulations for the type- I nonlocal model. In (a) the L^2 errors of displacement are shown whereas in (b) the L^2 errors of the mixed variables (that is \mathbf{H}^h for the formulations incorporating full gradients and \mathbf{E}^h for the formulations P2_u-P2_E-P1_Σ and P2_u-P1B_E-P0_Σ) are shown. It becomes visible that while all elements incorporating full gradients as mixed solution variable the formulations P2_u-P2_E-P1_Σ and P2_u-P1B_E-P0_Σ are not suitable for type- I models since $\nabla \mathbf{F}^h$ can not solely be expressed in terms of \mathbf{E}^h and $\nabla \mathbf{E}^h$ (cf. section 7.1).

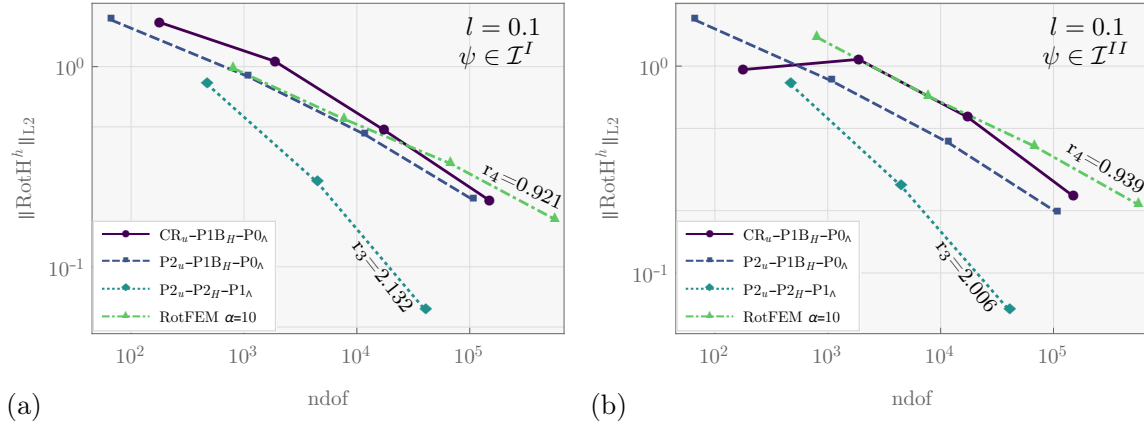


Figure 7.4: Convergence of the L^2 -norm $\|\text{Rot} \mathbf{H}^h\|_{L^2}$ of all the formulations incorporating the mixed solution variable \mathbf{H}^h . (a): results corresponding to the study of figure 7.3. (b): results corresponding to the study of figure 7.2. It becomes clear, that for all formulations for both types of nonlocal model the rotation of \mathbf{H}^h converges towards zero, marking the characteristic of gradient fields (cf. identity (2.24)).

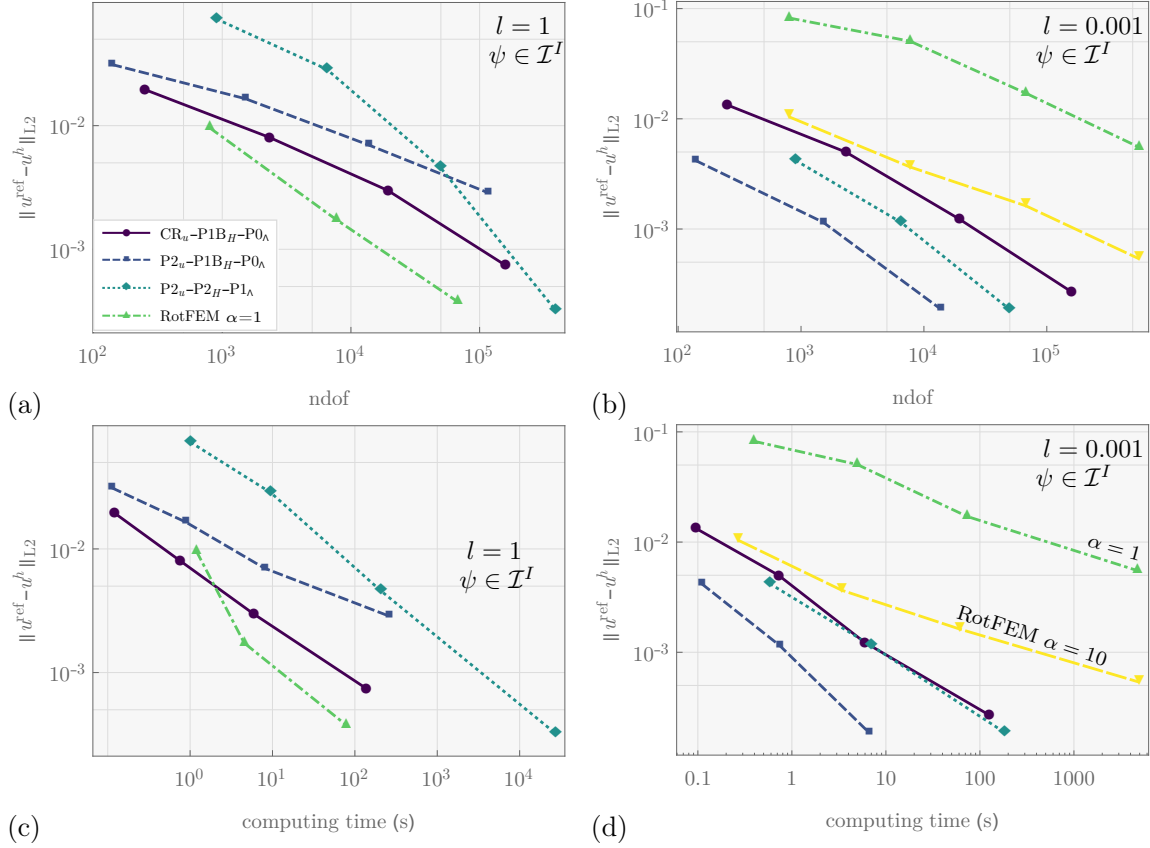


Figure 7.5: Convergence plots comparing the results of the proposed formulations on the unit cube type-I problem for varying values of the nonlocal parameter l . (a) and (c) show the convergence and performance plots of the displacement error, respectively, at a relatively large value of $l = 1$ mm. (b) and (d) show the convergence and performance plots of the displacement error, respectively, at a smaller value of $l = 0.001$ mm. It becomes visible that for large values of l the performance of the RotFEM formulation is significantly higher than the performance of the straightforward approach ($\text{P2}_u\text{-P2}_H\text{-P0}_\Lambda$ and $\text{P2}_u\text{-P2}_H\text{-P1}_\Lambda$). Yet, for the smaller value of $l = 0.001$ mm the reverse behavior can be observed. The performance of the $\text{CR}_u\text{-P1B}_H\text{-P0}_\Lambda$ appears not to be affected by the numerical value of l .

displacement error over number of degrees of freedom and total computing time, respectively at a relatively large value of $l = 1$ mm, whereas figure (b) and (d) show the convergence over number of degrees of freedom and total computing time, respectively at a smaller value of $l = 0.001$ mm. It becomes visible that for large values of l the performance of the RotFEM formulation is significantly higher than the performance of the $P2_{\mathbf{u}}-P2_{\mathbf{H}}-P0_{\Lambda}$ and $P2_{\mathbf{u}}-P2_{\mathbf{H}}-P1_{\Lambda}$ formulations. Meanwhile, for the smaller value of $l = 0.001$ mm the reverse behavior can be observed, where the convergence behavior of the latter is significantly higher than the convergence of the RotFEM element. Here, the performance can be improved by increasing the value of α from $\alpha = 1$ (green) to $\alpha = 10$ (yellow). Interestingly, for the present study the convergence behavior of the $CR_{\mathbf{u}}-P1B_{\mathbf{H}}-P0_{\Lambda}$ appears not to be affected by the numerical value of l . Moreover, when comparing in the plots (b) and (c) the results of the formulations $CR_{\mathbf{u}}-P1B_{\mathbf{H}}-P0_{\Lambda}$ and $P2_{\mathbf{u}}-P2_{\mathbf{H}}-P1_{\Lambda}$ it can be observed that although the $CR_{\mathbf{u}}-P1B_{\mathbf{H}}-P0_{\Lambda}$ requires one refinement step more than the $P2_{\mathbf{u}}-P2_{\mathbf{H}}-P1_{\Lambda}$ element to arrive at similar error values, due to the reduced size of the first the performance behavior with respect to computing times is similar. Yet, for the results corresponding to the smaller value $l = 0.001$ mm for the $CR_{\mathbf{u}}-P1B_{\mathbf{H}}-P0_{\Lambda}$ element a rot-rot parameter $\alpha = 1$ is necessary to maintain numerical robustness, whereas for larger values (analogous to the RotFEM formulation) $\alpha = 0$ can be zero (cf. table 7.1). The subsequent study of figure 7.6 shows analogous plots to figure 7.5 but now with a type-II elastic strain energy making on the one hand side the use of the symmetric solution field formulations $P2_{\mathbf{u}}-P1B_{\mathbf{E}}-P0_{\Sigma}$ and $P2_{\mathbf{u}}-P1B_{\mathbf{E}}-P0_{\Sigma}$ feasible. On the other side, all formulations incorporating the full gradient \mathbf{H}^h as solution variable require the rot-rot term to be switched on (cf. (5.7), see also table 7.1 for the values of α). For the case of a large nonlocal contribution ($l = 1$ mm, figure 7.6(a) and (c)) for the $P2_{\mathbf{u}}-P2_{\mathbf{E}}-P1_{\Sigma}$ formulation issues with respect to numerical robustness are observed as the iterative solution procedure fails to produce results beyond mesh refinement step 2. The same behavior is observed for the $P2_{\mathbf{u}}-P1B_{\mathbf{E}}-P0_{\Sigma}$ formulation, where the same issue occurs beyond mesh refinement step 2. For large l the results of the $CR_{\mathbf{u}}-P1B_{\mathbf{H}}-P0_{\Lambda}$ show the most favorable convergence behavior. Meanwhile, from the results of figure 7.6 (b) and (d) it becomes obvious that at lower values of $l = 0.001$ mm clearly the performance of the $P2_{\mathbf{u}}-P1B_{\mathbf{E}}-P0_{\Sigma}$ is most favorable.

7.3 Cook's Problem

The following study aims to investigate the convergence behavior of the presented formulations in a bending dominated problem with mixed boundary conditions. Therefore, the 3D modified Cook's problem (cf. figure 7.7(a)) is considered where the boundary is taken to be of first and second order Dirichlet type $\Gamma_D = \Gamma_H$ on the left side ($X = 0$ mm) with $\mathbf{u} = \nabla \mathbf{u} \cdot \mathbf{n} = \mathbf{0}$ and to be of first and second order (natural) Neumann type everywhere else. On the right side ($X = 48$ mm) the geometry is loaded with the surface traction $\mathbf{t} = [0, 0, p_0]^T$ with $p_0 = 100$ MPa. In the finite element simulations the surface traction is imposed via surface elements corresponding to the discretization of the surface integral $\int_{\Gamma_N} \mathbf{u} \cdot \mathbf{t} \, dA$ (cf. section 3.2) and on the Dirichlet boundary all components of $\mathbf{u}^h|_{\Gamma_D} = \mathbf{0}$ and $\mathbf{H}^h|_{\Gamma_D \cap \Gamma_H} = \mathbf{0}$ are set to zero. Another relevant feature of Cook's problem is that it is known of non-gradient enhanced formulations to produce solutions that possess a stress localization at the corner point denoted B in figure 7.7(a). Thus, it is a suitable benchmark problem to investigate the ability of the gradient elasticity formulations to avoid excessive stress concentrations. In figure 7.7(b)-(d) contour plots of the volume averaged strain energy

$$\langle \psi \rangle_T = \frac{\int_T \psi \, dV}{\int_T dV} \quad (7.16)$$

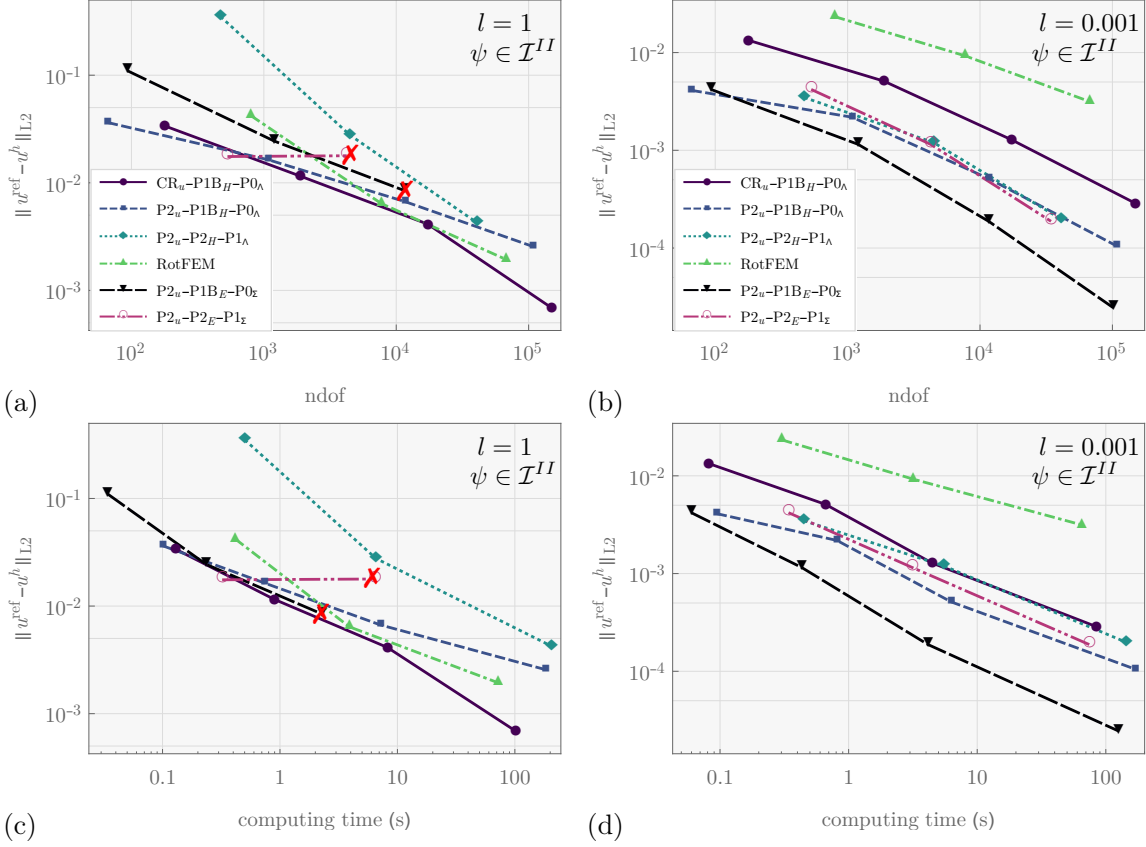


Figure 7.6: Convergence plots comparing the results of the proposed formulations on the unit cube type-II problem for varying values of the nonlocal parameter l . (a) and (c) show the convergence and performance plots of the displacement error, respectively, at a relatively large value of $l = 1$ mm. (b) and (d) show the convergence and performance plots of the displacement error, respectively, at a smaller value of $l = 0.001$ mm. When the nonlocal contribution becomes dominant at large values of $l = 1$ mm ((a) and (c)) the P2_u-P2_E-P1_Σ formulation faces issues with respect to numerical robustness as the iterative solution procedure fails to produce results beyond mesh refinement step 2 (marked with red cross). Meanwhile, at $l = 1$ mm ((a) and (b)) the results of the CR_u-P1B_H-P0_Λ show the most favorable convergence behavior. On the other hand, from the results of (b) and (d) the superior convergence behavior of the symmetric solution field formulation P2_u-P1B_E-P0_Σ stands out.

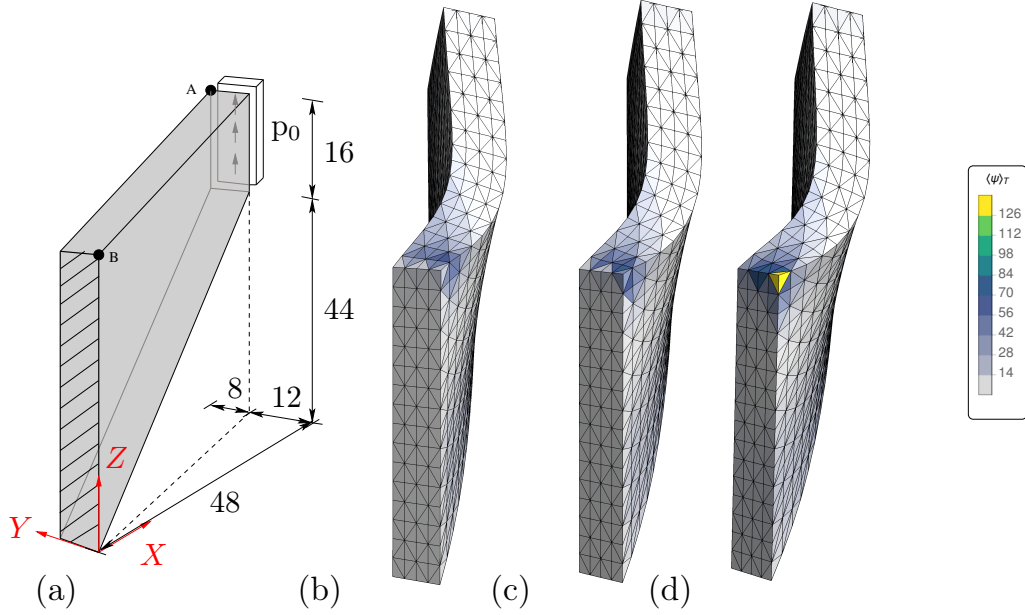


Figure 7.7: 3D Cook's problem: (a) geometry description. Non-smoothed $\langle \psi \rangle_T$ (7.16) contour plots of the (d) local displacement element $P2_{\mathbf{u}}$ and of the RotFEM and $CR_{\mathbf{u}}-P1B_{\mathbf{H}}-P0_{\Lambda}$ element (b) and (c), respectively for $l = 0.0005L$. Here at the corner point B the stress concentration of the local formulation compared to the gradient elasticity formulation becomes visible.

visualize the localized strain energy response at point B for the local $P2_{\mathbf{u}}$ -element (b) firstly and secondly the non-localized response of the gradient elasticity formulations (c)-(d). Moreover, the ability to model size effects due to the additional stiffness introduced by the nonlocal parameter l can be investigated. The numerical results of corresponding studies are presented in figure 7.8. Here, firstly in figure 7.8(a) the ability to model size effects is shown as for various values of the nonlocal parameter l the displacements u_Z at point A (cf. description in figure 7.7(a)) yield results that dependent on the value of l . The results are compared to the results of a purely local $P2_{\mathbf{u}}$ standard displacement element. Here, it becomes visible that the results of all proposed formulations coincide. Moreover, for $l = 0$ the results of the proposed formulations coincide with the results of the local reference $P2_{\mathbf{u}}$ element. Note, that since the displacement degrees of freedom of the $CR_{\mathbf{u}}-P1B_{\mathbf{H}}-P0_{\Lambda}$ formulation are located at the midface nodes and not on the vertex nodes, in order to get results of the vertex-node corner point A the same post-processing equation (6.28) as used for the RotFEM formulation is employed to compute vertex displacement values from \mathbf{H}^h . In (b) convergence of the volume averaged norm

$$\langle \mathbf{H}^h \rangle_T := \frac{\int_T \mathbf{H}^h \cdot \mathbf{H}^h \, dV}{\int_T \, dV} \quad (7.17)$$

of the displacement gradient of the element adjacent to point B (cf. figure 7.7(a)) is shown for a nonlocal parameter $l = 0.05L$ (labeled in (a)). On the one hand side, for the local $P2_{\mathbf{u}}$ element, the tendency to produce increasing values of (7.17) as the mesh gets finer becomes visible. This is in line with the appearance of stress localization at this point (cf. figure 7.7(b)). Meanwhile, it becomes clear that the values of the gradient elasticity formulations remain bounded. Moreover, as the mesh gets finer the values even decrease, which can be attributed to the higher order Dirichlet boundary inducing a surface layer of zero displacements and displacement gradients (see e.g. REZAEI ET AL. [2022]). As the element diameter decreases

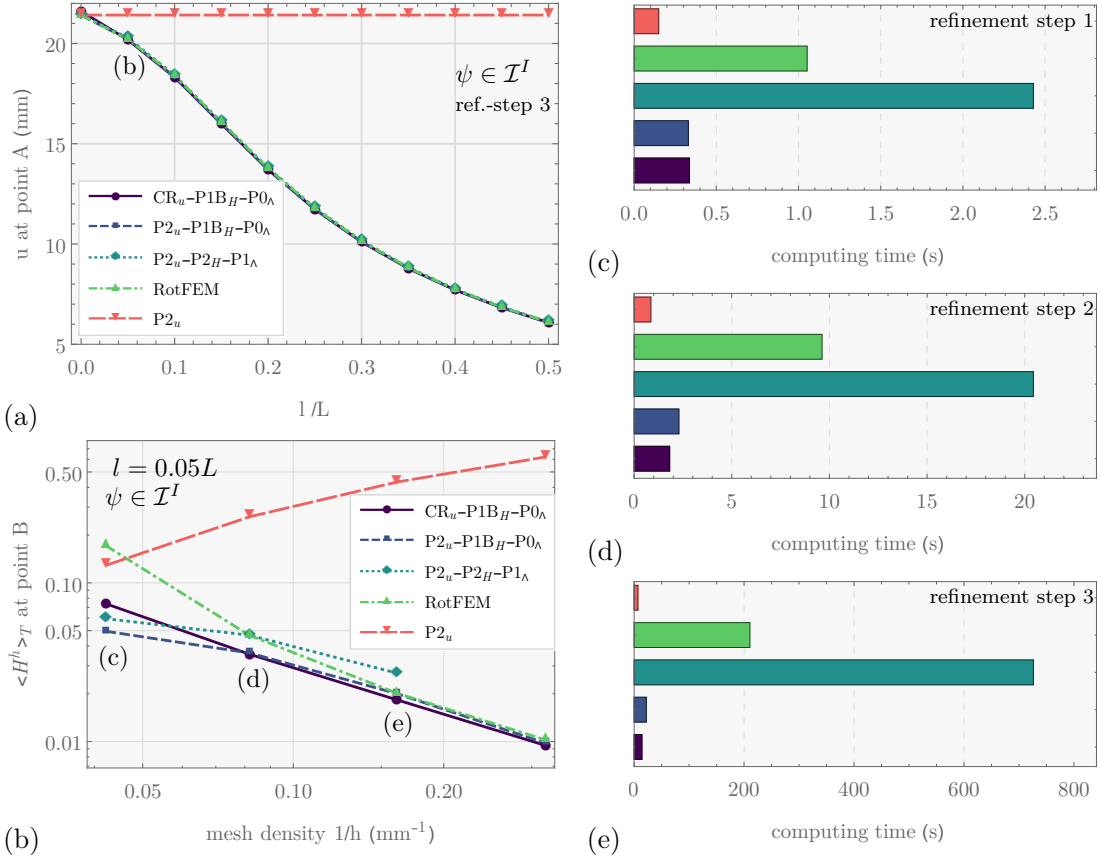


Figure 7.8: Results of the proposed formulations on the 3D modified Cook's problem. (a) shows the ability to model size effects as displacements u_Z at point A (cf. description in figure 7.7(a)) depend on the value of the length scale parameter l . Here it becomes visible that the results of all proposed formulations coincide. Moreover, for $l = 0$ the results of the proposed formulations coincide with the results of the reference element. In (b) convergence of the volume averaged norm (7.17) of the element adjacent to point B (cf. figure 7.7(a)) is shown for a nonlocal parameter $l = 0.05L$ (labeled in (a)). On the one hand side, the tendency of the local $P2_u$ element to produce increasing values of (7.17) as the mesh gets finer becomes visible. On the other side, it becomes clear that the values of the gradient elasticity formulations remain bounded and even decrease due to the non-locality of the surface layer induced by the higher order Dirichlet boundary condition. (c)-(e) compare the computing times of the proposed formulations for the various refinement steps marked in (b). It becomes visible, that the condensed elements are significantly cheaper than the non-condensed elements and computing times of the first are rather in the order of magnitude of the purely local $P2_u$ element.

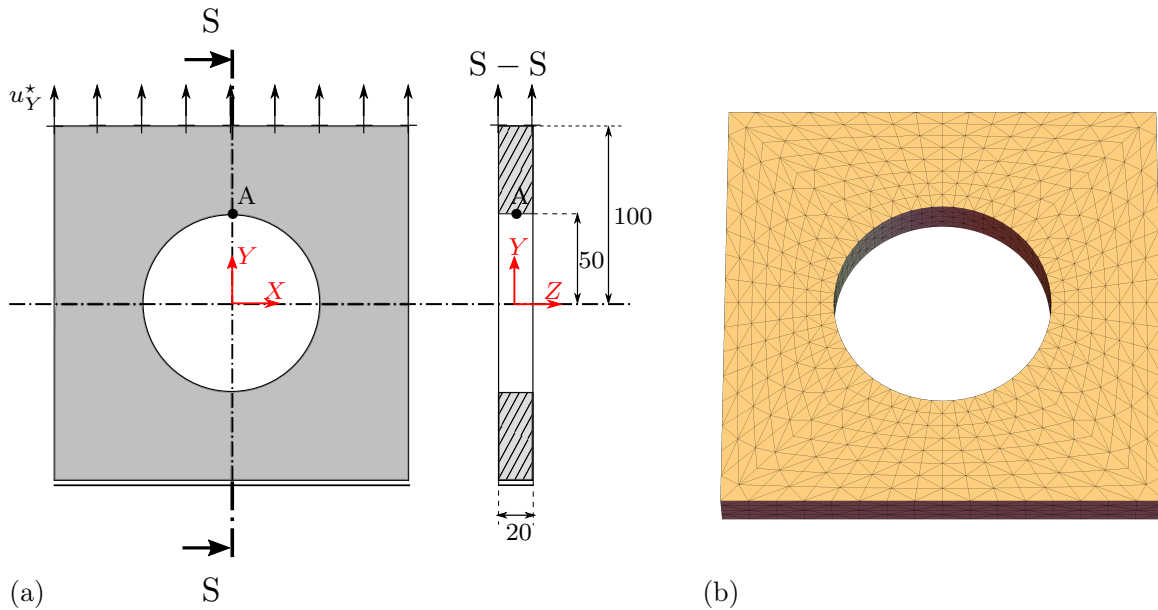


Figure 7.9: (a) Geometry description of the plate with hole benchmark problem. The full domain is modeled. (b) Example mesh.

the volume portion of the element that lies within the surface layer induced by the higher order Dirichlet condition becomes larger leading to results converging towards zero. Finally, the plots (c)-(e) compare the computing times of the proposed formulations for the various refinement steps marked in (b). It becomes visible, that the computing times of the condensed elements $P2_u-P1B_H-P0_\Lambda$ and $CR_u-P1B_H-P0_\Lambda$ are significantly lower than those of the non-condensed RotFEM and especially the $P2_u-P2_H-P1_\Lambda$ element. This tendency becomes even more prevalent as the problem gets larger. Moreover, the order of magnitude of the computing times of the condensed elements the same as the order of magnitude of the purely local elasticity element.

7.4 Plate With Hole

The goal of the third benchmark problem of this chapter is to test the proposed formulations on a geometry that is non-simply connected (that is non-contractible due to the hole in the middle) and has non-connected Dirichlet boundary conditions. Therefore, the entire domain of the plate with hole geometry (cf. figure 7.9(a)) is considered. A corresponding example mesh is shown in figure 7.9(b). The geometry is fixed in Y -direction on the bottom ($Y = -100$ mm) and a large displacement load $u_Y^* = 250$ mm is applied at the top ($Y = 100$ mm). At the top, the geometry is also fixed in X - and Z -direction. In figure 7.10 deformed contour plots of the volume averaged strain energy (7.16) for the proposed formulations of Hu-Washizu type are shown. It becomes clear that all formulations yield the same strain energy distribution. Note, that without further modifications, the RotFEM formulation is not applicable to the plate with hole boundary value problem. Since the displacements are not part of the main step (6.37) of the RotFEM formulation, the information of the constant non-zero prescribed displacement value u_Y^* does not directly enter the problem. Meanwhile, imposing the prescribed displacement indirectly via the displacement equations (6.27) and (6.28) is not possible without coupling the equation to the main step. Yet, the investigation of a possible remedy of imposing to the main step additional integral expressions connecting the Dirichlet

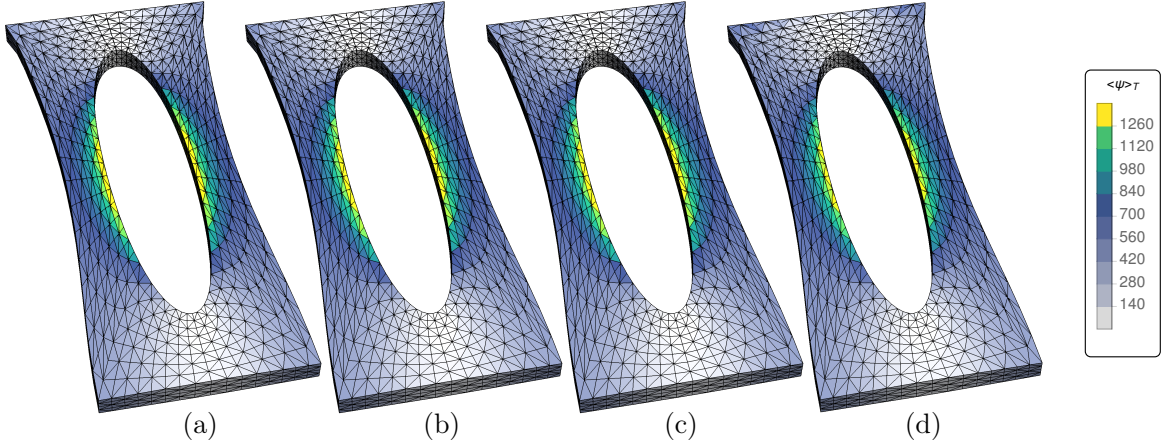


Figure 7.10: Contour plots of the strain energy $\langle \psi \rangle_T$ for the (a) $P2_u$ - $P2_E$ - $P1_\Sigma$, (b) $P2_u$ - $P1B_E$ - $P0_\Sigma$, (c) $P2_u$ - $P2_H$ - $P1_\Lambda$ (d) CR_u - $P1B_H$ - $P0_\Lambda$ formulations

boundary and inducing the missing information about the non-zero displacement values is left for future research. In figure 7.11 convergence results of the Hu-Wahizu formulations on the plate with hole problem are shown. Here, in (a) the convergence of the displacements u_Y at point A (cf. description in figure 7.9(a)) are presented. It can be observed that the condensed formulations $P2_u$ - $P1B_H$ - $P0_\Lambda$, $P2_u$ - $P1B_E$ - $P0_\Sigma$ and CR_u - $P1B_H$ - $P0_\Lambda$ converge towards the same solution. Meanwhile, the results of the non-condensed elements $P2_u$ - $P2_H$ - $P1_\Lambda$ and $P2_u$ - $P2_E$ - $P1_\Sigma$ could not entirely reach an agreement with the results of the condensed formulations within the considered mesh refinements. Still taking into account the relatively large magnitude of displacement the remaining deviation is with less than $239.80/239.55 \approx 0.08\%$ relatively small. Furthermore, corresponding rates of change (%) from the second to the third step relative to the converged value are shown in figure 7.11(c), where similar rates of change for all formulations become visible. Similar to the results of the Cook's problem of the previous section this showcases that the increased polynomial order for the interpolation of \mathbf{H}^h of the non-condensed formulations in the present problem does not improve the rates of convergence (other than in the unit cube example, where due to the smoothness of the solution the non-condensed formulations showed in some cases superior convergence behavior). Meanwhile, the convergence of the L^2 -norm of the displacement gradients is presented in figure 7.9(b). Here, since the formulations $P2_u$ - $P2_E$ - $P1_\Sigma$ and $P2_u$ - $P1B_E$ - $P0_\Sigma$ incorporate \mathbf{E}^h instead of \mathbf{H}^h as mixed variable the $\|\mathbf{H}^h\|_{L^2}$ -norm is evaluated in terms of the gradient of the displacement solution $\nabla \mathbf{u}^h$. From the curves in figure 7.9(b) it becomes visible that the results converge towards the same value. The corresponding computing times of the third refinement step are visualized in figure (d) showing an increase of computing efficiency of the condensed elements by more than an order of magnitude.

7.5 Summary

In this chapter, an overview of the numerical results of the proposed formulations evaluated on various benchmark tests have presented. An overview of the values of the rot-rot parameters imposed via Π_{rot} (cf. (5.7)) that are used throughout the tests of this chapter is given in table 7.1. The elements $P2_u$ - $P1B_E$ - $P0_\Sigma$ and $P2_u$ - $P2_E$ - $P1_\Sigma$ do not require the rot-rot term but are, however restricted to type-II problems. Yet, the type-II models include the rather common linear strain gradient elasticity model of MINDLIN [1964]. Meanwhile, the

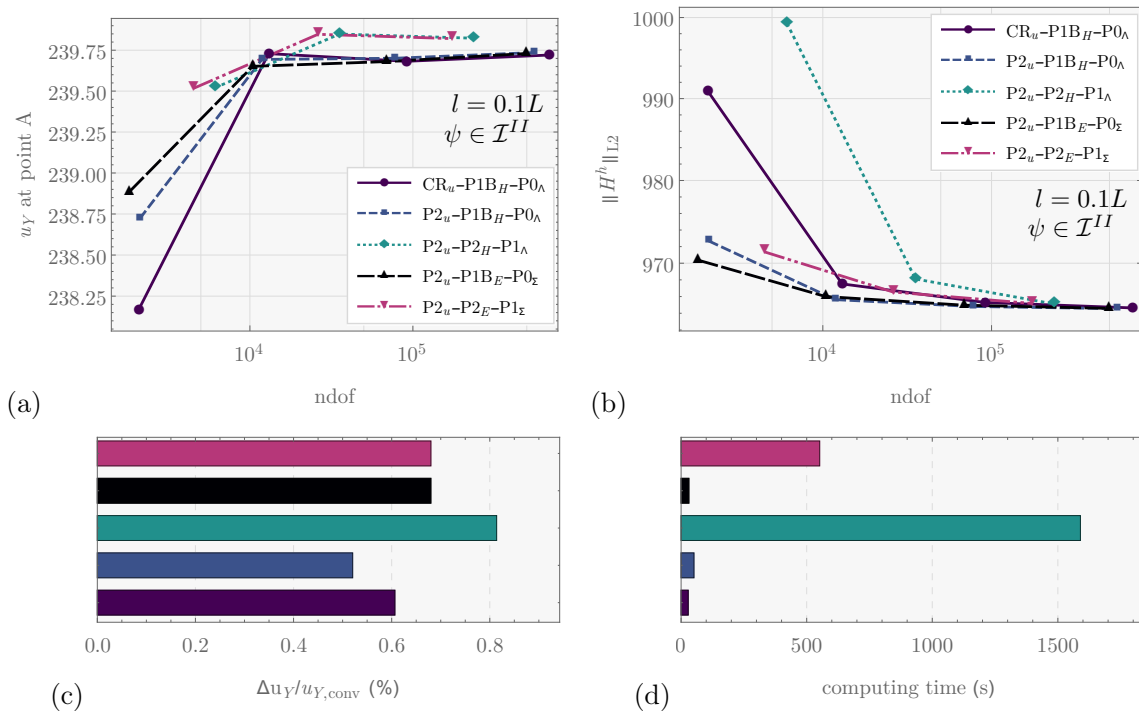


Figure 7.11: Convergence results of the plate with hole benchmark test. (a) shows the convergence of the displacements u_Y at point A (cf. description in figure 7.9(a)). It becomes visible that the condensed formulations converge towards the same solution whereas the results of the non-condensed elements could not entirely reach an agreement with the other results within the considered mesh refinements. (c) shows the corresponding rates of change (%) from the second to the third step relative to the converged value. Similar rates of change become visible, showcasing that the increased polynomial order for the interpolation of \mathbf{H}^h of the non-condensed formulations in the present problem does not improve the rates of convergence. (b) shows the convergence of the $\|\mathbf{H}^h\|_{L^2}$ -norm of the displacement gradient values. The corresponding computing times of the third refinement step are visualized in figure (d) showing a significantly superior efficiency of the condensed elements.

Benchmark	Problem			FE-Formulation					
	Figure	$\psi \in$	l (mm)	1	2	3	4	5	6
Unit Cube	7.2,7.4(b)	\mathcal{I}^{II}	0.1	10	1	1	1	✓	✓
	7.3,7.4(a)	\mathcal{I}^I	0.1	10	0	0	0	-	-
	7.5(a),(c)	\mathcal{I}^I	1	0	0	0	0	-	-
	7.5(b),(d)	\mathcal{I}^I	0.001	1,10	1	0	0	-	-
	7.6(a),(c)	\mathcal{I}^{II}	1	100	1	1	10	⚡	⚡
	7.6(b),(d)	\mathcal{I}^{II}	0.001	100	1	1	1	✓	✓
Cook's Problem	7.8(a)	\mathcal{I}^I	0	100 L	1 L	1	1	-	-
	7.8(a)-(d)	\mathcal{I}^I	$\geq 0.05L$	0	0	0	0	-	-
Plate with Hole	7.11	\mathcal{I}^{II}	$0.1L$	-	10 L	10 L	10 L	✓	✓

Table 7.1: Overview of values of rot-rot Parameter α (cf. (5.7)) used throughout the numerical tests of this section. The formulations are indexed as follows: 1: RotFEM 2: $P2_{\mathbf{u}}-P1B_{\mathbf{H}}-P0_{\Lambda}$, 3: $P2_{\mathbf{u}}-P2_{\mathbf{H}}-P1_{\Lambda}$, 4: $CR_{\mathbf{u}}-P1B_{\mathbf{H}}-P0_{\Lambda}$ 5: $P2_{\mathbf{u}}-P1B_{\mathbf{E}}-P0_{\Sigma}$ 6: $P2_{\mathbf{u}}-P2_{\mathbf{E}}-P1_{\Sigma}$. Here, ✓ indicates a formulation without rot-rot term and no issues, ⚡ indicates issues with numerical robustness and “-” indicates that results are not relevant and/or not computed because the formulation is not suitable for the problem (cf. section 7.1).

formulations incorporating the full gradient \mathbf{H}^h as solution variable are applicable to both types of problems, require however in the case of type-II models the rot-rot stabilization. Further, the RotFEM formulation and the $CR_{\mathbf{u}}-P1B_{\mathbf{H}}-P0_{\Lambda}$ require rot-rot stabilization in the case of type-II energies and small values of l . The elements of the straightforward approach do not require the rot-rot stabilization in the case of type-I energies, yet lose performance for larger values of l . At this point it shall be mentioned again that the rot-rot term Π_{rot} (cf. (5.7)) ensures rank sufficiency of the tangent matrix \mathbf{k}_H , yet it does not change the converged solutions of any of the formulations, since in all approaches in the limit \mathbf{H} is rot-free (cf. (5.7), the stability discussion of section 5.1.1 see also results of figure 7.4). In order to give an overview of the results with respect to performance, that is rates of convergence, numerical robustness and computing efficiency in table 7.2 the main observations are summarized and briefly discussed in the following. Generally, it can be observed that the condensed elements exhibit significantly lower computing times that are even in the same order of magnitude as

Element	Usability				Performance			
	\mathcal{I}^I	\mathcal{I}^{II}	Non-con. Γ_D	Large l	Small l	Cook's Probl.	Plate w. Hole	
$P2_{\mathbf{u}}-P1B_{\mathbf{E}}-P0_{\Sigma}$	✗	✓	✓	-	++	n/a	++	
$P2_{\mathbf{u}}-P2_{\mathbf{E}}-P1_{\Sigma}$	✗	✓	✓	⚡	+	n/a	-	
$P2_{\mathbf{u}}-P1B_{\mathbf{H}}-P0_{\Lambda}$	✓	✓	✓	--	++	++	++	
$P2_{\mathbf{u}}-P2_{\mathbf{H}}-P1_{\Lambda}$	✓	✓	✓	-	+	--	--	
$CR_{\mathbf{u}}-P1B_{\mathbf{H}}-P0_{\Lambda}$	✓	✓	✓	++	+/-	++	++	
RotFEM (3D)	✓	✓	✗	++	--	-	n/a	

Table 7.2: Overview of the main observations of the numerical tests comparing the proposed formulations. Here, ✓ denotes that the formulation is applicable to the corresponding problem and ✗ that it is not. The ⚡ symbol denotes that issues with respect to numerical robustness were observed. The symbols --, -, + and ++ rate the observed relative performance from least to most favorable.

the simple local $P2_{\mathbf{u}}$ displacement element at in most cases similar convergence rates as the non-condensed elements. Furthermore, from the results it can be concluded that the $P2_{\mathbf{u}}-P1B_{\mathbf{E}}-P0_{\Sigma}$ - formulation can be considered most favorable for strain gradient elasticity type problems ($\psi \in \mathcal{I}^{II}$). Meanwhile, the $CR_{\mathbf{u}}-P1B_{\mathbf{H}}-P0_{\Lambda}$ element can be considered the most versatile and meanwhile efficient formulation that is applicable to both type- I and type- II problems and any range of numerical value of l . The RotFEM formulation (applicable to geometries with connected Γ_D) has superior convergence behavior for large values of l and type- I energies, whereas the $P2_{\mathbf{u}}-P1B_{\mathbf{H}}-P0_{\Lambda}$ performs well for small values of l and type- I energies.

Part II

Finite Element Formulations for Gradient Damage

Chapter 8

Introduction to Gradient Damage Formulations and Some Challenges

The present chapter starts by introducing the framework of damage modeling by means of a local formulation. To motivate for the gradient damage approach, the challenges of mesh dependency and lack of numerical robustness are shown in corresponding numerical examples. In the following the general gradient damage formulation is presented followed by two example corresponding finite element approaches and some remaining numerical challenges they are facing. Presented are a penalty approach used as reference in RIESELMANN AND BALZANI [2023] and the finite strain neighbored element approach of JUNKER ET AL. [2022] (see also the related contribution RIESELMANN ET AL. [2021a]). In corresponding numerical studies the ability to produce mesh independent results and some challenges of the penalty approach (i.e. dependency of the solution and numerical robustness on the value of the penalty parameter) are presented motivating for the mixed approach of the next chapter 9.

8.1 Local Damage Formulation

This section presents an example local damage formulation and visualizes in a corresponding numerical study the challenge of mesh sensitivity and lack of numerical robustness discussed in the introduction of chapter 1. For the following, the finite strain kinematic framework introduced in section 2.2 is considered. Based on the idea of modeling the stiffness reduction due to deterioration of the microstructure, the strain energy function can be written as

$$\psi(\mathbf{F}, \alpha) := (1 - D(\alpha))\psi_0(\mathbf{F}). \quad (8.1)$$

Here, ψ_0 denotes the fictitiously undamaged hyperelastic strain energy function and the damage function $D : \mathbb{R}^+ \rightarrow [0, 1)$ models the material softening, where the limit $D \rightarrow 1$ corresponds to the complete deterioration and loss of stiffness, whereas $D = 0$ corresponds to the completely undamaged state. In what follows, the simple damage function

$$D(\alpha) := 1 - e^{-\alpha} \quad (8.2)$$

is considered, which models the damage propagation in terms of an internal damage variable α . In order to maintain thermodynamic consistency, the internal variable is constrained to

change value only in positive direction ($\dot{\alpha} \geq 0$). Under the assumption of adiabatic, isothermal and quasi static conditions the local damage problem can be written as follows. Find \mathbf{u} and α such that

$$-\operatorname{Div} \mathbf{P} = \mathbf{f} \text{ on } \mathcal{B} \quad (8.3)$$

$$\mathbf{P} \cdot \mathbf{n} = \mathbf{t} \text{ on } \Gamma_N \quad (8.4)$$

$$\mathbf{u} = \mathbf{u}^* \text{ on } \Gamma_D \quad (8.5)$$

$$\dot{\alpha} \geq 0 \text{ in } \mathcal{B} \quad (8.6)$$

holds at any given time in the considered time domain $t \in [t_0, t_{\text{end}}]$ and for any given rate $\dot{\mathbf{u}}, \dot{\alpha}$. Here, $\mathbf{P} := \partial_{\mathbf{F}} \psi$ denotes the first Piola Kirchhoff stress tensor. Throughout this contribution, a discontinuous damage model (cf. MIEHE [1995]) is considered. Therefore, a model for the evolution of the damage variable can be given via the Karush-Kuhn Tucker inequality conditions (further reading on constrained optimization in BERTSEKAS [1982])

$$\Phi \dot{\alpha} = 0 \quad \dot{\alpha} \geq 0, \quad \text{and} \quad \Phi \leq 0 \quad \text{with} \quad \Phi(\mathbf{F}, \alpha) := \varphi(\mathbf{F}, \alpha) - Y. \quad (8.7)$$

Here, Φ can be denoted as dissipation surface, level set- or threshold function. Depending on the reference, $\varphi(\mathbf{F}, \alpha)$ is denoted as equivalent stress, energy release rate or driving force, which can be defined by $\varphi(\mathbf{F}, \alpha) = -\partial_{\alpha} \psi$ and Y denotes a threshold value. For references, see MENZEL AND STEINMANN [2001], see also LIEBE ET AL. [2001]. The Clausius Duhem inequality corresponding to problem (8.3)-(8.6) reads

$$\mathbf{P} \cdot \dot{\mathbf{F}} - \dot{\psi} = \dot{\gamma} \geq 0 \quad (8.8)$$

where $\gamma := \gamma(\alpha, \dot{\alpha})$ is a function modeling the volume specific dissipated energy due to the damage evolution. It becomes clear that with (8.6) thermodynamic consistency is maintained if γ is a continuously monotonic increasing function of its arguments. From (8.3)-(8.8) the global energy balance

$$\int_{\mathcal{B}} \dot{\psi} + \dot{\gamma} \, dV = \int_{\mathcal{B}} \mathbf{f} \cdot \dot{\mathbf{u}} \, dV + \int_{\Gamma_N} \mathbf{t} \cdot \dot{\mathbf{u}} \, dA \quad (8.9)$$

can be obtained¹. Throughout this contribution, for the dissipation a rate independent model with the simple quadratic function

$$\gamma := \frac{d_1}{2} \alpha^2 + d_0 \alpha \quad (8.11)$$

(cf. RIESSELMANN AND BALZANI [2023]) is considered with the damage modeling parameters d_0 and d_1 . By the relation $Y = \partial_{\alpha} \gamma$ the threshold value Y appearing in the update function (8.7) can be modeled in terms of the derivative of the dissipation function γ (cf. analogous ideas eg. in JUNKER AND BALZANI [2021] or JUNKER ET AL. [2022]). Note, that choosing d_1 equal to zero corresponds to the model used in DIMITRIJEVIC AND HACKL [2008]. Using both parameters d_0 and d_1 leads to a model similar to the model used in WAFFENSCHMIDT ET AL.

¹Using the integration by parts formula

$$\int_{\partial \mathcal{B}} (\mathbf{P} \cdot \mathbf{n}) \cdot \dot{\mathbf{u}} \, dA = \int_{\mathcal{B}} (\mathbf{P} \cdot \nabla \dot{\mathbf{u}} + \operatorname{Div} \mathbf{P} \cdot \dot{\mathbf{u}}) \, dV \quad (8.10)$$

and inserting (8.3), (8.4) and (8.5) (with $\dot{\mathbf{F}} = \nabla \dot{\mathbf{u}}$) yields the relation $\int_{\mathcal{B}} \mathbf{P} \cdot \dot{\mathbf{F}} \, dV = \int_{\mathcal{B}} \mathbf{f} \cdot \dot{\mathbf{u}} \, dV + \int_{\Gamma_N} \mathbf{t} \cdot \dot{\mathbf{u}} \, dA$, which is inserted into the domain integral of equation (8.8).

[2013]. Moreover, choosing $d_1 = 0$ leads to a constant threshold value $\partial_\alpha \gamma =: Y = d_0$ used in the formulation of JUNKER ET AL. [2019] and JUNKER ET AL. [2022] (see also the following section 8.3.2). Finally, choosing either d_0 or d_1 equal to zero corresponds to the cases AT1 or AT2 used in GERASIMOV AND DE LORENZIS [2019]. Note that in the case of both nonzero d_1 and d_0 the resulting release rate $Y = \partial_\alpha \gamma = d_0 + d_1 \alpha$ takes the form described in MENZEL AND STEINMANN [2001], where α concurrently serves as hardening variable. In what follows, for the virtually undamaged hyperelastic energy density ψ_0 the Neo-Hooke function (7.12) is used.

8.1.1 Mesh Dependency and Lack of Robustness

The following study aims to visualize the numerical problems that finite element formulations based on the previously introduced problem face. Therefore, the plate with hole geometry with description and model parameters given in figure 8.1 is considered. Note, that due to the symmetry only the upper right quarter of the total structure needs to be considered. Therefore, the geometry is fixed in Y -direction at the lower surface ($Y = 0$ mm) and fixed in X -direction at the left surface $X = 0$ mm. A prescribed displacement $\mathbf{u}^* = (0, u_Y^*, 0)^T$ mm is applied at the upper surface ($Y = 100$ mm). The following numerical results of figure 8.2 are an extension of the study given in RIESSELMANN AND BALZANI [2023] providing results of local finite element computations corresponding to the solution of problem (8.3)-(8.6). In the present study, the maximal value of the prescribed displacement is $u_Y^* = 3.5$ mm is applied with a linear increasing load function and $n_{\text{steps}} = 500$ load steps. Here, in the plots of figure 8.2(a) and (b) force displacement curves for various mesh hexahedral (a) and tetrahedral (b) mesh refinements are shown. Therefore, as in all subsequent force displacement plots of the plate with hole problem, the value of the reaction forces F in Y direction (which is recovered from the upper surface $Y = L$) is plotted over the value of the prescribed displacement \mathbf{u}_Y^* . From results which in both plots vary significantly and do not converge for the different mesh refinement stages the problem of mesh dependency becomes clear. Moreover, the lack of numerical robustness of local formulations manifests in the present study through the failure of the iterative solution to produce results beyond the chosen prescribed displacement of 3.5 mm. Due to the localization of the damage accumulation, the finer meshes encounter this issue at even earlier load stages that is in both plots a prescribed load of ≈ 2.4 mm (marked with a red cross). Figure 8.2(a)-(c) presents contour plots of the damage field D corresponding to the different meshes at the final load stage marked with bullets in figure 8.2(d) and (e).

8.2 The Gradient Damage Problem

The present section introduces the gradient damage problem and corresponding potential functionals, on which the finite element formulations of this contribution (discussed in the following section 8.3 and in the following chapter 9) are based. The gradient enhanced damage formulation is obtained by enriching the local strain energy introduced in the previous section by the nonlocal contribution ψ^{nlloc} with

$$\psi = \psi^{\text{loc}}(\mathbf{F}, \alpha) + \psi^{\text{nlloc}}(\nabla \alpha) \quad (\text{cf. LIEBE ET AL. [2001]}), \quad (8.12)$$

where the local part ψ^{loc} is given by (8.1). Inserting (8.12) into the energy balance (8.9) and integrating the Clausius Duhem inequality (8.8) over the domain yields the global form of first and second law of thermodynamics

$$\dot{\Pi} = 0 \quad \text{and} \quad \dot{\Gamma} \geq 0, \quad (8.13)$$

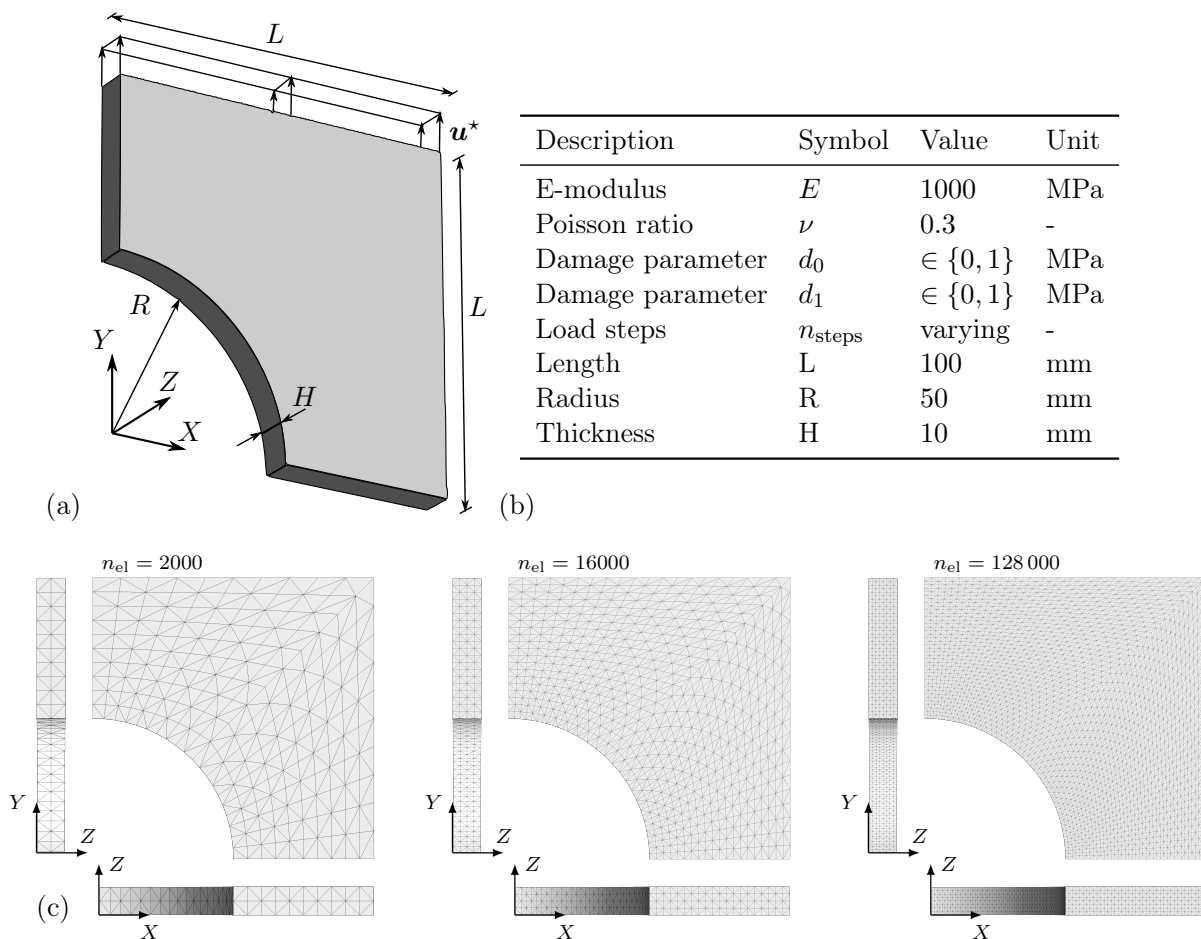


Figure 8.1: (a) Description of the geometry of the plate with hole benchmark problem. (b) Geometric and boundary parameters used throughout the tests of this contribution. (c) Mesh visualizations of exemplary mesh refinement steps (view from the side, front and bottom for each step).

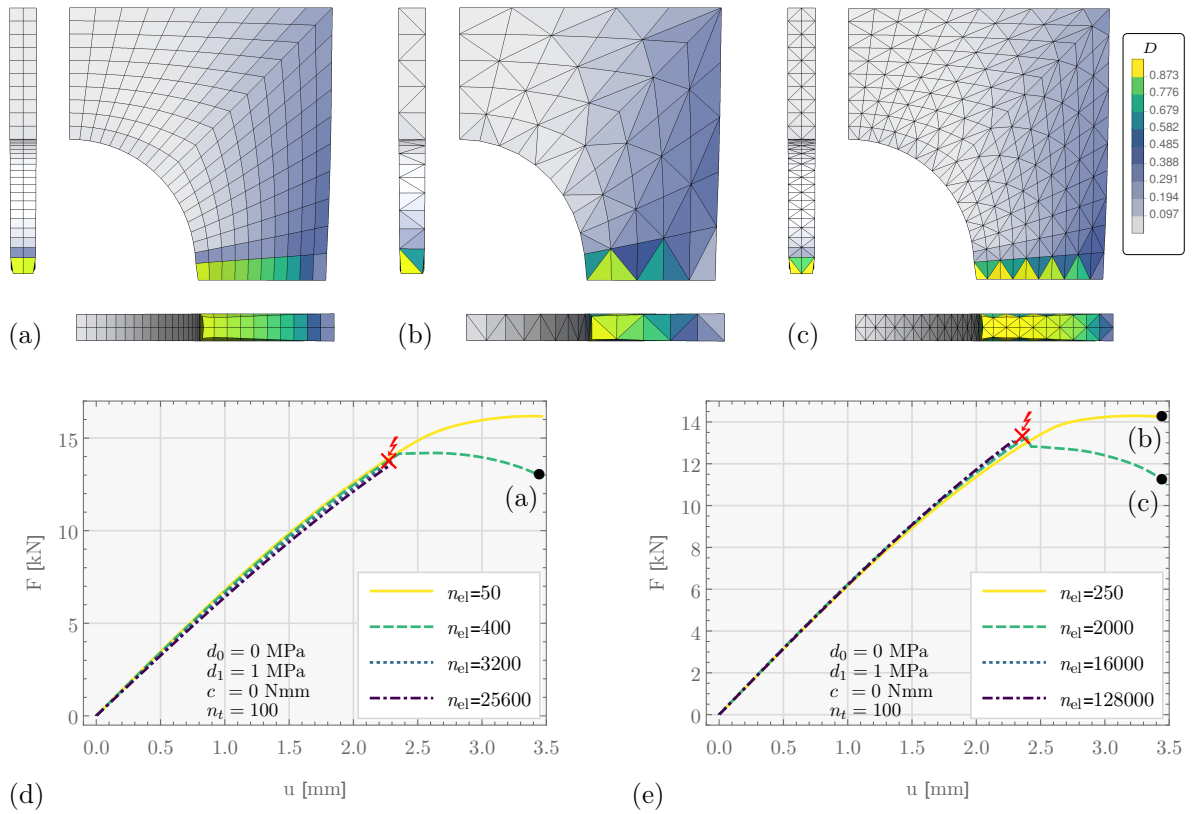


Figure 8.2: Visualization of the mesh dependency of the local damage formulation with (a): contour plot of the hexahedral mesh corresponding to the final load stage and $n_{el} = 400$ marked in the plot (d). (b)-(c): contour plots of the tetrahedral mesh corresponding to the first and second refinement at final load stage marked in the force displacement curves in the plot (e). (d): force displacement curves of the hexahedral element. (e): force displacement curves of the tetrahedral element. The lightning symbol marks the divergence of the iterative solution procedure (occurring for both meshes at mesh refinements above step 3 ($n_{el} = 3200$, $n_{el} = 16000$) in the load range $u_Y^* \approx 2.25 - 2.4$ mm).

respectively, with the corresponding potential functions defined as

$$\Pi := \underbrace{\int_{\mathcal{B}} \left(\psi^{\text{loc}}(\mathbf{F}, \alpha) + \psi^{\text{nloc}}(\nabla \alpha) + \gamma(\alpha) \right) dV}_{\Pi_{\text{int}}} - \underbrace{\int_{\mathcal{B}} \mathbf{u} \cdot \mathbf{f} dV - \int_{\Gamma_N} \mathbf{u} \cdot \mathbf{t} dA}_{\Pi_{\text{ext}}} \quad \text{and} \quad (8.14)$$

$$\Gamma := \int_{\mathcal{B}} \gamma(\alpha) dV. \quad (8.15)$$

From (8.13) and integrating by parts² (cf. RIESELDMANN AND BALZANI [2023]) the gradient damage problem can be postulated as following local set of equations: Find α and \mathbf{u} such that the balance of linear momentum (8.3), Cauchy theorem (8.4) Dirichlet conditions (8.5) and surface flux

$$\nabla \alpha \cdot \mathbf{n} = 0 \quad \text{on } \partial \mathcal{B} \quad (8.17)$$

holds at any given time in the considered time domain $t \in [t_0, t_{\text{end}}]$ and for any given rate $\dot{\mathbf{u}}$, $\dot{\alpha}$ with the Karush Kuhn Tucker constraint conditions

$$\Phi \dot{\alpha} = 0 \quad \dot{\alpha} \geq 0, \quad \text{and} \quad \Phi \leq 0 \quad \text{with} \quad \Phi := -\partial_{\alpha} \psi + \text{Div } \partial_{\nabla \alpha} \psi - \partial_{\alpha} \gamma. \quad (8.18)$$

For the sake of clarity, here it is worth pointing out, that Φ in (8.18) is defined such that the equation $\Phi \dot{\alpha}$ is contained in the energy balance (8.13). Or, following the reverse argumentation the definition of Φ and the equation $\Phi \dot{\alpha} = 0$ follows from the energy balance (8.13). This can be checked by simply evaluating

$$\dot{\psi} + \dot{\gamma} = \mathbf{P} \cdot \dot{\mathbf{F}} + \partial_{\alpha} \psi \dot{\alpha} + \partial_{\nabla \alpha} \psi \cdot \nabla \dot{\alpha} + \partial_{\alpha} \gamma \dot{\alpha}$$

in $\dot{\Pi}$ and using the integration by parts formula (8.16), which yields equations (8.17) and (8.18).

8.3 Some Challenges of Existing Gradient Damage Formulations

The goal of this section is to present two existing gradient damage finite element approaches with an extract of corresponding numerical results, highlighting favorable features and some of the challenges discussed in the introduction of chapter 1. Presented are a penalty formulation similar to WAFFENSCHMIDT ET AL. [2013] based on DIMITRIJEVIC AND HACKL [2008] and the neighbored element approach of JUNKER ET AL. [2022] based on JUNKER ET AL. [2019] (see also VOGEL AND JUNKER [2019]).

8.3.1 Penalty Formulation

The following approach is introduced as comparative approach in RIESELDMANN AND BALZANI [2023] and is similar to the approaches of WAFFENSCHMIDT ET AL. [2013] and DIMITRIJEVIC AND HACKL [2008]. In order to enable a finite element discretization with standard Lagrange interpolation functions while maintaining the evolution criterion in the form of the update of

²Here, besides the integration by parts formula (8.10) the following formula is used

$$\int_{\mathcal{B}} \partial_{\nabla \alpha} \psi \cdot \nabla \dot{\alpha} dV = \int_{\partial \mathcal{B}} (\partial_{\nabla \alpha} \psi \cdot \mathbf{n}) \dot{\alpha} dA - \int_{\mathcal{B}} \text{Div } \partial_{\nabla \alpha} \psi \dot{\alpha} dV. \quad (8.16)$$

a local history variable, the penalty approach introduces an additional variable and enforces compatibility via a penalty term. Therefore, the potential (8.14) is modified as follows

$$\Pi_{\text{pen}} := \int_{\mathcal{B}} \left(\psi^{\text{loc}}(\mathbf{F}, \alpha) + \psi^{\text{nloc}}(\nabla \alpha) + \gamma(\tilde{\alpha}) + \frac{p}{2} (\alpha - \tilde{\alpha})^2 \right) dV + \Pi_{\text{ext}}, \quad (8.19)$$

where $\tilde{\alpha}$ denotes the additionally introduced purely local history variable and $p/2(\alpha - \tilde{\alpha})^2$ denotes the penalty term enforcing compatibility. Following the same steps analogous to the previous section under consideration of the balance equations (8.13) yields the following update conditions

$$\tilde{\Phi} \dot{\tilde{\alpha}} = 0 \quad \dot{\tilde{\alpha}} \geq 0, \quad \text{and} \quad \tilde{\Phi} \leq 0 \quad \text{with} \quad \tilde{\Phi} := p(\alpha - \tilde{\alpha}) - \partial_{\alpha} \gamma \quad (8.20)$$

and the additional compatibility equation

$$- \partial_{\alpha} \psi + \text{Div} \partial_{\nabla \alpha} \psi = p(\alpha - \tilde{\alpha}). \quad (8.21)$$

Meanwhile, the displacement equations (8.3)-(8.5) and the surface flux equation (8.17) remain unchanged. The penalty finite element approach is based on finding the minimizer

$$\Pi_{\text{pen}} \Rightarrow \min_{\mathbf{u}, \alpha, \tilde{\alpha}} \quad \text{subject to} \quad \tilde{\Phi} \leq 0. \quad (8.22)$$

Following the well known arguments of constrained optimization (see e.g. BERTSEKAS [1982]), as the penalty parameter with $p \rightarrow \infty$ reaches infinity the corresponding minimizers α and $\tilde{\alpha}$ become equal. Thus, by inserting $\tilde{\alpha} = \alpha$ into (8.19) and (8.20) it can easily be verified that for the limit case of an infinite penalty parameter value the solution to problem (8.22) is equivalent to the solution of the original problem. In return, in the numerical application case, where the penalty parameter is not infinity, the solution to (8.22) is not exactly the same as the solution to the original problem. Corresponding numerical results showcasing this issue can be found in figure 8.3 (see also figure 9.3, where a comparative study with the proposed approach of chapter 9 is given).

Discretization The discretization of the body and subdividing integration over the elements follows the standard approach presented in section 3.3. In the potential (8.19) first gradients of the variables \mathbf{u} and α are apparent. Thus, they are elements of the Sobolev spaces $\mathbf{u} \in H_0^1(\mathcal{B}; \mathbf{R}^3)$ and $\alpha \in H_0^1(\mathcal{B})$ and can conformingly be discretized with standard Lagrange interpolation functions. Here, piecewise quadratic functions are chosen for the interpolation of

$$\mathbf{u}^h|_T = \sum_{I=1}^{10} \mathbf{d}_I^{(u)} N_I^{(P2)} \quad \text{with} \quad \nabla \mathbf{u}^h|_T = \sum_{I=1}^{10} \mathbf{d}_I^{(u)} \otimes \nabla N_I^{(P2)} \quad (8.23)$$

and piecewise linear functions are chosen for the interpolation of

$$\alpha^h|_T = \sum_{I=1}^4 d_I^{(\alpha)} N_I^{(P1)} \quad \text{with} \quad \nabla \alpha^h|_T = \sum_{I=1}^4 d_I^{(\alpha)} \nabla N_I^{(P1)}. \quad (8.24)$$

where $N_I^{(P2/P1)}$ denote quadratic/linear Lagrange shape functions and $\mathbf{d}_I^{(u)} = (d_I^{(u_1)}, d_I^{(u_2)}, d_I^{(u_3)})^T$ and $d_I^{(\alpha)}$ denote the standard corresponding nodal degrees of freedom. Meanwhile, the additional variable $\tilde{\alpha} \in L^2(\mathcal{B})$ is a purely local variable and is stored as history variable at each

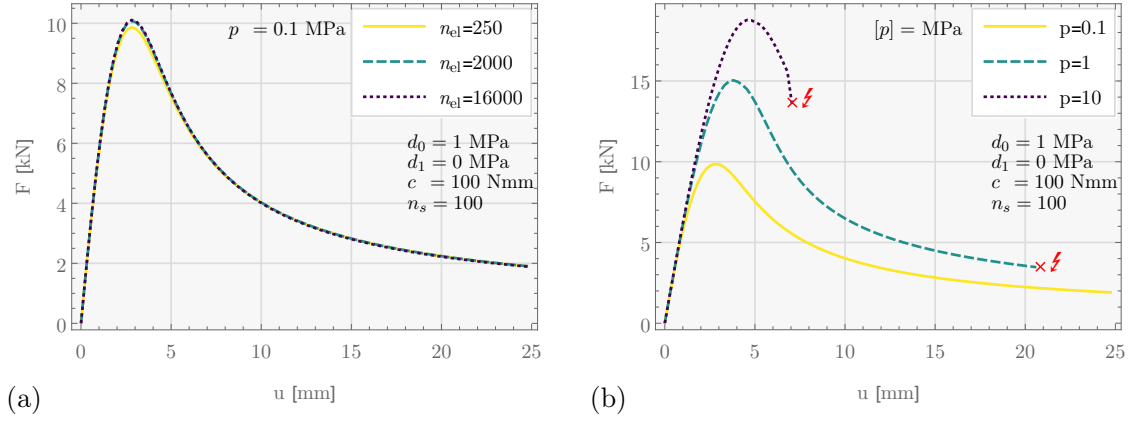


Figure 8.3: Results of the gradient damage penalty formulation (P2 \mathbf{u} -P1 α -pen) on the plate with hole problem. (a) Convergence of the force displacement curves for a penalty parameter value of $p = 0.1$ MPa. (b) Force displacement curves for varying values of the penalty parameter. Since the results vary significantly, clearly the value of the penalty parameter $p = 0.1$ MPa is not high enough in order to arrive at results that are consistent with the original problem (cf. section 8.2). However, solutions for higher values of p can not be computed as the formulation loses numerical robustness and the iterative solution procedure fails to converge (failure is marked with red cross). The issue becomes more severe as the value of p gets larger.

Gauss point of each element. The history variable needs to fulfill the constraint condition $\tilde{\Phi} \leq 0$, is defined as

$$\tilde{\alpha}^h := \begin{cases} \text{root } \tilde{\Phi}(\alpha^h, \tilde{\alpha}^h) & \text{if } \tilde{\Phi}(\alpha^h, \tilde{\alpha}^h) > 0 \\ \tilde{\alpha}^h & \text{else} \end{cases} \quad (8.25)$$

and is updated at each step of the incremental load step solution procedure. The discrete Lagrangian reads

$$\Pi_{\text{pen}}^h := \sum_{T \in \mathcal{T}} \int_T \left(\psi(\mathbf{F}^h, \alpha^h, \nabla \alpha^h) + \gamma(\tilde{\alpha}^h) + \frac{p}{2} (\alpha^h - \tilde{\alpha}^h)^2 \right) dV + \Pi_{\text{ext}}^h. \quad (8.26)$$

Since the constraint term is posed in terms of a penalty parameter, no Lagrange multipliers are present and no inf-sup condition needs to be fulfilled for stability. Yet, as will be shown in the following (figure 8.3) the choice of the numerical value of the penalty parameter is crucial for the robustness of the iterative solution procedure of the non-linear problem. Throughout the numerical studies of this section and those of in the following chapter 9 the penalty approach is referred to as P2 \mathbf{u} -P1 α -pen“X” formulation, where “X” denotes the numerical value of the penalty parameter p .

Numerical Results In the present study the plate with hole problem is considered (cf. figure 8.1), where a prescribed displacement is applied with a linear increasing load up to a value of $u_Y^* = 25$ mm (which is significantly higher than in the local study of figure 8.2). The values of all further corresponding problem parameters are given in figure 8.1 and figure 8.3. Following the references mentioned in this subsection 8.3.1, for the nonlocal strain energy the simple quadratic function

$$\psi^{\text{nlloc}} = \frac{c}{2} \nabla \alpha \cdot \nabla \alpha \quad (8.27)$$

is considered, where c constitutes the nonlocal parameter. The local strain energy and dissipation function were given in section 8.1. The plots of figure 8.3 show force displacement curves corresponding to the results obtained with the penalty formulation. Here, in figure 8.3(a) the different curves corresponding to the various steps of the uniform mesh refinement are presented. The results of figure 8.3(a) are obtained for a penalty parameter value of $p = 0.1$ MPa. In this case, the ability of the formulation to produce mesh independent results becomes visible and converging iterative solution procedures up to the final load stage are observed, showcasing the increased numerical robustness due to the gradient enhancement. Yet, when considering the results of figure 8.3(b), in which force displacement curves for varying values of the penalty parameter are shown (for a fixed mesh with $n_{\text{el}} = 250$ elements), it becomes also visible that the results vary significantly depending on the value of the penalty parameter. This suggests that the value of $p = 0.1$ MPa considered in figure 8.3(a) is not sufficiently high to produce results that are consistent with the original formulation, because otherwise in the case of p approaching sufficiently high values converging curves should be observed. However, for the present problem choosing higher values for p causes numerical problems as the iterative solution procedure fails to converge after a certain load stage, which becomes even lower as the penalty parameter gets higher. Summarizing, the penalty approach offers increased robustness compared to local formulations and mesh independent results that are, however, dependent on the penalty parameter. In addition to that, a loss of numerical robustness for larger values of the penalty parameter is observed, further limiting the choice of possible penalty parameter values to a rather low range.

8.3.2 Neighbored Element Formulation

The formulation discussed in this section was introduced for large strains in JUNKER ET AL. [2022] and is based on the small strain approach of JUNKER ET AL. [2019] (see also VOGEL AND JUNKER [2019]). In the mentioned references, the continuous formulation is presented in terms of integrals in the framework of the so-called extended Hamilton's principle (cf. JUNKER AND BALZANI [2021]). In the notation of the present contribution, the formulation is given by the minimization problem

$$\Pi \Rightarrow \min_{\mathbf{u}} \quad \text{subject to} \quad \Phi \leq 0 \quad (8.28)$$

with Π given in (8.14) and Φ given by (8.18). Other than in the previously discussed penalty formulation and the formulation presented in the next chapter 9 in the present case different functions are used for the nonlocal strain energy function

$$\psi^{\text{nlloc}} := \frac{\beta}{2} \nabla f \cdot \nabla f \quad (8.29)$$

with $f := 1 - D(\alpha) = \exp(-\alpha)$ and β being the nonlocal parameter and the dissipation function

$$\gamma(\alpha) := r \alpha \quad (8.30)$$

with $r \equiv d_0$ being the damage threshold parameter also referred to as dissipation parameter. Note, that the displacement and surface equations (8.3)-(8.5) resulting from (8.28) and the update conditions remain unchanged from (8.3)-(8.5), (8.17) and (8.18), respectively. Yet, for the present case the specific expressions presented in JUNKER ET AL. [2022] are obtained by

making the insertions³

$$-\partial_\alpha \psi = f \psi_0, \quad \text{Div}(\partial_{\nabla \alpha} \psi) = -\beta f \Delta f \quad \text{and} \quad \partial_\alpha \gamma = r, \quad (8.31)$$

where $\Delta(\bullet) := \text{Div} \nabla(\bullet)$ denotes the Laplace operator. With the insertions, the first variation of (8.28) reads

$$\int_{\mathcal{B}} \frac{1}{2} \mathbf{S} \cdot \delta \mathbf{C} \, dV + \delta \Pi^{\text{ext}} = 0 \quad \text{subject to} \quad \Phi := f \psi_0 - \beta f \Delta f - r \leq 0 \quad (8.32)$$

where $\mathbf{C} = \mathbf{F}^T \cdot \mathbf{F}$ denotes the right Cauchy Green tensor (cf. section 2.2) $\mathbf{S} := 2 \partial_{\mathbf{C}} \psi^{\text{loc}}$ denotes the second Piola Kirchhoff stress tensor. Here, the balance of linear momentum is considered in weak integral form (as usual), whereas the update condition is considered in local form. Due to the appearance of the non-local operator $\Delta(\bullet)$ in the update conditions, corresponding discretizations require special treatment (cf. following subsection).

Discretization While the previously discussed penalty approach considers a coupled formulation with two finite element solution variables and incorporates the inequality in terms of the update of a local history variable, in the present formulation only $\mathbf{u} \in H_0^1(\mathcal{B}; \mathbf{R})$ is considered as global finite element solution variable. In the present approach, hexahedral elements are considered and \mathbf{u}^h is interpolated with corresponding Lagrange shape functions. For the inequality condition, f is considered as solution variable. Due to the appearance of the second order differential operator $\Delta(\bullet)$ information about the neighboring elements is required for a consistent discretization. Therefore, a finite difference related discretization scheme is used. The discrete system is solved with a staggered solution procedure, therefore numerical robustness can be expected (cf. GERASIMOV AND DE LORENZIS [2019], see also following numerical results). Yet, from the practitioner's point of view the combination of finite element and the special finite difference related discretization can be considered as drawback, since common finite element interfaces can not be used. Details regarding the discretization and the algorithmic treatment can be found in JUNKER ET AL. [2022].

Numerical Results The present study from JUNKER ET AL. [2022] aims to highlight the robustness and efficiency of the approach, yet show that results are not independent of the chosen step size. For the study the geometry parameters from figure 8.1 are considered, whereas for the material parameters the values $E = 500$ MPa, $\nu = 0.3$, $r = 5$ MPa and $\beta = 100$ N are used. In the force displacement curves of figure 8.4 (a) (enlargement in (b)) the convergence of the curves under uniform mesh refinement becomes visible. Moreover, since the solution algorithm incorporates a feature, which numerically imposes a complete loss of element stiffness once the damage has reached the critical value $D_{\text{crit}} = 1 - f_{\text{crit}} = 0.95$ the reaction forces can be modeled to become zero. Thus, in the present study after surpassing the softening transition zone, the reaction forces reach completely zero values. This corresponds to a complete detachment from the lower boundary $Y = 0$ along which the damage propagated. The contour plots of figure 8.4 (c) visualize the evolution of the damage field $D = 1 - f$ corresponding to different load stages marked with bullets in figure 8.4 (a) and (b). No loss of robustness of the solution procedure is observed. The subsequent study of figure 8.5 (a) shows the force displacement curves for a fixed mesh over varying values of load increments

³Here, the specific choice of the function $f(\alpha)$ leads to $-\partial_\alpha \psi = -\partial_\alpha f \psi_0 = f \psi_0$. Meanwhile, application of the chain rule $\nabla f = \nabla(\exp(-\alpha)) = -\exp(-\alpha) \nabla \alpha = -f \nabla \alpha$ yields with the nonlocal energy (8.29) the expression $\partial_{\nabla \alpha} \psi = \partial_{\nabla \alpha}(\beta/2(-f \nabla \alpha)(-f \nabla \alpha)) = -\beta f \nabla f$.

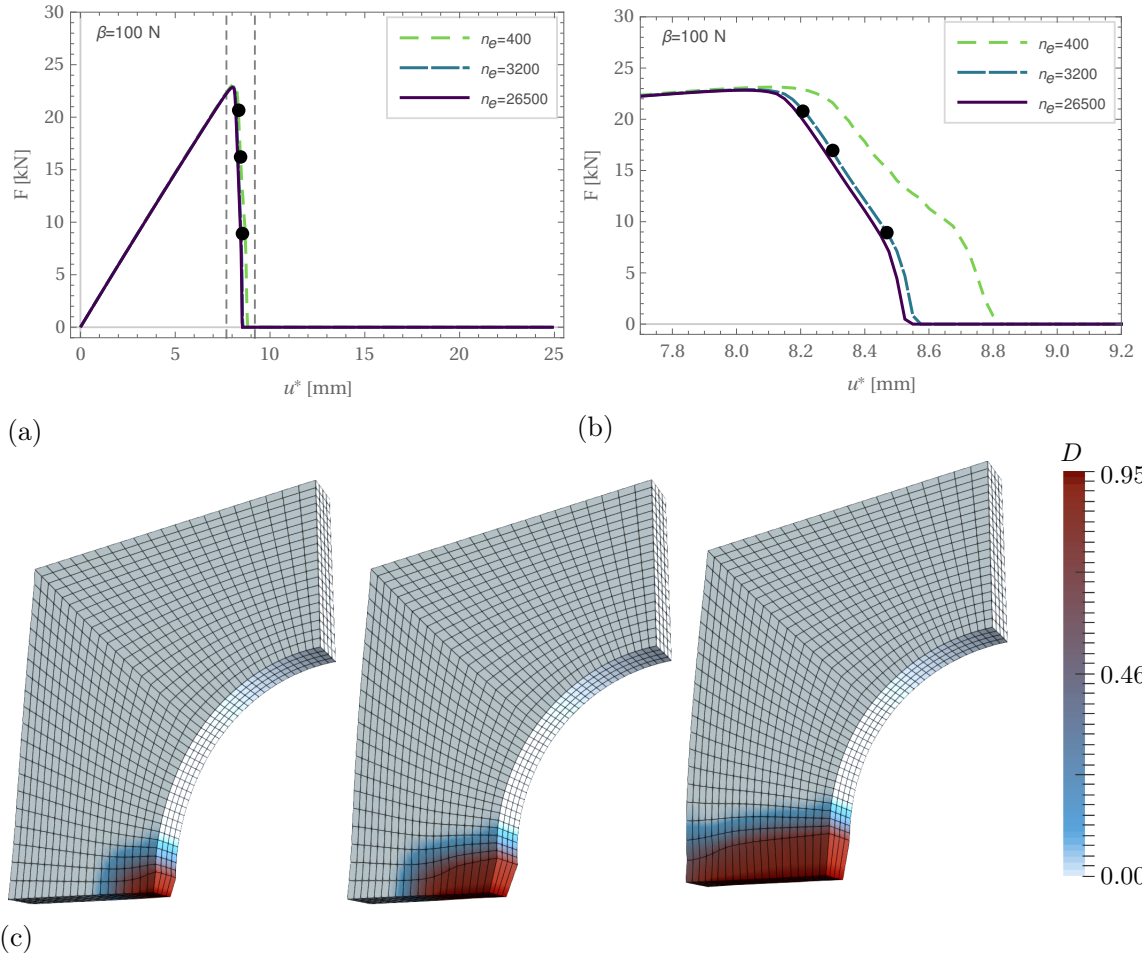


Figure 8.4: Convergence results (cf. JUNKER ET AL. [2022]) showing for the large strain neighbored element method (a) force/displacement curves (higher resolution in (b)). In (c) corresponding contour plots depict the damage evolution for a mesh with 3200 elements at three different load steps which are depicted as bullets in (a). The load increment is 0.025 mm. The results suggest mesh independence, since the curves converge as the mesh gets finer.

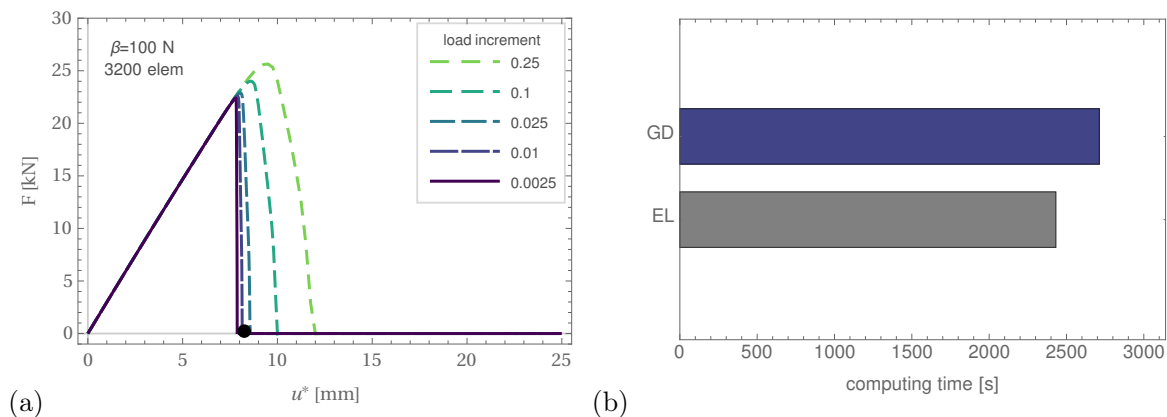


Figure 8.5: Time step convergence and computing efficiency study (cf. JUNKER ET AL. [2022]). (a) shows force/displacement curves for varying load increments for a 3200 element mesh and $\beta = 100$ N. It becomes visible that the results converge as the load increments get finer. Yet, for the coarser time step resolutions of 100 and 250 time steps (first two curves) the deviations are rather significant. (b) GD: Computing time until reaching the marked point at $u^* = 8.575$ mm in (a) with the load increment 0.01 mm. EL: computing time of a purely elastic 8-node hexahedral reference element until the same load of $u^* = 10.85$ mm

of the load step solution procedure. Here, it becomes visible that the results converge as the load increments get finer. Yet, for the coarser time step resolutions of 100 and 250 time steps (first two curves) the deviations are rather significant. Thus, in order to achieve convergence a relatively high time step resolution compared to other approaches (cf. section 9.2) can be necessary taking a toll on the overall computing time. Yet, as shown in figure 8.5 (b) when comparing the present approach with the same formulation and the same preset number of load steps but purely elastic problem parameters similar computing times can be observed. In summary, the present formulation provides mesh independent numerically robust and relatively cost-efficient results with a numerical feature that enables to model complete material failure. Yet, load increments have to be chosen sufficiently small in order to provide accurate results.

Chapter 9

A Simple and Efficient Mixed Finite Element Formulation for Gradient Damage

The present chapter introduces the mixed finite element formulation for gradient damage proposed in RIESELDMANN AND BALZANI [2023]. The proposed approach takes into account the non-locality of the damage variable by incorporating it as a nodal solution variable (see also RIESELDMANN AND BALZANI [2022]) and the damage evolution constraint is included in terms of a Lagrange multiplier term. Presented are the continuous formulation and a corresponding suitable choice of interpolation functions enabling for the static condensation of the Lagrange multiplier variable. The proposed formulation neither requires cross-element information (as eg. the formulation of section 8.3.2) nor does it incorporate a penalty parameter which might deduce numerical robustness (as eg. the formulation of 8.3.1). Moreover, numerical tests of the proposed approach show mesh-independent solutions, robustness of the solution procedure for states of severe damage and under cyclic loading conditions at computing times in the same order of magnitude as purely elastic computations. Adding to RIESELDMANN AND BALZANI [2023], here some considerations with respect to inf-sup stability are given and the incorporation of an element erosion technique (cf. JUNKER ET AL. [2022]) with corresponding numerical results showing mesh convergence.

9.1 The Proposed Approach

In the following, both the continuous and discrete formulation as well as the algorithmic treatment of the proposed approach is presented.

9.1.1 Continuous Formulation

While the comparative formulations of section 8.3 incorporate the inequality conditions (8.18) by evaluating the constraint $\Phi \leq 0$, the present approach considers directly the condition $\dot{\alpha} \geq 0$ as primary constraint. In what follows the time discrete setting is considered with the simple time discretization $\dot{\alpha} \leftarrow (\alpha - \alpha_n)/\Delta t$ where α_n denotes the value of the previous time

step and $\Delta t = t - t_n$ denotes the time step. The problem is formulated as follows:

$$\text{Find } \Pi_\lambda \Rightarrow \text{stat}_{\mathbf{u}, \alpha, \lambda} \quad \text{subject to } \alpha - \alpha_n \geq 0 \quad (9.1)$$

with the Lagrangian defined as

$$\Pi_\lambda := \Pi + \int_{\mathcal{B}} \lambda (\alpha - \alpha_n) \, dV, \quad (9.2)$$

where $\Pi = \Pi^{\text{int}} + \Pi^{\text{ext}}$ is the total potential defined by (8.14) and λ denotes the Lagrange multiplier. Note, that since the used material models are rate independent and the conditions are considered quasi static Δt has no influence of the solution other than a scaling the constraint term. Thus, Δt is considered to be contained in λ and the problem is written as in (9.2). The Karush Kuhn Tucker conditions corresponding to problem (9.1) read

$$\lambda \leq 0, \quad \alpha - \alpha_n \geq 0 \quad \text{and} \quad \lambda (\alpha - \alpha_n) = 0 \quad (9.3)$$

where the sign of the (trial) value of the Lagrange multiplier λ (evaluated from previous iterations of corresponding numerical solution procedures) can be used to identify the evolution and no-evolution case. Moreover, by replacing α_n by the local control variable $\bar{\alpha}$ defined as

$$\bar{\alpha} := \begin{cases} \alpha_n & \text{for no damage evolution} \\ \alpha & \text{for damage evolution} \end{cases} \quad (9.4)$$

the inequality condition is per definition fulfilled, since in the no-evolution case with $\lambda (\alpha - \alpha_n)$ damage evolution is suppressed whereas in the evolution case with $\lambda (\alpha - \alpha)$ the constraint term vanishes and α is allowed to evolve. Further details with respect to the numerical treatment of the constraint are given in section 9.1.3. The solution variables are sought in the following solution spaces (defined in section 2.1.3)

$$\mathbf{u} \in H_0^1(\mathcal{B}; \mathbf{R}^3), \quad \alpha \in H_0^1(\mathcal{B}) \quad \text{and} \quad \lambda \in H^{-1}(\mathcal{B}) \quad (9.5)$$

To ensure boundedness of the bilinear form $a_2(\delta\alpha, \Delta\alpha)$ corresponding to α (defined in appendix A.2) and resulting therefrom increased numerical robustness α is defined to have a compact support (cf. BRAESS [2007]) meaning it lives in $H_0^1(\mathcal{B})$ and not in $H^1(\mathcal{B})$ ¹. Therefore, α can be either defined to be fixed with $\alpha = \alpha^*$ on some subdomain $\Gamma_D^\alpha \in \partial\mathcal{B}$ or its volume mean integral can be fixed by imposing $\int_{\mathcal{B}} \alpha \, dV = 0$. Here the space for the Lagrange multiplier is given by $H^{-1}(\mathcal{B})$, since it denotes the proper dual space to $H_0^1(\mathcal{B})$ given through the pairing $\int_{\mathcal{B}} \lambda \alpha \, dV$ (cf. BRAESS [2007]). Note, that in RIESELMANN AND BALZANI [2023] the space for λ is given by $L^2(\mathcal{B})$. Nevertheless, the corresponding proposed L^2 -conforming piecewise constant discretization for λ^h (cf. section 9.1.2) is with $L^2(\mathcal{B}) \in H^{-1}(\mathcal{B})$ (cf. BRAESS [2007], p.117) also conforming with the space $H^{-1}(\mathcal{B})$. In what follows for the non-local strain energy ψ^{nlloc} the quadratic function (8.27) is considered. Variation of (9.2) and integrating

¹This is necessary because for the case $D \rightarrow 1$ and $\gamma = d_0\alpha$ in the potential (9.2) only gradients $\nabla\alpha$ (and not the variable α itself) appear in the terms that correspond to the bilinear form $a_1(\alpha, \delta\alpha)$ of the linearized problem (cf. section 9.1.1) resulting in the tangent matrix \mathbf{k}_α of the discretized system (cf. section 9.1.2). Here, without prescribing the support, the tangent matrix \mathbf{k}_α would possess a zero singular value. This observation is analogous to the appearance of three zero singular values in the matrix \mathbf{k}_u of standard local quasi static elasticity finite elements for which no Dirichlet conditions are prescribed, since the bilinear form from which \mathbf{k}_u in that case is derived also only contains derivatives of \mathbf{u} and not \mathbf{u} itself. In some references imposing the support condition is referred to as “fixing the constant”. Moreover, by defining α to be in $H_0^1(\mathcal{B})$ and not in $H^1(\mathcal{B})$ the inf-sup condition (cf. next subsection) is fulfilled by definition (cf. BRAESS [2007]).

by parts (cf. appendix of RIESELMAANN AND BALZANI [2023]) yields the displacement and surface equations (8.3)-(8.5) and (8.17) as well as the equation

$$\Phi(\mathbf{F}, \alpha, \nabla \alpha) = \lambda \text{ in } \mathcal{B}, \quad (9.6)$$

which shows, that the Lagrange multiplier λ is associated to the function Φ .

Hints on the Stability of the Linearized Continuous Formulation The subsequent part discusses some aspects concerning the mathematical stability (cf. section 2.4) of the linearized continuous formulation. It should be noted that the extension of Brezzi's conditions to the nonlinear scenario involving gradient damage remains an unresolved research matter, to the best of the authors' knowledge. However, the insights provided on the linear system could offer clues regarding the stability of the nonlinear problem, leaving further exploration for future studies. The variation and linearization of (9.2) result in the following linear problem to be solved in each iteration. For given $(\mathbf{f}, \mathbf{t}, \mathbf{u}^*) \in H^{-1}(\mathcal{B}; \mathbf{R}^3) \times H^{-1/2}(\Gamma_N; \mathbf{R}^3) \times H^{1/2}(\Gamma_D; \mathbf{R}^3)$ find the solution $(\Delta \mathbf{u}, \Delta \alpha, \Delta \lambda) \in H_0^1(\mathcal{B}; \mathbf{R}^3) \times H_0^1(\mathcal{B}) \times H^{-1}(\mathcal{B})$ such that

$$\begin{aligned} a_1(\delta \mathbf{u}, \Delta \mathbf{u}) + b_1(\delta \mathbf{u}, \Delta \alpha) &= l_u(\delta \mathbf{u}) \\ b_1(\Delta \mathbf{u}, \delta \mathbf{u}) + a_2(\delta \alpha, \Delta \alpha) + b_2(\delta \alpha, \Delta \lambda) &= l_\alpha(\delta \alpha) \\ b_2(\Delta \alpha, \delta \lambda) &= l_\lambda(\delta \lambda) \end{aligned} \quad (9.7)$$

holds for all $(\delta \mathbf{u}, \delta \alpha, \delta \lambda) \in H_0^1(\mathcal{B}; \mathbf{R}^3) \times H_0^1(\mathcal{B}) \times H^{-1}(\mathcal{B})$. The explicit expressions corresponding to all bilinear- and linear forms can be found in appendix A.2. Problem (9.7) can be considered as the two-field mixed formulation

$$\begin{aligned} a_2(\delta \alpha, \Delta \alpha) + b_2(\delta \alpha, \Delta \lambda) &= l_\alpha(\delta \alpha) \\ b_2(\Delta \alpha, \delta \lambda) &= l_\lambda(\delta \lambda) \end{aligned} \quad (9.8)$$

coupled to the weak form of the balance of linear momentum (9.7)₁ via the coupling term b_1 . In what follows some considerations are presented suggesting inf-sup stability of 9.8. In the present case the inf-sup condition (cf. section 2.4) reads

$$\sup_{\alpha \in H_0^1(\mathcal{B}) \setminus \{0\}} \frac{b_2(\alpha, \lambda)}{\|\alpha\|_{H^1}} \gtrsim \|\lambda\|_{H^{-1}} \quad \forall \lambda \in H^{-1}(\mathcal{B}) \quad (9.9)$$

with b_2 defined by $b_2(\alpha, \lambda) := \int_{\mathcal{B}} \lambda \alpha \, dV$. Here, since the bilinear form b_2 is the simple L^2 -scalar product and the H^{-1} -norm is defined as

$$\|\lambda\|_{H^{-1}} = \sup_{\alpha \in H_0^1(\mathcal{B}) \setminus \{0\}} \frac{\int_{\mathcal{B}} \lambda \alpha \, dV}{\|\alpha\|_{H^1}} \quad (\text{cf. (2.50)}), \quad (9.10)$$

the fulfillment of the inf-sup condition is trivial: Inserting (9.10) into (9.9) yields with

$$\sup_{\alpha \in H_0^1(\mathcal{B}) \setminus \{0\}} \frac{b_2(\alpha, \lambda)}{\|\alpha\|_{H^1}} \gtrsim \sup_{\alpha \in H_0^1(\mathcal{B}) \setminus \{0\}} \frac{\int_{\mathcal{B}} \lambda \alpha \, dV}{\|\alpha\|_{H^1}}$$

on both sides the same expression always fulfilling the condition. The proof of the remaining necessary stability conditions (ellipticity and continuity of a_2 on the kernel of b_2 and ellipticity and continuity of a_1) is left for the future. For further reading see BREZZI AND FORTIN [1991] p.44 ff.

9.1.2 Discretizations

Since the solution variables \mathbf{u} and α belong to the standard H^1 -Sobolev spaces Lagrange interpolation functions can be used. Meanwhile, for the Lagrange multiplier λ a piecewise constant interpolation is sufficient. In the following the shape functions and degrees of freedom of the corresponding interpolation functions are presented both for elements T of a tetrahedral mesh \mathcal{T} and for elements T_Q of a hexahedral mesh \mathcal{T}_Q .

Tetrahedral Interpolation The interpolation functions for the displacements $\mathbf{u}^h \in H^1(\mathcal{B}; \mathbf{R}^3) \cap P2(\mathcal{T}; \mathbf{R}^3)$ and the deformation gradient \mathbf{F}^h read for the tetrahedron $T \in \mathcal{T}$

$$\mathbf{u}^h|_T = \sum_{I=1}^{10} \mathbf{d}_I^{(u)} N_I^{(P2)} \quad \text{and} \quad \mathbf{F}^h|_T = \left(\sum_{I=1}^{10} \mathbf{d}_I^{(u)} \otimes \nabla N_I^{(P2)} \right) + \mathbf{1}, \quad (9.11)$$

where $N_I^{(P2)} : T \rightarrow H^1(T) \cap P2(T)$ are the quadratic tetrahedral Lagrange interpolation functions and $\mathbf{d}_I^{(u)} = (d_I^{(u_1)}, d_I^{(u_2)}, d_I^{(u_3)})^T$ denote the standard degrees of freedom $d_I^{(u_i)} : H^1(\mathcal{B}) \rightarrow \mathbf{R}$ giving the values of the components u_i at the corresponding nodes. As also discussed in chapter 5 a necessary condition for rank sufficiency of the resulting finite element tangent matrix is that for any possible mesh configuration the number of degrees of freedom corresponding to α^h surpasses the number of degrees of freedom corresponding to the Lagrange multiplier λ^h (the criterion is also referred to as count criterion). Therefore, in line with BOFFI ET AL. [2013] for the interpolation of the damage variable with $\alpha^h \in H_0^1(\mathcal{B}) \cap (P1(\mathcal{T}) \oplus B4(\mathcal{T}))$ a composition of P1-linear Lagrange functions and the volume bubble Lagrange function is used similar to the elements of chapter 5, just that here the field is scalar valued and not tensor-valued. The interpolation reads

$$\alpha^h|_T = \sum_{I=1}^4 d_I^{(\alpha)} N_I^{(P1)} + d_B^{(\alpha)} N_B^{(P4)} \quad \text{and} \quad \nabla \alpha^h|_T = \sum_{I=1}^4 d_I^{(\alpha)} \nabla N_I^{(P1)} + d_B^{(\alpha)} \nabla N_B^{(P4)} \quad (9.12)$$

with standard linear tetrahedral interpolation functions $N_I^{(P1)} : T \rightarrow H^1(T) \cap P1(T)$ and degrees of freedom $d_I^{(\alpha)} : H^1(\mathcal{B}) \rightarrow \mathbf{R}$ corresponding to the vertex nodes I . Meanwhile, $d_B^{(\alpha)}$ denotes the degree of freedom corresponding to the element center node and the corresponding shape function $N_B^{(P4)} : T \rightarrow H^1(T) \cap P4(T)$ is given by the quartic Lagrange function $N_B^{(P4)} = 1/256 \gamma_1 \gamma_2 \gamma_3 \gamma_4$. The shape function $N_B^{(P4)}$ takes the value 1 at the center node and is zero valued at the boundary of the tetrahedron and thus referred to as “bubble” function. Here, γ_i denote the barycentric coordinates of the tetrahedron. The element-wise constant interpolation of the Lagrange multiplier $\lambda^h \in H^{-1}(\mathcal{B}) \cap P0(\mathcal{T})$ reads

$$\lambda^h|_T = d^{(\lambda)} N^{(P0)}, \quad (9.13)$$

where $d^{(\lambda)} : H^{-1}(\mathcal{B}) \rightarrow \mathbf{R}$ denotes the element-constant degree of freedom and the nodal basis function is $N^{(P0)} = 1$. In what follows the tetrahedral interpolation scheme is denoted by $P2_{\mathbf{u}}\text{-}P1B_{\alpha}\text{-}P0_{\lambda}$. A numerical example evaluating the count criterion of the present formulation can be found in RIESSELMANN AND BALZANI [2023].

Hexahedral Interpolation Analogous to the previous subsection in the following the interpolation functions for hexahedral elements are presented. The hexahedral displacement

interpolations $\mathbf{u}^h \in H^1(\mathcal{B}; \mathbf{R}^3) \cap Q2(\mathcal{T}_Q; \mathbf{R}^3)$ read:

$$\mathbf{u}^h|_{T_Q} = \sum_{I=1}^{27} \mathbf{d}_I^{(u)} N_I^{(Q2)} \quad \text{and} \quad \mathbf{F}^h|_{T_Q} = \left(\sum_{I=1}^{27} \mathbf{d}_I^{(u)} \otimes \nabla N_I^{(Q2)} \right) + \mathbf{1}. \quad (9.14)$$

Here, $N_I^{(Q2)} : T \rightarrow H^1(T_Q) \cap Q2(T_Q)$ are the tri-quadratic hexahedral Lagrange interpolation functions and $d_I^{(u_i)} : H^1(\mathcal{B}) \rightarrow \mathbf{R}$ the components of the degrees of freedom corresponding to the 27 Q2-nodes. The bubble-enriched interpolation of $\alpha^h \in H^1(\mathcal{B}) \cap (Q1(\mathcal{T}_Q) \oplus BQ2(\mathcal{T}_Q))$ is given by

$$\alpha^h|_{T_Q} = \sum_{I=1}^8 d_I^{(\alpha)} N_I^{(Q1)} + d_B^{(\alpha)} N_B^{(Q2)} \quad \text{and} \quad \nabla \alpha^h|_{T_Q} = \sum_{I=1}^8 d_I^{(\alpha)} \nabla N_I^{(Q1)} + d_B^{(\alpha)} \nabla N_B^{(Q2)} \quad (9.15)$$

with the 8 trilinear Lagrange shape functions $N_I^{(Q1)} : T_Q \rightarrow H^1(T_Q) \cap Q1(T_Q)$ and degrees of freedom $d_I^{(\alpha)} : H^1(\mathcal{B}) \rightarrow \mathbf{R}$. In the hexahedral case the volume bubble function $N_B^{(Q2)} : T \rightarrow H^1(T) \cap Q2(T)$ is given by the tri-quadratic Lagrange shape function ($N_B^{(Q2)} \equiv N_{27}^{(Q2)}$)² associated to the center node degree of freedom $d_B^{(\alpha)}$. Unchanged from the tetrahedral case the discrete Lagrange multiplier $\lambda^h \in H^1(\mathcal{B}) \cap P0(\mathcal{T}_Q)$ is element-wise constant with

$$\lambda^h|_{T_Q} = d^{(\lambda)} N^{(P0)}, \quad (9.16)$$

where now the element is a hexahedron and the basis is again $N^{(P0)} = 1$. The tetrahedral interpolation scheme is denoted by Q2_u-Q1B_α-P0_λ.

Discretized Lagrangian Since in the present approach only Lagrange interpolation functions occur, kinematic relations for mapping from the reference element and numerical integration are standard and follow the concepts introduced in section 3.2 (see also ZIENKIEWICZ AND TAYLOR [2000], where also explicit expression for the Lagrange shape functions are provided). For the tetrahedral formulation a four point Gauss integration and for the hexahedral formulation a 27 point Gauss point integration is used. The discretized problem is obtained by inserting the interpolation function into (9.1) giving the discretized Lagrangian

$$\Pi_\lambda^h := \sum_{T \in \mathcal{T}} \left(\int_T \psi^{\text{loc}}(\mathbf{F}^h, \alpha^h) + \frac{c}{2} \nabla \alpha^h \cdot \nabla \alpha^h + \gamma(\alpha^h) + \lambda^h (\alpha^h - \bar{\alpha}^h) \, dV \right) + \Pi_{\text{ext}}^h \quad (9.17)$$

with the discrete external potential Π_{ext}^h defined in (3.66). The tetrahedral formulation and the hexahedral formulation are the same only with the change of notation $T \leftarrow T_Q$ and $\mathcal{T} \leftarrow \mathcal{T}_Q$. Here, $\bar{\alpha}^h$ refers to the control variable (cf. definition (9.4)), whose values in the discrete setting are provided by the Gauss point values of α^h or α_n^h depending on the sign of λ^h (cf. section 9.1.3).

Matrix Notation In the following the notation corresponding to the tangent matrix and residual is presented. Therefore, the following element-wise vectors of degrees of freedom associated to the different solution variables are defined by

$$\underline{\mathbf{d}}_u := [d_1^{(u_1)}, d_1^{(u_2)}, \dots, d_{10}^{(u_2)}, d_{10}^{(u_3)}]^T, \quad \underline{\mathbf{d}}_\alpha := [d_1^{(\alpha)}, \dots, d_4^{(\alpha)}, d_B^{(\alpha)}]^T, \quad \underline{\mathbf{d}}_\lambda := [d^{(\lambda)}]. \quad (9.18)$$

²That is, assuming in the general Q2-interpolation over the 27 Q2-hexahedral nodes the center node has the number $I = 27$.

Define the element degree of freedom vector

$$\underline{\mathbf{d}} := [\underline{\mathbf{d}}_u^T, \underline{\mathbf{d}}_\alpha^T, \underline{\mathbf{d}}_\lambda^T]^T \quad \text{and the global solution vector} \quad \underline{\mathbf{D}} := \bigcup_{T \in \mathcal{T}} \underline{\mathbf{d}}_T, \quad (9.19)$$

with the union operator defined in (3.69). Note that for the sake of simplicity for the expressions of this section whenever the notations $|_T$ and \mathcal{T} appear it is assumed to include both the tetrahedral and the hexahedral case. Following the element residual and tangent matrix definition (3.72) the element sub-residuals are given by

$$\underline{\mathbf{r}}_u := \frac{\partial \Pi^h|_T}{\partial \underline{\mathbf{d}}_u}, \quad \underline{\mathbf{r}}_\alpha := \frac{\partial \Pi^h|_T}{\partial \underline{\mathbf{d}}_\alpha}, \quad \underline{\mathbf{r}}_\lambda := \frac{\partial \Pi^h|_T}{\partial \underline{\mathbf{d}}_\lambda}, \quad (9.20)$$

the element residual by

$$\underline{\mathbf{r}} := [\underline{\mathbf{r}}_u^T, \underline{\mathbf{r}}_\alpha^T, \underline{\mathbf{r}}_\lambda^T]^T \quad \text{and the global residual by} \quad \underline{\mathbf{R}} := \mathbf{A} \underline{\mathbf{r}}|_T, \quad (9.21)$$

with the assembly operator (3.74). The element sub-matrices are given by

$$\underline{\mathbf{k}}_u := \frac{\partial \underline{\mathbf{r}}_u}{\partial \underline{\mathbf{d}}_u}, \quad \underline{\mathbf{k}}_\alpha := \frac{\partial \underline{\mathbf{r}}_\alpha}{\partial \underline{\mathbf{d}}_\alpha}, \quad \underline{\mathbf{k}}_\lambda := \frac{\partial \underline{\mathbf{r}}_\lambda}{\partial \underline{\mathbf{d}}_\lambda}, \quad \underline{\mathbf{k}}_{u\alpha} := \frac{\partial \underline{\mathbf{r}}_u}{\partial \underline{\mathbf{d}}_\alpha}, \quad \underline{\mathbf{k}}_{u\lambda} := \frac{\partial \underline{\mathbf{r}}_u}{\partial \underline{\mathbf{d}}_\lambda}, \quad \text{and} \quad \underline{\mathbf{k}}_{\alpha\lambda} := \frac{\partial \underline{\mathbf{r}}_\alpha}{\partial \underline{\mathbf{d}}_\lambda} \quad (9.22)$$

of which the former three are coupling matrices. The element tangent matrix is symmetric and analogous computations lead to the counterparts of the coupling sub matrices with the relations $\underline{\mathbf{k}}_{u\alpha} = (\underline{\mathbf{k}}_{\alpha u})^T$, $\underline{\mathbf{k}}_{u\lambda} = (\underline{\mathbf{k}}_{\lambda u})^T = \mathbf{0}$, $\underline{\mathbf{k}}_{\alpha\lambda} = (\underline{\mathbf{k}}_{\lambda\alpha})^T$. Moreover, the diagonal sub matrix $\underline{\mathbf{k}}_\lambda = \mathbf{0}$ corresponding to the Lagrange multiplier is zero. The stationary point $\Pi^{\lambda,h} \rightarrow \underset{u^h, \alpha^h, \lambda^h}{\text{stat}}$ corresponds to the solution of the nonlinear problem $\underline{\mathbf{R}} = \mathbf{0}$. At each time interval $[t, t_n]$ the linearized system of equations $\underline{\mathbf{R}}|_i + \underline{\mathbf{K}}|_i \Delta \underline{\mathbf{D}} = \mathbf{0}$ ³ is updated with Newton-Raphson iterations, where i denotes the previous iteration and $\Delta \underline{\mathbf{D}}$ is the solution increment. The linear system of equations expressed in terms of the element sub-matrices reads

$$\mathbf{A} \left(\begin{bmatrix} \underline{\mathbf{k}}_u & \underline{\mathbf{k}}_{u\alpha} & \mathbf{0} \\ \underline{\mathbf{k}}_{\alpha u} & \underline{\mathbf{k}}_\alpha & \underline{\mathbf{k}}_{\alpha\lambda} \\ \mathbf{0} & \underline{\mathbf{k}}_{\lambda\alpha} & \mathbf{0} \end{bmatrix}_i \begin{bmatrix} \Delta \underline{\mathbf{d}}_u \\ \Delta \underline{\mathbf{d}}_\alpha \\ \Delta \underline{\mathbf{d}}_\lambda \end{bmatrix} + \begin{bmatrix} \underline{\mathbf{r}}_u \\ \underline{\mathbf{r}}_\alpha \\ \underline{\mathbf{r}}_\lambda \end{bmatrix}_i \right) = \mathbf{0}. \quad (9.23)$$

where $[\bullet]_i$ denotes the matrix values corresponding to the previous Newton iteration. Following the steps given in appendix B.1 the internal degrees of freedom are statically condensed yielding the reduced system

$$\mathbf{A} \left(\begin{bmatrix} \underline{\mathbf{k}}_u^{**} & \underline{\mathbf{k}}_{u\alpha}^{**} \\ \underline{\mathbf{k}}_{\alpha u}^{**} & \underline{\mathbf{k}}_\alpha^{**} \end{bmatrix}_i \begin{bmatrix} \Delta \underline{\mathbf{d}}_u \\ \Delta \underline{\mathbf{d}}_\alpha \end{bmatrix} + \begin{bmatrix} \underline{\mathbf{r}}_u^{**} \\ \underline{\mathbf{r}}_\alpha^{**} \end{bmatrix}_i \right) = \mathbf{0} \quad (9.24)$$

9.1.3 Algorithmic Treatment

In this section the solution algorithm including the incorporation of the inequality condition for the present approach is discussed. Moreover, an extension of the solution algorithm given in RIESELMANN AND BALZANI [2023] by the element erosion technique (cf. JUNKER ET AL. [2022]) is presented. As shown in algorithm 1, in the time incremental setting, at each time

³The linearized system of equations corresponds to the discretization of (9.7).

Algorithm 1 Solution strategy for each time step $[t_n, t]$

```

initialize  $\underline{D}_u|_0 = \underline{D}_u^n$ ,  $\underline{D}_\alpha|_0 = \underline{D}_\alpha^n$  and  $\underline{D}_\lambda|_0 = \underline{D}_\lambda^n$   $\triangleright$  initialize from previous time step
update  $\mathbf{f} = \mathbf{f}|_t$ ,  $\mathbf{t} = \mathbf{t}|_t$ ,  $\mathbf{u}^B = \mathbf{u}^B|_t$   $\triangleright$  update time-dependent boundary conditions
for  $i = 0, \dots$  do  $\triangleright$  Newton-Iterations
  FE-update  $\underline{D}^{i+1} = \underline{D}^i - (\underline{K}^i)^{-1} \underline{R}^i$   $\triangleright$  solve linear system of equations
  for each Gauss point  $g \in \mathcal{G}|_T$  in each element  $T \in \mathcal{T}$  do
    *apply erosion strategy algorithm 2
     $\bar{\alpha}^h|^{i+1} = \alpha_n^h$   $\triangleright$  turn on constraint
    if  $\lambda^h|^{T,i+1} > 0 \wedge i \neq 1$  then  $\triangleright$  check evolution criterion
       $\bar{\alpha}^h|^{i+1} = \alpha^h|^{i+1}$   $\triangleright$  switch off constraint
    end if
  end for
  if  $\|\underline{D}^{i+1} - \underline{D}^i\| < tol$  then  $\triangleright$  Newton-Iteration exit criterion
    exit
  end if
end for

```

step $t_n \rightarrow t$ after the initialization of the solution values from the previous time step n and update of the boundary conditions, the algorithm enters the Newton-Loop, in which for each iteration $i \rightarrow i + 1$ the global linearized system of equations is solved for the nodal solution vector \underline{D}^{i+1} . After the global update the history variables $\bar{\alpha}^h|^{i+1}$ are updated at each integration as follows:

$$\bar{\alpha}^h|^{i+1} \leftarrow \begin{cases} \alpha_n^h & \text{if } \lambda^h|^{i+1} \leq 0 \quad (\text{no evolution: constraint switched on}) \\ \alpha^h|^{i+1} & \text{if } \lambda^h|^{i+1} > 0 \quad (\text{evolution: constraint switched off}) \end{cases} \quad (9.25)$$

In the first case, with $\lambda^h|^{i+1}(\alpha^h|^{i+1} - \alpha_n^h)$ the constraint is switched on and evolution is suppressed in the upcoming iteration. In the second case, with $\lambda^h|^{i+1}(\alpha^h|^{i+1} - \alpha^h|^{i+1}) = 0$ the constraint is switched off enabling the damage variable to evolve in the upcoming iteration, since the value of the Lagrange multiplier remains fixed. Note, that in the iteration $i = 0$ the constraint term is automatically always switched off ($\lambda^h|_0(\alpha^h|_0 - \bar{\alpha}^h|_0) = \lambda_n^h(\alpha_n^h - \alpha_n^h)$). For $i = 1$ the internal variable is always updated with the first case of (9.25) to enable reactivation of the constraint term (which becomes relevant in the case of transition from damage loading to de-loading). At an example Gauss point, where damage loading ($\lambda_n^h > 0$) occurred in the previous step n , the update sequence reads

$$\lambda_n^h > 0 \quad \begin{array}{c} \xrightarrow{i=0} \\ \text{constraint off} \end{array} \quad \lambda^h|_1 = \lambda_n^h \quad \begin{array}{c} \xrightarrow{i=1} \\ \text{constraint on} \end{array} \quad \begin{cases} \lambda^h|_2 \leq 0 \quad (\text{de-loading, constraint on}) & \xrightarrow{i=3} \dots \\ \lambda^h|_2 > 0 \quad (\text{further loading, constraint off}) & \xrightarrow{i=3} \dots \end{cases} \quad (9.26)$$

Here, the first case depicts the transition to the de-loading state, while the second case depicts further damage loading. Note that, no additional storage space for the history parameter is needed, since with (9.25) in both cases the value of the history parameter is assigned with quantities that are given from the global iterative procedure (α_n^h and $\alpha^h|^{i+1}$). Moreover, while additional computational resources are needed for the numerical evaluation of some trial function Φ as e.g. in LIEBE ET AL. [2001], DIMITRIJEVIC AND HACKL [2008], WAFFENSCHMIDT ET AL. [2013] (see also section 8.3), in the present case the value of $\lambda^h|^{i+1}$ is already given from the global Newton iteration (without increasing the size of the global system due to the static condensation).

Algorithm 2 Element erosion strategy for the proposed $P2_{\mathbf{u}}-P1B_{\alpha}-P0_{\lambda}$ formulation

```

if  $\alpha^{|i+1} > \alpha_{\max}$  then                                ▷ check erosion criterion
    set  $\underline{\mathbf{r}} = \mathbf{0}$                                        ▷ eliminate element residual
    set  $(\underline{\mathbf{k}})_{ij} = \delta_{ij}s_{\text{crit}}$                        ▷ erode element stiffness
    exit                                                         ▷ exit Gauss loop
end if

```

Element Erosion Strategy The present approach is extended by an element erosion strategy (similar to the strategy presented in JUNKER ET AL. [2022]), which enables to model the complete loss of stiffness of the element once a certain maximal damage value is succeeded. Therefore, in the present case, if this feature is switched on, the erosion algorithm 2 is embedded into the element Gauss point loop of algorithm 1 (at the position marked with asterisk). Here, once at one Gauss point of the element the maximal damage value $\alpha^{|i+1} > \alpha_{\max}$ (with α_{\max} being a prescribed model parameter) is surpassed⁴ the element erosion is set to occur for the current element and the Gauss loop exited, moving forward to the next element. The element erosion consists of setting the corresponding element residual vector and tangent matrix to zero. In order to maintain numerical robustness, the value $s_{\text{crit}} = 10\text{e}-10$ is set to remain on the diagonal of the element tangent matrix. Corresponding numerical studies testing the influence of the element erosion technique can be found in sections 9.2.4 and 9.2.5.

9.2 Numerical Results

In this section, the tetrahedral $P2_{\mathbf{u}}-P1B_{\alpha}-P0_{\lambda}$ and the hexahedral $Q2_{\mathbf{u}}-Q1B_{\alpha}-P0_{\lambda}$ finite element discretizations of the gradient damage formulation of the previous section are numerically tested on a variety of boundary value problem settings. The aim is to prove numerical robustness and the ability to avoid mesh-dependency, which appears in simulations using local damage formulations (cf. section 8.1). Further, a comparative study aims to establish the computing efficiency compared to competitive approaches. Moreover, the incorporation of the element erosion technique is analyzed for the proposed approach. Finally, the functionality of the formulation is tested for various parameter ranges. For the following studies the same damage model as given in section 8.1 (i.e. the strain energy $\psi(\mathbf{F}, \alpha)$ given by definition (8.2) and the dissipation function $\gamma(\alpha)$ given in (8.11)) is utilized. The gradient damage formulations are tested on the plate with hole benchmark problem also introduced in section 8.1 (cf. figure 8.1). The geometry, boundary- and local constitutive parameters of the problem are shown in the table (b) of figure 8.1. For the solution of the linearized system of equations a Newton-Raphson solution scheme with the PARDISO linear solver and the Newton exit parameter value $tol = 10^{-8}$ (cf. algorithm 1) is considered.

9.2.1 Convergence Study

For the following study the gradient damage parameter is set to $c = 100$ Nmm, the number of load steps is set to $n_s = 500$ and all further parameters are taken from table 8.1(b). The value of the prescribed displacement u_Y^* increases linearly with each time step until for $n = 500$ the value $u_{Y,\max}^* = 25$ mm is reached. In figure 9.1 the results of the tetrahedral $P2_{\mathbf{u}}-P1B_{\alpha}-P0_{\lambda}$ element and in figure 9.2 the results of the hexahedral $Q2_{\mathbf{u}}-Q1B_{\alpha}-P0_{\lambda}$ element are shown. Figures 9.1 (a)-(b) and 9.2 (a)-(b) present the force displacement curves of the values of the reaction force F_Y recovered from the FE-solution at the upper surface ($Y = L$) over the value

⁴The criterion can with (8.2) be translated to the criterion $D(\alpha^{|i+1}) > D(\alpha_{\max})$.

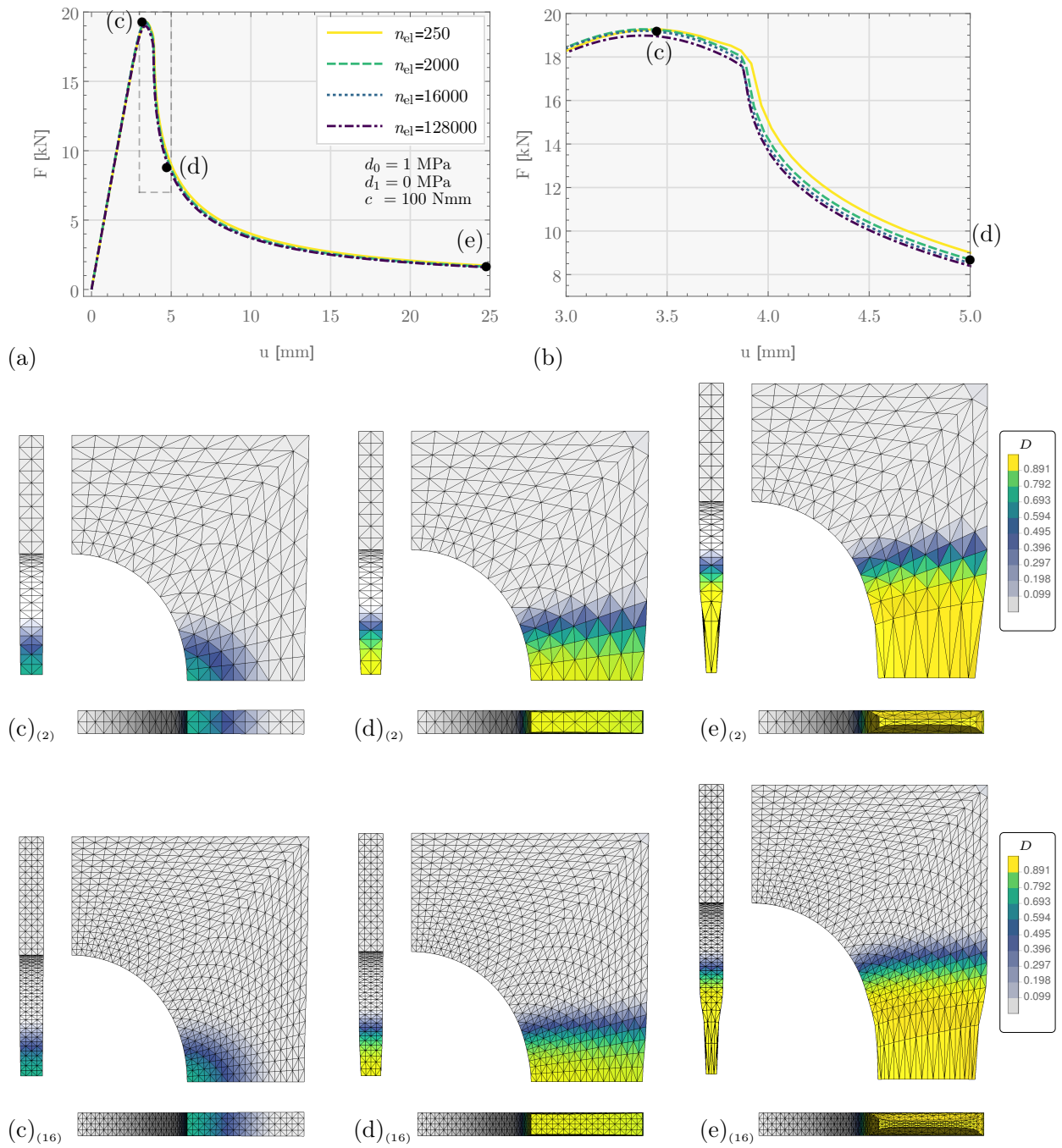


Figure 9.1: Visualization of the mesh independence of the tetrahedral $P2_u$ - $P1B_\alpha$ - $P0_\lambda$ gradient damage formulation with: (a),(b) force displacement curves corresponding to the different mesh refinement stages $n_{el} \in \{250, 2000, 16000, 128000\}$ ((b) shows the enlargement of the transition area framed with a dashed line in (a)). (c)₍₂₎-(e)₍₂₎ show damage contour plots corresponding to the load stages $u_Y^* \in \{3.5, 5, 25\}$ mm (marked with bullets in (a) and (b)) for mesh refinement stage 2 ($n_{el} = 2000$). (c)₍₁₆₎-(e)₍₁₆₎ show damage contour plots corresponding to the same load stages for mesh refinement stage 3 ($n_{el} = 16000$).

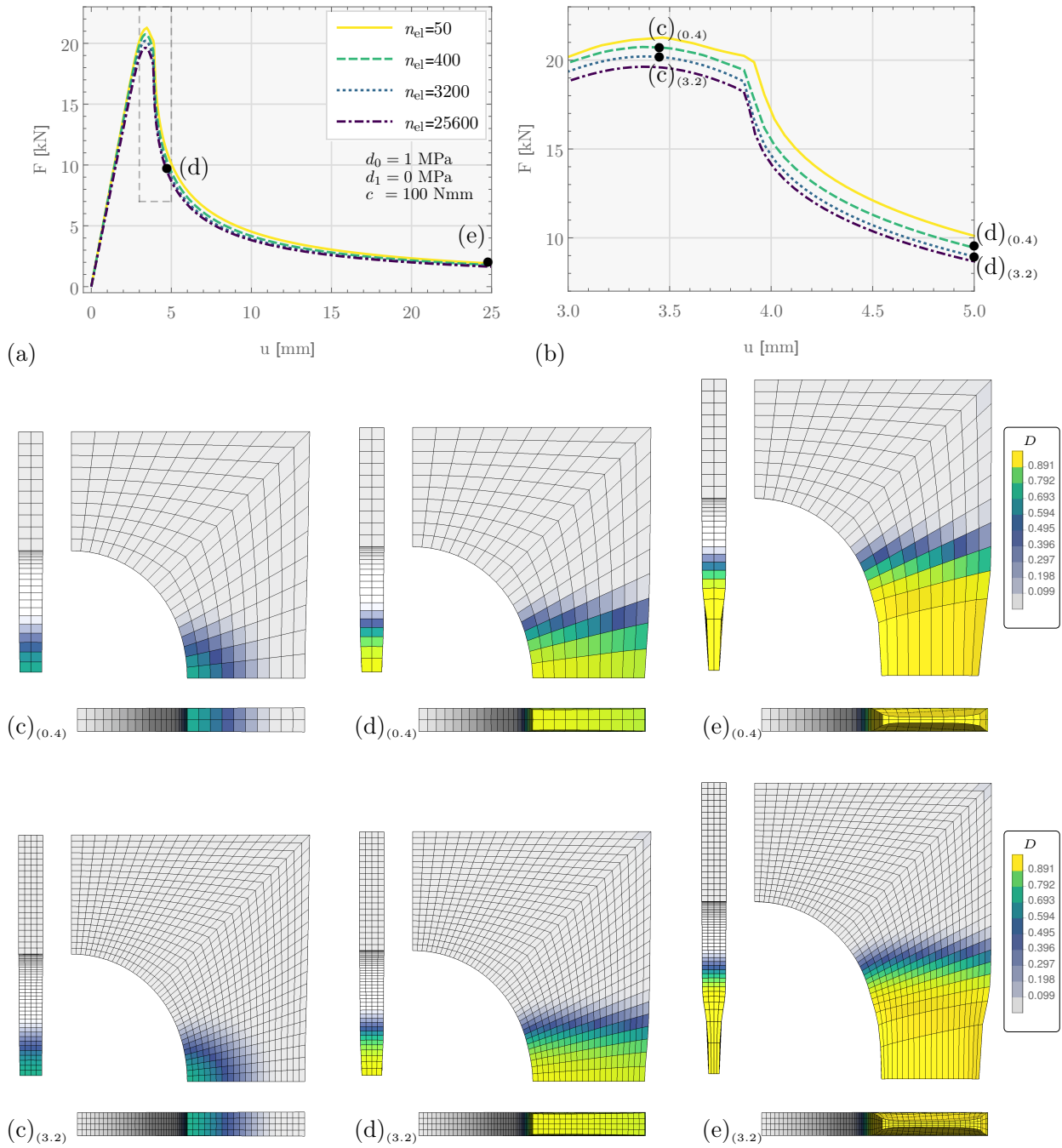


Figure 9.2: Visualization of the mesh independence of the hexahedral $Q2_u$ - $Q1B_\alpha$ - $P0_\lambda$ gradient damage formulation with: (a),(b) force displacement curves corresponding to the different mesh refinement stages $n_{el} \in \{50, 400, 3200\}$ ((b) shows the enlargement of the transition area framed with a dashed line in (a)). (c)₍₂₎-(e)₍₂₎ show damage contour plots corresponding to the load stages $u_{\check{\gamma}}^* \in \{3.5, 5, 25\}$ mm (marked with bullets in (a) and (b)) for mesh refinement stage 2 ($n_{el} = 400$). (c)₍₁₆₎-(e)₍₁₆₎ show damage contour plots corresponding to the same load stages for mesh refinement stage 3 ($n_{el} = 3200$).

of the prescribed displacement u_Y^* . While figures 9.1 and 9.2 (a) depict the results of the entire load spectrum, in figures 9.1 and 9.2 (b) an enlargement of the softening transition area framed with a dashed line in figures (a) is displayed in order to make the convergence behavior of the curves visible. Both in figures 9.1 (a)-(b) and 9.2 (a)-(b) the mesh independence become visible. In fact, for each single curve corresponding to one refinement step, the deviation from the curve of the previous step becomes smaller. Yet, when comparing figures 9.1 (a) and (b) of the tetrahedral element to figures 9.2 (a) and (b) of the hexahedral element it can be observed that for the given meshes the first exhibit slightly superior rates in which the curves converge. This can be explained by the following: In both cases, the number and distribution of vertex nodes is the same for each refinement step. Let us denote the domain enclosed by 8 vertex node by one “cell unit”. While in the hexahedral mesh one “cell unit” is populated by one element, in the corresponding tetrahedral mesh the same cell unit is populated by five elements. Since the Lagrange multiplier is piecewise constant over one element, the resolution of the constraint condition is therefore higher in the tetrahedral mesh than in the hexahedral mesh (cf. RIESELMAANN AND BALZANI [2023]).

Figures 9.1 (c)-(e) and figures 9.2 (c)-(e) show the contour plots visualizing the distribution of the damage field where the value of $\|D(\alpha)\|_{L^2}$ is plotted for each element. Each plot shows a view on the computational domain from the front, from the side and from below. To illustrate the evolution of the damage field the plots from (c) to (e) correspond to the different load stages marked with bullets in figure 9.1 (a)-(b) and 9.2 (a)-(b), respectively. Further, to exemplify the mesh independence by comparing the distribution of the damage field for different refinement steps, in each figure the contour plots are shown for the second and third refinement step, respectively. To be specific, although the resolution of the plots of figure 9.1 (c)₍₂₎-(e)₍₂₎ and figure 9.2 (c)_(0.4)-(e)_(0.4) of the lower refinement stages is of course lower compared to the plots of the higher refinement stages of figure 9.1 (c)₍₁₆₎-(e)₍₁₆₎ and figure 9.2 (c)_(3.2)-(e)_(3.2), respectively, the qualitative distribution is very similar.

9.2.2 Comparative Study

The present study aims to investigate the performance of the $P2_{\mathbf{u}}-P1B_{\alpha}-P0_{\lambda}$ and the $Q2_{\mathbf{u}}-Q1B_{\alpha}-P0_{\lambda}$ element with respect to convergence behavior and computing time compared to an existing penalty approach and a purely elastic reference computation with a standard $P2_{\mathbf{u}}$ Lagrange displacement element. Therefore, the same parameters as in the previous section are used and again a linear increasing load with $u_{Y,\max}^* = 5$ mm is applied. Figure 9.3 (a) shows the total value of the displacement L^2 -norm $\|\mathbf{u}\|_{L^2(\mathcal{T})}$ at the final load stage plotted over the total number of degrees of freedom corresponding to each mesh refinement step. Compared are the proposed formulations with the comparative penalty formulation $P2_{\mathbf{u}}-P1_{\alpha}$ -pen-“X” described in section 8.3.1. Here, “X” denotes the various numerical values of the penalty parameter. From figure 9.3 (a) it can be seen that both the $P2_{\mathbf{u}}-P1B_{\alpha}-P0_{\lambda}$ and the $Q2_{\mathbf{u}}-Q1B_{\alpha}-P0_{\lambda}$ converge towards the same value. Yet, the convergence behavior of the $P2_{\mathbf{u}}-P1B_{\alpha}-P0_{\lambda}$ element is slightly superior to the behavior of the $Q2_{\mathbf{u}}-Q1B_{\alpha}-P0_{\lambda}$ element (cf. discussion of section 9.2.1). Further, as to be expected, for increasing numerical values of the penalty parameter the results of the penalty formulation converge towards the results of the proposed Lagrange multiplier formulations. However, for the penalty formulation, the increased accuracy when using higher penalty values comes at the cost of loss of numerical robustness: In the present problem for numerical values of the penalty parameter $\gtrsim 1000$ the iterative solution procedure fails to converge. Figure 9.3 (b) shows the rates of change of the norm $\|\mathbf{u}\|_{L^2(\mathcal{T})}$ for each refinement step relative to the value of the previous step. Here, the

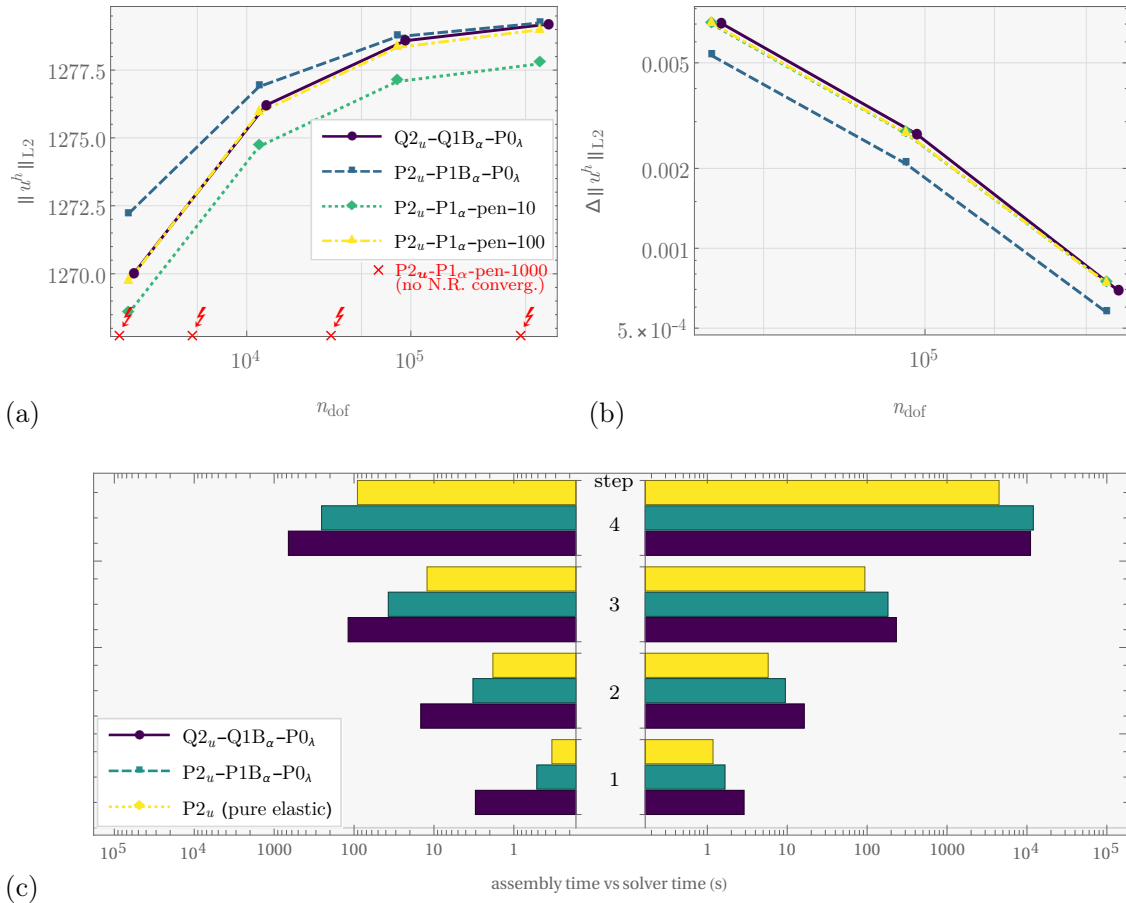


Figure 9.3: Comparative study: (a): Convergence plot of the L^2 -norm $\|\mathbf{u}^h\|_{L^2(\mathcal{T})}$ of the displacement solution over number of degrees of freedom of the $\text{P2}_u\text{-P1B}_\alpha\text{-P0}_\lambda$, $\text{Q2}_u\text{-Q1B}_\alpha\text{-P0}_\lambda$ and the comparative penalty formulation. (b): Rate of change $\Delta\|\mathbf{u}^h\|_{L^2(\mathcal{T})}$ (cf. (9.27)) of the displacement norm over number of degrees of freedom. (c): Total assembly times (left) and solver times (right) of the $\text{P2}_u\text{-P1B}_\alpha\text{-P0}_\lambda$ - and $\text{Q2}_u\text{-Q1B}_\alpha\text{-P0}_\lambda$ - element for each refinement step compared to corresponding times of a purely elastic reference computation. As can be seen from (c), the computational effort is not far from a simple elastic simulation with a standard P2-element.

rate is defined as

$$\Delta \|\mathbf{u}^h\|_{L^2} := \|\mathbf{u}^h\|_{L^2}^{(s+1)} - \|\mathbf{u}^h\|_{L^2}^{(s)}, \quad (9.27)$$

where s denotes the previous mesh refinement step. The results are plotted over the total number of degrees of freedom corresponding to the refinement steps $s + 1 \in \{2, 3, 4\}$. It can be observed that the rates of change tend towards zero indicating mesh convergence for all formulations. Moreover, the slightly superior accuracy of the results of the $P2_{\mathbf{u}}-P1B_{\alpha}-P0_{\lambda}$ becomes visible through the lower rates of change in figure 9.3 (b) compared to the results of the other elements. Finally, the overall computing times of the $P2_{\mathbf{u}}-P1B_{\alpha}-P0_{\lambda}$ - and $Q2_{\mathbf{u}}-Q1B_{\alpha}-P0_{\lambda}$ compared to a purely elastic quadratic tetrahedral Lagrange element (denoted by $P2_{\mathbf{u}}$) is visualized in figure 9.3 (b). Compared are the assembly times (left-hand side) and solution times (right-hand side) for the refinement steps 1-4. The solution times of both the hexahedral and the tetrahedral proposed formulations are not too far from the solution times of the simple purely elastic reference element. Also, assembly times of the tetrahedral $P2_{\mathbf{u}}-P1B_{\alpha}-P0_{\lambda}$ element are in similar orders of magnitude as the assembly times of the elastic reference element. The slightly increased assembly time of the hexahedral $Q2_{\mathbf{u}}-Q1B_{\alpha}-P0_{\lambda}$ element can be attributed to the higher number of Gauss points (i.e. 27 points) compared to the tetrahedral elements. Both the $P2_{\mathbf{u}}-P1B_{\alpha}-P0_{\lambda}$ element and the $P2_{\mathbf{u}}$ elastic element incorporate a four point Gauss integration.

9.2.3 Behavior Under Cyclic Loading

In order to investigate the numerical behavior of the proposed approach under loading-unloading conditions a boundary value problem with the increasing cyclic load function

$$u_Y^*(t) = \frac{t^{0.6} \sin(t) + t^{0.6}}{2(8.5\pi)^{0.6}} u_Y^{*,\max} \quad \text{with } u_Y^{*,\max} = 25 \text{ mm} \quad (9.28)$$

is considered, where $u_Y^*(t)$ is again the prescribed Y -component of the displacement at the upper surface of the geometry (cf. figure 8.1). A plot of the function (9.28) is given in the upper right of figure 9.4 (a). The geometry and material parameters are unchanged from the previous subsections and the tetrahedral $P2_{\mathbf{u}}-P1B_{\alpha}-P0_{\lambda}$ element is used. Figure 9.4 (a) and (b) show the resulting force displacement curves for the various mesh refinement stages for a prescribed number of load steps of $n_s = 500$ and $n_s = 200$, respectively. It can be observed, that the results of (b) corresponding to the coarser load step refinement are qualitatively very similar to the results of the finer load step refinement in (a). For the 200 load step time discretization despite the larger propagation of the solution quantities within one Newton loop, no loss of convergence is observed. In figure 9.4 (c) and (d) the mesh convergence of the total norm $\|\alpha\|_{L^2(\mathcal{T})}$ of the damage variable is plotted for various load step refinements over (c)-the total number of degrees of freedom and (d)-the total computing time. The range of the chosen number of load steps is $n_s \in \{50, 500, 1000, 2000\}$. From (c) it becomes obvious that the results remain independent on the chosen load step refinement. For the load step discretizations $n_s = 500$ and $n_s = 1000$ the deviation

$$\text{relative deviation} = \left| 1 - \frac{(\|\alpha\|_{L^2(\mathcal{T})})_{n_s}}{(\|\alpha\|_{L^2(\mathcal{T})})_{2000}} \right|$$

relative to the converged solution $(\|\alpha\|_{L^2(\mathcal{T})})_{2000}$ of the finest load step discretization is computed. The very small deviation of the numerical values of the results are shown in the upper right-hand side of figure 9.4 (c). Only at the (for the given load scenario impractical) load step resolution of $n_s = 50$ a loss of convergence of the iterative solution procedure for larger

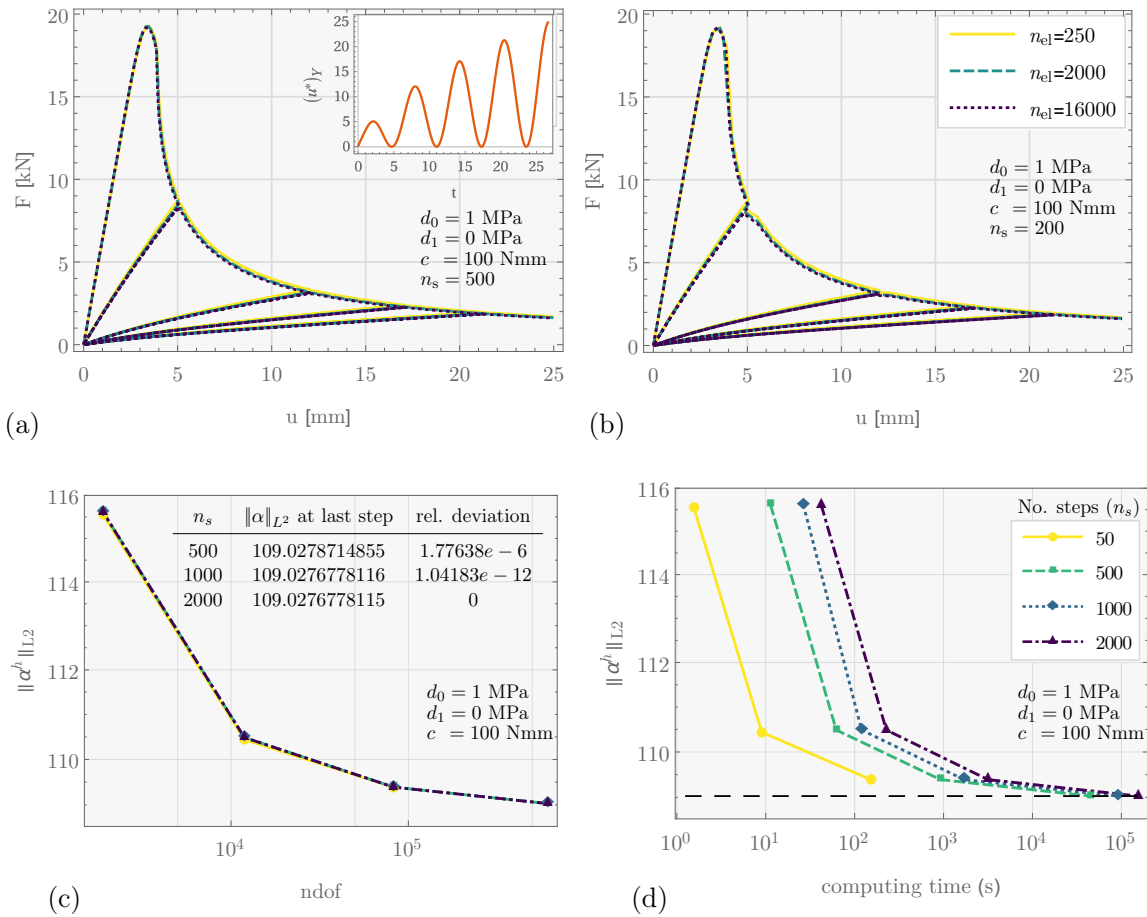


Figure 9.4: Force displacement plots for the cyclic prescribed displacement function (9.28) for varying number of time steps. ((a) $n_s = 500$, (b) $n_s = 200$). As can be seen, the resulting mesh independence turns out to be insensitive to the choice of the time step size. Plot (c) and (d) show for various numbers of time steps the convergence of the L^2 norm of the damage variable $\|\alpha\|_{L^2}$ over total number of degrees of freedom (c) and overall computing time (d), respectively. Again, it becomes visible that the results are almost identical for the various time step refinements. Even for the impractically coarse time refinement $n_s = 50$ results could be obtained, yet for the finest mesh the iterative solution procedure failed to converge.

systems $n_{\text{dof}} > 10^5$ can be observed. The loss of convergence can be attributed to the large jumps of the damage and displacement propagation in each Newton iteration and the more challenging matrix condition numbers of the larger sized systems.

9.2.4 Element Erosion

The study of this subsection aims to investigate the ability of the proposed $P2_{\mathbf{u}}-P1B_{\alpha}-P0_{\lambda}$ formulation to model complete material degradation by incorporation of the element erosion technique described in section 9.1.3. Therefore, a problem setting identical to the convergence study corresponding to figure 9.1 is chosen, but now with element erosion switched on. For the present study the erosion is set to appear once the maximum damage value $D_{\text{max}} = 0.95$ ⁵ is reached. Figure 9.5 (a) and (b) show the resulting force displacement curves, where (b) provides an enlargement of the softening and erosion transition area marked with a dashed line in (a). The corresponding contour plots visualizing both the damage evolution and the element erosion are provided in figures (c)-(d) for meshes corresponding to the second and third refinement step, respectively. Here, the transparent elements correspond to the completely eroded state. Since the propagation of the erosion follows the propagation of the damage evolution, for the present boundary value problem the erosion propagates along the lower boundary, resulting in a complete detachment of the geometry from the boundary. This behavior corresponds to the results of the force displacement curves, where, once the element erosion has propagated, zero resulting reaction forces are computed. Further, in figure (b) when comparing the results corresponding to the finer meshes, it appears that for the present example even with element erosion mesh convergence can be obtained. Yet, for the coarser meshes a deviation of the results in the regime of propagating erosion can be observed. This might be due to the fact that the element size is larger than the domain where D_{max} -values are succeeded yielding non-instantaneous propagation of the erosion. A corresponding observation can be made when comparing the contour plot (d)₍₂₎ to (d)₍₁₆₎ (both corresponding to load stage $u_{\gamma}^* = 5$ mm), where in the first some elements of the row closest to the lower boundary are not eroded completely.

9.2.5 Parameter Study

The plots of figure 9.6 show results of the proposed $P2_{\mathbf{u}}-P1B_{\alpha}-P0_{\lambda}$ formulation for a variation of parameters. Shown are force displacement curves for a linear increasing loading scenario as in the previous subsection. The mesh size for all curves corresponds to $n_{\text{el}} = 16000$ elements and a time discretization with $n_s = 500$ load steps. First, in order to investigate the functionality of the approach for a variation of the local damage parameters, in figures 9.6 (a) and (b) the results for the parameter ranges $(d_0, d_1) \in \{0.5, 1, 2, 4\}$ MPa are shown. For the chosen nonlocal parameter $c = 100$ Nmm for all variations of d_0 and d_1 the formulation remains robust and convergence of the solution procedure can be observed. In order to analyze the behavior with respect to varying values of the nonlocal parameter for the results in figure 9.6 (c) parameters $c \in \{50, 100, 200, 400\}$ Nmm are used. Here, the regularizing effect of the nonlocal parameter becomes clear: As the value of the nonlocal parameter c increases, the softening occurs less rapidly ie. the slope in the softening regime of the curves of figure (c) decreases. This corresponds to the fact that for higher values of c the penalization of the gradient $\nabla\alpha$ is stronger leading to a more distributed but less rapid damage propagation as the load increases. On the other hand, once the degree of regularization becomes small, the

⁵Correspondingly, the threshold parameter in algorithm 1 is set to $\alpha_{\text{max}} = -\ln(1 - 0.95)$.

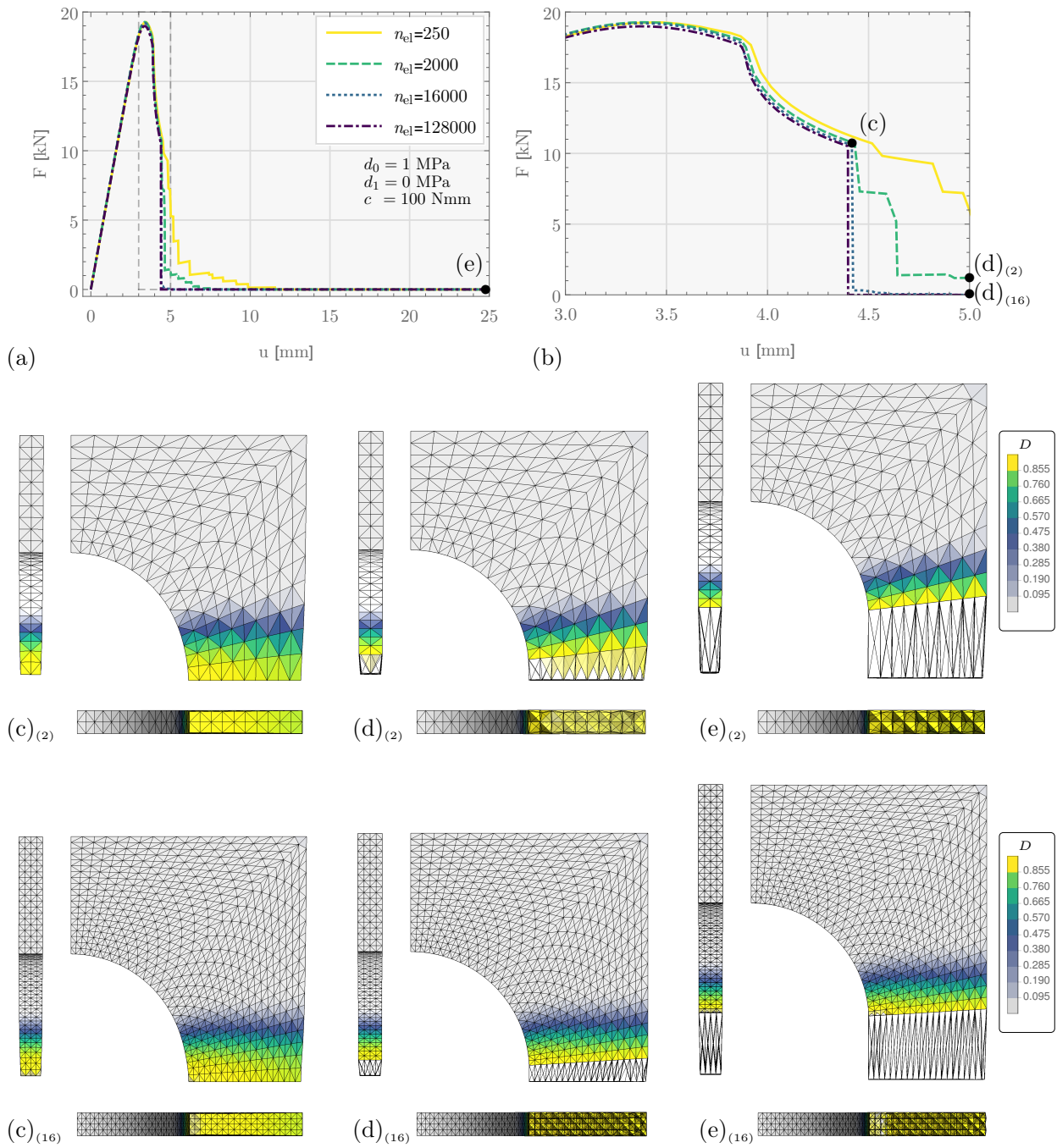


Figure 9.5: Visualization of the mesh independence of the $P2_{\mathbf{u}}\text{-}P1B_{\alpha}\text{-}P0_{\lambda}$ element with erosion (cf. section 9.1.3). Plots (a) and (b) show force displacement curves corresponding to the different mesh refinement stages ($n_{el} \in \{250, 2000, 16000, 128000\}$) (figure (b) shows the enlargement of the transition area framed with a dashed line in (a)). $(c)_{(2)}\text{-}(e)_{(2)}$ show damage contour plots corresponding to the load stages $u_Y^* \in \{4.42, 5, 25\}$ mm (marked with bullets in (a) and (b)) for mesh refinement stage 2 ($n_{el} = 2000$). $(c)_{(16)}\text{-}(e)_{(16)}$ show damage contour plots corresponding to the same load stages for mesh refinement stage 3 ($n_{el} = 16000$).

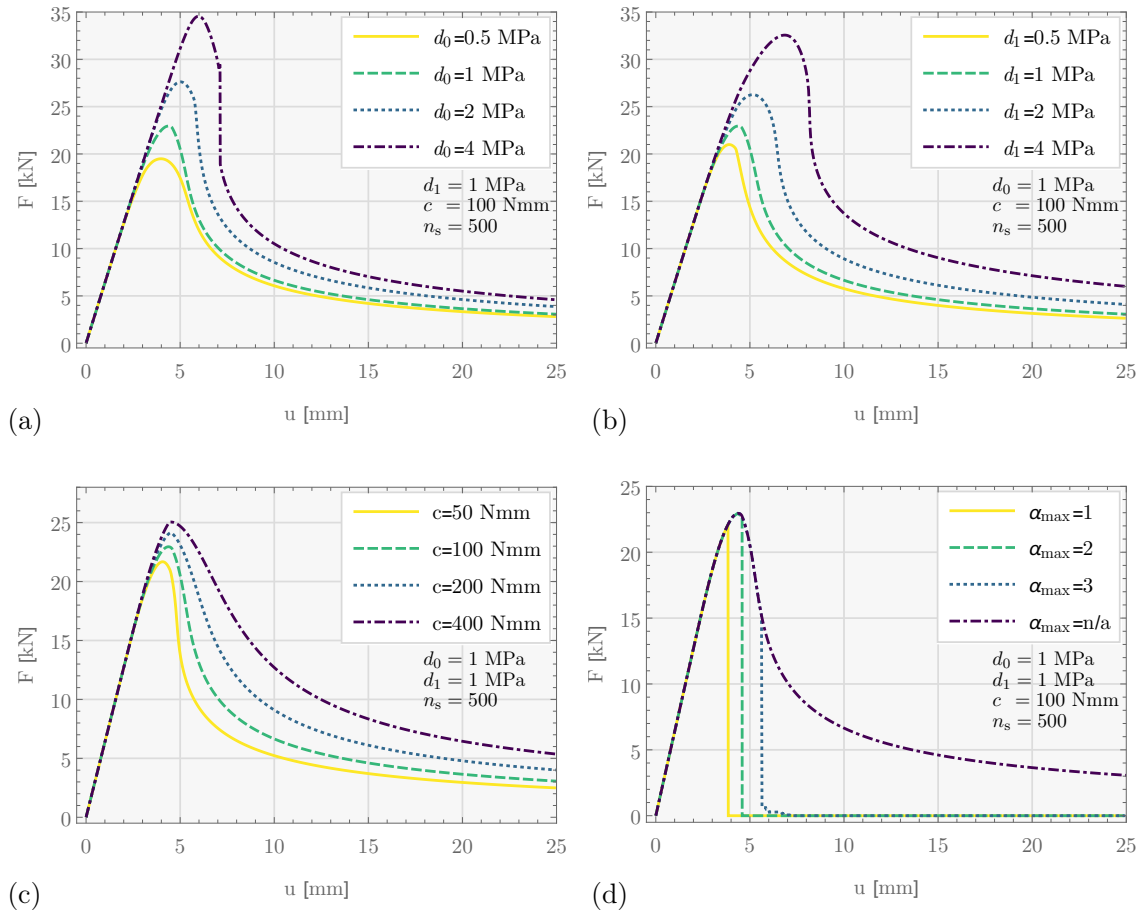


Figure 9.6: Force displacement plots of the $P2_u$ - $P1B_\alpha$ - $P0_\lambda$ element for various parameter ranges: Plots (a) and (b) show results for varying values of the local damage parameters d_0 and d_1 , respectively. Plot (c) shows results for varying values of the nonlocal parameter c . For plot (d) the element erosion is switched on. The plot shows results for various threshold parameter values for which the erosion is set to occur. Here, the threshold values of the damage variable $\alpha_{\max} \in \{1, 2, 3\}$ correspond to maximal values $D_{\max} \in \{0.632, 0.865, 0.950\}$ of the damage field. All curves correspond to a mesh with $n_{el} = 16000$ elements (i.e. the third refinement step of previous studies).

formulation approaches the purely local formulation (cf. section 8.1) and correspondingly shows loss of numerical robustness. For the present parameter setting a loss of robustness of the solution procedure is observed for values going below $c = 10 \text{ Nmm}$. Lastly, for the parameter study of figure 9.6 (d) the element erosion technique (cf. algorithm 1) is activated. The plot shows the force displacement curves for a variation of the threshold parameters $\alpha_{\max} \in \{1, 2, 3\}$ at which the erosion in the element is set to occur. With the conversion according to (8.2) the threshold parameters correspond to activation of the erosion at the damage percentages of $D_{\max} = 63.2\%$, 86.5% and 95.0% , respectively. Here, models with lower numerical values of the parameter α_{\max} correspond to material responses which account for less softening until failure and vice versa. Accordingly, in the force displacement curves of figure 9.6 (d) the lower the value of α_{\max} the lower the load stage at which the reaction force jumps to zero due to the element erosion. For the present parameter variations, the propagation of the erosion of the elements (see also the contour plots of figure 9.5 (c)₍₁₆₎- (e)₍₁₆₎) occurs almost instantaneous. Yet, no loss of convergence of the solution procedure is observed for the present choices of α_{\max} .

Treatise Conclusion and Outlook

Conclusion and Outlook

The present work dealt with the development of mixed finite element formulations for gradient enhanced elasticity and gradient enhanced damage models. The main focus was to establish formulations that ensure numerical robustness and cost efficiency. Therefore, various mixed formulations and corresponding suitable numerical approximation schemes were proposed that keep computation cost low while possessing numerical stability. The proposed formulations were numerically tested on various benchmark problems, confirming the stability in terms of convergence, numerical robustness and relative computing efficiency.

Part I of this thesis was focused on finite element formulations for gradient elasticity. Firstly, the original displacement based formulation and some challenges of corresponding fully C^1 continuous primal formulations were illustrated. Then, in the following chapter, various mixed three field formulations that allow for much simpler C^0 continuous approximations have been presented. For each formulation, some investigation regarding consistency with the original problem as well as stability was provided. Moreover, suitable approximation schemes that allow for static condensation while keeping the number of degrees of freedom at a minimum were proposed. In addition to that, in the subsequent chapter the so called RotFEM approach was presented. The special feature of this formulation is the incorporation of a mixed rotation-free variable associated to the displacement gradients. This enables for a set of variational equations in which the displacements are decoupled from the main problem and thereby reduce the size of the problem. Moreover, the corresponding linearized formulation has been shown to fulfill the relevant stability conditions both in the continuous and the presented discrete framework, promising numerical robustness. Finally, the stability, robustness and efficiency of the proposed formulations were verified on several numerical tests on various benchmark problems. Remarkably, for some of the three field formulations (cf. figure 7.8) computing times could be achieved that are not far off the times of simple standard local elasticity elements.

Yet, future research efforts could extend the approximation schemes of the additional surface terms, which were proposed in RIESELMANN ET AL. [2024] for the framework of the symmetric three field formulation, to all proposed formulations as these surface terms may further enhance the convergence behavior for special configurations of higher order boundary conditions. Another area of interest of future research efforts could be to find specialized interpolation schemes for the mixed variable that are by design rotation free and symmetric. Corresponding schemes could be applicable to both the three field approaches and the RotFEM approach, might eliminate the necessity of the rot-rot stabilization and in the case of the RotFEM approach even entirely remove the need for Lagrange multipliers in the main problem. However, the construction of corresponding schemes is not trivial and might require again higher order polynomials. See e.g. the approach of ARNOLD ET AL. [2008] which introduces a suitable approximation scheme of symmetric tensors in $H(\text{Div}; \mathcal{B}; \mathbb{S})$. In the context of the RotFEM formulation another remaining challenge is the applicability to problems with

non-connected Dirichlet conditions and the fact that information about the constant parts of prescribed displacement functions on the boundary does (without modification) not enter the main problem. Here, a remedy could be the incorporation of additional line integral terms connecting the boundaries and carrying information about the missing constant parts.

Part II of this work was concerned with mixed finite element formulations for gradient damage. Therefore, firstly the comparative formulations, namely the penalty approach and the neighbored element approach have been presented and some challenges of the penalty approach have been illustrated. In the following chapter an efficient mixed formulation has been presented, which ensures compatibility between the nodal damage variable and a local variable through a Lagrange multiplier constraint eliminating the need for a penalty term while providing more accurate solutions. The key aspect of this constraint term lies in the integration of the damage evolution inequality conditions. By utilizing the Lagrange multiplier value to distinguish between damage loading and unloading scenarios, along with updating a local variable, the no-healing inequality has effectively been incorporated. This proposed method offers the advantage of not requiring additional computational resources for evaluating the evolution/no-evolution condition and storing history parameter values, as these quantities are already available from the global iterative solution process. Through volume-bubble-enhanced interpolation of the damage variable, an approximation scheme that provides rank-sufficient tangent matrices for piecewise constant Lagrange multipliers has been proposed. The proposed approach has been accompanied by a stability analysis of the corresponding linear system indicating inf-sup stability. Additionally, the discretization allows for static condensation, resulting in a positive symmetric global matrix with a reduced number of equations, similar to competitive penalty methods. Numerical tests of the proposed approach have shown mesh-independent solutions, robustness of the solution procedure for states of severe damage and under cyclic loading conditions. Worth mentioning are the computing times that in the numerical studies have been observed to be in the same order of magnitude as purely elastic computations. Moreover, the integration of a method for element erosion to account for complete failure has been discussed and accompanied by numerical outcomes demonstrating mesh convergence, further validating the reliability of the proposed approach.

Possible future research efforts in the context of the proposed gradient damage formulation could further explore various suitable pairings of higher order interpolation schemes together with higher order integration schemes in order to increase the resolution of the damage field and corresponding points of evaluation of the evolution criterion. This might be especially of interest when applying the approach to phase-field type of models by providing the possibility for p-adaptive refinement schemes in intricate subdomains of the geometry, e.g. in the vicinity of crack tips. In this context, also a comparison with h-adaptive schemes might be worth investigating. Of course, corresponding studies would have to include a comparison of computing efficiency to establish if possible trade-offs with respect to cost increase are feasible. Moreover, model extensions in order to account for plasticity could also be considered.

Appendix

Appendix A

Continuous Expressions

A.1 Continuous Gradient Elasticity Formulations

In order to shorten the expressions in what follows, the L^2 product over the volume, surface and edge is denoted by

$$\int_{\mathcal{B}} \bullet \cdot \blacksquare \, dV := \langle \bullet, \blacksquare \rangle \quad \sum_i^3 \int_{\Gamma^{(i)}} (\bullet)_i (\blacksquare)_i \, dA := \langle\langle \bullet, \blacksquare \rangle\rangle_{\Gamma} \quad \text{and} \quad \sum_i^3 \int_{\Upsilon^{(i)}} (\bullet)_i (\blacksquare)_i \, dA := \langle\langle\langle \bullet, \blacksquare \rangle\rangle\rangle_{\Upsilon} \quad (\text{A.1})$$

respectively. Here, $\Gamma^{(i)} \in \{\Gamma_{\text{D}}^{(i)}, \Gamma_{\text{H}}^{(i)}, \Gamma_{\text{N}}^{(i)}, \Gamma_{\text{M}}^{(i)}\}$ is a placeholder for any surface subdomain. For the sake of readability, a simplified notation is used, which implies the sum of the surface subdomain integrals corresponding to the three coordinate components i (cf. section 4.1). If the entire surface $\Gamma = \partial\mathcal{B}$ is considered, the subscript is omitted. Thus, the variational equation corresponding to the original problem (4.4) reads

$$\langle \mathbf{P}, \nabla \delta \mathbf{u} \rangle + \langle \mathbf{G}, \nabla \nabla \delta \mathbf{u} \rangle + \delta \Pi^{\text{ext}} = 0 \quad \text{with} \quad (\text{A.2})$$

$$\delta \Pi^{\text{ext}} := -\langle \mathbf{f}, \delta \mathbf{u} \rangle - \langle\langle \mathbf{t}, \delta \mathbf{u} \rangle\rangle_{\Gamma_{\text{N}}} - \langle\langle \mathbf{r}, \nabla \delta \mathbf{u} \cdot \mathbf{n} \rangle\rangle_{\Gamma_{\text{M}}} - \langle\langle\langle \mathbf{l}, \delta \mathbf{u} \rangle\rangle\rangle_{\Upsilon_{\text{N}}}$$

where the stress tensors \mathbf{P} and \mathbf{G} are defined in (7.3). Following the steps of integrating by parts and application of Stoke's theorem (for details see MINDLIN [1964]) yields the corresponding Euler-Lagrange equations

$$\begin{aligned} -\text{Div } \mathbf{P} + \text{Div Div } \mathbf{G} &= \mathbf{f} && \text{in } \mathcal{B} \\ (\mathbf{P} \cdot \mathbf{n} + (\text{Div}_{\Gamma} \mathbf{n}) \mathbf{G} : (\mathbf{n} \otimes \mathbf{n}) - \text{Div}_{\Gamma}(\mathbf{G} \cdot \mathbf{n}) - (\text{Div } \mathbf{G}) \cdot \mathbf{n} &= \mathbf{t})_i && \text{on } \Gamma_{\text{N}}^{(i)} \\ ([\mathbf{G} : (\mathbf{m} \otimes \mathbf{n})]_{\Upsilon} = \mathbf{l})_i &&& \text{on } \Upsilon_{\text{N}}^{(i)} \\ (\mathbf{G} : (\mathbf{n} \otimes \mathbf{n}) = \mathbf{r})_i &&& \text{on } \Gamma_{\text{M}}^{(i)} \\ (\mathbf{u} = \mathbf{u}^*)_i &&& \text{on } \Gamma_{\text{D}}^{(i)} \\ (\nabla \mathbf{u} \cdot \mathbf{n} = \mathbf{h}^*)_i &&& \text{on } \Gamma_{\text{H}}^{(i)} \end{aligned} \quad (\text{A.3})$$

where Υ denotes the surface tangential vector pointing in the direction normal to the edge Υ and $[\bullet]$ denotes the difference between the values of the neighboring surfaces across the edge (cf. MINDLIN [1964], see also RIESELDMANN ET AL. [2024]). Meanwhile, making use of the concepts introduced in section 2.3.3 and for the sake of simplicity assuming pure Dirichlet boundary conditions for the linearization of (A.2) the bilinear form

$$a(\nabla \delta \mathbf{u}, \nabla \Delta \mathbf{u}) := \langle \nabla \delta \mathbf{u}, \mathbb{C} : \nabla \Delta \mathbf{u} \rangle + \langle \nabla \nabla \delta \mathbf{u}, \mathbb{L} \dot{;} \nabla \nabla \Delta \mathbf{u} \rangle \quad (\text{A.4})$$

can be defined, where $\Delta \mathbf{u}$ are small displacement increments, $\mathbb{C} = \mathbb{C}|_i := \partial_{\nabla \mathbf{u}} \mathbf{P}|_i$ and $\mathbb{L} = \mathbb{L}|_i := \partial_{\nabla \nabla \mathbf{u}} \mathbf{G}|_i$ are first and second order tangent operators, respectively and i refers to values of the previous Newton iteration. For the commonly used elastic energy functions, the symmetries $(\mathbb{C})_{ijkl} = (\mathbb{C})_{jilk}$ can be assumed. Therefore, due to the symmetrizing effect of \mathbb{C} the bilinear form (A.4) can together with the linear form equivalently be written as

$$\begin{aligned} a(\nabla \delta \mathbf{u}, \nabla \Delta \mathbf{u}) &:= \langle \text{sym } \nabla \delta \mathbf{u}, \mathbb{C} : \text{sym } \nabla \Delta \mathbf{u} \rangle + \langle \nabla \nabla \delta \mathbf{u}, \mathbb{L} : \nabla \nabla \Delta \mathbf{u} \rangle \\ l(\delta \mathbf{u}) &:= \langle \mathbf{f}, \delta \mathbf{u} \rangle - \langle \nabla \delta \mathbf{u}, \mathbf{P}|_i \rangle - \langle \nabla \nabla \delta \mathbf{u}, \mathbf{G}|_i \rangle \end{aligned} \quad (\text{A.5})$$

The linearized problem corresponding to (A.2) is given in section 6.1.5

A.1.1 Formulations Corresponding to Section 5.1.1

In the following, the explicit expressions of the variational equation corresponding to problem (5.2) are given and equivalence to the original problem is shown. Therefore, due to the existence of the Dirichlet boundary conditions (5.5) and (5.6) only the components of Π_Γ of (5.4) that do not belong to the Dirichlet boundaries (5.5) and (5.6) are considered yielding the following explicit expressions:

$$\begin{aligned} \langle \bar{\mathbf{G}} \cdot \mathbf{n}, \nabla \mathbf{u} \rangle &\Rightarrow \langle \bar{\mathbf{G}} \cdot \mathbf{n}, \nabla_\Gamma \mathbf{u} \rangle_{\Gamma_N} + \langle \bar{\mathbf{G}} : (\mathbf{n} \otimes \mathbf{n}), \nabla \mathbf{u} \cdot \mathbf{n} \rangle_{\Gamma_M} \\ \langle \bar{\mathbf{G}} \cdot \mathbf{n}, \mathbf{H} \rangle &\Rightarrow \langle \bar{\mathbf{G}} \cdot \mathbf{n}, (\mathbf{H})^{(t)} \rangle_{\Gamma_N} + \langle \bar{\mathbf{G}} : (\mathbf{n} \otimes \mathbf{n}), \mathbf{H} \cdot \mathbf{n} \rangle_{\Gamma_M} \end{aligned} \quad (\text{A.6})$$

where \mathbf{H} and $\nabla \mathbf{u}$ have been decomposed into surface normal and surface tangential components according to (2.15) and (2.20), respectively¹. Variation of (5.1) leads to the following set of equations

$$\begin{aligned} \langle \mathbf{P}^{\text{loc}}, \nabla \delta \mathbf{u} \rangle - \langle \mathbf{\Lambda}, \nabla \delta \mathbf{u} \rangle + \langle \bar{\mathbf{G}} \cdot \mathbf{n}, \nabla_\Gamma \delta \mathbf{u} \rangle_{\Gamma_N} + \langle \bar{\mathbf{G}} : (\mathbf{n} \otimes \mathbf{n}), \nabla \delta \mathbf{u} \cdot \mathbf{n} \rangle_{\Gamma_M} + \delta_{\mathbf{u}} \Pi_{\text{ext}} &= 0 \\ \langle \mathbf{P}^{\text{nloc}}, \delta \mathbf{H} \rangle + \langle \bar{\mathbf{G}}, \nabla \delta \mathbf{H} \rangle + \langle \mathbf{\Lambda}, \delta \mathbf{H} \rangle - \langle \bar{\mathbf{G}} \cdot \mathbf{n}, (\delta \mathbf{H})^{(t)} \rangle_{\Gamma_N} - \langle \bar{\mathbf{G}} : (\mathbf{n} \otimes \mathbf{n}), \delta \mathbf{H} \cdot \mathbf{n} \rangle_{\Gamma_M} \\ + \langle \delta \bar{\mathbf{G}} \cdot \mathbf{n}, \nabla_\Gamma \mathbf{u} - (\mathbf{H})^{(t)} \rangle_{\Gamma_N} + \langle \delta \bar{\mathbf{G}} : (\mathbf{n} \otimes \mathbf{n}), (\nabla \mathbf{u} \cdot \mathbf{n} - \mathbf{H} \cdot \mathbf{n}) \rangle_{\Gamma_M} + \delta_{\mathbf{H}} \Pi_{\text{rot}} &= 0 \\ \langle \delta \mathbf{\Lambda}, \mathbf{H} - \nabla \mathbf{u} \rangle &= 0 \end{aligned} \quad (\text{A.7})$$

With $\mathbf{P}^{\text{loc}} := \partial_{\nabla \mathbf{u}} \psi^{\text{loc}}$, $\mathbf{P}^{\text{nloc}} := \partial_{\mathbf{H}} \psi^{\text{nloc}}$ and $\mathbf{P} = \mathbf{P}^{\text{loc}} + \mathbf{P}^{\text{nloc}}$ accounting for nonlocal components of the first order stress tensor (cf. section 7.1). The following argumentation shows that the solution \mathbf{H} that solves (A.7)₃ for any $\delta \mathbf{\Lambda} \in H^{-1}(\mathcal{B}; \mathbb{R}^{3 \times 3})$ is rotation-free ($\text{Rot } \mathbf{H} = \mathbf{0}$). With the Helmholtz decompositions, splitting any L^2 function into a rotation and a gradient part (cf. SCHEDENSACK [2015]) $\delta \mathbf{\Lambda} = \text{Rot } \delta \tilde{\mathbf{\Lambda}} + \nabla \delta \tilde{\boldsymbol{\lambda}}$ and $\mathbf{H} = \text{Rot } \tilde{\mathbf{H}} + \nabla \tilde{\mathbf{h}}$ equation (A.7)₃ reads

$$\langle \delta \mathbf{\Lambda}, \mathbf{H} - \nabla \mathbf{u} \rangle = \langle \text{Rot } \delta \tilde{\mathbf{\Lambda}} + \nabla \delta \tilde{\boldsymbol{\lambda}}, \text{Rot } \tilde{\mathbf{H}} + \nabla \tilde{\mathbf{h}} - \nabla \mathbf{u} \rangle = \langle \text{Rot } \delta \tilde{\mathbf{\Lambda}}, \text{Rot } \tilde{\mathbf{H}} \rangle + \langle \nabla \delta \tilde{\boldsymbol{\lambda}}, \nabla \tilde{\mathbf{h}} - \nabla \mathbf{u} \rangle.$$

(Recall the identity (2.26)). Moreover, due to the orthogonality (2.26) of rotations and gradients both terms on the right-hand side of the previous equation must vanish independently. In other words, the solution \mathbf{H} must be such that the term $\langle \text{Rot } \delta \tilde{\mathbf{\Lambda}}, \text{Rot } \tilde{\mathbf{H}} \rangle$ vanishes, which is only the case for any $\delta \mathbf{\Lambda}$ if (with $\langle \text{Rot } \delta \tilde{\mathbf{\Lambda}}, \text{Rot } \tilde{\mathbf{H}} \rangle \Rightarrow \langle \delta \tilde{\mathbf{\Lambda}}, \text{Rot } \text{Rot } \tilde{\mathbf{H}} \rangle$ after applying the divergence theorem) $\text{Rot } \text{Rot } \tilde{\mathbf{H}} = \text{Rot } \mathbf{H}$ vanishes. Therefore, the term $\delta_{\mathbf{H}} \Pi_{\text{rot}} = 0$ does not

¹Note the relation $\langle \bar{\mathbf{G}} \cdot \mathbf{n}, (\bullet)^{(n)} \rangle = \langle \bar{\mathbf{G}} : (\mathbf{n} \otimes \mathbf{n}), (\bullet) \cdot \mathbf{n} \rangle$ (verifiable via index notation).

affect the continuous solution² and can be omitted in the following expressions. With the integration by parts formula

$$\langle \bar{\mathbf{G}}, \nabla \delta \mathbf{H} \rangle = -\langle \text{Div } \bar{\mathbf{G}}, \delta \mathbf{H} \rangle + \langle \langle \bar{\mathbf{G}} \cdot \mathbf{n}, (\delta \mathbf{H})^{(t)} \rangle \rangle_{\Gamma_N} + \langle \langle \bar{\mathbf{G}} : (\mathbf{n} \otimes \mathbf{n}), \delta \mathbf{H} \cdot \mathbf{n} \rangle \rangle_{\Gamma_M} \quad (\text{A.8})$$

(here, under the consideration of the Dirichlet conditions $(\delta \mathbf{H})^{(t)} = \mathbf{0}$ on Γ_D and $(\delta \mathbf{H})^{(n)} = \mathbf{0}$ on Γ_H) equation (A.7)₂ can be written as

$$\begin{aligned} \langle \mathbf{P}^{\text{nlloc}}, \delta \mathbf{H} \rangle - \langle \text{Div } \bar{\mathbf{G}}, \delta \mathbf{H} \rangle + \langle \mathbf{\Lambda}, \delta \mathbf{H} \rangle + \langle \langle \delta \bar{\mathbf{G}} \cdot \mathbf{n}, \nabla_{\Gamma} \mathbf{u} - (\mathbf{H})^{(t)} \rangle \rangle_{\Gamma_N} \\ + \langle \langle \delta \bar{\mathbf{G}} : (\mathbf{n} \otimes \mathbf{n}), (\nabla \mathbf{u} \cdot \mathbf{n} - \mathbf{H} \cdot \mathbf{n}) \rangle \rangle_{\Gamma_M} = 0, \end{aligned} \quad (\text{A.9})$$

since the fourth and fifth term of (A.7)₂ cancel out with the second and third term of (A.8). In the following (analogously to RIESELNANN ET AL. [2019], Lemma 1 but with consideration of the surface terms) it is shown that for every solution $\mathbf{u} \in \mathcal{U}$ to (A.2) there exists a $(\mathbf{H}, \mathbf{\Lambda})$ such that (A.7) holds. Conversely, if $(\mathbf{u}, \mathbf{H}, \mathbf{\Lambda})$ is a solution to (A.7) then \mathbf{u} coincides with the solution of (A.2) and is in the space \mathcal{U} (cf. (4.5)).

Proof. First it is shown that for $\mathbf{H} = \nabla \mathbf{u}$ (and therefore $\bar{\mathbf{G}} := \partial_{\nabla \mathbf{H}} \psi = \partial_{\nabla \nabla \mathbf{u}} \psi =: \bar{\mathbf{G}}$) problem (A.7) is identical to problem (A.3). Inserting $\mathbf{H} = \nabla \mathbf{u}$ into (A.9) makes the last two terms vanish giving

$$\langle \mathbf{P}^{\text{nlloc}}, \delta \mathbf{H} \rangle - \langle \text{Div } \mathbf{G}, \delta \mathbf{H} \rangle + \langle \mathbf{\Lambda}, \delta \mathbf{H} \rangle = 0$$

which holds only true if $-\mathbf{P}^{\text{nlloc}} + \text{Div } \mathbf{G} = \mathbf{\Lambda}$ in \mathcal{B} . Inserting this result into (A.7)₁ yields with $\mathbf{P} = \mathbf{P}^{\text{loc}} + \mathbf{P}^{\text{nlloc}}$

$$\langle \mathbf{P}, \nabla \delta \mathbf{u} \rangle - \langle \text{Div } \mathbf{G}, \nabla \delta \mathbf{u} \rangle + \langle \langle \mathbf{G} \cdot \mathbf{n}, \nabla_{\Gamma} \delta \mathbf{u} \rangle \rangle_{\Gamma_N} + \langle \langle \mathbf{G} : (\mathbf{n} \otimes \mathbf{n}), \nabla \delta \mathbf{u} \cdot \mathbf{n} \rangle \rangle_{\Gamma_M} + \delta \Pi_{\text{ext}} = 0$$

Now, inserting the integration by parts formula

$$-\langle \text{Div } \mathbf{G}, \nabla \delta \mathbf{u} \rangle = \langle \mathbf{G}, \nabla \nabla \delta \mathbf{u} \rangle - \langle \langle \mathbf{G} \cdot \mathbf{n}, \nabla_{\Gamma} \delta \mathbf{u} \rangle \rangle_{\Gamma_N} - \langle \langle \mathbf{G} : (\mathbf{n} \otimes \mathbf{n}), \nabla \delta \mathbf{u} \cdot \mathbf{n} \rangle \rangle_{\Gamma_M} \quad (\text{A.10})$$

(here, under consideration of the Dirichlet boundary conditions (5.5) and (5.6)) equation (A.7)₁ becomes

$$\langle \mathbf{P}, \nabla \delta \mathbf{u} \rangle + \langle \mathbf{G}, \nabla \nabla \delta \mathbf{u} \rangle + \delta \Pi_{\text{ext}} = 0.$$

showing that if $\mathbf{H} = \nabla \mathbf{u}$ problems (A.3) and (A.7) are equivalent.

The following sentences conclude the proof. Let $\mathbf{u} \in \mathcal{U} \subseteq H_0^1(\mathcal{B}; \mathbf{R}^3)$ be the solution to (A.2). Then, the choice $\mathbf{H} := \nabla \mathbf{u}$ and $\mathbf{\Lambda} := \text{Div } \mathbf{G}$ makes $(\mathbf{u}, \mathbf{H}, \mathbf{\Lambda})$ a solution to (A.7). Reversely, let $(\mathbf{u}, \mathbf{H}, \mathbf{\Lambda})$ be the solution to (A.7). When looking at (A.7)₃ it becomes clear, that for arbitrary $\delta \mathbf{\Lambda} \in H^{-1}(\mathcal{B}; \mathbf{R}^{3 \times 3})$ the conditions $\mathbf{H} = \nabla \mathbf{u}$ and $\text{Rot } \mathbf{H} = \mathbf{0}$ must hold. Therefore, the corresponding solution \mathbf{u} is a solution to (A.3), since for $\nabla \mathbf{u} = \mathbf{H}$ problems (A.3) and (A.7) are equivalent. Moreover, $\nabla \mathbf{u} = \mathbf{H} \in H_0^1(\mathcal{B}; \mathbf{R}^{3 \times 3})$ implies $\mathbf{u} \in \mathcal{U}$. \square

A.1.2 Formulations Corresponding to Section 5.2.1

Variation of the potential (5.23) yields

$$\begin{aligned} \langle \text{Div } \mathbf{\Lambda}, \delta \mathbf{u} \rangle - \langle \langle \mathbf{\Lambda} \cdot \mathbf{n}, \delta \mathbf{u} \rangle \rangle + \delta_{\mathbf{u}} \Pi_{\Gamma} + \delta \Pi_{\text{ext}} = 0 \\ \langle \bar{\mathbf{P}}, \delta \mathbf{H} \rangle + \langle \bar{\mathbf{G}}, \nabla \delta \mathbf{H} \rangle + \langle \mathbf{\Lambda}, \delta \mathbf{H} \rangle + \delta_{\mathbf{H}} \Pi_{\Gamma} + \delta_{\mathbf{H}} \Pi_{\text{rot}} = 0 \\ \langle \delta \mathbf{\Lambda}, \mathbf{H} \rangle + \langle \delta \text{Div } \mathbf{\Lambda}, \mathbf{u} \rangle - \langle \langle \delta \mathbf{\Lambda} \cdot \mathbf{n}, \mathbf{u} \rangle \rangle = 0 \end{aligned} \quad (\text{A.11})$$

²It is, however, for some strain energy models necessary in order to ensure rank sufficiency of the element stiffness matrix of the corresponding discrete system (cf. chapter 7).

where $\bar{\mathbf{P}} := \partial_{\mathbf{H}}\psi$ denotes the first order stress tensor (7.3) formulated entirely in terms of \mathbf{H} . The expressions $\delta_{\mathbf{u}}\Pi_{\Gamma}$ and $\delta_{\mathbf{H}}\Pi_{\Gamma}$ stand for all the terms that correspond to the variation of (A.6) and are unchanged from (A.7). By applying the divergence theorem back in the other direction giving

$$\langle \delta \operatorname{Div} \mathbf{\Lambda}, \mathbf{u} \rangle - \langle \delta \mathbf{\Lambda} \cdot \mathbf{n}, \mathbf{u} \rangle = -\langle \delta \mathbf{\Lambda}, \nabla \mathbf{u} \rangle$$

it becomes clear that (A.11)₃ is equivalent to (A.7)₃ and therefore for the function \mathbf{H} that solves (A.11) the relations $\mathbf{H} = \nabla \mathbf{u}$ and $\operatorname{Rot} \mathbf{H} = \mathbf{0}$ must hold as before. Further, with $\mathbf{H} = \nabla \mathbf{u}$ follows $\bar{\mathbf{P}} = \mathbf{P}$ and $\bar{\mathbf{G}} = \mathbf{G}$ and (A.11)₂ holds true only if

$$\mathbf{\Lambda} = -\mathbf{P} + \operatorname{Div} \mathbf{G}$$

holds (Note, that the terms corresponding to $\delta_{\mathbf{H}}\Pi_{\Gamma}$ are vanishing, analogous to the previous section (cf. (A.9))). Inserting this into (A.11)₁ yields together with (A.10) again as in the previous section the original weak form (A.2). In what follows, the explicit expressions of the linearization of (A.11) are presented in terms of the bilinear- and linear forms used in (5.25). After that, the inf sup conditions are discussed. Linearization of (A.11) yields for Dirichlet boundary conditions the system of equation (5.25), where the linear- and bilinear forms are defined as

$$\begin{aligned} a(\delta \mathbf{H}, \Delta \mathbf{H}) &:= \langle \delta \mathbf{H}, \mathbb{C}|_i : \Delta \mathbf{H} \rangle + \langle \nabla \delta \mathbf{H}, \mathbb{L}|_i : \nabla \Delta \mathbf{H} \rangle + \alpha \langle \operatorname{Rot} \delta \mathbf{H}, \operatorname{Rot} \Delta \mathbf{H} \rangle \\ l(\delta \mathbf{H}) &:= -\langle \delta \mathbf{H}, \bar{\mathbf{P}}|_i \rangle - \langle \nabla \delta \mathbf{H}, \bar{\mathbf{G}}|_i \rangle - \alpha \langle \operatorname{Rot} \delta \mathbf{H}, \operatorname{Rot} \mathbf{H}|_i \rangle - \langle \delta \mathbf{H}, \mathbf{\Lambda}|_i \rangle \\ b_1(\delta \mathbf{\Lambda}, \Delta \mathbf{H}) &:= \langle \delta \mathbf{\Lambda}, \Delta \mathbf{H} \rangle \\ l(\delta \mathbf{\Lambda}) &:= -\langle \delta \mathbf{\Lambda}, \mathbf{H}|_i \rangle - \langle \operatorname{Div} \delta \mathbf{\Lambda}, \mathbf{u}|_i \rangle \\ b_2(\Delta \mathbf{\Lambda}, \delta \mathbf{u}) &:= \langle \operatorname{Div} \Delta \mathbf{\Lambda}, \delta \mathbf{u} \rangle \\ l(\delta \mathbf{u}) &:= \langle \mathbf{f}, \delta \mathbf{u} \rangle - \langle \operatorname{Div} \mathbf{\Lambda}|_i, \delta \mathbf{u} \rangle \end{aligned} \tag{A.12}$$

and the tangent operators defined as $\mathbb{C} := \partial_{\mathbf{H}}\bar{\mathbf{P}}$ and $\mathbb{L} := \partial_{\nabla \mathbf{H}}\bar{\mathbf{G}}$. In the following, the inf-sup stability (5.26) is shown. As shown in the proof of proposition 3 in RIESELMANN ET AL. [2021] based on the proven inf-sup condition for the Stokes equation (Ladyzhenskaya lemma, AMROUCHE AND GIRAULT [1992]) the condition

$$\sup_{\mathbf{\Lambda} \in H(\operatorname{Div}; \mathcal{B}; \mathbb{R}^{3 \times 3}) \setminus \{0\}} \frac{\langle \operatorname{Div} \mathbf{\Lambda}, \mathbf{u} \rangle}{\|\mathbf{\Lambda}\|_{H(\operatorname{Div})}} \gtrsim \|\mathbf{u}\|_{L^2} \quad \forall \mathbf{u} \in L^2(\mathcal{B}; \mathbb{R}^3)$$

holds. Following BRAESS [2007] (p.117, def 3.1) the relation $\|(\bullet)\|_{L^2} \geq \|(\bullet)\|_{H^{-1}}$ holds. Therefore, from definitions (2.54), (2.42) and (2.51) it can directly be seen that $\|(\bullet)\|_{\mathcal{L}} := \|(\bullet)\|_{H^{-1}(\operatorname{Div})} \leq \|(\bullet)\|_{H(\operatorname{Div})}$ must be true. Therefore, since the space \mathcal{L} is larger than the space $H(\operatorname{Div}; \mathcal{B}; \mathbb{R}^{3 \times 3})$ ($L^2(\mathcal{B}) \subseteq H^{-1}(\mathcal{B}) \Rightarrow H(\operatorname{Div}; \mathcal{B}; \mathbb{R}^{3 \times 3}) \subseteq \mathcal{L}$, see again BRAESS [2007], p.117, def 3.1) it can be written

$$\begin{aligned} \sup_{\mathbf{\Lambda} \in \mathcal{L} \setminus \{0\}} \frac{b_2(\mathbf{\Lambda}, \mathbf{u})}{\|\mathbf{\Lambda}\|_{\mathcal{L}}} &\geq \sup_{\mathbf{\Lambda} \in H(\operatorname{Div}; \mathcal{B}; \mathbb{R}^{3 \times 3}) \setminus \{0\}} \frac{b_2(\mathbf{\Lambda}, \mathbf{u})}{\|\mathbf{\Lambda}\|_{\mathcal{L}}} \\ &\geq \sup_{\mathbf{\Lambda} \in H(\operatorname{Div}; \mathcal{B}; \mathbb{R}^{3 \times 3}) \setminus \{0\}} \frac{\langle \operatorname{Div} \mathbf{\Lambda}, \mathbf{u} \rangle}{\|\mathbf{\Lambda}\|_{H(\operatorname{Div})}} \gtrsim \|\mathbf{u}\|_{\mathcal{U}} \quad \forall \mathbf{u} \in \mathcal{U}, \end{aligned}$$

which shows that the inf-sup condition (5.26) holds with \mathcal{U} and \mathcal{L} defined in (5.24). That the other inf-sup condition (5.27) holds is shown in the proof of proposition 4 in RIESELMANN ET AL. [2021]. The key ingredient for the proof is that the kernel space $\mathbf{\Lambda} \in \mathcal{Z}(\mathbf{\Lambda})$ is divergence-free and thus with $\|\operatorname{Div} \mathbf{\Lambda}\|_{L^2} = 0$ the norm for \mathcal{L} simplifies to

$$\|\mathbf{\Lambda}\|_{\mathcal{L}} = \|\mathbf{\Lambda}\|_{H^{-1}}$$

which per definition (2.50) fulfills the inf-sup condition with

$$\sup_{\mathbf{H} \in \mathcal{H} \setminus \{0\}} \frac{b_2(\mathbf{H}, \mathbf{\Lambda})}{\|\mathbf{H}\|_{\mathcal{H}}} \gtrsim \sup_{\mathbf{H} \in H_0^1(\mathcal{B}; \mathbb{R}^{3 \times 3}) \setminus \{0\}} \frac{\langle \mathbf{H}, \mathbf{\Lambda} \rangle}{\|\mathbf{H}\|_{H^1}} =: \|\mathbf{\Lambda}\|_{\mathcal{L}} \quad \forall \mathbf{\Lambda} \in \mathcal{Z}(\mathbf{\Lambda})$$

since on both sides of the inequality appears the same expression. Note, that equation (5.25)₃ differs from the corresponding equation treated in RIESELDMANN ET AL. [2021] in the fact that in the present case the right-hand side is not zero. This, however, does not change the result, since problem (5.25) can always be reduced to a problem where the corresponding right-hand side is zero (cf. BRENNER AND SCOTT [1994]). This can also be shown by the following consideration: Introduce the function $\tilde{\mathbf{\Lambda}} \in \mathcal{L}$ with $b_2(\tilde{\mathbf{\Lambda}}, \delta \mathbf{u}) = b_2(\mathbf{\Lambda}, \delta \mathbf{u}) - l(\delta \mathbf{u})$ and the following relations $\tilde{\mathbf{\Lambda}} = \mathbf{\Lambda} + \hat{\mathbf{\Lambda}}$, $\delta \tilde{\mathbf{\Lambda}} = \delta \mathbf{\Lambda}$, $\text{Div } \tilde{\mathbf{\Lambda}} = \text{Div } \mathbf{\Lambda} - \mathbf{f}$, $\text{Div } \delta \tilde{\mathbf{\Lambda}} = \text{Div } \delta \mathbf{\Lambda}$, with $\hat{\mathbf{\Lambda}} \in \mathcal{L}$. Then, problem (5.25) can be expressed by the identical problem but formulated in $\tilde{\mathbf{\Lambda}}$:

$$\begin{aligned} b_2(\Delta \tilde{\mathbf{\Lambda}}, \delta \mathbf{u}) &= 0 \\ a(\delta \mathbf{H}, \Delta \mathbf{H}) + b_1(\delta \mathbf{H}, \Delta \tilde{\mathbf{\Lambda}}) &= l_H(\delta \mathbf{H}) \\ b_2(\delta \tilde{\mathbf{\Lambda}}, \Delta \mathbf{u}) + b_1(\Delta \mathbf{H}, \delta \tilde{\mathbf{\Lambda}}) &= l_{\Lambda}(\delta \tilde{\mathbf{\Lambda}}) \end{aligned} \quad (\text{A.13})$$

From the inf-sup condition (5.27) on the kernel space $\mathcal{Z}(\mathbf{\Lambda})$ which is associated to the present representation (A.13), the inf-sup condition for the problem (5.25) follows as well, since (A.13) and (5.25) are equivalent. In consequence, the appearance of the linear forms $l(\bullet)$ is irrelevant to the stability analysis as long as the values of the prescribed functions in the residual are bounded. Thus, whether they contain only the integrals including the load functions or also the integrals incorporating the values of the previous iteration resulting from the linearization makes no difference to the stability of the linear system. Nevertheless, Brezzi's conditions can of course only make a prediction about the stability of the solution of the linearized system and give in general no conclusion about the convergence of the superordinate iterations of the load step solution procedure.

A.1.3 Formulations Corresponding to Section 5.3.1

The following shows that the variational equations corresponding to the potential Π_{H3} of section 5.3.1 are equivalent to the original problem (A.2). Variation of the potential Π_{H3} defined in (5.41) reads

$$\begin{aligned} \langle \mathbf{S}^{\text{loc}}, \delta \mathbf{E}(\mathbf{u}) \rangle - \langle \mathbf{\Sigma}, \delta \mathbf{E}(\nabla \mathbf{u}) \rangle + \langle \bar{\mathbf{B}} \cdot \mathbf{n}, \delta \mathbf{E}(\nabla \mathbf{u}) \rangle + \delta_{\mathbf{u}} \Pi_{\text{ext}} &= 0 \\ \langle \mathbf{S}^{\text{nlloc}}, \delta \mathbf{E} \rangle + \langle \bar{\mathbf{B}}, \nabla \delta \mathbf{E} \rangle + \langle \mathbf{\Sigma}, \delta \mathbf{E} \rangle - \langle \bar{\mathbf{B}} \cdot \mathbf{n}, \delta \mathbf{E} \rangle + \langle \delta \bar{\mathbf{B}} \cdot \mathbf{n}, \mathbf{E}(\nabla \mathbf{u}) - \mathbf{E} \rangle &= 0 \\ \langle \delta \mathbf{\Sigma}, \mathbf{E} - \mathbf{E}(\nabla \mathbf{u}) \rangle &= 0 \end{aligned} \quad (\text{A.14})$$

with the second Piola Kirchhoff stress tensor $\mathbf{S}^{\text{loc}} := \partial_{\mathbf{E}(\nabla \mathbf{u})} \psi^{\text{loc}}$ formulated in terms of $\nabla \mathbf{u}$ and the nonlocal contribution $\mathbf{S}^{\text{nlloc}} := \partial_{\mathbf{E}} \psi^{\text{nlloc}}$ formulated in terms of \mathbf{E} adding up with $\mathbf{S} = \mathbf{S}^{\text{loc}} + \mathbf{S}^{\text{nlloc}}$ to the first order stress tensor as defined in section 7.1 (see also DELL'ISOLA ET AL. [2018]). The solution of (A.14)₃ implies $\mathbf{E} = \mathbf{E}(\nabla \mathbf{u})$ resulting in $\bar{\mathbf{B}} = \mathbf{B}$ and simplifying equation (A.14)₂ to

$$\langle \mathbf{S}^{\text{nlloc}}, \delta \mathbf{E} \rangle + \langle \mathbf{B}, \nabla \delta \mathbf{E} \rangle + \langle \mathbf{\Sigma}, \delta \mathbf{E} \rangle - \langle \mathbf{B} \cdot \mathbf{n}, \delta \mathbf{E} \rangle = \langle \mathbf{S}^{\text{nlloc}}, \delta \mathbf{E} \rangle - \langle \text{Div } \mathbf{B}, \delta \mathbf{E} \rangle + \langle \mathbf{\Sigma}, \delta \mathbf{E} \rangle = 0 \quad (\text{A.15})$$

after applying the divergence theorem

$$\langle \mathbf{B}, \nabla \delta \mathbf{E} \rangle = \langle \langle \mathbf{B} \cdot \mathbf{n}, \delta \mathbf{E} \rangle \rangle - \langle \text{Div } \mathbf{B}, \delta \mathbf{E}(\nabla \mathbf{u}) \rangle$$

and canceling out the surface term. Equation (A.15) implies $\boldsymbol{\Sigma} = -\mathbf{S}^{\text{nlloc}} + \text{Div } \mathbf{B}$. Inserting this together with (A.18) into (A.14)₁ yields

$$\langle \mathbf{S}, \delta \mathbf{E}(\nabla \mathbf{u}) \rangle - \langle \text{Div } \mathbf{B}, \delta \mathbf{E}(\nabla \mathbf{u}) \rangle + \langle \langle \mathbf{B} \cdot \mathbf{n}, \delta \mathbf{E}(\nabla \mathbf{u}) \rangle \rangle + \delta_{\mathbf{u}} \Pi_{\text{ext}} = 0 \quad (\text{A.16})$$

The divergence theorem applied to the surface term of (A.16) reads

$$\langle \langle \mathbf{B} \cdot \mathbf{n}, \delta \mathbf{E}(\nabla \mathbf{u}) \rangle \rangle = \langle \text{Div } \mathbf{B}, \delta \mathbf{E}(\nabla \mathbf{u}) \rangle + \langle \mathbf{B}, \nabla \delta \mathbf{E}(\nabla \mathbf{u}) \rangle,$$

which inserted into (A.16) leads to

$$\langle \mathbf{S}, \delta \mathbf{E}(\nabla \mathbf{u}) \rangle + \langle \mathbf{B}, \nabla \delta \mathbf{E}(\nabla \mathbf{u}) \rangle + \delta_{\mathbf{u}} \Pi_{\text{ext}} = 0 \quad (\text{A.17})$$

Finally, following from the kinematics discussed in section 7.1 for any L^2 integrable second and second order tensor $(\bullet) \in L^2(\mathcal{B}; \mathbb{S})$ and $(\blacksquare) \in L^2(\mathcal{B}; \mathbb{S} \times \mathbb{R}^3)$, respectively with the present symmetries we note the relations

$$\langle \langle (\bullet), \delta \mathbf{E}(\nabla \mathbf{u}) \rangle \rangle = \langle \langle \mathbf{F} \cdot (\bullet), \nabla \delta \mathbf{u} \rangle \rangle \quad \text{and} \quad \langle \langle (\blacksquare), \nabla \delta \mathbf{E}(\nabla \mathbf{u}) \rangle \rangle = \langle \langle \mathbf{F} \cdot (\blacksquare), \nabla \nabla \delta \mathbf{u} \rangle \rangle \quad (\text{A.18})$$

(note also the relations $\nabla \delta \mathbf{u} = \delta \mathbf{F}$ and $\nabla \nabla \delta \mathbf{u} = \nabla \delta \mathbf{F}$). Together with the relations $\mathbf{F} \cdot \mathbf{S} = \mathbf{P}$ and $\mathbf{F} \cdot \mathbf{B} = \mathbf{G}$ yields after applying (A.18) to (A.17) the equation

$$\langle \mathbf{P}, \nabla \delta \mathbf{u} \rangle + \langle \mathbf{G}, \nabla \nabla \delta \mathbf{u} \rangle + \delta \Pi^{\text{ext}} = 0$$

which is the original problem (A.2).

A.2 Continuous Proposed Gradient Damage Formulation

Variation of (9.1) leads to the set of equations

$$\begin{aligned} \langle \mathbf{P}, \nabla \delta \mathbf{u} \rangle - \langle \mathbf{f}, \delta \mathbf{u} \rangle - \langle \langle \mathbf{t}, \delta \mathbf{u} \rangle \rangle_{\Gamma_N} &= 0 \\ \langle \partial_{\alpha} \psi, \delta \alpha \rangle + \langle \partial_{\nabla \alpha} \psi, \nabla \delta \alpha \rangle + \langle \partial_{\alpha} \gamma, \delta \alpha \rangle + \langle \lambda, \delta \alpha \rangle &= 0 \\ \langle \delta \lambda, \alpha - \alpha_n \rangle &= 0 \end{aligned} \quad (\text{A.19})$$

with the first Piola Kirchhoff stress tensor $\mathbf{P} := \partial_{\mathbf{F}} \psi$. Note, that applying the divergence theorem to equation (A.19)₂ yields the relation (9.6) and the surface flux equation (8.17). Linearization of (A.19) leads to the system of equations (9.7), where the linear- and bilinear forms are defined by

$$\begin{aligned} a_1(\delta \mathbf{u}, \Delta \mathbf{u}) &:= \langle \delta \nabla \mathbf{u}, \mathbb{C}|_i : \Delta \nabla \mathbf{u} \rangle \\ a_2(\delta \alpha, \Delta \alpha) &:= \langle \delta \alpha, d|_i \Delta \alpha \rangle + \langle \nabla \delta \alpha, c|_i \Delta \alpha \rangle \\ b_1(\delta \mathbf{u}, \Delta \alpha) &:= \langle \Delta \alpha \mathbf{D}|_i, \nabla \delta \mathbf{u} \rangle \\ b_2(\delta \alpha, \Delta \lambda) &:= \langle \delta \alpha, \Delta \lambda \rangle \\ l(\delta \mathbf{u}) &:= \langle \mathbf{f}, \delta \mathbf{u} \rangle + \langle \langle \mathbf{t}, \delta \mathbf{u} \rangle \rangle_{\Gamma_N} - \langle \mathbf{P}|_i, \nabla \delta \mathbf{u} \rangle \\ l(\delta \alpha) &:= -\langle \partial_{\alpha}(\psi + \gamma)|_i, \delta \alpha \rangle - \langle \partial_{\nabla \alpha} \psi|_i, \nabla \delta \alpha \rangle - \langle \lambda|_i, \delta \alpha \rangle \\ l(\delta \lambda) &:= -\langle \delta \lambda, \alpha|_i - \alpha_n \rangle \end{aligned} \quad (\text{A.20})$$

where $(\bullet)|_i$ denotes the values of the previous iteration, $\Delta(\bullet) := (\bullet) - (\bullet)_i$ denotes the solution increment and the tangent operators are defined as $\mathbb{C} := \partial_{\nabla \mathbf{u}} \mathbf{P}$, $d := \partial_{\alpha} \partial_{\alpha}(\psi + \gamma)$, $c := \partial_{\nabla \alpha} \partial_{\nabla \alpha}(\psi + \gamma)$ and $\mathbf{D} := \partial_{\alpha} \mathbf{P}$. Further, note the relations $\nabla \delta \mathbf{u} = \delta \mathbf{F}$ and $\nabla \Delta \mathbf{u} = \Delta \mathbf{F}$.

Appendix B

Discrete Expressions

B.1 Static Condensation

Since throughout this contribution the static condensation procedure starting from the same structure of element submatrix-expressions is applied repeatedly, the present section presents the transformation steps with a generic example linearized system that has the same structure as those of presented formulations. Starting point is the system of equations

$$\mathbf{A}_{T \in \mathcal{T}} \left(\begin{bmatrix} \underline{\mathbf{k}}_v & \underline{\mathbf{k}}_{vh_I} & \underline{\mathbf{k}}_{vh_B} & \underline{\mathbf{k}}_{v\rho} \\ \underline{\mathbf{k}}_{h_I v} & \underline{\mathbf{k}}_{h_I} & \underline{\mathbf{k}}_{h_I h_B} & \underline{\mathbf{k}}_{h_I \rho} \\ \underline{\mathbf{k}}_{h_B v} & \underline{\mathbf{k}}_{h_B h_I} & \underline{\mathbf{k}}_{h_B} & \underline{\mathbf{k}}_{h_B \rho} \\ \underline{\mathbf{k}}_{\rho v} & \underline{\mathbf{k}}_{\rho h_I} & \underline{\mathbf{k}}_{\rho h_B} & \underline{\mathbf{0}} \end{bmatrix} \begin{bmatrix} \underline{\mathbf{d}}_v \\ \underline{\mathbf{d}}_{h_I} \\ \underline{\mathbf{d}}_{h_B} \\ \underline{\mathbf{d}}_\rho \end{bmatrix} + \begin{bmatrix} \underline{\mathbf{r}}_v \\ \underline{\mathbf{r}}_{h_B} \\ \underline{\mathbf{r}}_{h_B} \\ \underline{\mathbf{r}}_\rho \end{bmatrix} \right) = \underline{\mathbf{0}}, \quad (\text{B.1})$$

of which v, h and ρ are placeholders for the solution variables corresponding to the actual proposed formulations. Here, h denotes the submatrices of the discrete solution field that is enriched with volume bubble functions and ρ denotes the discrete solution field corresponding to the first Lagrange multiplier variable. For example, in the case of the formulation of section 5.1.2 u, h and ρ correspond to \mathbf{u}, \mathbf{H} and $\mathbf{\Lambda}$, respectively. Note, that (B.1) constitutes a more detailed notation in which the sub-matrixes and vectors corresponding to the vertex degrees of freedom $\underline{\mathbf{d}}_{h_I}$ and the internal degrees of freedom $\underline{\mathbf{d}}_{h_B}$ of the variable h are considered separately. Moreover, the most general case in which all non-zero tangent submatrices except for the submatrix corresponding to the Lagrange multiplier ρ is considered. By multiplying the third row of (B.1) from the left by $(\underline{\mathbf{k}}_{h_B})^{-1}$ we obtain for the internal degrees of freedom corresponding to the volume bubble function

$$\underline{\mathbf{d}}_{h_B} = -(\underline{\mathbf{k}}_{h_B})^{-1}(\underline{\mathbf{k}}_{h_B v} \underline{\mathbf{d}}_v + \underline{\mathbf{k}}_{h_B h_I} \underline{\mathbf{d}}_{h_I} + \underline{\mathbf{k}}_{h_B \rho} \underline{\mathbf{d}}_\rho + \underline{\mathbf{r}}_{h_B}) \quad (\text{B.2})$$

Inserting (B.2) into rows 1,2 and 4 for each element on the left-hand side of (B.1) yields the expressions

$$\begin{aligned} & \underline{\mathbf{k}}_v \underline{\mathbf{d}}_v + \underline{\mathbf{k}}_{vh_I} \underline{\mathbf{d}}_{h_I} - \underline{\mathbf{k}}_{vh_B} (\underline{\mathbf{k}}_{h_B})^{-1} (\underline{\mathbf{k}}_{h_B v} \underline{\mathbf{d}}_v + \underline{\mathbf{k}}_{h_B h_I} \underline{\mathbf{d}}_{h_I} + \underline{\mathbf{k}}_{h_B \rho} \underline{\mathbf{d}}_\rho + \underline{\mathbf{r}}_{h_B}) + \underline{\mathbf{k}}_{v\rho} \underline{\mathbf{d}}_\rho + \underline{\mathbf{r}}_v \\ & \underline{\mathbf{k}}_{h_I v} \underline{\mathbf{d}}_v + \underline{\mathbf{k}}_{h_I} \underline{\mathbf{d}}_{h_I} - \underline{\mathbf{k}}_{h_I h_B} (\underline{\mathbf{k}}_{h_B})^{-1} (\underline{\mathbf{k}}_{h_B v} \underline{\mathbf{d}}_v + \underline{\mathbf{k}}_{h_B h_I} \underline{\mathbf{d}}_{h_I} + \underline{\mathbf{k}}_{h_B \rho} \underline{\mathbf{d}}_\rho + \underline{\mathbf{r}}_{h_B}) + \underline{\mathbf{k}}_{h_I \rho} \underline{\mathbf{d}}_\rho + \underline{\mathbf{r}}_{h_I} \\ & \underline{\mathbf{k}}_{\rho v} \underline{\mathbf{d}}_v + \underline{\mathbf{k}}_{\rho h_I} \underline{\mathbf{d}}_{h_I} - \underline{\mathbf{k}}_{\rho h_B} (\underline{\mathbf{k}}_{h_B})^{-1} (\underline{\mathbf{k}}_{h_B v} \underline{\mathbf{d}}_v + \underline{\mathbf{k}}_{h_B h_I} \underline{\mathbf{d}}_{h_I} + \underline{\mathbf{k}}_{h_B \rho} \underline{\mathbf{d}}_\rho + \underline{\mathbf{r}}_{h_B}) + \underline{\mathbf{r}}_\rho, \end{aligned} \quad (\text{B.3})$$

from which the following substitute expressions can be identified:

$$\begin{aligned}
\mathbf{k}_v^* &:= \mathbf{k}_v - \mathbf{k}_{vh_B}(\mathbf{k}_{h_B})^{-1}\mathbf{k}_{h_Bv} & \mathbf{r}_v^* &:= \mathbf{r}_v - \mathbf{k}_{vh_B}(\mathbf{k}_{h_B})^{-1}\mathbf{r}_{h_B} \\
\mathbf{k}_{vh}^* &:= \mathbf{k}_{vh_I} - \mathbf{k}_{vh_B}(\mathbf{k}_{h_B})^{-1}\mathbf{k}_{h_Bh_I} = (\mathbf{k}_{hv}^*)^T & \mathbf{r}_h^* &:= \mathbf{r}_{h_I} - \mathbf{k}_{vh_B}(\mathbf{k}_{h_B})^{-1}\mathbf{r}_{h_B} \\
\mathbf{k}_{v\rho}^* &:= \mathbf{k}_{v\rho} - \mathbf{k}_{vh_B}(\mathbf{k}_{h_B})^{-1}\mathbf{k}_{h_B\rho} = (\mathbf{k}_{\rho v}^*)^T & \mathbf{r}_\rho^* &:= \mathbf{r}_\rho - \mathbf{k}_{vh_B}(\mathbf{k}_{h_B})^{-1}\mathbf{r}_{h_B} \\
\mathbf{k}_h^* &:= \mathbf{k}_{h_I} - \mathbf{k}_{h_Ih_B}(\mathbf{k}_{h_B})^{-1}\mathbf{k}_{h_Bh_I} \\
\mathbf{k}_{h\rho}^* &:= \mathbf{k}_{h_I\rho} - \mathbf{k}_{h_Ih_B}(\mathbf{k}_{h_B})^{-1}\mathbf{k}_{h_B\rho} = (\mathbf{k}_{\rho h}^*)^T \\
\mathbf{k}_\rho^* &:= -\mathbf{k}_{\rho h_B}(\mathbf{k}_{h_B})^{-1}\mathbf{k}_{h_B\rho},
\end{aligned} \tag{B.4}$$

so that problem (B.1) can now be written as

$$\mathbf{A}_{T \in \mathcal{T}} \left(\begin{bmatrix} \mathbf{k}_v^* & \mathbf{k}_{vh}^* & \mathbf{k}_{v\rho}^* \\ \mathbf{k}_{hv}^* & \mathbf{k}_h^* & \mathbf{k}_{h\rho}^* \\ \mathbf{k}_{\rho v}^* & \mathbf{k}_{\rho h}^* & \mathbf{k}_\rho^* \end{bmatrix} \begin{bmatrix} \mathbf{d}_v \\ \mathbf{d}_{h_I} \\ \mathbf{d}_\rho \end{bmatrix} + \begin{bmatrix} \mathbf{r}_v^* \\ \mathbf{r}_h^* \\ \mathbf{r}_\rho^* \end{bmatrix} \right) = \mathbf{0}. \tag{B.5}$$

The second step of the condensation procedure is based on multiplying (B.5) from the left by $(\mathbf{k}_\rho^*)^{-1}$, which yields for the Lagrange multiplier degrees of freedom

$$\mathbf{d}_\rho = -(\mathbf{k}_\rho^*)^{-1}(\mathbf{k}_{\rho v}^*\mathbf{d}_v + \mathbf{k}_{\rho h}^*\mathbf{d}_{h_I} + \mathbf{r}_\rho^*) \tag{B.6}$$

At this point it becomes obvious that the additional volume bubble degrees of freedom \mathbf{d}_{h_B} are necessary for the condensation of \mathbf{d}_ρ , because only due to the previously discussed condensation (B.2)-(B.5) the sub-matrix \mathbf{k}_ρ^* on the lower right of (B.5) is not zero and (B.6) computable. Inserting (B.6) for each element into the second and third row on the left-hand side of (B.5) yields the expressions

$$\begin{aligned}
\mathbf{k}_v^*\mathbf{d}_v + \mathbf{k}_{vh}^*\mathbf{d}_{h_I} - \mathbf{k}_{v\rho}^*(\mathbf{k}_\rho^*)^{-1}(\mathbf{k}_{\rho v}^*\mathbf{d}_v + \mathbf{k}_{\rho h}^*\mathbf{d}_{h_I} + \mathbf{r}_\rho^*) + \mathbf{r}_v^* \\
\mathbf{k}_{hv}^*\mathbf{d}_v + \mathbf{k}_h^*\mathbf{d}_{h_I} - \mathbf{k}_{h\rho}^*(\mathbf{k}_\rho^*)^{-1}(\mathbf{k}_{\rho v}^*\mathbf{d}_v + \mathbf{k}_{\rho h}^*\mathbf{d}_{h_I} + \mathbf{r}_\rho^*) + \mathbf{r}_h^*
\end{aligned} \tag{B.7}$$

from which we identify the substitute matrix and residuals

$$\begin{aligned}
\mathbf{k}_v^{**} &:= \mathbf{k}_v^* - \mathbf{k}_{v\rho}^*(\mathbf{k}_\rho^*)^{-1}\mathbf{k}_{\rho v}^* & \mathbf{r}_v^{**} &:= \mathbf{r}_v^* - \mathbf{k}_{v\rho}^*(\mathbf{k}_\rho^*)^{-1}\mathbf{r}_\rho^* \\
\mathbf{k}_{vh}^{**} &:= \mathbf{k}_{vh}^* - \mathbf{k}_{v\rho}^*(\mathbf{k}_\rho^*)^{-1}\mathbf{k}_{\rho h}^* = (\mathbf{k}_{hv}^{**})^T & \mathbf{r}_h^{**} &:= \mathbf{r}_h^* - \mathbf{k}_{h\rho}^*(\mathbf{k}_\rho^*)^{-1}\mathbf{r}_\rho^* \\
\mathbf{k}_h^{**} &:= \mathbf{k}_h^* - \mathbf{k}_{h\rho}^*(\mathbf{k}_\rho^*)^{-1}\mathbf{k}_{\rho h}^*
\end{aligned} \tag{B.8}$$

and problem (B.5) can be written as the reduced equation system

$$\mathbf{A}_{T \in \mathcal{T}} \left(\begin{bmatrix} \mathbf{k}_v^{**} & \mathbf{k}_{vh}^{**} \\ \mathbf{k}_{hv}^{**} & \mathbf{k}_h^{**} \end{bmatrix} \begin{bmatrix} \mathbf{d}_v \\ \mathbf{d}_{h_I} \end{bmatrix} + \begin{bmatrix} \mathbf{r}_v^{**} \\ \mathbf{r}_h^{**} \end{bmatrix} \right) = \mathbf{0} \tag{B.9}$$

B.2 Interpolation Matrices of the RotFEM Approach

The subsequent relationships demonstrate the shift from tensor notation to matrix notation.

$$\begin{aligned}
\mathbf{u}^h &= \sum_I \mathbf{d}_I^{(u)} N_I & \Rightarrow & \quad \mathbf{u}^h = \mathbf{N}_u \mathbf{d}_u, \\
\mathbf{H}^h &= \sum_I \mathbf{d}_I^{(H)} N_I & \Rightarrow & \quad \mathbf{H}^h = \mathbf{N}_H \mathbf{d}_H, \\
\nabla \mathbf{u}^h &= \sum_I \mathbf{d}_I^{(u)} \otimes \nabla N_I & \Rightarrow & \quad \nabla \mathbf{u}^h = \mathbf{B}_u \mathbf{d}_u, \\
\nabla \mathbf{H}^h &= \sum_I \mathbf{d}_I^{(H)} \otimes \nabla N_I & \Rightarrow & \quad \nabla \mathbf{H}^h = \mathbf{B}_H \mathbf{d}_H.
\end{aligned}$$

In this context, the representation in tensor notation is shown in the left column, where $\mathbf{d}_{(\bullet)}^I$ represents the vector/tensor of degrees of freedom and N_I represents the Lagrangian shape function corresponding to the I -th element node. The specific suitable choices of the Lagrange shape functions corresponding to the 2D and 3D cases, respectively, are given in section 6.2. When expressed in matrix notation, the solution variables (e.g. $\underline{\mathbf{H}}^h, \nabla \underline{\mathbf{H}}^h, \dots$) and the associated element-wise vectors of nodal degrees of freedom ($\underline{\mathbf{d}}_H, \underline{\mathbf{d}}_u, \dots$) are treated as column-matrices, while the element-wise interpolation operators (e.g. $\underline{\mathbf{N}}_H, \underline{\mathbf{B}}_H, \dots$) are considered as matrix quantities. The piecewise constant interpolation of the second Lagrange multiplier variable of section (6.2) is carried out in a similar manner through

$$\underline{\boldsymbol{\mu}}^h = \mathbf{d}^{(\mu)} N^{(P0)} \quad \Rightarrow \quad \underline{\boldsymbol{\mu}}^h = \underline{\mathbf{N}}_{\mu} \underline{\mathbf{d}}_{\mu},$$

with $N^{(P0)} = 1$ and the vector $\mathbf{d}^{(\mu)}$ corresponding to the degrees of freedom of the internal node of the element. For the construction of the rotation operator matrix, consider the relation:

$$\text{Rot } \mathbf{H}^h \tag{B.10}$$

where $\text{Rot } \mathbf{H}^h$ is obtained by inserting $\nabla \mathbf{H}^h$ into the relations and (2.22) and (2.23) for $d = 2$ and $d = 3$, respectively. Similarly to the preceding explanations, the Raviart-Thomas interpolation matrices can be constructed from the following relations

$$\begin{aligned} \underline{\boldsymbol{\Phi}}^h &= \sum_{I=1}^4 \text{sgn}(\mathbf{n}_I) \mathbf{d}_I^{(\Phi)} \otimes N_I^{(\text{RT0})} & \Rightarrow & \quad \underline{\boldsymbol{\Phi}}^h = \underline{\mathbf{S}}_{\Phi} \underline{\mathbf{d}}_{\Phi} \\ \text{Div } \underline{\boldsymbol{\Phi}}^h &= \sum_{I=1}^4 \text{sgn}(\mathbf{n}_I) \mathbf{d}_I^{(\Phi)} \text{Div } N_I^{(\text{RT0})} & \Rightarrow & \quad \text{Div } \underline{\boldsymbol{\Phi}}^h = \underline{\mathbf{D}}_{\Phi} \underline{\mathbf{d}}_{\Phi} \end{aligned}$$

where for the implementation of the physical basis functions $\mathbf{N}_I^{(\text{RT0})}$ the kinematic relations (3.53) and (3.54) are used (details in section 3.2.1). Note that here, the vector-approximation scheme (3.53) corresponds to each row of the second order tensor $\underline{\boldsymbol{\Phi}}^h$. Thus, the corresponding nodal degrees of freedom $\mathbf{d}_I^{(\Phi)}$ are vector-valued yielding together with the vector-valued basis a tensor-valued approximation function (see also SCHWARZ [2009] and VIEBAHN ET AL. [2018]).

B.3 Details on the H-Div Λ Discretization

Starting from the approach of RAVIART AND THOMAS [1977] in the following, the constraint term (5.29) is derived following the approach of ARNOLD AND BREZZI [1985] together with the Crouzeix-Raviart interpolation (5.32) for the displacements. Note, that for the sake of readability we use the simplified notation $\bar{\boldsymbol{\Lambda}}^h := \boldsymbol{\Lambda}^h|_T$ and $\bar{\mathbf{u}}^h := \mathbf{u}^h|_T$. The RAVIART AND THOMAS [1977]-discretization of the bilinear form b_2 defined in (A.12) would read

$$b_2(\bar{\mathbf{u}}^h, \bar{\boldsymbol{\Lambda}}^h) = \sum_{T \in \mathcal{T}} \int_T \text{Div } \bar{\boldsymbol{\Lambda}}^h \cdot \bar{\mathbf{u}}^h \, dV \tag{B.11}$$

with the finite element spaces for $(\bar{\boldsymbol{\Lambda}}^h, \bar{\mathbf{u}}^h) \in \text{RT0}(\mathcal{B}; \mathbb{R}^{3 \times 3}) \times (P0(\mathcal{T}; \mathbb{R}^3) \cap L_0^2(\mathcal{B}; \mathbb{R}^3))$ where $\text{RT0}(\mathcal{T}; \mathbb{R}^{3 \times 3})$ is defined as (cf. section 3.1.2):

$$\text{RT0}(\mathcal{T}; \mathbb{R}^{3 \times 3}) := \left\{ \begin{array}{l} \bar{\boldsymbol{\Lambda}}^h = \mathbf{a}_T + \mathbf{b}_T \otimes \mathbf{X} \text{ with } \\ \mathbf{a}_T \in P0(\mathcal{T}; \mathbb{R}^{3 \times 3}), \mathbf{b}_T \in P0(\mathcal{T}; \mathbb{R}^3) : \end{array} \begin{array}{l} \bar{\boldsymbol{\Lambda}}^h \text{ is continuous in normal di-} \\ \text{rection across elem. interfaces} \\ \Leftrightarrow \bar{\boldsymbol{\Lambda}}^h \in H(\text{Div}; \mathcal{B}; \mathbb{R}^{3 \times 3}) \end{array} \right\} \tag{B.12}$$

Since the degrees of freedom corresponding to the Raviart-Thomas discretization $\bar{\mathbf{\Lambda}}^h$ live on the interelement boundaries, static condensation on the element level is not possible. The aim of the following is to enable static condensation of the Lagrange multiplier by using a piecewise continuous interpolation. Therefore, following ARNOLD AND BREZZI [1985] (Lemma 1.2 ff), discretization (B.11) can be replaced by the following

$$\sum_{T \in \mathcal{T}} \int_T \text{Div } \bar{\mathbf{\Lambda}}^h \cdot \bar{\mathbf{u}}^h \, dV \leftarrow \sum_{T \in \mathcal{T}} \left(\int_T \text{Div } \mathbf{\Lambda}^h \cdot \mathbf{u}^h \, dV - \int_{\partial T \setminus \partial \mathcal{B}} \mathbf{\Lambda}^h \cdot \mathbf{n}|_{\partial T} \cdot \mathbf{d}_{\mathcal{F}_T} \right) \quad (\text{B.13})$$

with the finite element space $\mathbf{\Lambda}^h \in P0(\mathcal{T}; \mathbf{R}^{3 \times 3}) \cap H(\text{Div}; \mathcal{B}; \mathbf{R}^{3 \times 3})$,¹ where $\mathbf{d}_{\mathcal{F}_T} \in P0(\mathcal{F}; \mathbf{R}^3)$ are discrete Lagrange multipliers defined on the midface nodes of the element interfaces \mathcal{F}_T enforcing normal continuity of $\mathbf{\Lambda}^h$ across element interfaces. Further, in ARNOLD AND BREZZI [1985] (Theorem 1.4 ff) it is shown that the Lagrange multipliers $\mathbf{d}_{\mathcal{F}_T}$ approximate the displacements \mathbf{u} on the element mid-interfaces. Thus, the Crouzeix Raviart interpolation (5.32) (cf. BRAESS [2007])

$$\mathbf{u}^h = \sum_{I \in \mathcal{F}_T} \mathbf{d}_I^{(u)} N_I^{(\text{CR})}$$

is introduced and the Lagrange multipliers $\mathbf{d}_{\mathcal{F}_T} \equiv \mathbf{d}_I^{(u)}$ are considered as displacement degrees of freedom. The Crouzeix Raviart finite element space is defined as follows:

$$CR0(\mathcal{T}; \mathbf{R}^3) := \left\{ \mathbf{u}^h \in P1(\mathcal{T}; \mathbf{R}^3) \cap L_0^2(\mathcal{B}; \mathbf{R}^3) : \begin{array}{l} \mathbf{u}^h \text{ is continuous at the midpoints} \\ \text{of the element faces } \mathcal{F}_T \end{array} \right\}. \quad (\text{B.14})$$

Note, that in our specific case (5.32) is a conforming discretization of \mathbf{u} with $CR0(\mathcal{T}; \mathbf{R}^3) \subset \mathcal{U}$, because \mathcal{U} is not defined over H^1 but over L^2 (cf. (5.24)). In the following, it is shown that (5.29) is equivalent to the replacement (B.13).

Proof. For this, we consider the divergence theorem on one tetrahedron applied to the following expression:

$$\int_{\partial T} \mathbf{\Lambda}^h \cdot \mathbf{n}|_{\partial T} \cdot \mathbf{u}^h \, dA = \int_T \mathbf{\Lambda}^h \cdot \nabla \mathbf{u}^h + \text{Div } \mathbf{\Lambda}^h \cdot \mathbf{u}^h \, dV \quad (\text{B.15})$$

In the following it is shown, that for the discretization (5.28) and the Crouzeix-Raviart interpolation (5.32) the left-hand side and the first term of the right-hand side of (B.15) are identical and therefore $\int_T \text{Div } \mathbf{\Lambda}^h \cdot \mathbf{u}^h \, dV = 0$.

Left-hand side of (B.15): With (5.32) and $\mathbf{\Lambda}^h$ chosen constant over the element and therefore taken out of the element volume integral, the left-hand side of (B.15) can be written as

$$\int_{\partial T} \mathbf{\Lambda}^h \cdot \mathbf{n}|_{\partial T} \cdot \mathbf{u}^h \, dV = \sum_{I \in \mathcal{F}_T} \mathbf{\Lambda}^h \mathbf{n}|_{A_I} \cdot \int_{A_I} N_I^{(\text{CR})} \, dA \, \mathbf{d}_I^{(u)} \quad (\text{B.16})$$

Since at each element face A_I , where the surface integral is evaluated, the corresponding Crouzeix Raviart basis function has the value $N_I^{(\text{CR})} = 1$ it follows:

$$\sum_{I \in \mathcal{F}_T} \mathbf{\Lambda}^h \mathbf{n}|_{A_I} \cdot \int_{A_I} N_I^{(\text{CR})} \, dA \, \mathbf{d}_I^{(u)} = \sum_{I \in \mathcal{F}_T} \mathbf{\Lambda}^h \mathbf{n}|_{A_I} \cdot A_I \, \mathbf{d}_I^{(u)}$$

¹ $\mathbf{\Lambda}^h$ is embedded in $H(\text{Div}; \mathcal{B}; \mathbf{R}^{3 \times 3})$, since normal continuity is enforced through the interface constraint term.

Table B.1: Comparing $\nabla_{\boldsymbol{\xi}^R} N_I^{(\text{CR})}$ with geometric quantities of the reference tetrahedron. The volume of the reference tetrahedron is $V^R = 1/6$

I	A_I^R	$\mathbf{n} _{A_I^R}$	$\frac{A_I^R}{V^R} \mathbf{n} _{A_I^R}$	$\nabla_{\boldsymbol{\xi}^R} N_I^{(\text{CR})}$
1	$\sqrt{3}/2$	$1/\sqrt{3}(1, 1, 1)^T$	$3(1, 1, 1)^T$	$3(1, 1, 1)^T$
2	$1/2$	$(0, 0, -1)^T$	$3(-1, 0, 0)^T$	$3(-1, 0, 0)^T$
3	$1/2$	$(0, -1, 0)^T$	$3(0, -1, 0)^T$	$3(0, -1, 0)^T$
4	$1/2$	$(-1, 0, 0)^T$	$3(0, 0, -1)^T$	$3(0, 0, -1)^T$

Reordering leads to the notation

$$\sum_{I \in \mathcal{F}_T} \boldsymbol{\Lambda}^h \mathbf{n}|_{A_I} \cdot A_I \mathbf{d}_I^{(u)} = \boxed{\boldsymbol{\Lambda}^h \cdot \sum_{I \in \mathcal{F}_T} (\mathbf{d}_I^{(u)} \otimes A_I \mathbf{n}|_{A_I})} \quad (\text{B.17})$$

Right-hand side of (B.15) (first term): Inserting (5.32) into the first term of the right-hand side of (B.15) and rearranging terms similar to (B.17) leads to the following expression:

$$\int_T \boldsymbol{\Lambda}^h \cdot \nabla \mathbf{u}^h \, dV = \boldsymbol{\Lambda}^h \cdot \sum_{I \in \mathcal{F}_T} (\mathbf{d}_I^{(u)} \otimes \int_T \nabla N_I^{(\text{CR})} \, dV) \quad (\text{B.18})$$

We now show that $\int_T \nabla N_I^{(\text{CR})} \, dV = A_I \mathbf{n}|_{A_I}$ and therefore (B.17) being identical to (B.18). For this we consider the reference tetrahedron and compute $\nabla_{\boldsymbol{\xi}^R} N_I^{(\text{CR})}$, where $\nabla_{\boldsymbol{\xi}^R}(\bullet)$ is the gradient with respect to the reference coordinates $\boldsymbol{\xi}^R$. A simple comparison of $\nabla_{\boldsymbol{\xi}^R} N_I^{(\text{CR})}$ with geometric quantities of the reference tetrahedron (cf. table B.1) yields

$$\nabla_{\boldsymbol{\xi}^R} N_I^{(\text{CR})} = \frac{A_I^R}{V^R} \mathbf{n}|_{A_I^R}$$

where A_I^R , $\mathbf{n}|_{A_I^R}$ and V^R denote the face area, corresponding normal vector and volume of the reference tetrahedron. From inserting relations (3.21), (3.29) and (3.30) it follows:

$$\nabla N_I^{(\text{CR})} = \nabla_{\boldsymbol{\xi}^R} N_I^{(\text{CR})} \mathbf{J}^{-1} = \frac{A_I}{V} \mathbf{n}|_{A_I}$$

Since all coefficients are constant, the volume integral simplifies to $\int_T dV/V = 1$ so that

$$\int_T \nabla N_I^{(\text{CR})} \, dV = A_I \mathbf{n}|_{A_I}$$

holds. Inserting into (B.18) yields

$$\int_T \boldsymbol{\Lambda}^h \cdot \nabla \mathbf{u}^h \, dV = \boxed{\boldsymbol{\Lambda}^h \cdot \sum_{I \in \mathcal{F}_T} (\mathbf{d}_I^{(u)} \otimes A_I \mathbf{n}|_{A_I})} \quad (\text{B.19})$$

Since (B.17) and (B.19) are equivalent, the remaining term $\int_T \text{Div} \boldsymbol{\Lambda}^h \cdot \mathbf{u}^h \, dV = 0$ must be zero and expression (B.13) simplifies to (5.29)². \square

Note, that as a consequence, for the chosen spaces $\boldsymbol{\Lambda}^h \in P0(\mathcal{T}; \mathbf{R}^{3 \times 3}) \cap H(\text{Div}; \mathcal{B}; \mathbf{R}^{3 \times 3})$ and $\mathbf{u}^h \in CR0(\mathcal{T}; \mathbf{R}^3)$ constraint term (5.29) and $\int_T \boldsymbol{\Lambda}^h \cdot \nabla \mathbf{u}^h \, dV$ are interchangeable.

²Again, due to all coefficients being constant the integral is replaced by $\int_{\partial T \setminus \partial \mathcal{B}} \mathbf{n}|_{\partial T} = \sum_{I \in \mathcal{F}_T} A_I \mathbf{n}_I$

List of Figures

4.1	Visualization of dofs of the P9-C1-Element and polynomial space dimensions	51
4.2	Interpolation convergence of the P9-C1 element	54
4.3	Visualizations of the C^0 continuity condition	55
4.4	Visualizations of the C^1 continuity condition	56
4.5	Convergence of the displacement based formulations (biharmonic- and Laplace problem)	58
4.6	Singular value spectra of the P9-C1 element compared to the P2-Lagrange element	59
5.1	Visualization of the dofs of the $\text{CR}_{\mathbf{u}}\text{-P1B}_{\mathbf{H}}\text{-P0}_{\mathbf{\Lambda}}$ formulation	73
7.1	Unit cube problem description	92
7.2	Unit cube convergence results for $l = 0.1$ mm and type- II nonlocal model . .	93
7.3	Unit cube convergence results for $l = 0.1$ mm and type- I nonlocal model . . .	94
7.4	Unit cube convergence of $\ \text{Rot } \mathbf{H}^h\ _{L^2}$	94
7.5	Unit cube convergence for $\psi \in \mathcal{I}^I$ and varying values of l	95
7.6	Unit cube convergence for $\psi \in \mathcal{I}^{II}$ and varying values of l	97
7.7	3D Cook's problem description and contour plots	98
7.8	3D Cook's problem: Size effect-, avoiding localization and performance plots .	99
7.9	Plate with hole problem description and example mesh	100
7.10	Plate with hole contour plots showing $\langle \psi \rangle_T$ for the Hu-Washizu formulations .	101
7.11	Convergence results of the plate with hole benchmark test	102
8.1	Plate with hole benchmark problem description	110
8.2	Visualization of the mesh dependency of the local damage formulation	111
8.3	F-u curves of the gradient damage penalty formulation ($\text{P2}_{\mathbf{u}}\text{-P1}_{\alpha}\text{-pen}$)	114
8.4	Convergence results of the neighbored element gradient damage formulation .	117
8.5	Time step convergence of the neighbored element gradient damage formulation	118
9.1	F-u curves and contour plots of the tetrahedral $\text{P2}_{\mathbf{u}}\text{-P1B}_{\alpha}\text{-P0}_{\lambda}$ gradient damage formulation	127
9.2	F-u curves and contour plots of the hexahedral $\text{Q2}_{\mathbf{u}}\text{-Q1B}_{\alpha}\text{-P0}_{\lambda}$ gradient damage formulation	128

9.3	Comparative study of convergence and total computing time of the proposed gradient damage approach	130
9.4	F-u curves and contour plots of the $P2_{\mathbf{u}}-P1B_{\alpha}-P0_{\lambda}$ element for cyclic loading	132
9.5	F-u curves and contour plots of the $P2_{\mathbf{u}}-P1B_{\alpha}-P0_{\lambda}$ element with erosion . . .	134
9.6	F-u curves of the $P2_{\mathbf{u}}-P1B_{\alpha}-P0_{\lambda}$ element for various parameter ranges	135

List of Tables

3.1	Overview of traces of selected Sobolev spaces	33
6.1	Overview of 2D RotFEM interpolation schemes	84
6.2	Overview of 3D RotFEM interpolation schemes	85
7.1	Overview of values of the rot-rot parameter used throughout the tests of chapter 7	103
7.2	Overview of the main observations made throughout the tests of chapter 7	103
B.1	Kinematic relations specific to Crouzeix Raviart functions	153

Bibliography

- B.E. Abali. Revealing the physical insight of a length-scale parameter in metamaterials by exploiting the variational formulation. *Continuum Mech. Thermodyn.*, 31:885–894, 2018.
- B.E. Abali, W.H. Müller, and F. dell’Isola. Theory and computation of higher gradient elasticity theories based on action principles. *Arch. Appl. Mech.*, 87:1495–1510, 2017.
- P. Alfeld. A trivariate clough-tocher scheme for tetrahedral data. *Computer Aided Geometric Design*, 1:169–181, 1984.
- H. Altenbach. *Kontinuumsmechanik*. Springer Vieweg, 2 edition, 2012.
- C. Amrouche and V. Girault. Problèmes généralisés de Stokes. *Portugal. Math.*, 49(4): 463–503, 1992. ISSN 0032-5155.
- J. Argyris and D.W. Scharpf. The tuba family of plate elements for the matrix displacement method. *Aeronautical Journal*, 72:701–709, 1968.
- D. Arnold. Mixed finite element methods for elliptic problems. *Comp. Methods Appl. Mech. Eng.*, 82:291–300, 1990.
- D. Arnold and F. Brezzi. Mixed and nonconforming finite element methods: implementation, postprocessing and error estimates. *Math. Anal. Numer.*, 19(1):7–32, 1985.
- D.N Arnold and R. Winther. Mixed finite elements for elasticity. *Numer. Math.*, 92:401–419, 2002.
- D.N Arnold, R.S. Falk, and R. Winter. *Finite element exterior calculus, homological techniques, and applications*. Acta Numerica, pp.1-155, 2006.
- D.N Arnold, G. Awanou, and R. Winther. Finite elements for symmetric tensors in three dimensions. *Mathematics of Computations*, 77(263):1229–1251, 2008.
- H. Askes and E.C. Aifantis. Gradient elasticity in statics and dynamics: An overview of formulation, length scale identification procedures, finite element implementations and new results. *Int. J. Solids Struct.*, 48:1962–1990, 2011.
- I. Babuška. The finite element method with lagrangian multipliers. *Numerische Mathematik*, 20(3):179–192, 1973.
- I. Babuška and J. Pitkäranta. The plate paradox for hard and soft simple support. *SIAM J. Math. Anal.*, 21:551–576, 1990.
- D. Balzani and M. Ortiz. Relaxed incremental variational formulation for damage at large strains with application to fiber-reinforced materials and materials with truss-like microstructures. *Int. J. Numer. Meth. Eng.*, 92:551–570, 2012. .DOI: 10.1002/nme.4351.

- D. Balzani, J. Schröder, and D. Gross. Simulation of discontinuous damage incorporating residual stresses in circumferentially overstretched atherosclerotic arteries. *Acta Biomaterialia*, 2006.
- D. Balzani, S. Brinkhues, and G. Holzapfel. Constitutive framework for the modeling of damage in collagenous soft tissues with application to arterial walls. *Comp. Methods Appl. Mech. Engrg.*, 2012.
- H. Bayat, J. Krämer, L. Wunderlich, S. Wulfinghoff, S. Reese, B. Wohlmuth, and C. Wieners. Numerical evaluation of discontinuous and nonconforming finite element methods in nonlinear solid mechanics. *Computational Mechanics*, 62:1413–1427, 2019.
- T. Belytschko. *Computational methods for transient analysis*. North-Holland, 1986. ISBN 97804444864796.
- A. Bentley. Explicit construction of computational bases for rtk and bdmk spaces in r3. *Computers and Mathematics with Applications*, 73:1421–1432, 2017.
- A. Bertram. *Compendium on Gradient Materials*. Springer, 2022.
- F. Bertrand and G. Starke. Parametric raviart-thomas elements for mixed methods on domains with curved surfaces. *SIAM*, 54(6):3648–3667, 2016.
- D. Bertsekas. *Constrained Optimization and Lagrange Multiplier Methods*. Academic Press, 1982.
- D. Boffi, F. Brezzi, and M. Fortin. *Mixed Finite Element Methods and Applications*. Springer, 2013.
- B. Bourdin, A. Francfort, and J. Marigo. Numerical experiment in revisited brittle fracture. *J. Mech. and Phys. of Solids*, 48(4), 2000. doi: 10.1016/S0022-5096(99)00028-9.
- D. Braess. *Finite Elemente*. Springer, 2007. pp.162-163.
- S.C Brenner and L.R. Scott. *The mathematical theory of finite element methods*. Springer, 1994.
- S.C Brenner and L.Y. Sung. c^0 interior penalty methods for fourth order elliptic boundary value problems on polygonal domains. *Journal of Scientific Computing*, 22 and 23, 2005.
- F. Brezzi. On the existence, uniqueness and approximation of saddle-point problems arising from lagrangian multipliers. *Rev. fr. d'autom., inform. rech. op.. Analyse numer.*, 8(2): 129–151, 1974.
- F. Brezzi and M. Fortin. *Mixed and Hybrid Finite Element Methods*. Springer, New York, 1991.
- Franco Brezzi, Jim Douglas, and L. Donatella Marini. Two families of mixed finite elements for second order elliptic problems. *Numerische Mathematik*, 47:217–235, 1985. doi: 10.1007/BF01389710.
- C. Carstensen, D. Gallistl, and J. Gedicke. Residual-based a posteriori error analysis for symmetric mixed arnold-winther fem. *Numer. Math.*, 142:205–234, 2019.
- A.-L. Cauchy. Recherches sur l'équilibre et le mouvement intérieur des corps solides ou fluides, élastiques ou non élastiques. *Bull. Soc. Philomath. Paris*, 1823.

- P. Ciarlet. *The finite element method for elliptic problems*. North-Holland, 1978.
- P.G. Ciarlet and P.A. Raviart. General lagrange and hermite interpolation in rn with applications to finite element methods. *Archive for Rational Mechanics and Analysis*, 46:177–199, 1972.
- R.W. Clough and J.L Tocher. Finite element stiffness matrices for analysis of plates in bending. page 515–545, October 1965.
- E. Cosserat and F. Cosserat. Théorie des corps déformables. *Nature*, 81(67), 1909.
- M. Crouzeix and P.A. Raviart. Conforming and nonconforming finite element methods for solving the stationary stokes equations i. *RAIRO Anal. Numer.*, 7(33):33–75, dec 1973.
- R. de Borst and C.V. Verhoosel. Gradient damage vs phase-field approaches for fracture: Similarities and differences. *Computer Methods in Applied Mechanics and Engineering*, 312: 78–94, December 2016.
- F. dell’Isola, G. Sciarra, and S. Vidoli. Generalized hooke’s law for isotropic second gradient materials. *Proceedings of the Royal Society A*, 465(2107), 2018.
- B.J. Dimitrijevic and K. Hackl. A method for gradient enhancement of continuum damage models. *Techn. Mech.*, 28(1), 2008.
- A. Eringen. *Nonlocal Continuum Field Theories*. Springer, New York, 1 edition, 2002.
- A.C. Eringen. *Microcontinuum field theories I: foundations and solids*. Springer, 1999.
- A. Ern and J.L. Guermond. *Theory and practice of finite elements*. Springer, 2004.
- L. Euler. Découverte d’un nouveau principe de mécanique. *Mémoires de l’académie des sciences de Berlin*, (6):185–217, 1752.
- M. Fortin. An analysis of the convergence of mixed finite element methods. *RAIRO Anal. Numer.*, 11:341–354, 1977.
- C. Fox. *An Introduction to the Calculus of Variations*. Dover Publications, 1987.
- A. Francfort and J. Marigo. Revisiting brittle fracture as an energy minimization problem. *J. Mech. and Physics of Solids*, 46(8):1319–1342, 1998. doi: 10.1016/S0022-5096(98)00034-9.
- D. Gallistl. Stable splitting of polyharmonic operators by generalized stokes systems. *Math. Comp.*, 86(308):2555–2577, 2017.
- I.M. Gelfand and S.V. Fomin. *Calculus of Variations*. Dover Publications, 2000.
- T. Gerasimov and L. De Lorenzis. On penalization in variational phase-field models of brittle fracture. *Comput. Methods Appl. Mech. Engrg.*, 354:990–1026, 2019. doi: 10.1016/j.cma.2019.05.038.
- A. Grundmann and H.M. Möller. Invariant integration formulas for the n-simplex by combinatorial methods. *SIAM J. Numer. Anal.*, 15(2):282–290, April 1978.
- E. Gürses and C. Miehe. On evolving deformation microstructures in non-convex partially damage solids. *Journal of Mechanics and Physics of Solids*, 59:1268–1290, 2011. doi: 10.1016/j.jmps.2011.01.002.

- E. Hellinger. *Die allgemeinen Ansätze der Mechanik der Kontinua*, volume 5 of *Encyklopädie der mathematischen Wissenschaften*. 1913.
- H. Helmholtz. Über integrale der hydrodynamischen gleichungen, welche den wirbelbewegungen entsprechen. *Journal für die reine und angewandte Mathematik*, 55:25–55, 1858.
- R. Hooke. *Lectures De Potentia Restitutiva, or of Spring Explaining the Power of Springing Bodies*. 1678.
- H.C. Hu. On some variational principles in the theory of elasticity and the theory of plasticity. *Science Sinica*, 4:33–54, 1955.
- T.J.R. Hughes, J.A. Cottrell, and Bazilevs Y. Isogeometric analysis: Cad, finite elements, nurbs, exact geometry and mesh refinement. *Comp. Methods Appl. Mech. Eng.*, 194(39): 4135–4195, 2005.
- Freund. J. and R. Stenberg. On weakly imposed boundary conditions for second order problems. October 1995.
- P. Junker and D. Balzani. An extended hamilton principle as unifying theory for coupled problems and dissipative microstructure evolution. *Continuum. Mech. Thermodyn.*, 2021. doi: 10.1007/s00161-021-01017-z.
- P. Junker, S. Schwarz, D.R Jantos, and K. Hackl. A fast and robust numerical treatment of a gradient-enhanced model for brittle damage. *Int. J. Multisc. Comp. Eng.*, 17(2):151–180, 2019.
- P. Junker, J. Riesselmann, and D. Balzani. Efficient and robust numerical treatment of a gradient-enhanced damage model at large deformations. *Int. J. Numer. Methods Eng.*, 123(3):774–793, 2022. doi: 10.1002/nme.6876.
- L.M. Kachanov. *Introduction to continuum damage mechanics*. Mechanics of elastic stability. Springer-Science+Business Media, 1986.
- R.C. Kirby. A general approach to transforming finite elements. *SIAM J.Comp.Math.*, 4: 197–224, 2018.
- M. Köhler and D. Balzani. Evolving microstructures in relaxed continuum damage mechanics for the modeling of strain softening. *J. Mech. Phys. Solids*, 173, April 2023.
- O. Ladyzhenskaya. *The mathematical theory of viscous incompressible flow*, volume 76. Gordon and Breach, 1969.
- M.J. Lai and L.L Schumaker. *Spline functions on triangulations*, volume 110 of *Encyclopedia of Mathematics and its Applications*. Cambridge University Press, 2007.
- P. Lax and A. Milgram. Parabolic equations. In *Contributions to the theory of partial differential equations*, number 33 in Annals of Mathematics Studies, page 167–190, 1954.
- J. Lemaitre. How to use damage mechanics. *Nuclear Engineering and Design*, 1984.
- J. Lemaitre and J.L. Chaboche. *Mechanics of solid materials*. Cambridge University Press, 1990.

- T. Liebe, P. Steinmann, and A. Benallal. Theoretical and computational aspects of a thermodynamically consistent framework for geometrically linear gradient damage. *Comput. Methods Appl. Mech. Engrg.*, 2001.
- L.D. Marini. An inexpensive method for the evaluation of the solution of the lowest order raviart-thomas mixed method. *SIAM*, 22(3):493–496, 1985. doi: 10.1137/0722029.
- B. Marussig and T.J.R. Hughes. A review of trimming in isogeometric analysis: challenges, data exchange and simulation aspects. *Archives of Computational Methods in Engineering*, 25:1059–1127, 2018.
- A. Menzel and P. Steinmann. A theoretical and computational framework for anisotropic continuum damage mechanics at large strains. *Int. J. Solids Structures*, 38(52):9505–9523, 2001. doi: 10.1016/S0020-7683(01)00136-6.
- C. Miehe. Discontinuous and continuous damage evolution in ogden-type large-strain elastic materials. *Eur. J. Mech. A-Solid*, 14:697–720, 1995.
- C. Miehe. A multi-field incremental variational framework for gradient-extended standard dissipative solids. *Journal of Mechanics and Physics of Solids*, 59:898–923, 2011.
- C. Miehe, M. Hofacker, and F. Welschinger. A phase field model for rate-independent crack propagation: Robust algorithmic implementation based on operator splits. *Comp. Methods Appl. Mech. Engrg.*, 199:2765–2778, 2010a. doi: 10.1016/j.cma.2010.04.011.
- C. Miehe, F. Welschinger, and M. Hofacker. Thermodynamically consistent phase-field models of fracture: Variational principles and multi-field fe implementations. *Int. J. Numer. Meth. Engrg.*, 83:1273–1311, 2010b. doi: 10.1002/nme.2861.
- C. Miehe, F. Aldakheel, and A. Raina. Phase field modeling of ductile fracture at finite strains: A variational gradient-extended plasticity-damage theory. *International Journal of Plasticity*, 84:1–32, 2016. doi: 10.1016/j.ijplas.2016.04.011.
- R. Mindlin. Micro-structure in linear elasticity. *Arch. Ration. Mech. Anal.*, 16:51–78, 1964.
- L. S. D. Morley. The triangular equilibrium element in the solution of plate bending problems. *Aeronautical Quarterly*, 19(2):149–169, 1968. doi: 10.1017/S0001925900004546.
- I. Münch and P. Neff. Rotational invariance conditions in elasticity, gradient elasticity and its connection to isotropy. *Mathematics and Mechanics of Solids*, 23(1):3–42, 2018.
- J. Nedèlec. Mixed finite element in \mathbb{R}^3 . *Numer. Math.*, 35:315–341, 1980.
- J.C. Nedèlec. A new family of mixed finite elements in \mathbb{R}^3 . *Numer. Math.*, (50):57–81, 1986.
- N.M. Newmark. A method of computation for structural dynamics. *Journal of Engineering Mechanics*, 85(EM3):67–94, 1959.
- I. Newton. 1687.
- T.K. Nilssen, X.Ch. Tai, and R. Winther. A robust nonconforming h^2 -element. *Mathematics of Computations*, 70(234):489–505, 2000.
- J. Nitsche. Über ein variationsprinzip zur lösung von dirichlet-problemen bei verwendung von teilräumen, die keinen randbedingungen unterworfen sind. *Abhandlungen aus dem Mathematischen Seminar der Univ. Hamburg*, 36:9–15, 1971.

- M. Okabe. Full-explicit interpolation formulas for the argyris triangle. *Computer Methods in Applied Mechanics and Engineering*, 106:381–394, 1993.
- M. Ortiz and G.R. Morris. C0 finite element discretization of kirchhoff’s equations of thin plate bending. *Int. J. Numer. Meth. Eng.*, 1988.
- S. Papanicolopoulos, A. Zervos, and I. Vardoulakis. A three-dimensional c^1 finite element for gradient elasticity. *Int. J. Numer. Meth. Eng.*, 77:1396–1415, 2008.
- R.H.J. Peerlings, A.M. de Borst, R. an Breckelmans, and J.H.P. de Vree. Gradient enhanced damage for quasi-brittle materials. *International Journal for Numerical Methods in Engineering*, 39:3391–3403, 1996.
- L Placidi., E. Barchiesi, A. Misra, and D. Timofeev. Micromechanics-based elasto-plastic-damage energy formulation for strain gradient solids with granular microstructure. *Continuum Mech. Thermodyn.*, 33:2213–2241, 2021.
- H. Pulte. *Das Prinzip der Kleinsten Wirkung und die Kraftkonzeptionene der Rationalen Mechanik - Eine Untersuchung zur Grundlegungsproblematik bei Leonard Euler, Pierre Louis Moreau de Maupertuis und Joseph Louis Lagrange*. Franz Steiner Verlag, 1989.
- P.A. Raviart and J.M. Thomas. A mixed finite element method for 2-nd order elliptic problems. In *Mathematical aspects of finite element methods*, Lecture notes in mathematics, page 292–315, 1977.
- E. Reissner. On a variational theorem in elasticity. *J. Mathematical Physics*, 29:90–95, 1950.
- N. Rezaei, E. Barchiesi, D. Timofeev, C.A. Tran, A. Misra, and L Placidi. Solution of a paradox related to the rigid bar pull-out problem in standard elasticity. *Mechanics Research Communications*, 126, 2022.
- J. Riesselmann and D. Balzani. A simple and efficient lagrange multiplier based mixed finite element for gradient damage. *Computers and Structures*, 281:107030, 2023. doi: 10.1016/j.compstruc.2023.107030.
- J. Riesselmann, J.W. Ketteler, M. Schedensack, and D. Balzani. Three-field mixed finite element formulations for gradient elasticity at finite strains. *GAMM Mitteilungen*, 2019. doi: 10.1002/gamm.20200002.
- J. Riesselmann, J. Ketteler, M. Schedensack, and D. Balzani. Rot-free mixed finite elements for gradient elasticity at finite strains. *Int. J. Numer. Methods Eng.*, 122(6):1602–1628, 2021. doi: 10.1002/nme.6592.
- J. Riesselmann, N. Rezaei, L Placidi., and D. Balzani. An efficient mixed finite element formulation for 3d strain gradient elasticity. *Comp. Methods Appl. Mech. Engrg.*, 432, 2024. doi: 10.1016/j.cma.2024.117422.
- S. Rudraraju, A. Van der Ven, and K. Garikipati. Three-dimensional isogeometric solutions to general boundary value problems of toupin’s gradient elasticity theory at finite strains. *Comp. Methods Appl. Mech. Engrg.*, 278:705–728, 2014.
- M. Schedensack. *A class of mixed finite element methods based on the Helmholtz decomposition in computational mechanics*. PhD thesis, Humboldt University Berlin, 2015.

- T. Schmidt and D. Balzani. Relaxed incremental variational approach for the modeling of damage-induced stress hysteresis in arterial walls. *J. of the Mech. Behavior of Biomedical Materials*, 58:149–162, 2016.
- A. Schwarz. *Least-Squares Mixed Finite Elements for Solid Mechanics*. PhD thesis, University Duisburg Essen, 2009.
- S. Schwarz, P. Junker, and K. Hackl. Variational regularization of damage models based on the emulated rve. *Cont. Mech. and Thermodyn.*, 2020.
- J. Schöberl. Numerical methods for maxwell equations, 2009.
- P. Serrao and S. Kozinov. Robust mixed fe for analyses of higher order electromechanical coupling in piezoelectric solids. *Computational Mechanics*, November 2023.
- J.Y. Shu, W.E. King, and N.A. Fleck. Finite elements for materials with strain gradient effects. *Int. J. Numer. Meth. Engng.*, 44:373–391, 1999.
- P. Solin, K. Segeth, and I. Dolezel. *Higher-Order Finite Element Methods*. Chapman and Hall/CRC, 2004.
- M. Tabata and Y. Ueda. A set of variant hermite tetrahedral elements for three-dimensional problems. *Journal of Math for Industry*, 1(2009B-6):131–138, 2009.
- K Tannhäuser, P. Serrao, and S. Kozinov. A three-dimensional collocation finite element method for higher-order electromechanical coupling. *Computers and Structures*, 291, January 2024.
- A. Ten Eyck and A. Lew. Discontinuous galerkin methods for nonlinear elasticity. *Int. J. Numer. Meth. Eng.*, 00:1–6, 2000.
- R. Toupin. Theories of elasticity with couple-stress. *Arch. Ration. Mech. Anal*, 17:85–112, 1964.
- N. Triantafyllidis and E.C. Aifantis. A gradient approach to localization of deformation in hyperelastic materials. *Journal of Elasticity*, 16:225–237, 1986.
- J. Ventura, D. Codony, and S. Fernández-Méndez. A c^0 interior penalty finite element method for flexoelectricity. *J. Scientific Comp.*, 88, 2021.
- N. Viebahn. *A contribution to stress-displacement based mixed galerkin finite elements for hyperelasticity*. PhD thesis, Universitaet Duisburg-Essen, 2019.
- N. Viebahn, K. Steeger, and J. Schröder. A simple and efficient hellinger-reissner type mixed finite element for nearly incompressible elasticity. *Comp. Methods Appl. Mech. Engrg.*, 340: 278–295, 2018.
- A. Vogel and P. Junker. Adaptive and highly accurate numerical treatment for a gradient-enhanced brittle damage model. *Int. J. Numer. Meth. Eng.*, 2019.
- T. Waffenschmidt, C. Polindara, A. Menzel, and S. Blanco. A gradient-enhanced large-deformation continuum damage model for fibre-reinforced materials. *Comp. Methods Appl. Mech. Engrg.*, 268:801–842, 2013.
- N.J. Walkington. A c^1 tetrahedral finite element without edge degrees of freedom. *SIAM J. Numer. Anal.*, 52(1):330–342, 2014.

- Z. Wang, S. Rudraraju, and K. Garikipati. A three-dimensional field formulation and isogeometric solutions to point and line defects using toupin's theory of gradient elasticity at finite strains. *Journal of the Mechanics and Physics of Solids*, 94:336–361, 2016.
- K. Washizu. On the variational principles of elasticity and plasticity. Technical report, March 1955.
- P. Wriggers. *Nonlinear Finite Element Methods*. Springer, 2008.
- P. Wriggers and B. Hudobivnik. Virtual element formulation for gradient elasticity. *Acta Mechanica Sinica*, 39, 2023.
- H. Yang, B.E. Abali, D. Timofeev, and W.H. Müller. Determination of metamaterial parameters by means of a homogenization approach based on asymptotic analysis. *Continuum Mech. Thermodyn.*, DOI <https://doi.org/10.1007/s00161-019-00837-4>, 2019.
- S. Zhang. A family of 3d continuously differentiable finite elements on tetrahedral grids. *Applied Numerical Mathematics*, 59:219–233, 2008.
- O.C. Zienkiewicz and R.L. Taylor. *The Finite Element Method Volume 1: The Basis*. Butterworth-Heinemann, 5 edition, 2000.
- L. Zybelle, U. Mühlich, M. Kuna, and Z.L. Zhang. A three-dimensional finite element for gradient elasticity based on a mixed-type formulation. *Computational Materials Science*, 52:268–273, 2012.
- A. Ženišek. Polynomial approximation on tetrahedrons in the finite element method. *Journal of Approximation Theory*, 7:334–351, 1973.

List of Publications

- Riesselmann, J., Ketteler, J., Schedensack, M., and Balzani, D. Three-field mixed finite element formulations for gradient elasticity at finite strains. *GAMM Mitteilungen*, 2019a. doi:10.1002/gamm.20200002.
- Riesselmann, J., Ketteler, J., Schedensack, M., and Balzani, D. A new C0-continuous FE-formulation for finite gradient elasticity. *Proceedings in Applied Mathematics and Mechanics*, 19:1, 2019b. doi:10.1002/pamm.201900341.
- Riesselmann, J., Ketteler, J., Schedensack, M., and Balzani, D. C0 continuous finite elements for gradient elasticity at finite strains. *Proceedings of the 8th GACM Colloquium on Computational Mechanics for Young Scientists from Academia and Industry*, page 27–30, 2019c. doi:10.19211/KUP9783737650939.
- Riesselmann, J., Junker, P., and Balzani, D. Efficient numerical treatment of a gradient damage model for materials undergoing large deformations. *Proceedings in Applied Mathematics and Mechanics*, 21(1):e202100153, 2021a. doi:10.1002/pamm.202100153.
- Riesselmann, J., Ketteler, J., Schedensack, M., and Balzani, D. Rot-free finite elements for gradient-enhanced formulations at finite strains. *Proceedings in Applied Mathematics and Mechanics*, 20(1):e202000069, 2021b. doi:10.1002/pamm.202000069.
- Riesselmann, J., Ketteler, J., Schedensack, M., and Balzani, D. Rot-free mixed finite elements for gradient elasticity at finite strains. *Int. J. Numer. Methods Eng.*, 122(6):1602–1628, 2021c. doi:10.1002/nme.6592.
- Junker, P., Riesselmann, J., and Balzani, D. Efficient and robust numerical treatment of a gradient-enhanced damage model at large deformations. *Int. J. Numer. Methods Eng.*, 123(3):774–793, 2022. doi:10.1002/nme.6876.
- Riesselmann, J. and Balzani, D. Finite element formulations for gradient damage at finite strains. In F. e. a. Aldakheel, editor, *Current Trends and Open Problems in Computational Mechanics*, page 443–452. Springer, 2022. doi:10.1007/978-3-030-87312-7_43.
- Riesselmann, J., Ketteler, J., Schedensack, M., and Balzani, D. Robust and efficient finite element discretizations for higher-order gradient formulations. In *Non-standard Discretisation Methods in Solid Mechanics*, page 69–90. Springer, 2022. doi:10.1007/978-3-030-92672-4_3.
- Riesselmann, J. and Balzani, D. A simple and efficient lagrange multiplier based mixed finite element for gradient damage. *Computers and Structures*, 281:107030, 2023. doi:10.1016/j.compstruc.2023.107030.

- Rezaei, N., Riesselmann, J., Misra, A., Balzani, D., and Placidi, L. A procedure for the experimental identification of the strain gradient characteristic length. *Z. Angew. Math. Phys.*, page 75:80, 2024. doi:10.1007/s00033-023-02181-9.
- Riesselmann, J., Rezaei, N., Placidi, L., and Balzani, D. An efficient mixed finite element formulation for 3d strain gradient elasticity. *Comp. Methods Appl. Mech. Engrg.*, 432, 2024. doi:10.1016/j.cma.2024.117422.

Personal Information

AUTHOR'S NAME Johannes Riesselmann

PLACE OF BIRTH Münster, Germany

DATE OF BIRTH 18 December 1989

Education

2018 - 2024 PhD student and member of RUB Research School
Chair of Continuum Mechanics, Ruhr University Bochum, Germany

2015 - 2017 Mechanical Engineering (Master of Science)
focus on Applied Mechanics, Ruhr University Bochum, Germany

2012 - 2015 Environmental Technology and Resource Management (Bachelor of Science)
Ruhr University Bochum, Germany

2009 Abitur (A-levels): Ruhr Gymnasium, Witten, Germany

**Mitteilungen aus dem Institut für Mechanik
RUHR-UNIVERSITÄT BOCHUM
Nr. 194**

ISBN 978-3-935892-72-8